Dark Substructures and Model Complexity in Strong Gravitational Lensing

SAMUEL CHARLES LANGE

Dark Substructures and Model Complexity in Strong Gravitational Lensing

Relationships between subhalos, multipoles and the external shear of lens galaxies

A thesis presented for the degree of Doctor of Philosophy

by

Samuel C. Lange

Centre for Computational Cosmology

The University of Durham

United Kingdom

November 2025

First submitted August 2025

Dedicated to

Professor Roderyk Lange, my Grandpa, whose determination and work ethic in life inspired me to continue in academia in the most difficult and stressful moments.

Dark Substructures and Model Complexity in Strong Gravitational Lensing

Samuel C. Lange

Supervisors: Carlos Frenk and Shaun Cole

Abstract

This work investigates our ability to use strong gravitational lensing as a tool to constrain the nature of dark matter. The assumption is that if we can detect dark subhalos below some cut-off mass in the subhalo mass function, then we can use these detections to place limits on the mass of a dark matter particle. In this Thesis, I first investigate two strong lenses imaged with the relatively new James Webb Space Telescope (JWST), attempting to model the mass distribution of the main deflector including different 'multipole' perturbations to induce angular complexity and also including subhalos in the model. The results for multipole-only additions show strong bayesian evidence for angular mass complexity in on lens - SPT2147, with multipole strengths of 0.3-1.7% for $m = 3, 4$ and 2.4-9.5% for $m = 1$, whilst the other lens - SPT0418 shows no such preference. For lens models with only substructures, I find a strong preference for a substructure in SPT2147-50 with a Bayes factor of ~ 60, however the addition of multipoles as well as substructure reduces the substructure bayesian evidence. With no reasonable prior information that can be placed upon what we expect of multipole strengths, I treat all model structures (multipole-only, substructure-only and multipole+substructure) as equally likely. I find that we return an increase in log bayesian evidence of ~ 11 (still corresponding to a 5σ detection) for a subhalo detection with a mass of $\log_{10}(M_{200}/M_{\odot}) = 10.87^{+0.53}_{-0.71}$ (for a Navarro-Frenk-White model) in a model that also has orders $m = 1$ and $m = 4$ multipoles. I conclude that while SPT2147-50 could represent a new detection of a dark matter substructure in a strong lens, further analysis is needed to confirm that the signal is not due to systematics associated with the lens mass model.

In the second section, I analyse a selection of lenses that have Hubble Space Telescope imaging (from the SLACS and BELLS-GALLERY samples) and attempt to determine

mass-to-light agreement, relationships of model complexity to the external shear, and the effects of multipole perturbations. Comparing a simple model that fits elliptical isophotes of the lens light, where the ellipses have radially constant parameters, I find that there is good agreement between the radially-constant light model, and the commonly used elliptical power-law (EPL) mass distribution (which has parameters that are also radially constant). Comparing this to a model where the angles and ellipticity of the isophotes can vary, I find that the model parameters of these isophotes around the einstein radius match the parameters of the constant model fairly well, demonstrating that for these lenses, it is unlikely that we need to change the EPL for a model with more angular freedom. For the external shear, I find strong evidence that shears that would be considered anomalously high strength ($\gamma > 0.05$) are correlated to the angular variance with the variable-ellipse model, with $p = 0.004$ and $c = 0.73$ for the p-value and linear relationship coefficient.

I also compare the mass and light multipole perturbations of these same lens galaxies, and find that these lens samples are not suitable for an in-depth study of multipoles as the GALLERY lenses are too faint and the SLACS lenses are too smooth. I find no correlation between a change in external shear magnitude and the multipole strength when going from the EPL model to EPL+Multipoles, however there is a correlation between the $m = 4$ multipole strength and the magnitude of external shear itself ($p = 1 \cdot 10^{-4}$, $c = 0.60$). I find that there are generally correlations between k_3 and k_4 multipole strengths, and that mass and light are in general agreement to 3-sigma regarding $m = 4$ strength, but exhibit less agreement on $m = 3$ strength. I also discuss possible origins of mass-light mismatches from high central dark matter fractions and dark halos not being able to match the morphology of strong stellar disks.

Overall, this Thesis contributes to the growing body of work regarding galaxy-scale strong gravitational lensing in three ways. Firstly, it provides a detailed investigation into lenses from one of the newest sources (JWST) and provides an opportunity to discuss the possible degeneracies when trying to detect dark substructures. Second, the Thesis contributes to the understanding of what drives anomalously high external shear magnitudes. Third, it addresses the origins and meaning of different aspects of lens model complexity and considers whether the models we are using are accurate enough, which is essential for the new era of high-quality lenses from JWST and high-volume samples from Euclid.

Acknowledgements

I would like to thank firstly my supervisors, Prof. Carlos Frenk and Prof. Shaun Cole for their committent and attentiveness throughout my PhD. Both being well published and in high demand, I cannot imagine finding the time to mentor me would have been easy. To Carlos in particular, the care shown for my health and wellbeing really allowed me to look after myself properly and avoid (most of) the burnout that often comes alongside doing a PhD, especially when suffering from chronic health conditions! Major thanks is also due to my informal supervisors Dr. James Nightingale, Dr. Aristeidis Amvrosiadis, and Dr. Qiuhan He, who gave up time out of their own postdoctoral work to assist me in learning the basics of strong lensing, getting to grips with paper writing, and pretty much all day-to-day aspects of academic research. James in particular I would not have been able to achieve what I have without; a fount of knowledge, always ready to assist in my academic development, and with an amazing capacity to teach in a friendly way - thank you. In addition I must thank Dr. Russell Smith and Dr. Hannah Stacey for being my PhD examiners and providing feedback which led to important improvements in this Thesis.

Thanks is also due to the entire lensing collaboration that I am a part of - my colleagues at Durham, the USA and Beijing: Prof. Richard Massey, Dr. Andrew Robertson, Prof. Ran Li, Dr. Xiaoyue Cao, Kaihao Wang, Dr. Maximillian von Wietersham-Kramsta, Dr. Leo Fung, Shubo Li and Dr. David Lagattuta - who have all contributed at one time or another in group meetings and corridor conversations to the development of the ideas presented in my work. As well as this, I want to thank to all my friends in the department who have made my time here so special and enjoyable, including Emmy, who in particular has been a rock in times of stress, as well as Marcus, Nency, Zoe, Sarah, Ciera, Dom - you have all made coming to the office fun. I would like to thank my non-academic friends for putting up with my random fluctuations in availability, attention span, and the rest that comes with academic work - my friends from back home: Cameron, Rich, Toby,

Kelly, Alice, Meggan, Conrad, Erin, Jamie; my friends from Durham: Nimet, Nat and everyone at both the Instep Dance Society, and Durham University Dancesport Team. Special thanks goes to my two housemates over the four years - Ziva and Cara, and my dance partner Annabel, I would not have been able to do this without your support and friendship.

My final thanks must go to my family. The dedication of this thesis is to my grandpa who was a choreologist, dance anthropologist, and professor of movement analysis and notation before his passing in 2017, but whose inspiration drives me to this day to keep striving for academic success. To my parents Siobhaun and Anthony, and my sister Rebecca, who have supported me through every day of my PhD, and all the days before it, despite concerns over my health and resulting motivation. Without you I would not have achieved what I have.

Contents

Declaration

The work in this thesis is based on research carried out at the Institute for Computational Cosmology, Department of Physics, University of Durham, England. No part of this thesis has been submitted elsewhere for any other degree or qualification, and it is the sole work of the author unless referenced to the contrary in the text.

Some of the work presented in this thesis has been published in journals and conference proceedings - the relevant publications are listed below.

Publications

The work in Chapter 3 has been published in the form of a paper and included in two conference proceedings:

- Lange, Samuel. C.; Amvrosiadis, Aristeidis.; Nightingale, James. W.; He, Qiuhan; Frenk, Carlos S.; Robertson, Andrew; Cole, Shaun; Massey, Richard; Cao, Xiaoyue; Li, Ran and Wang, Kaihao. (2025). **'Galaxy mass modelling from multi-wavelength JWST strong lens analysis: dark matter substructure, angular mass complexity, or both?'** In: *Monthly Notices of the Royal Astronomical Society* 539 (2), pp. 704–726.

- Lange, S. (2023). 'A bright (or dark!) future with JWST: Dark Matter detection and Sensitivity Mapping from Early Release strong lenses'. In: EAS2023, European Astronomical Society Annual Meeting, 993.

- Lange, S. (2024). 'Galaxy Mass Modelling from Multi-Wavelength JWST Strong Lens Analysis: Dark Matter Substructure, Angular Mass Complexity, or Both?' In: 32nd General Assembly International Union (IAUGA 2024), 2295.

A co-incident study was led on the source galaxies in Chapter 4 by Dr. Aristeidis Amvrosiadis, who produced the source reconstruction images in this chapter, with the work published in:

- Amvrosiadis, A.; Lange, S. C.; Nightingale, J. W.; He, Q.; Frenk, C. S. ; Oman, K. A.; Smail, I.; Swinbank, A. M.; Fragkoudi, F.; Gadotti, D. A.; Cole, S. ; Borsato, E.; Robertson, A.; Massey, R.; Cao, X. and Li, R. (2025). **'The onset of bar formation in a massive galaxy at z $\sim$ 3.8'**. In: *Monthly Notices of the Royal Astronomical Society* 537 (2), pp. 1163–1181.

The mass models in Chapters 4 and 5 were produced by Dr. James Nightingale in a continuation of the published work listed below. All analyses and light modelling was performed by Samuel Lange (the author).

- Nightingale, J. W.; He, Q.; Cao, X.; Amvrosiadis, A.; Etherington, A.; Frenk, C.S.; Hayes, R.G.; Robertson, A.; Cole, S.; Lange, S.; Li, R. and Massey, R. (2024). **'Scanning for dark matter subhaloes in Hubble Space Telescope imaging of 54 strong lenses'**. In: *Monthly Notices of the Royal Astronomical Society* 527 (4), pp. 10480–10506.

List of Figures

List of Tables

Nomenclature

The following acronyms are used regularly through this Thesis.

DM dark matter

CDM Cold dark matter

ΛCDM Lambda-Cold dark matter

WDM Warm dark matter

HDM Hot dark matter

FDM Fuzzy dark matter

SIDM Self-Interacting dark matter

WIMPs Weakly interacting massive particles

JWST James Webb Space Telescope

HST Hubble Space Telescope

ALMA Atacama Large Millimeter Array

SLACS Sloan Lens ACS (Advanced Camera for Surveys)

BELLS-GALLERY Baryon Oscillation Spectroscopic Survey (BOSS) Emission-Line Lens Survey - GALaxy-Lα EmitteR sYstems

SIE Singular Isothermal Ellipsoid

SIS Singular Isothermal Sphereoid

EPL Elliptical Power-Law

MGE Multiple-gaussian expansion

NFW Navarro-Frenk-White

EPLγ Elliptical Power-Law plus External Shear

EPLγ+Multipole Elliptical Power-Law plus External Shear and Multipole(s)

RMS root mean-squared

PSF point spread function

SED Spectral Energy Distribution

SNR signal-to-noise ratio

MEV minimum error value

Chapter 1

Introduction

1.1 The general scope of my PhD work

This PhD began with the sole aim of attempting to falsify or confirm the nature of dark matter (DM) to be 'Cold' or otherwise. The main tool that would be used in this case is galaxy-scale strong gravitational lensing, with the specifics of the methodology to be discussed in later chapters. Almost immediately the scope of the various projects changed from this narrow goal to more general investigation of the structure of the galaxies involved in this type of gravitational lensing, and the systematics and uncertainties which come with this. In this introductory chapter, I will begin by discussing dark matter, its theoretical history and where the field is today, before moving on to introduce the basics of the strong lensing formalism and how this can be used to constrain the nature of dark matter.

1.2 Dark Matter

1.2.1 A brief early history

Dark matter was first theorised in 1933 by Zwicky based on his observations of the mass of the Coma Cluster from the virial theorem (Zwicky, 1933; Zwicky, 1937). Babcock followed Zwicky's theory in 1939 when he published his results on the rotation curve of M31, finding this to require a large amount of mass at large radii - further than that to

which the luminous matter extended (Babcock, 1939). Despite these early indications of problems in the standard theory of the time, over the next few decades the need for Dark Matter was downplayed, with many studies of galactic rotation curves showing relative consistency with the current understanding of galaxies, if the mass-to-light ratios of the different components were adjusted (see e.g. Bertone et al., 2018, for a review).

In the 1970s, the situation changed with the improvements to galaxy rotation measurements brought about by Ford and Rubin's work on M31 (Rubin et al., 1970). Roberts, Whitehurst and Rots (Whitehurst et al., 1972; Roberts et al., 1973) then convinced many that this was a real problem by measuring rotation curves of M31, M101 and M81 via 21cm lines (reaching out to much further than the luminous part of the galaxy). From this, galaxies were theorised to exist within DM halos (Ostriker et al., 1973; White et al., 1978), with initial DM candidates including massive neutrinos (the precursor to Weakly interacting massive particles (WIMPs): Cowsik et al., 1973) and ultra-low-mass or burnt-out-high-mass stellar remnants ('MACHOs': White et al., 1978).

The nature of the DM particle(s) thus began to be (and remains) a subject of fierce debate amongst physicists, as did the process of structure formation, with the contrasting options of 'bottom-up' isothermal hierarchical merging versus 'top-down' adiabatic large-structure fragmentation (see e.g. Frenk et al., 2012). The debate over structure formation, however, provided a useful way to constrain the nature of the DM particle, as certain candidates preclude different structure sizes - for example, the massive standard neutrino, as a candidate for the 'top-down' approach, was calculated to dampen small-scale structure formation by erasing it at early epochs (e.g. Bond et al., 1980). This method of looking at how different candidates affected structure formation led to the coining of the three general classes of Dark Matter: 'hot', 'warm', and 'cold'; based on the typical early-time velocity of the particle. Hot dark matter (HDM), theorised to be a standard model neutrino, was fairly quickly ruled out to constitute the bulk of the dark matter by the use of cosmological simulations (e.g. White et al., 1983; Frenk et al., 1985). This left two options, firstly Warm dark matter (WDM) particles, generally theorised to be non-standard neutrinos such as the sterile neutrino (Dodelson et al., 1994) which is the theoretical right-handed

counterpart to the standard neutrino and has low but non-negligible velocity at early epochs of the Universe, allowing more initial density perturbations to survive compared to the HDM standard-model neutrinos. Alternatively, there could be Cold dark matter (CDM) particles, which initially fell into two categories - supersymmetric particles such as the neutralino (e.g. Goldberg, 1983; Ellis et al., 1984), or axions (e.g. Preskill et al., 1983) - particles whose existence arises due to the broken *U(1)* symmetry in Quantum Chromodynamics (Weinberg, 1978; Wilczek, 1978).

1.2.2 Lambda Cold Dark Matter and its alternatives

Since the 1980s, the accepted standard cosmological model includes CDM as the dark component of the mass of the Universe alongside the cosmological constant - Λ (Lambda). The Lambda-Cold dark matter (ΛCDM) model has been generally highly successful, however there are still some disagreements over the precise particle nature and even the general DM theory (see e.g. Bull et al., 2016; Bullock et al., 2017, for recent reviews). These disagreements arise initially since, although ΛCDM is very successful on large scales, it can still struggle on smaller scales (e.g. Weinberg et al., 2015). Additionally, the large-scale success of CDM does not rule out WDM, since the differences between these models only arise on small scales, hence a lot of work has been undertaken on 'small scale structure' problems. However, many 'problems' that are claimed to affect CDM on small scales simply arise because of the lack of inclusion of baryonic physics in simulations or theory - examples of these 'problems' include the 'cusp vs. core' problem, where CDM predicts an increasing Navarro-Frenk-White (NFW) 'cuspy' density profile towards the centre of a galaxy (Navarro et al., 1997), whereas observations suggest a flatter 'cored' density profile (e.g. Walker et al., 2011); the 'too big to fail' problem, where observations of dwarf galaxies show a much lower density at their half-light radius than expected from simulations (Boylan-Kolchin et al., 2012); and the 'missing satellites' and 'satellite planes' problems where CDM simulations predict many more satellites ($\sim$500) of the Milky Way than are observed (Klypin et al., 1999; Moore et al., 1999) and also do not predict the alignment of Milky Way and M31 satellites, which are in a relatively thin plane (Kroupa et al., 2005).

All of these proposed problems can be solved with the inclusion of baryonic physics in the models, keeping CDM as a successful model until the smallest scales, where we can finally begin to test the differentiation between dark matter candidates (e.g. Weinberg et al., 2015).

Alternative dark matter types that are consistent with CDM on large scales but could be differentiated on small-scales go beyond simply WDM, where the main difference is the reduction in abundance of lower-mass haloes (due to the dampening of structure formation). One strong alternative to CDM is Self-Interacting dark matter (SIDM) (Carlson et al., 1992; Spergel et al., 2000) where, differently to cold or warm dark matter, the dark particle has a non-negligible self-interaction (elastic scattering) cross section, leading to structural changes to inner regions of the DM halo. The inner regions of SIDM haloes have a wide diversity in their density profiles (e.g. Creasey et al., 2017) - the interactions change initially cuspy CDM-like distributions into cores, which can then collapse after further interactions, leading to extreme cusps. These density profile variations allow a comparison to CDM through for example the explanation of the low central density of dwarf galaxies (e.g. Rocha et al., 2013), or through a comparison of the diversity itself (e.g. Robertson et al., 2018). Additionally, there is Fuzzy dark matter (FDM), also known as 'Wave' dark matter (Hu et al., 2000) where the DM is composed of ultralight bosons or axions; these particles have strong wave properties which suppress the power spectrum on small scales (similarly to WDM) and can also give stability to gravitational collapse leading to the halo cores.

The primary constraints on the dark matter particle now come from a mixture of strong gravitational lensing (see next section), the distribution and mass function of Milky Way satellites (e.g. Lovell et al., 2021; Lovell et al., 2023), dwarf galaxy counts (e.g. Newton et al., 2021) and the power spectrum Lyman-α forest (e.g. Narayanan et al., 2000; Iršič et al., 2017). A recent study from Enzi et al. (2021) used a combination of these methods to place constraints on the WDM particle mass and rule out one model of SIDM, and we refer the reader to this paper for more information about the application and combination of these methods, since this is outside the scope of this work.

1.3 Strong gravitational lensing

Strong gravitational lensing is a key tool for astronomers when investigating the nature of dark matter. Whilst strong lensing has other uses such as imaging of sources too faint to directly detect (due to flux magnification) or measurement of cosmological parameters such as the Hubble constant H_0 (e.g. Birrer et al., 2024) (due to image time delays), we will focus on its application in the context of dark matter. For further information on gravitational lensing in general, Meneghetti (2021) and Schneider et al. (2006) are textbooks suitable for a wide range of interests. In terms of review articles, Saha et al. (2024) provides a good overview of the strong lensing essentials, Treu (2010) and Shajib et al. (2024) provide reviews in the context of lensing by galaxies, which is the focus of the work presented in this Thesis, and Vegetti et al. (2024) provides a review in the context of detecting dark matter with strong lensing.

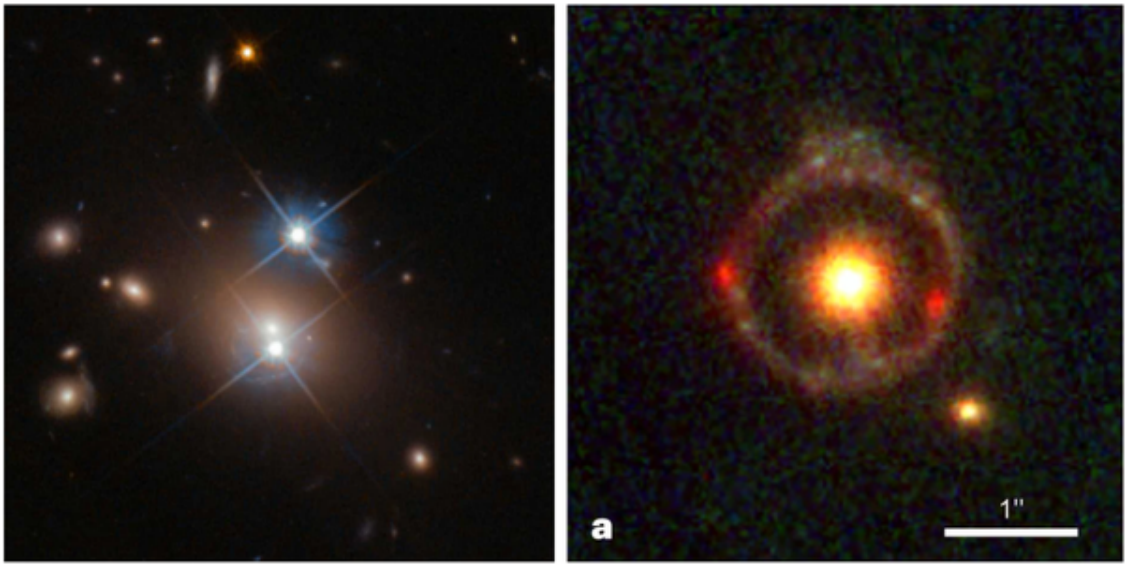

Figure 1.1: Left panel: the first detected strong gravitational lens, the double-imaged quasar Q0957+561 Walsh et al. (1979), image taken from Saha et al. (2024). Right panel: JWST imaging of JWST-ER1, aka the 'Cosmos-Web Ring', one of the most recent gravitational lens discoveries (Mercier et al., 2024; van Dokkum et al., 2024), image from van Dokkum et al. (2024).

1.3.1 Basic lensing formalism

Gravitational lensing is an outcome of the fact that as photons travel through the cosmos from some source, they will pass through an inhomogeneous mass distribution, and in doing so, their trajectory will be perturbed by the spatial curvature imprinted by the mass distribution. Strong lensing specifically describes the situation where light rays from one source pass by a large overdensity in the mass field (e.g. another galaxy) and the various light ray paths are bent in producing multiple images of the source, or rings/arcs of light. This can be seen in Figure 1.1, where the left panel is a double-imaged quasar Q0957+561, which was the first ever gravitational lens discovered (Walsh et al., 1979), and the right panel is a complete Einstein ring known as the 'Cosmos-Web Ring' (Mercier et al., 2024; van Dokkum et al., 2024).

There are three main assumptions made in strong lensing formalism: firstly, that we are in a geometric optics regime, rather than a wave optics regime, such that the light is treated as rays rather than waves; secondly that the 'thin lens' approximation holds - i.e. that the distances between the lens-source and lens-observer are much larger than the size of the deflector; and thirdly that the deflection of light is due to a gravitational field which is assumed to be weak - therefore the perturbations from straight lines are small. Following on from these simplifying assumptions, the basis of lensing theory relies on a very simple equation, that relates the observed sky coordinate of a source to its actual coordinate:

$$\beta = \theta - \alpha(\theta). \tag{1.1}$$

This equation (1.1) is known as the 'lens' equation, and shows that the true travel line of a light ray (β) is related to the observed travel line (θ), via the 'scaled' or 'reduced' deflection angle, α. Note that α itself is dependent upon the observed line θ, since it will be related to the surface mass density at the lens, and is related to the actual deflection angle ($\hat{\alpha}$) that a light ray experiences, through:

$$\alpha = \frac{D_{\mathrm{LS}}\hat{\alpha}}{D_{\mathrm{S}}} \tag{1.2}$$

where D denotes a distance of either $D_{\rm L}$ (distance from the observer to the lens plane), $D_{\rm S}$ (distance from the observer to the source plane), or $D_{\rm LS}$ (distance from the lens plane to the source plane). Note that all distances in equations 1.2 and 1.3 are angular diameter distances.

The lens equation allow us to take the light of an individual pixel in some image that we have taken of a lens, and 'ray-trace' it back through some model mass distribution to find its origin location in the source plane. Gravitational lensing conserves surface brightness, and so we can accurately reconstruct the projected surface area of a source given a certain surface brightness of the lensed source that we have an image of. Areas of the lensed image that trace back to the same region in the source plane are the multiple images of that source, and by applying regularisation to models to ensure the sources are of reasonable shapes (e.g. no random holes), we can use this to constrain the mass model.

The (arguably) most important definition of a lensing parameter is the Einstein Radius, θ_E, which is the circular radius within which the average surface mass density of the deflector is equal to the lensing critical density (i.e. the threshold density for the appearance of multiple images), and is also the circle that a point source directly behind a circular lens will be lensed on to (creating an Einstein ring like the one seen in the right hand panel of Figure 1.1). The Einstein radius can be notionally defined by extension of a non-circular deflector as the radius where the mean of the enclosed convergence is 1, where the convergence κ is the projected surface mass density in units of the critical density Σ_c:

$$\kappa(\boldsymbol{\theta}) = \frac{\Sigma(\boldsymbol{\theta})}{\Sigma_c} \equiv \frac{\nabla^2\psi(\boldsymbol{\theta})}{2}, \qquad \Sigma_c = \frac{c^2 D_{\rm S}}{4\pi G D_{\rm L} D_{\rm LS}} \tag{1.3}$$

where ψ is the 2D lensing potential, and we do not explicitly state the derivations from the lens equation, since they are well documented, but refer the reader to Kormann et al. (1994) Treu (2010) and Saha et al. (2024).

1.3.2 Constraining the nature of dark matter through strong lensing

The mass distribution on small (subgalactic) scales can affect lensing observables such as the image positions and magnifications of the lensed source. This therefore means that dark subhalos of the main deflector galaxy can slightly perturb the paths of the light rays, leading to residuals in model images when the model only takes into account the main deflector mass. If we include these subhalos in the models of galaxy-scale lenses, we can infer whether they make the model residuals better, or have a negligible effect (see Chapter 2) - if it is the former, we can use this 'detection' to put a constraint on the subhalo mass function, which governs how many subhalos should be expected at various masses. The way that this constrains the nature of dark matter is that the nature of the mass function at small (dark) halo masses is different for cold and warm dark matter due to their free-streaming lengths at early epochs (Gao et al., 2004; Benson et al., 2012; Lovell et al., 2014), and thus, the detection rate of subhalos can be used to constrain CDM versus WDM.

The constraints on WDM from this method have largely come thus far from non-detections of substructure - that is studies that have calculated how many substructures *should* be detectable in a lens sample for a given dark matter particle mass (i.e. the 'sensitivity function') and compared this to the number of actually detected substructures (often none) in that sample (e.g. Vegetti et al., 2014; Li et al., 2016; Vegetti et al., 2018; Ritondale et al., 2019; Gilman et al., 2020). In fact, only a very few substructure detections have been claimed in the literature*: Vegetti et al. (2010) and (Vegetti et al., 2012) are the two widely cited and reproduced detections thus far, Nierenberg et al. (2014) claim a substructure detection by using a method of comparing the flux ratios of the multiple lensed images, and during the finalising stages of this thesis, Powell et al. (2025) published a very low mass object detection using very long baseline interferometry of radio wavelength data. Upcoming surveys from telescopes such as Euclid and LSST expect to find of the order

*Hezaveh et al. (2016) claim a subhalo detection using long-baseline interferometry of radio wavelength data, however it has been shown in Stacey et al. (2025) that this was likely a false-positive due to an inadequate model of the complexity in the main deflector

of tens of thousands of strong lenses (Collett, 2015), and we already have the beginnings of new samples from James Webb Space Telescope (JWST) (the COWLS survey: Mahler et al., 2025), and as such we expect that we will be able to build up a large enough sample of subhalo detections that we can fully constrain the subhalo mass function.

The 'gold standard' of the current set of detections is that of Vegetti et al. (2010), who found a subhalo of mass* $(3.51 \pm 0.15) \times 10^9 M_\odot$ in the system SDSSJ0946+1006 (aka the 'jackpot' lens) at redshift $z_l = 0.222$. This system not only has this substructure detection, but also has three† multiply imaged background source galaxies (Collett et al., 2020), and has thus been studied intensely both with a view to modelling effects (e.g. Cao et al., 2025; Johnson et al., 2025), and the nature of the substructure itself since it has a very high central concentration which could be an indicator of SIDM (e.g. Enzi et al., 2024; Li et al., 2025), the presence of baryons (e.g. He et al., 2025), or some other non-CDM subhalo explanation (e.g. Ballard et al., 2024).

1.4 Outline of Thesis

The next chapter (Chapter 2) will run through the specific methods of lens modelling that all the work in this Thesis is based upon, including the software tools, model parameter choices, and an overview of the bayesian framework in which we operate. This chapter will also address the issues of angular complexity in the models of the main deflector, which is the second running theme to this work, alongside dark subhalo detection. Following this, we will have three chapters of the application of strong lensing methods. Chapter 3 will discuss direct application of the lens modelling framework to two lenses with new JWST imaging, including attempts at subhalo detection and discussion of the degeneracies between the main deflector model and substructure. Chapters 4 & 5 will investigate the angular complexity in the light and the mass of lens galaxies, motivated by the discussions in Chapter 3 through applications of increasingly complex models. Finally, Chapter 6

*Vegetti et al. (2010) use a pseudo-Jaffe density profile.

†At the time of the Vegetti et al. (2010) substructure detection, only two of the three background sources were visible in imaging.

will summarise all of the work presented in Chapters 3 to 5, bringing the motivation and conclusions together, and present an outlook on future work that is required.

Chapter 2

Lens modelling: functional forms and general models

In this Chapter, I will describe the framework for lens modelling of the main deflector that is used in this Thesis, as well as introducing the concept of angular complexity in the models, which will be a topic of intense investigation throughout the forthcoming chapters. I take this opportunity remind the reader that 'log' refers to the natural log, and e.g. '$\log_{10}$' refers to the base-10 logarithm.

The basic idea in the modelling of strong gravitational lenses that will be followed in this thesis is the attempt to create a model of a source galaxy and lens galaxy that reproduces a given image. From a model source galaxy, we 'ray-trace' the path of the source light, as lensed by a model mass distribution, to create a model lensed source image; this model lensed source plus some model lens galaxy light distribution creates the model image. It is the individual pixel values of the model image that are compared to the observed image, and we attempt to construct a model that minimises the per-pixel residuals between these images.

2.1 The PyAuto framework and Bayesian analysis

To perform all the modelling described in this Thesis we use the open source lens modelling package PyAutoLens* (Nightingale et al., 2015a, 2018, 2021b) and its associated parent packages, including PyAutoFit†, an extension which provides a statistical fitting and analysis framework to our lens modelling (Nightingale et al., 2021a) and PyAutoGalaxy‡, a package which includes implementations of all galaxy mass and light profiles which may be needed for modelling (Nightingale et al., 2023).

For all mass modelling in this Thesis, we use the non-linear sampler nautilus§ (Lange, 2023), which uses Importance Nested Sampling to build a Bayesian Posterior estimate. For modelling of light distributions in Chapters 4&5, we use the dynesty¶ nested sampler (Speagle, 2020) with a static random-walk sampler.

We use the natural logarithm of the Bayesian Evidence - $\log(\mathcal{E})$ - as the discriminating factor between models. A simplified way to understand the Bayesian Evidence is to consider it to be the Likelihood of the model being the truth, but marginalised over the parameters that are being fit, such that say a small Prior which contains many bad solutions will have a lower evidence than a larger Prior that only contains good solutions. The equation

$$\mathcal{E} = p(\mathbf{X}|\alpha) = \int p(\mathbf{X}|\theta)p(\theta|\alpha)d\theta \tag{2.1}$$

formalizes this description, where $\mathbf{X}$ is some observed data, θ is a data parameter/set of parameters, α is some information given by the Prior, such that the Evidence is $p(\mathbf{X}|\alpha)$ (probability of getting this dataset given this specific set of prior constraints and information). This Evidence is therefore equal to the integral over all data parameters of the Likelihood ($p(\mathbf{X}|\theta)$, probability of getting this dataset given a certain set of parameters) multiplied by the Prior ($p(\theta|\alpha)$, probability of a certain set of parameters being correct given the input prior constraints).

*https://github.com/Jammy2211/PyAutoLens
†https://github.com/rhayes777/PyAutoFit
‡https://github.com/Jammy2211/PyAutoGalaxy
§https://github.com/johannesulf/nautilus
¶https://github.com/joshspeagle/dynesty

For reference, $\Delta\log(\mathcal{E}) = 10$ corresponds to roughly a 5-sigma result*, or a frequentist p-value of order 10^{-7}. Similarly, $\Delta\log(\mathcal{E}) = 5$ corresponds to roughly 3-sigma or a p-value of ~ 0.03. The use of $\Delta\log(\mathcal{E})$ can also be considered as the logarithm of the 'Bayes Factor' or 'Odds', since $\Delta\log(\mathcal{E}) = \log(\mathcal{E}_1) - \log(\mathcal{E}_2) = \log(\mathcal{E}_1/\mathcal{E}_2)$.

2.2 Data processing and Masking

In order to fit a strong lens model to a dataset that consists of an image of lens+lensed source, we use every pixel that is in the image, which can lead to a lot of equations to be solved, and a lot of computational resource usage. We therefore apply a mask to the data so as to restrict the number of pixels that will be involved in the computation to as few as possible whilst not losing any vital information. This is done in `PyAutoLens` by placing a circular mask (of radius 2.5 to 4.0 arcseconds) around the system (centred on the brightest pixel of the lens galaxy), beyond which the software fully ignores the pixels - not including them in any source reconstruction process.

An additional problem when fitting strong lensing data is the presence of external sources such as nearby or line of sight galaxies, that contribute negligibly to the lensing mass profiles, but contaminate the light of the image. We therefore 'mask' out these regions by scaling the data flux in this region to near 0, and the noise in the masked pixels to extremely high values, following the process in Etherington et al. (2022). This means that the pixels in this region will contribute effectively nothing to the likelihood function, but avoids removing the pixels from the analysis altogether, which can create holes/discontinuities in the source since the image pixels would not be ray-traced at all. These masks are created individually for each lens using a GUI† (user interface) in `PyAutoLens`.

*A useful online source for Bayes Factors in context can be found here: `https://ned.ipac.caltech.edu/level5/Sept13/Trotta/Trotta4.html`

†See details and examples of lens pre-processing at: `https://github.com/Jammy2211/autolens_workspace/tree/release/scripts/data_preparation/imaging`

2.3 Standard model components and functional forms

As mentioned at the beginning of this chapter, the fundamental principle of the lens modelling that is carried out in this Thesis revolves around creating a model image that best matches an observed image, by creating a model of the source galaxy's light distribution, and the lens galaxy's mass and light distributions. In general, we use a pixel-based model for the source light rather than a parametric model, since this allows for much greater freedom of the source morphology; we then use a multi-component set of parametric models for the lens light, to capture as much lens light complexity as possible without a pixelized model (since also allowing the lens light to be modelled on a pixel-by-pixel basis allows for large degeneracies). For the mass, we model the total mass distribution of the lens galaxy in one profile, rather than decomposing the model into stellar and dark matter components separately. Modelling the stellar and dark components of the mass distribution separately would allow for a greater freedom in the model to fit to the true distribution, specifically allowing the model mass to have a different shape in the centre (where the stars are concentrated) compared to the outskirts (where the galaxy mass is dark matter dominated) but choosing to model the total mass profile allows us to perform the fit with fewer parameters (thereby decreasing runtimes) and also means that we do not have to assume a specific type of dark matter by fitting a specific dark halo profile.

2.3.1 Lens mass: Elliptical Power-Law

We model the (total) lens mass through the Elliptical Power-Law (EPL) density profile (Tessore et al., 2015), which is commonly used in strong lens modelling (e.g. Vegetti et al., 2012; Nightingale et al., 2024). This profile represents the convergence of the lens in the following form

$$\kappa(\xi) = \frac{(3-\gamma_{\rm lens})}{1+q}\left(\frac{\theta_{\rm E}}{\xi}\right)^{\gamma_{\rm lens}-1}, \tag{2.2}$$

where the subscript 'lens' implies the parameters relating to the primary lens mass (i.e. the 'Macro-model', not any additional subhalo structures or external shear). Here, q is the

minor to major axis-ratio and ξ is the elliptical coordinate defined as $\xi = \sqrt{x^2 + y^2/q^2}$. Additionally, $\gamma_{\rm lens}$ is the density slope, and $\theta_{\rm E}$ is the Einstein Radius. $\gamma_{\rm lens} = 2.0$ gives the Singular Isothermal Ellipsoid (SIE) which is generally used to initialise the lens mass model.

All light and mass profile quantities are computed with regards to their 'elliptical components'

$$\begin{aligned} \epsilon_1 &= \frac{1-q}{1+q} \sin 2\phi, \\ \epsilon_2 &= \frac{1-q}{1+q} \cos 2\phi, \end{aligned} \tag{2.3}$$

where q is the axis-ratio and ϕ the anti-clockwise position angle, defined as $\phi = 0$ when aligned to the positive x-axis.

2.3.2 Multiple-Gaussian light expansion

To initialise the source galaxy light, and to fit the lens galaxy light, we apply a combined set of 2D elliptical Gaussian light profiles, known as a Multiple-gaussian expansion (MGE) (Cappellari, 2002), used instead of the usual elliptical Sérsic profile to attain increased model flexibility and accuracy, as described in He et al. (2024). The intensity of an MGE set is given as

$$I_{\rm set}(x, y) = \sum_{i}^{N} G_i(x, y). \tag{2.4}$$

with G_i the i-th Gaussian Profile,

$$G_i(x, y) = I_i \cdot \exp\left(-\frac{R_i^2(x, y)}{2\sigma_i^2}\right), \tag{2.5}$$

containing I_i as some intensity normalisation factor and σ_i as the full-width at half-maximum of the Gaussian profile. $R_i(x, y)$ is then the Gaussian elliptical radius, and given as

$$\begin{aligned} R_i(x, y) &= \sqrt{x'^2 + \left(\frac{y'}{q_i}\right)^2} \\ x' &= (x - x_i^c)\cos\phi_i + (y - y_i^c)\sin\phi_i \\ y' &= (y - y_i^c)\cos\phi_i - (x - x_i^c)\sin\phi_i, \end{aligned} \tag{2.6}$$

where q_i is the axis ratio, ϕ_i the position angle, and $(x_i^c,\ y_i^c)$ is the centre of the Gaussian. A "set" of Gaussians is used to refer to n Gaussians which share the same axis ratio and position angle, but have a set of σ values increasing in fixed $\log_{10}$ intervals. We do not allow any individual Gaussian intensity to be negative, in order to avoid lens-source light degeneracy, solved using a modified* fast non-negative least squares (fnnls) algorithm (Bro et al., 1997).

2.3.3 Pixelization: Voronoi mesh reconstruction

Source galaxies are projected onto a flexible pixel grid. The full formalism of this source reconstruction is described and tested in detail with regards to substructure investigations on Hubble Space Telescope (HST) imaging of strong lenses in Appendix A of He et al. (2024) and in Nightingale et al. (2024) and is based on Nightingale et al. (2015b). In general, for a given set of mass model parameters, once we subtract the lens light, the remaining lensed source emission is ray-traced back to the source plane and reconstructed onto an adaptive mesh "pixel grid". We use the Voronoi mesh, with a Natural Neighbour interpolation† (Sibson, 1981) and our own adaptive regularisation to smooth the reconstruction based on the source luminosity at that point‡.

Equations 2.7 describe the numerical implementation (without intermediate steps) of the "goodness of fit" function which optimises the balance between the MGE lens light and pixelized source light, allowing both to be fit simultaneously.

*The fnnls code we are using is modified from `https://github.com/jvendrow/fnnls`.

†More details about the natural neighbour interpolation technique can be found at `https://gwlucastrig.github.io/TinfourDocs/NaturalNeighborTinfourAlgorithm/index.html`.

‡In `PyAutoLens` these schemes are the `VoronoiNNBrightnessImage` pixelization and the `AdaptiveBrightnessSplit` regularization.

$$G = \chi^2 + G_S + G_M \tag{2.7a}$$

$$= \frac{1}{2}\left(\sum_{i=1}^{N_I}\left[\frac{\sum_{j=1}^{N_s} f_{ij}S_j + \sum_{k=1}^{N_g} I_k A_{ik} - d_i}{n_i}\right]^2 + G_L + G_M\right) \tag{2.7b}$$

$$= \frac{1}{2}\left|\left|\begin{pmatrix} Z & X \\ \sqrt{r}B_S & B_M \end{pmatrix} \cdot \begin{pmatrix} S \\ L \end{pmatrix} - \begin{pmatrix} Y \\ 0 \end{pmatrix}\right|\right|^2, \tag{2.7c}$$

Within equation 2.7a, G_S and G_M are regularisation terms for the pixelized source and the MGE light respectively. Equation 2.7b expands the chi-squared term in relation to the image-plane to source-plane mapping, where S_j is the j-th source-plane pixel flux, I_k is the k-th image-plane pixel flux, f_{ij} is the mapping matrix element quantifying the contribution of source pixel j to the flux of image pixel k (which includes point spread function (PSF) and image processing effects). In addition, the term includes A_{ik}, which is the exponential from the Gaussian profile of equation 2.5 G_k, for (x_i, y_i), as well as the data and noise d_i and n_i at the i-th pixel. All of this collapses down into equation 2.7c, where $Z_{ij} = f_{ij}/n_i$, $X_{ij} = A_{ij}/n_i$, r is the regularisation strength, B_S and B_M are 'square root' matrices of the source and MGE regularisations respectively, S and L are the source-plane and image-plane fluxes, and Y_i is the division d_i/n_i.

2.4 The External Shear

In strong lens modelling, we generally include an 'external shear', intended to account for the effect of line-of-sight and nearby galaxy perturbations to the deflection of a light ray (e.g. Witt et al., 1997; Hogg et al., 2023). The recovered parameters on the shear though generally result in much larger shear strengths than expected, or shears that do not align with the line-of-sight cosmic weak lensing shear (e.g. Keeton et al., 1997; Wong et al., 2010), leading to the conclusions that our models may be adjusting the external shear to rather model missing internal complexity of the main deflector mass model that is not captured in the EPL (Cao et al., 2021; Etherington et al., 2024).

We do fit an external shear in all mass modelling stages in this Thesis, and will discuss in Chapters 4&5 some possible physical explanations for anomalously high-magnitude shears. We fit the shear as two elliptical components ($\gamma_{\text{ext, 1}}, \gamma_{\text{ext, 2}}$), and akin to the elliptical components of the EPL, we relate the shear components to the magnitude, γ_{ext} and position angle ϕ_{ext} (again, with the angle defined counter-clockwise from the positive x-axis):

$$\begin{aligned} \gamma_{\text{ext}} &= \sqrt{\gamma^2_{\text{ext, 1}} + \gamma^2_{\text{ext, 2}}}, \\ \tan\left(2\phi_{\text{ext}}\right) &= \frac{\gamma_{\text{ext, 2}}}{\gamma_{\text{ext, 1}}} \end{aligned} \tag{2.8}$$

2.5 Angular complexity in the mass model: Multipole expansions

To introduce additional complexity to the main deflector model (as motivated by anomalously high external shears), one can apply an extension to the EPL profile where we include internal angular perturbations referred to as 'multipoles', building on the formalism of Chu et al. (2013). The multipoles are sinusoidal-based expansions of the underlying profile, and when applied to the EPL, we get a functional form of the convergence (in polar coordinates since multipoles are angle-based) of:

$$\kappa(r, \phi) = \frac{1}{2}\left(\frac{\theta_E}{r}\right)^{\gamma_{\text{lens}}-1} k_m \cos[m(\phi - \phi_m)]\,, \tag{2.9}$$

where r is the radial position in arcseconds, ϕ is the angle of interest for the calculation, and m is the defined multipole order. It is important to note that this is actually an approximation based on mathematical derivation starting from the *circular* power-law, and thus can be biased for highly-elliptical systems. A full mathematically-motivated implementation of 'elliptical multipoles' is currently under development in the `PyAutoLens` codespace, and has recently been formalised into other codespaces (Paugnat et al., 2025).

Multipole perturbations cause the mass distribution to lose angular symmetry, but maintain rotational symmetry at different orders, represented by m (i.e. $m = 1$ has one line of

symmetry, $m = 2$ has two lines of symmetry, etc) and so in theory any number of multipole perturbations could be added to the mass model, but it is generally accepted that only multipoles up to order 4 are physically motivated on the scale of the galaxy. Multipoles can be applied individually, or in a combination, in which case the perturbations sum together, giving

$$\kappa(r, \phi) = \frac{1}{2} \left(\frac{\theta_E}{r} \right)^{\gamma_{\rm lens}-1} \cdot \sum_m \left(k_m \cos(m(\phi - \phi_m)) \right). \tag{2.10}$$

When used within our modelling pipelines, the Einstein radius, θ_E, slope, $\gamma_{\rm lens}$ and (y, x) centre of the perturbing part of the multipole (second term of Equation 2.2) are linked to the values fit to the main EPL, and in addition, we fit for the multipole elliptical components ($\epsilon_1^{\rm mp}$, $\epsilon_2^{\rm mp}$) (meaning we have the six EPL parameters plus an additional two per multipole). The multipole elliptical components relate to the multipole strength, k_m and multipole position angle ϕ_m (defined counter-clockwise from the positive x-axis) in a similar way to the EPL elliptical components:

$$\begin{aligned} \phi_m &= \frac{1}{m} \arctan \frac{\epsilon_2^{\rm mp}}{\epsilon_1^{\rm mp}}, \\ k_m &= \sqrt{(\epsilon_1^{\rm mp})^2 + (\epsilon_2^{\rm mp})^2}. \end{aligned} \tag{2.11}$$

This formalism is an alternative to the commonly used 'signed' multipole formalism, where the 'sign' of the multipole indicates the shape and orientation. Here the shape of the multipole is defined by the 'shape angle' s_m:

$$s_m = \phi_{\rm base} - \phi_m \tag{2.12}$$

which is the difference between the position angle $\phi_{\rm base}$ of the underlying distribution, and the position angle of the multipole ϕ_m. The multipole is then aligned with the base position angle such that $s_m = 0^\circ$ for $\phi_m = \phi_{\rm base}$ and then values of $s_m \in [-180/m^\circ, 180/m^\circ)$ give certain shapes aligned to this angle ($\phi_{\rm base}$).

Note that the work in Chapter 3 was produced early in the development of multipoles into the code framework; as such the concept of 'shape angle' was not yet formalised and so the work in this Chapter only reports the multipole angle ϕ_m.

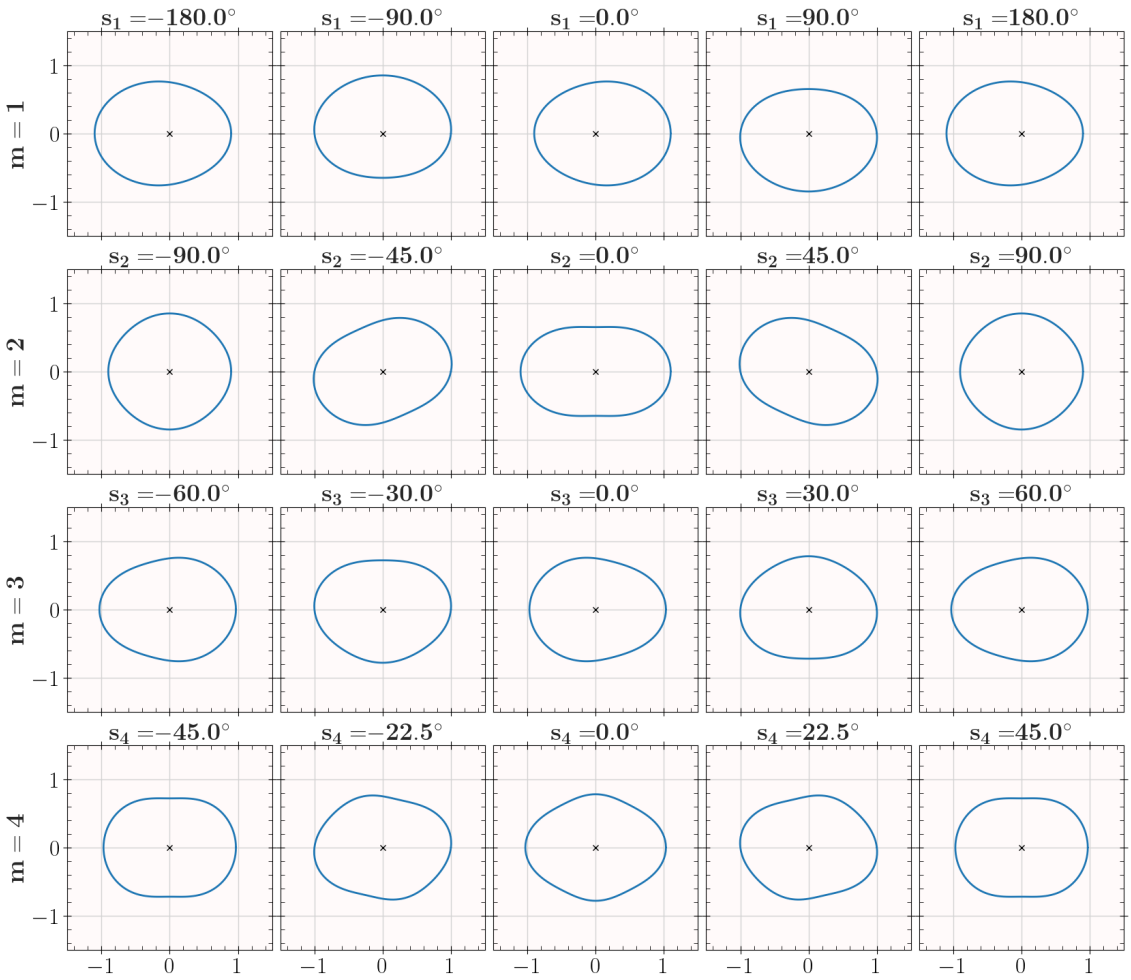

Figure 2.1: Key shapes of multipoles of orders $m = 1, 2, 3, 4$. All drawings are based on an ellipse with axis ratio $q = 0.75$, $\phi_{\text{base}} = 0°$ (i.e. aligned with the positive x-axis), and centred at $(0, 0)$, marked with a cross in each panel. Shapes repeat every $360/m$ degrees, so shape angles are given in the range $\pm 180/m°$. Multipole strengths are set higher than expected for real galaxies in order to make the effects more easily visible: $k_1, k_2 = 0.1$ and $k_3, k_4 = 0.03$.

2.5.1 Physical interpretations of multipoles

Figure 2.1 shows examples of the key multipole shapes for orders $m = 1, 2, 3, 4$, all based around $\phi_{\text{base}} = 0°$ (i.e. aligned to the positive x-axis). An additional example plot of the effect of individual and combined multipole perturbations on the critical curves and lensed source images of a simple circular mock system is shown in Appendix A.2.1. Although the $m = 2$ multipole is included in the figure for reference it is not used anywhere in this work since it is considered to be generally degenerate with the axis ratio/position

angle of the underlying distribution. Despite this, Figure 2.1 does show that for $\pm 90^\circ$ there is a boxy-circular type shape formed (although the multipole strengths $k_2 = 0.1$ are higher in the simulation than would be expected in real galaxies) and Shan et al. (2025) propose the idea that this order can be used in the case of lensing by a spiral galaxy to describe the central bar structure. Exhaustive visual tests and mathematical derivations are required to show whether the $m = 2$ multipole creates notably different perturbations to combinations of axis ratio, position angle and other multipoles but we are happy that the additional computational (and Bayesian) cost incurred by including the relevant additional parameters to fit the $m = 2$ are not worth any possible small extra flexibility it provides.

For a physical interpretation of the remaining multipoles, the $m = 1$ multipole corresponds to a skew in the mass distribution, which could, for example, be due to the galaxy being mid- or post-merger (e.g. Amvrosiadis et al., 2025b). The $m = 3$ and $m = 4$ multipoles are more frequently used in strong lensing (e.g. Hezaveh et al., 2016; Stacey et al., 2024) and demonstrate triangular-like symmetry from $m = 3$, which has long been a component of galaxy surface brightness fits (e.g. Benacchio et al., 1980; Tremblay et al., 1995), and boxiness/diskiness (e.g. Bender et al., 1989) from the $m = 4$ (seen in Figure 2.1 at $s_4 = \pm 45^\circ$ and $s_4 = 0^\circ$ respectively). The majority of physical intuition on these multipoles comes from the light profiles of galaxies - see e.g. Hao et al. (2006) and Padilla et al. (2008) for comprehensive applications of multipoles to Sloan Digital Sky Survey galaxies, or Cappellari (2016) for a review on galaxy structure using Spectroscopy. Note that work is ongoing to achieve a quantitative rather than qualitative view on what multipole strengths and realisations are to be expected directly from mass modelling of strong lensing galaxies (Stacey et al., 2024; Amvrosiadis et al., 2025b), but so far in the literature (also see Chapter 5) there is evidence that amplitudes of mass multipoles are in line with those from the light, but potentially misaligned in angle/shape (Stacey et al., 2024).

Chapter 3

Contrasting substructure with main deflector complexity

3.1 Preamble

This chapter largely covers work that is available in Lange et al. (2025). In this chapter, I focus on analysis of new lenses from JWST ('new' compared to the HST imaging that has been used by this field of study for over a decade). The work addresses two strong gravitational lenses, and our efforts to model them: I will discuss the challenges that a new telescope with higher resolving power and different source and lens selection effects has on the modelling process, in particular with regard to the angular complexity of the main deflector.

The chapter is structured as follows. In Section 3.2 we describe the JWST data and the systems studied. In Section 3.3 we discuss the specifics of the modelling pipeline and the details that are not included in Chapter 2. We also discuss how subhalos are modelled and evidence thresholds for detections. In Section 3.4 we show our model results for the multipole and subhalo fits, first to SPT2147, and then to SPT0418. In Section 3.5 we discuss the results, with focus on the question whether SPT2147 actually contains multipoles and/or a substructure. The chapter is then summarised in Section 3.6. A Planck 2015 (Planck Collaboration et al., 2016) cosmology is used throughout unless otherwise specified.

3.2 JWST and datasets

3.2.1 JWST and the Early Release Program

JWST *NIRCam* imaging provides an unprecedented multi-wavelength view of strong lenses (e.g. Bergamini et al., 2023; Mercier et al., 2024; Rigby et al., 2024; van Dokkum et al., 2024; Mahler et al., 2025). This capability is essential for testing lens models since the source morphology varies across wavelengths (e.g. Amvrosiadis et al., 2025a), producing different lensed images, whilst the mass model remains wavelength-independent. In this work, we perform independent lens model fits across multiple wavelengths for two strong lenses to assess: (i) whether angular mass complexity is consistently required for the lensing galaxies across wavelengths, and (ii) whether a dark matter substructure is *consistently* favoured in each waveband. This multi-wavelength approach allows a detailed exploration of the degeneracy between these two model components.

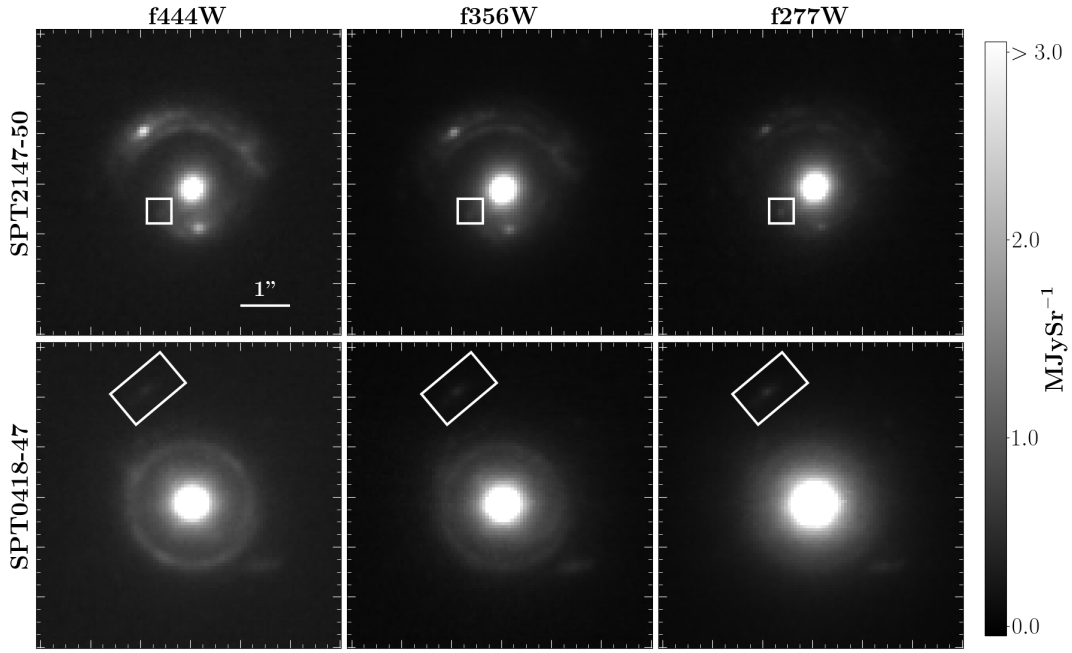

Figure 3.1: Data from the three reddest NIRCam filters (f277W, f356W, f444W) for SPT2147-50 (upper panels) and SPT0418-47 (lower panels). All panels are 6”x 6” squares. The signal is saturated above 3.0 MJy Sr^{-1} in order to see the lensed source emission clearly. Marked with white boxes are line-of-sight galaxies in each lens (note the line-of-sight object in SPT2147 is brightest in f277W).

	SPT0418			SPT2147		
	f444	**f356**	**f277**	**f444**	**f356**	**f277**
Max. Source signal-to-noise ratio (SNR) pix^{-1}	20.90	12.57	14.68	53.80	59.59	28.79
Avg. Source SNR pix^{-1}	7.67	5.20	4.65	9.65	9.61	5.93
RMS (Root Mean-Squared) noise MJy Sr^{-1}pix^{-1}	1.606	1.654	1.455	1.599	0.930	1.259

Table 3.1: Signal information for each filter of our two strong lenses. The source parameters are based on the lens-light subtracted model images and therefore approximations based on model results. The average (source) SNR was calculated as the mean of all pixels with SNR > 3. The root mean-squared (RMS) noise was calculated over all pixels.

We use one of the Early Release studies, the *TEMPLATES* survey (PI: Rigby et al. 2024), to study two lenses: SPT2147-50 and SPT0418-47 (of which the latter has also been imaged by the HST, providing little useable data due to low signal from the source). We use NIRCam imaging from filters f277W, f356W and f444W (2.77, 3.56 and 4.44 microns) for SPT2147 and f356W, f444W for SPT0418 - other (bluer) wavelength images exist but similarly to HST lack a sufficient source SNR to produce physically plausible models. Atacama Large Millimeter Array (ALMA) data is also available for these lenses and the SPT2147 source galaxy has been studied in Amvrosiadis et al. (2025a), with ALMA substructure analysis of both lenses to be released subsequently by my collaborators.

JWST-NIRCam imaging is shown in Figure 3.1 for SPT2147 (upper) and SPT0418 (lower), where we have saturated all pixels above 3.0 MJy Sr^{-1} (MegaJansky per Steradian - the unit received from the JWST data reduction outputs) in order to see the lensed source galaxy light, as it is strongly outshone by the lensing galaxy. Figure 3.2 shows SNR maps for only the source emission, based on the model image created by our best-fit models (see Section 3.4). We have normalised the colours to the same values across both lenses and all filters, to visualise the large difference between the maximum pixel SNR of the two lenses, with SPT2147 ranging from 2x to 5x higher SNR, depending on the filter. Specific values for maximal and average SNR are quoted in Table 3.1, where the average has been computed over all pixels with SNR > 3.

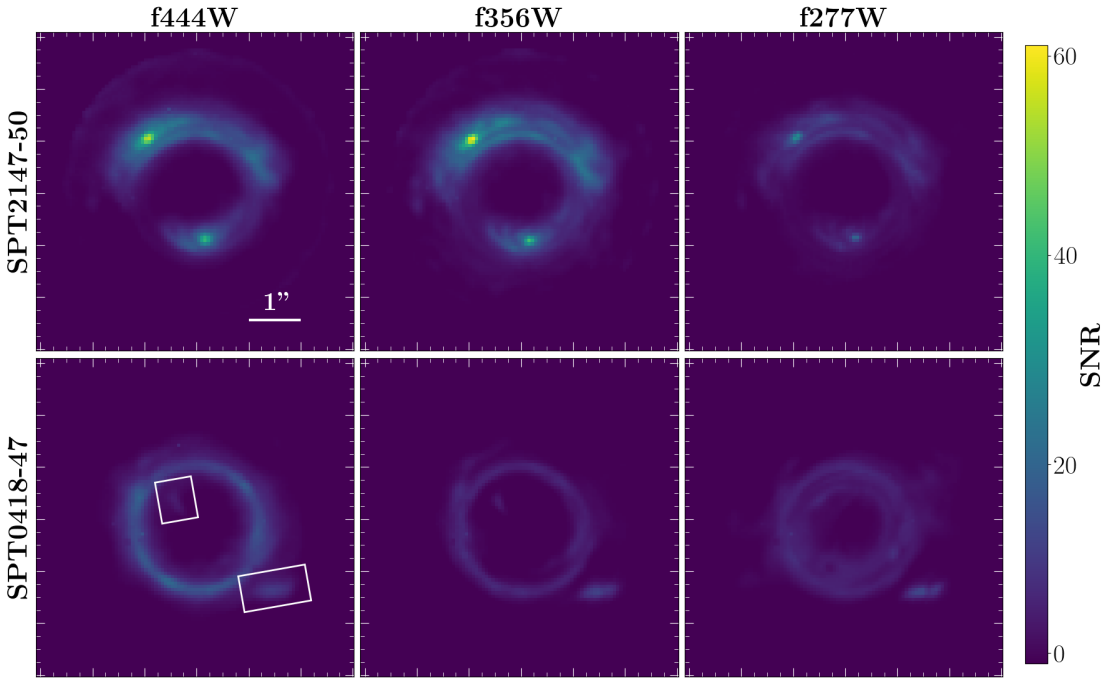

Figure 3.2: Signal-to-noise ratios for SPT2147-50 (upper panels) and SPT0418-47 (lower panels), based on the model lensed source emission from our best-fit models. All panels are 6”x 6” squares. All panels have colour normalisation to the same level ($0 < \mathrm{SNR} < 60$), but exact maximal and average values are shown in Table 3.1. The white boxes in SPT0418 (f444W) mark the image and counter-image of the source companion galaxy as this lens has a multi-object source.

3.2.1.1 JWST PSF

The PSF of JWST used in this work was produced using `WebbPSF`* (Perrin et al., 2012). The top row of Figure 3.3 shows the full 6-armed star-like PSF for each waveband; the PSF is waveband-dependant and although similar, one can notice that at shorter wavelengths the flux spread appears more concentrated into the arms. The size of the PSF is an issue for computational complexity - we did not use the full-size PSF in our analysis since firstly runtimes were untractably long, and secondly we only use 3x3 arcsecond square image cutouts, hence a 20x20 arcsecond square PSF does not make sense. Through trial-and-error modelling (running the first two stages of the fitting pipeline described in Section 3.3) we chose a cutout of the PSF in each filter that contains 93.5% of the PSF flux as this had acceptable model runtimes, whilst not causing any noticeable PSF-shaped residuals.

*`WebbPSF`: `https://shanosborne-webbpsf.readthedocs.io/en/latest/index.html`

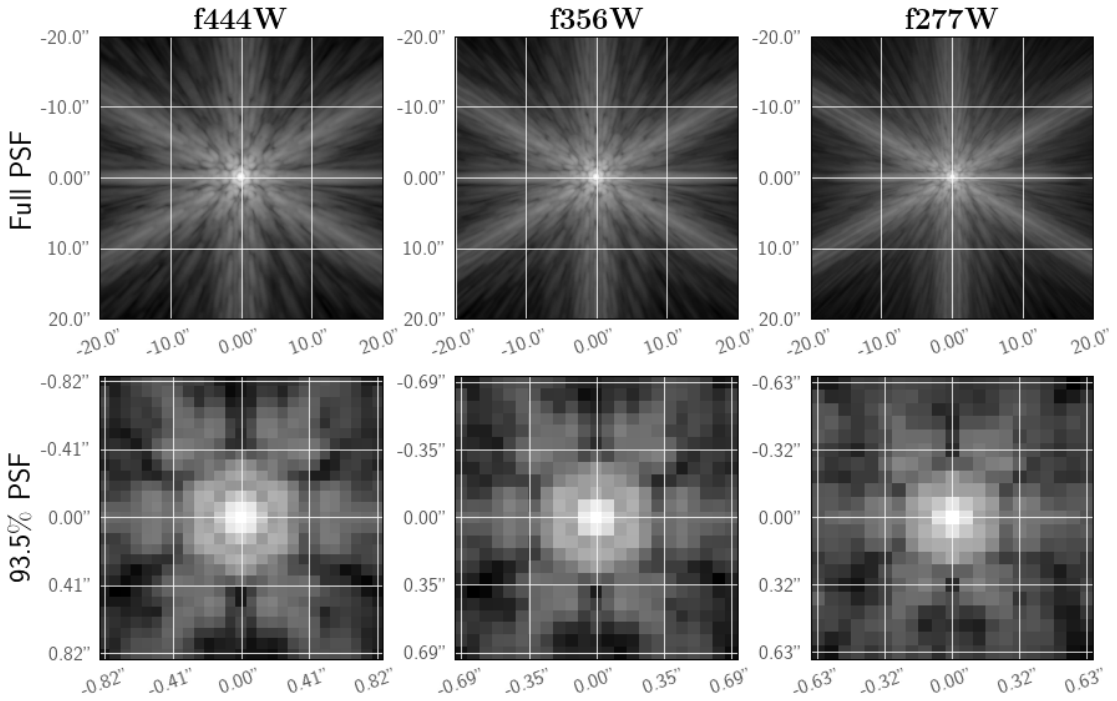

Figure 3.3: PSFs (point spread functions) for the JWST filters used in this work. Top row is the full PSF. Bottom row is the cut PSF used in this work containing 93.5% of the flux.

3.2.2 SPT2147-50

This lensing system is composed of a lensing galaxy at a spectroscopically confirmed redshift of $z = 0.845$ and a complex source galaxy at $z = 3.76$ (Weiß et al., 2013; Reuter et al., 2020). In conjunction with this work, this lens was studied in ALMA band 8 data by Amvrosiadis et al. (2025a), where we discover that the source galaxy is a spiral-barred galaxy, marking one of the highest redshift bars proposed in the literature at the time. The selection effects of NIRCam are clear for this case, since later in the evolutionary stages of this galaxy, rest-frame colour changes due to stellar ages and dust lanes would move the peak emission outside of the NIRCam band ranges, whereas earlier in evolution, we would not expect the stable intricate structure that we see in Figure 3.4, which one would expect to improve the lensing constraints due to the fact that a complex structure is harder to reconstruct in modelling than a simple elliptical blob.

We also note that there is a line-of-sight galaxy or star cluster south-west of centre, on the lower arc, marked with the white box in Fig.3.1. This object is primarily visible in

f277W, and not visible at all in the reddest f444W filter. In the SPT2147 SNR images of Figure 3.2 and in the rest of our analysis, we mask out the light from this object (see Section 2.2), so that the light at this point contributes nothing to our likelihood functions and is therefore ignored by the model. Modelling the Spectral Energy Distribution (SED) of this object was performed by Dr.Aristeidis Amvrosiadis using the `BAGPIPES`* fitting code (Carnall et al., 2018) applied to the three bands used in this work, plus one further band (f200W). This modelling gives a much lower redshift than our lens galaxy, in the range $z = 0.04$ to $z = 0.10$, and a best-fit stellar mass of the order $\log_{10}(M_*/M_\odot) \sim 6$, therefore being classed as a line-of-sight object and not part of the main deflector. We do not include the object mass in our modelling as the mass would not be high enough to have any discernible impact on the lensing in this system. For completeness, we do some tests where we include this 'clump' in the lens model, and we find no significant changes to model parameters, and no significant size mass fit to this area. Additionally, there are no residuals found in the modelling that appear to be associated to this object.

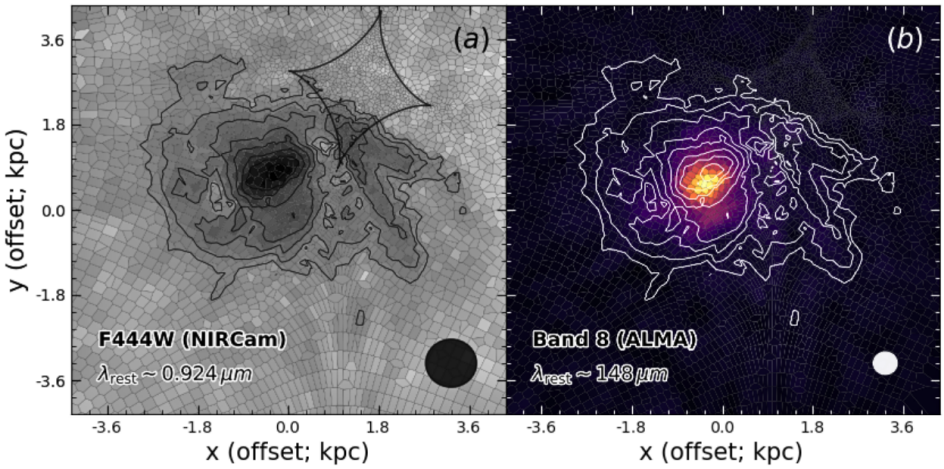

Figure 3.4: Source plane reconstructions from best fits to SPT2147 from JWST (my work) and ALMA (collaborator work). Left panel shows NIRCam f444W stellar continuum reconstruction and right shows ALMA band 8 dust continuum reconstruction. The contours on both panels are the f444W isophotes. Figure adapted from figure 4 of Amvrosiadis et al. (2025a), and originally created by Dr. Aristeidis Amvrosiadis. The NIRCam panel also shows the caustic diamond.

*`https://github.com/ACCarnall/bagpipes`

ALMA and JWST data for this lens has been studied previously in the literature with a narrow focus on parameters such as source gas properties and star formation rates (e.g. Ma et al. 2015; Birkin et al. 2023), with we believe only one attempt at lensing reconstruction (Dong et al., 2019) where analysis is performed in the visibility plane and not on reconstructed images, and which uses a reasonably simplistic multiple-SIE(Kormann et al., 1994) model for the lens mass and multiple-Sersic light profiles (Sersic, 1968) for the lens light, as it is focused only on source science, as in the rest of the existing literature.

3.2.3 SPT0418-47

This system is composed of a lensing galaxy at redshift $z = 0.263$ and a background source at redshift $z = 4.22$ (Weiß et al., 2013; Reuter et al., 2020). From our modelling and the literature, the source here is composed of two merging galaxies, with Cathey et al. (2024) reporting a projected separation of ~ 4.42kpc and a stellar mass-to-light ratio of 4:1 ($M_{\odot} : L_{\odot}$). Interestingly, the source companion galaxy is not visible in HST or ALMA and so has only been discovered through the JWST data (Peng et al., 2023; Cathey et al., 2024). This companion galaxy is visible in the south-east of the image, outside the Einstein ring, with its counter-image visible north-west of the centre, once the lens light has been removed. Both the primary and counter image are marked with the white boxes in the f444W panel of Figure 3.2, since the lens light has been subtracted here. There is also a nearby or line-of-sight galaxy, marked by the white box in Figure 3.1, which we mask out of our analysis since it was considered too far from the main system to have any appreciable gravitational effect.

The majority of studies (up to 2023) on this system have been focused on the dust and gas physics of the primary source galaxy due to it being a good example of an early stable dusty starburst (e.g. Aravena et al. 2016; Bothwell et al. 2017; Spilker et al. 2023), as well as an interesting comparison to simulations: the star formation and dust properties agree with EAGLE simulations, but its rotational stability is more akin to local spirals than simulated $z \sim 4$ galaxies (Rizzo et al., 2020), as well as its interstellar-medium being solar-metallicity enriched despite its early epoch (De Breuck et al., 2019).

3.3 Lens modelling pipeline

The lens modelling procedure is similar to previous works using this software e.g. Etherington et al., 2022, and follows a hierarchical modelling structure where simple models are first fit in order to reduce the parameter space, and then more complex models follow with priors based on the posteriors of the previous fit. For this work, the order of models applied is as follows:

1. **Initialise** - create a basic model for all light and lens mass using parametric profiles.
2. **Source pixelization** - reconstruct the source galaxy onto a pixel-based grid in order to capture higher levels of complexity.
3. **Lens refinement** - re-model the lens light based on this new pixelized source, and fit some more complex lens mass model.
4. **Angular mass complexity** - fit some perturbation to increase the angular mass complexity of the model (see Section 2.5)
5. **Subhalo search** - introduce a subhalo to the lens mass model and investigate (see Section 3.3.2).

3.3.1 Specific macromodel components

The specific model components for each section are specified in Table 3.2, along with how their priors are passed or reset for each stage of modelling, and which components are actually fit for and which are held fixed (so as to focus on just the light or just the mass). The main deflector mass models are fully described through Section 2.3 and Table 3.2, the specific light model details are described in the section below.

Stage:	Initialise	Source pixelisation	Lens light refinement	Lens mass refinement	Multipole perturbation	Subhalo search
Source Light	MGE: 1x30	Voronoi mesh with Natural Neighbour interpolation	FIX model: linear solve only	FIX model: linear solve only	FIX model: linear solve only	FIX model: linear solve only
Lens Light	MGE: 2x30 + 1x10 (+1x30 for SPT0418)	FIX model: linear solve only	NEW MGE: 2x30 + 1x10 (+1x30 for SPT0418)	FIX model: linear solve only	FIX model: linear solve only	FIX model: linear solve only
Lens Mass	Singular Isothermal Ellipsoid + External Shear	SIE + Shear (priors from previous)	FIX model: linear solve only	Elliptical Power-Law + New Shear	EPL+Shear (priors from previous) + Multipoles	EPL+Shear + Multipoles (priors from previous) + Spherical NFW

Table 3.2: Brief overview of the model parametrisations at the various stages of our fitting pipeline for the SPT lenses.

3.3.1.1 Light models

For the source initialisation, we use the MGE system (see Section 2.3.2) with a single set of 30 Gaussians. For all subsequent stages we then use the Voronoi mesh pixelisation (section 2.3.3) to reconstruct the source more flexibly.

The number of Gaussians used for the lens light varies between our two lenses; for SPT2147, we use two sets of 30 Gaussians (akin to a bulge and disk component) plus one set of 10 Gaussians to model central point-like emission. For SPT0418, the lens light is more blended with the lensed source emission and so we use three sets of 10 Gaussians (akin to a thin disk, thick disk and bulge, or bulge-disk-envelope system), plus one set of 10 Gaussians for central point-like emission. For both lenses, the centres of the sets of 30 Gaussians is fixed to be the same (i.e. only one centre is fit for all), with the point-source set free to have a different centre, and the position angle/axis ratio of Gaussians are the same throughout a set, but different between sets. The sigma values (controlling the 'width' of the Gaussian) are set between a lower limit of one-fifth the pixel scale (here 0.063"/5 = 0.0126") and an upper limit of 3 arcseconds for the main bulge/disk sets, and 0.126 arcseconds (twice the pixel scale) for the point-like sets.

3.3.2 Substructure detection tools

We use a Spherical NFW profile (Navarro et al., 1997) to model dark matter-only subhalo additions, and only model subhalos assuming the same redshift as the primary lensing galaxy. The density of the NFW with normalisation ρ_s and scale radius r_s is given as

$$\rho_{\rm NFW} = \frac{\rho_s}{(r/r_s)(1 + r/r_s)^2}. \tag{3.1}$$

We fit only for the (x, y) centre of the subhalo and the M_{200} mass (the enclosed mass at r_{200}, which is the radius at which the average enclosed density is 200 times $\rho_{\rm crit}$ for the Universe) and relate M_{200} to the scale radius through the mean mass-concentration relation given by Ludlow et al. (2016).

Lens models including a dark substructure produce complex multi-modal parameter spaces which are challenging for non-linear tools such as `Nautilus` to sample robustly. We therefore split the image into a 5×5 grid (each grid cell being 1 square arcsecond), and model a subhalo where the positional priors are within that grid cell only (see e.g. Nightingale et al., 2024). Following this, we can both visualize the effect of adding a subhalo at different locations, as well as use the result from the grid cell with the highest Bayesian evidence increase to initialise a new fit for a subhalo where the model has the freedom to place the subhalo anywhere, but the positional priors are Gaussians centred on the best-fit position of the highest-evidence grid search.

To claim a subhalo candidate against a standard EPL mass model, previous works (e.g. Nightingale et al., 2024) using this software and modelling framework set an a-priori requirement of $\Delta\log(\mathcal{E}) > 10$ for the subhalo addition. Our specific implementation of evidence thresholds in this work is to hold the requirement of $\Delta\log(\mathcal{E}) > 10$ when we add multipoles to the EPLγ model, and if these multipole-inclusive models pass the threshold then we continue to add a subhalo to the model. If the multipole evidence is not satisfied, we would only apply the subhalo to the base model*.

When using only single-filter imaging, if there are many different combinations of multipoles and multipoles+subhalos that create an evidence change of $\Delta\log(\mathcal{E}) > 10$ to the base model, it would be difficult to decide between taking just the highest evidence model, or requiring that a subhalo has a further evidence to the multipole (due to unknown degeneracies between multipoles and subhalos). Since we have multi-filter fitting available, we are able to apply the 'highest evidence model' approach and cross-reference by applying a $\Delta\log(\mathcal{E}) = 5$ (approx. 3σ) confidence region below this model - comparing results which fit into the confidence region across all filters. If more than one model was within this region, we choose the highest evidence model from across all filters as the primary candidate (i.e. the highest evidence model from f444W, since this has the highest source SNR).

*We add subhalos to some models in SPT0418 despite them not passing the set evidence threshold only to attain a more thorough comparison to SPT2147.

3.4 Results

3.4.1 SPT2147-50 Results

As mentioned in Section 3.2, the line-of-sight object in SPT2147 to the south-west of centre on the lower arc was modelled with `BAGPIPES` to estimate its redshift and mass. For completeness we initially try to include this object in our lens modelling as an extra Singular Isothermal Sphereoid (SIS), however the Einstein radius converges to zero in all fits meaning the object has no appreciable lensing effect in the system. We therefore remove the object from our subsequent fits by masking it out of the analysis as described in Section 2.2.

3.4.1.1 Base model substructure results for SPT2147

We show in Figure 3.5 our results from the subhalo grid-search analysis (see Section 3.3.2) in each filter, using the EPLγ as the base macromodel. This 'Base' model shows multiple high-evidence ($\Delta\log(\mathcal{E}) > 10$) grid squares repeated in similar locations in each filter. The subhalo's location with the highest evidence is north of the extended arc, with maximal evidence increases of $\sim 57, 27, 21$ in the grid-search for f444W, f356W and f277W (note

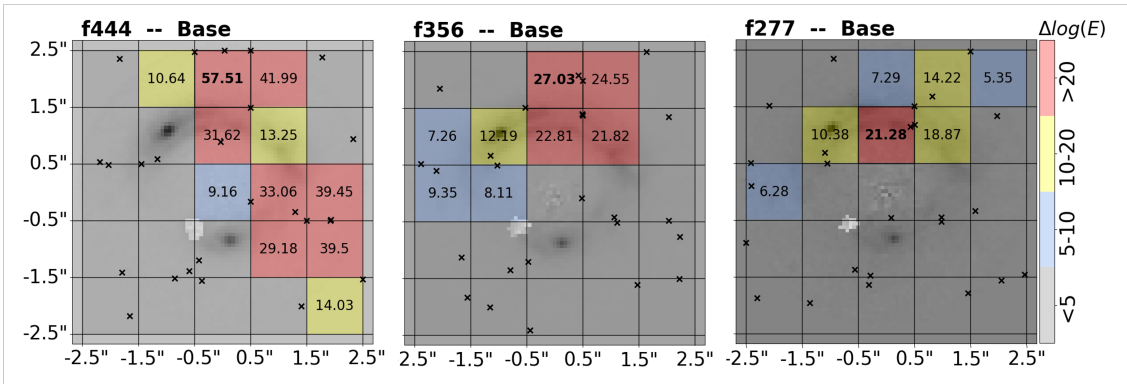

Figure 3.5: Results from the grid-based preliminary subhalo searches in SPT2147-50 for the 'base' EPLγ model. The values and colours correspond to the Log-Evidence change - $\Delta\log(\mathcal{E})$ - when a subhalo is modelled in a certain grid cell. Crosses mark the best fit position of the subhalo within each grid cell. The highest evidence grid-cells are marked in bold. $\Delta\log(\mathcal{E}) = 10$ is considered a roughly 5σ detection.

that these values adjust to $60.35, 42.13, 20.54$ for the final DM subhalo fit after the grid search, where the priors on its centre are not confined to a 1x1 arcsecond square).

The f444W filter also gives a secondary set of high-evidence grid-cells, east of the lensing galaxy, which are not seen in the bluer filters. The reason these right-hand cells do not show high evidences in the f356W and f277W filters may be related to the much lower source SNR in f277W, and potentially the source light morphology in f356W. We have seen from simulations that genuine subhalo signals can also produce residual signal in incorrect locations (Nightingale et al., 2024, section B2), so this could just be a residual effect of a genuine subhalo located towards the top of the image. There may also be a case where the substructure signals in f444W are not due to a genuine substructure, but rather a product of missing complexity from the EPLγ in that area, where the model uses the inclusion of substructure to compensate for this - the combination of any slight model differences with source morphology changes between filters could then also explain why these are not seen in f356W/f277W.

3.4.1.2 Results of multipole perturbations in SPT2147

Figure 3.6 shows the log-evidence increases - $\Delta\log(\mathcal{E})$ - when we include various multipole perturbations to our EPLγ model, instead of the subhalo additions from the previous section. We see that all multipole inclusions are preferred (give a positive evidence change), and all apart from M1-only and M3-only give $\Delta\log(\mathcal{E}) > 10$ in all three filters (where we will use the notation of 'MX' to denote the order $m = \mathrm{X}$ multipole). From here forwards therefore, we discount the M1-only and M3-only fits unless otherwise stated, similarly discounting the f277W fits due to the low SNR (and therefore low sensitivity to model changes).

From Figure 3.6, we also see that the M4-only (in f356W) and M3+M4 (in f444W and f356W) fits, show a lower evidence than the other multipole additions, which is a potential indication that, whilst an M1 multipole addition on its own cannot produce much difference to the base model, it may be required in order for the higher-order M3 and

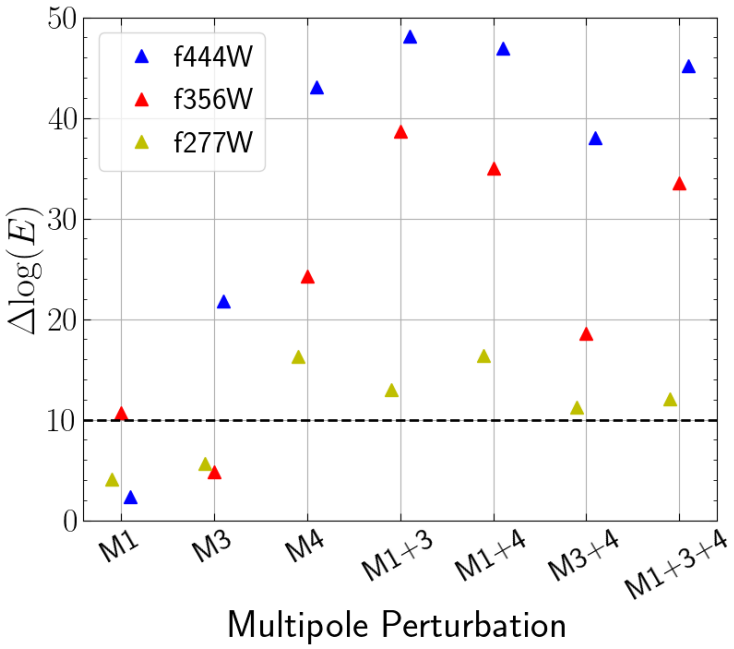

Figure 3.6: $\Delta\log(\mathcal{E})$ (Log-Evidence changes) with the addition of multipole perturbations to the base model of SPT2147-50. The dashed line marks $\Delta\log(\mathcal{E}) = 10$, which is our approximate 5σ significance threshold.

M4 perturbations to become fully effective - a possible sign again of multipoles having the potential to compensate for missing complexity which they are not primarily intended to capture. A similar effect is shown in Amvrosiadis et al. (2025b) where M1 addition changes the fit values of M3 and M4 components to galaxy light distributions.

Figure 3.7 shows the recovered parameters from the high-evidence multipole models to SPT2147, as well as the base EPLγ model. For each model, the parameters are consistent within the errors across all three filters, which shows that the fits are converging successfully since, again, the three filters offer independent source light structures and PSF instances but with the same mass distribution, and thus agreement between the three filters within a model provides an important cross-reference and confidence boost in the recovered parameters. Between different models however, we see one model notably deviate from the base model (and indeed most other model) parameters - the M1+M3 model - showing an offset centre, smaller Einstein Radius, smaller Power-Law Slope, smaller Shear Magnitude and higher M1 magnitude. Some of these M1+M3 parameters are consistent within errors to at least one filter of another model but the best-fit values are clearly

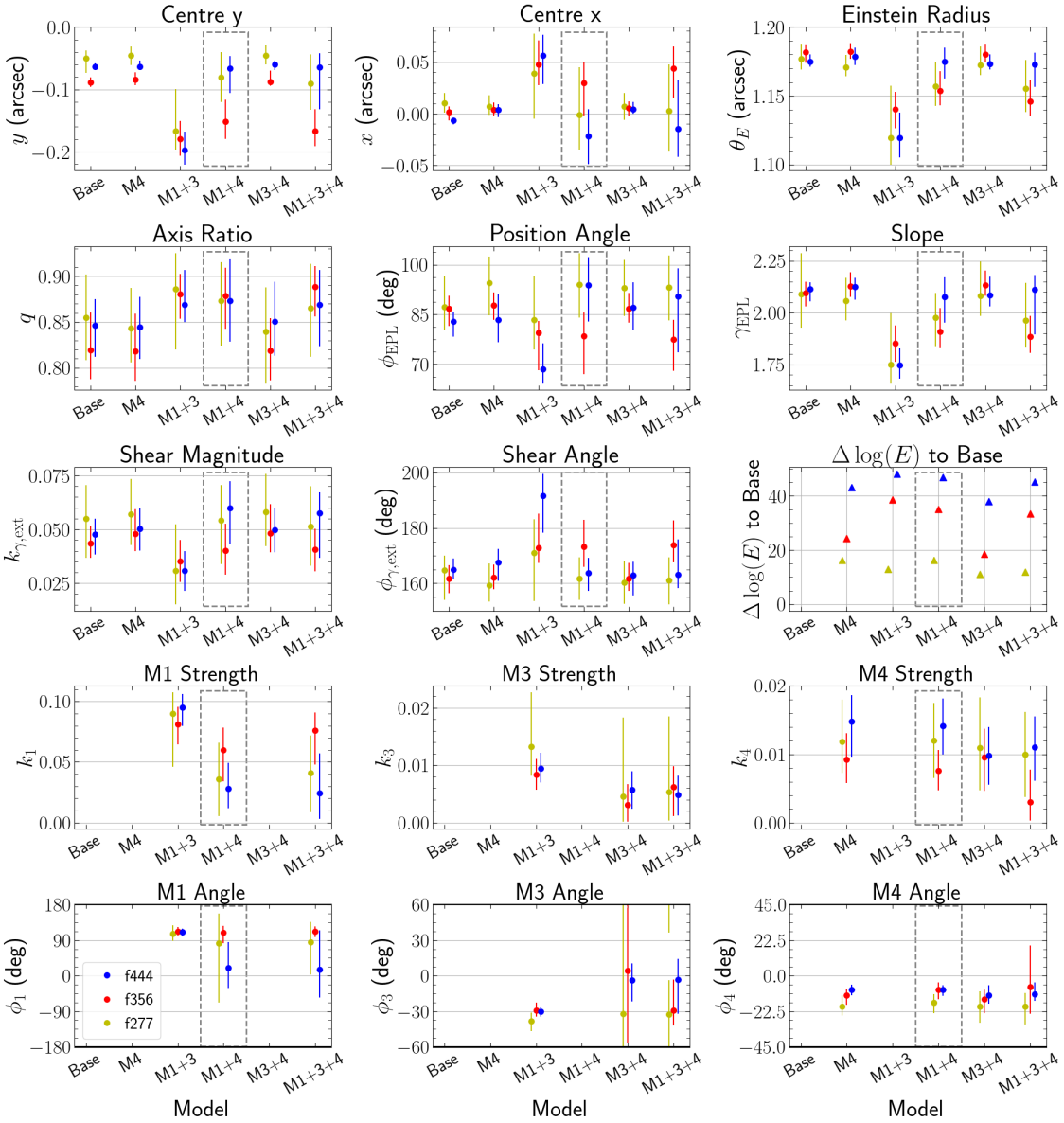

Figure 3.7: Reported parameters and associated 3σ errors for the highest evidence models without a subhalo in SPT2147-50, and the Base model. Multipole angles have a symmetry through $360/n$ - i.e. a 90 degree error on the M4 multipole means it is unconstrained as this multipole has rotational symmetry through 90 degrees, and so the errors are wrapped around $\pm(360/n)/2$. Evidence changes shown are in comparison to the Base EPL+Shear model. We highlight with the gray box our preferred final model of EPLγ+M1+M4.

offset, which is important as this model actually has the highest evidence of all the models in f444W ($\Delta\log(\mathcal{E}) = 48.16$) and f356W ($\Delta\log(\mathcal{E}) = 38.69$). In terms of result trends between multipoles, we do also see a relation between the M3 and M4 multipoles in this lens where the best-fit M3 magnitude slightly decreases and its angle becomes much less constrained once we add the M4 multipole (in M3+M4 and M1+M3+M4), and similarly for the M4 magnitude when the M3 is added. The M1 magnitude also shows decreases when the M4 is added compared to the M3.

3.4.1.3 Inclusion of both multipoles and substructure in SPT2147

Evidence increases from the addition of multipoles and the addition of substructures to the EPLγ model are very similar in magnitude, which again may be an indication that there is degeneracy between multipoles and substructure with each compensating for the absence of the other, as seen similarly in O'Riordan et al. (2024). Running the subhalo searches on the models which have multipole perturbations allows us to see if both can actually co-exist. Figure 3.8 shows the subhalo grid search results for the multipole models, with every multipole model shown having a grid cell with $\Delta\log(\mathcal{E}) > 10$ in f444W. No models show a cell with $\Delta\log(\mathcal{E}) > 10$ in f277W, but we do not draw strong conclusions from this filter due to the low source signal (and therefore low constraining power). The M3+M4 model has a high-evidence grid cell ($\Delta\log(\mathcal{E}) > 20$) in f356W, potentially accounting for the slight dip seen in the evidence for the multipole perturbation in this model. Importantly, most models in f444W and f356W (except for the M1+M3 and M1+M3+M4 models in f356W) still favour a subhalo in the same or similar position to the subhalo suggested from the base model search, showing that even with the addition of multipole perturbations, a substructure still obtains higher Bayesian Evidences for the model-fit.

Figure 3.9 shows the finalised multipole evidences and subhalo evidences for the base model and multipole models. We see two results here: firstly that multipole perturbations alone cannot reach the same evidence increase that just adding a subhalo to the base model can in the f444W filter but that they can reach and surpass this level in the f356W filter; second, we see that many models lie within a reasonable evidence range of one another, showing

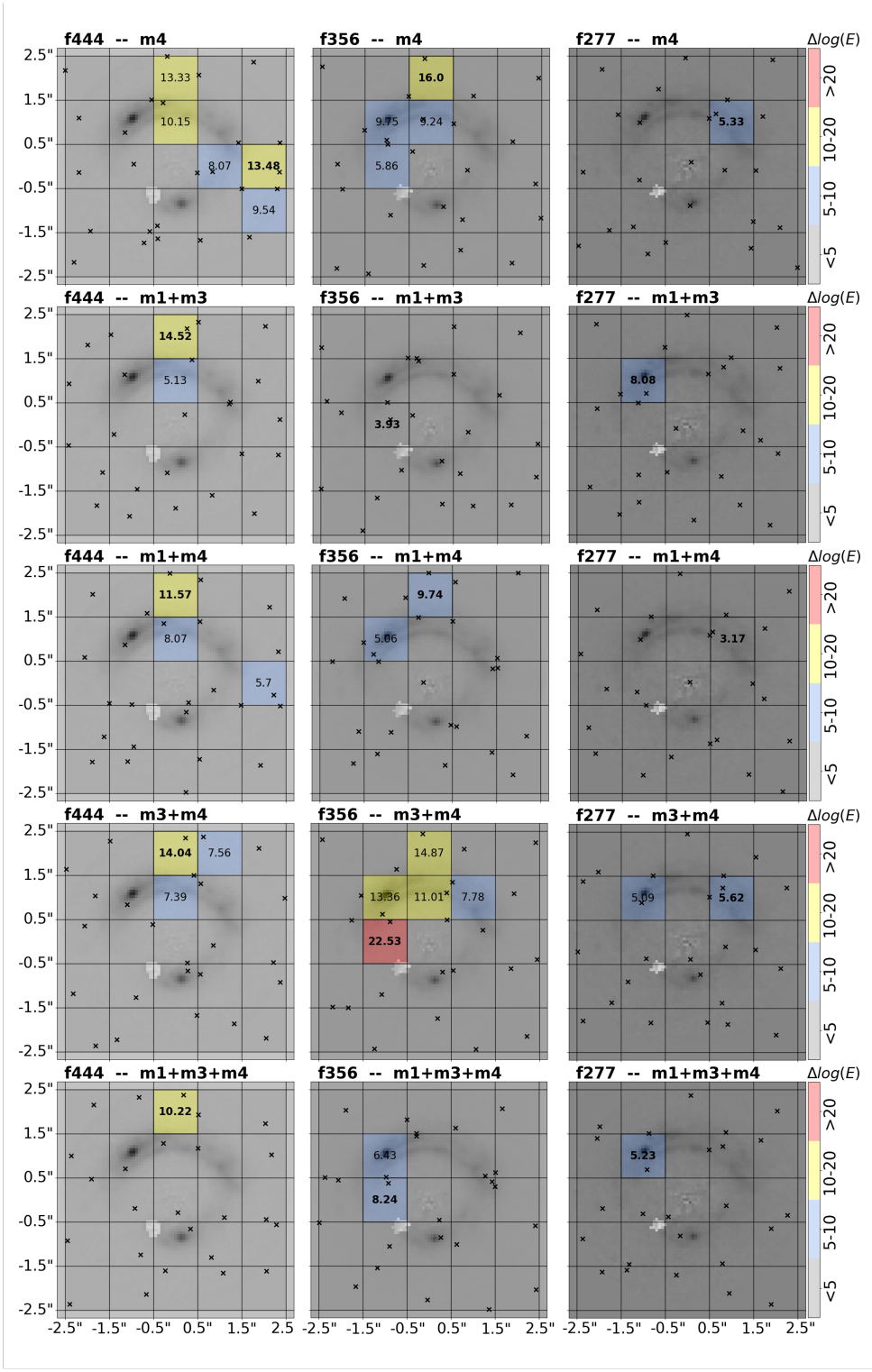

Figure 3.8: Results from the grid-based preliminary subhalo searches in SPT2147-50 for the EPLγ+Multipole models. The values and colours correspond to the Log-Evidence change - $\Delta\log(\mathcal{E})$ - when a subhalo is modelled in a certain grid cell. Crosses mark the best fit position of the subhalo within each grid cell. The highest evidence grid-cells are marked in bold. $\Delta\log(\mathcal{E}) = 10$ is considered a roughly 5σ detection.

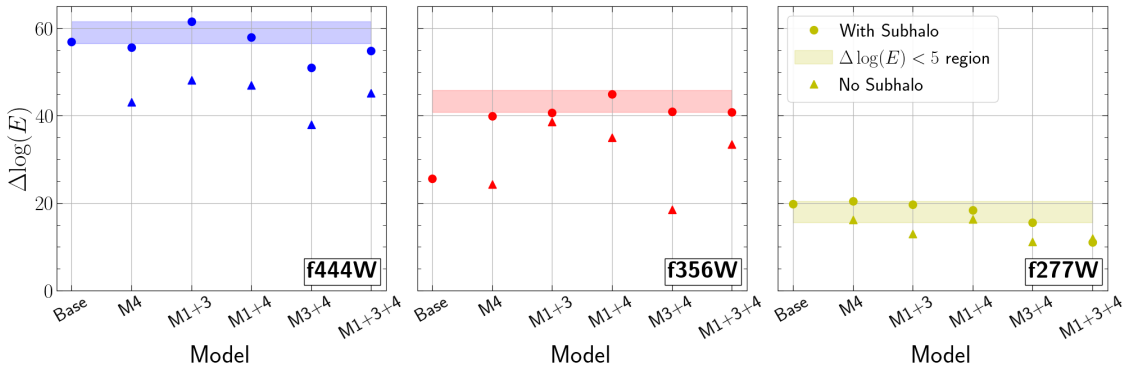

Figure 3.9: $\Delta\log(\mathcal{E})$ (Log-Evidence changes) for the addition of a multipole (triangles, for reference), and then subhalos (circles) to highest evidence models of SPT2147-50. All evidences are compared to the Base no-subhalo model. The shaded regions correspond to the (roughly 3σ) $\Delta\log(\mathcal{E}) < 5$ confidence region below the highest evidence models in each filter.

the difficulty we will have to choose the 'best' models confidently without informative physical priors and context. Following the method set out in Section 3.3.2, we utilise the multi-wavelength fitting advantages of these data and plot the confidence region of $\Delta\log(\mathcal{E}) < 5$ below the highest overall evidence models in each filter as the shaded regions in Figure 3.9. Again, neglecting the f277W filter due to its low constraining power, we see that the M1+M3+subhalo and M1+M4+subhalo models are the only models which lie within this region in both f444W and f356W. Since M1+M3+subhalo in f356W lies both at the edge of the region and only $\Delta\log(\mathcal{E}) \sim 2$ above the M1+M3 model, we take M1+M4+subhalo as the preferred model. Additionally, the M4 multipole perturbation is more easily related to physical structure than the M3 multipole, providing another reason to take this as the preferred model.

Table 3.3 shows the evidences, positions and masses for the recovered substructure in our favoured model, and Figure 3.10 shows the subhalo position and mass for all filters and models. Within individual models, all masses agree between filters, but there are some disagreements between f444W and f277W on position in the Base, M1+3 and M3+4 models. Between different models for each individual filter the f444W and f356W subhalo positions all agree, with some disagreements on the subhalo mass, which is to be expected from models which have different mass distributions in the macromodel. We will discuss in Section 3.5 the potential interpretations of the model-internal disagreements.

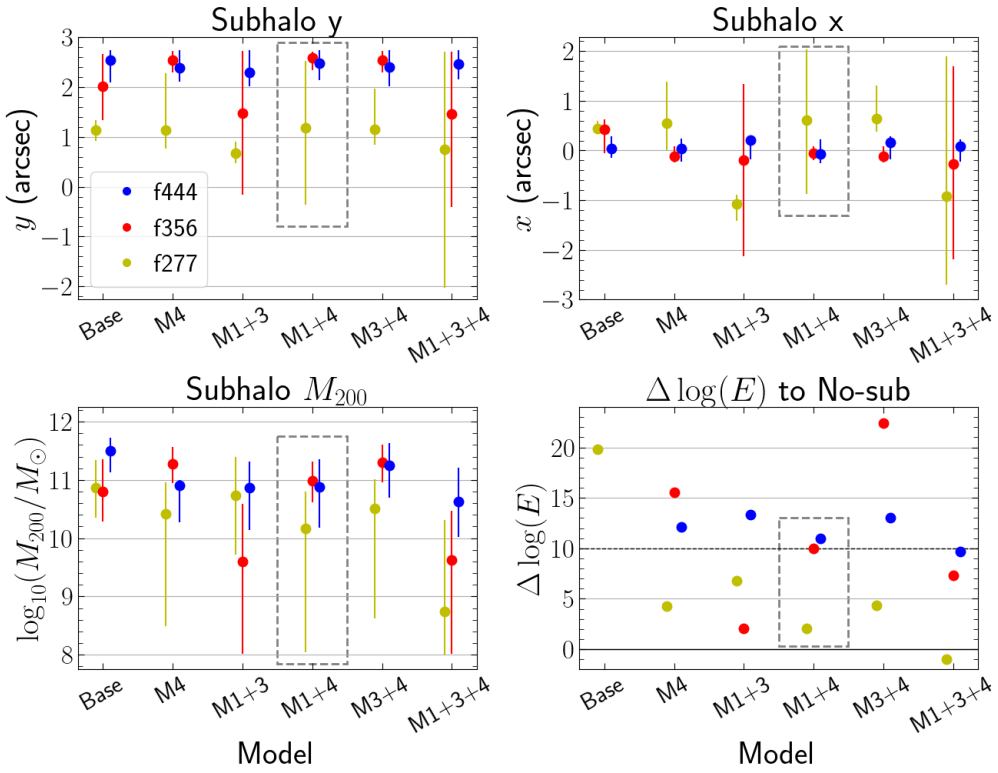

Figure 3.10: Reported subhalo parameters for the best-fit substructure to the Base and high-evidence multipole models of SPT2147-50. Our preferred model, EPLγ+M1+M4 is highlighted with the gray box. Log-evidence changes - $\Delta\log(\mathcal{E})$ - compared to the no-subhalo model of that type are also shown, but the Base f356W and f444W evidences are above the axis limit.

The macromodel parameters are shown in Appendix A.3.1, Figure A.2, as well as the changes in those parameters from the no-subhalo to the with-subhalo models in figure A.3. Generally, most changes are consistent with zero, although for best-fit values we see a general drop in M4 strength, and that the addition of a subhalo tends to bring the power-law slope closer to Isothermal ($\gamma_{\rm lens} = 2$). The most notable changes upon addition of a subhalo are to the Einstein radius, with the base, M4 and M3+M4 models showing a definitive drop in Einstein radius in f356W and f444W. For our preferred M1+M4 model however, the addition of the subhalo leads to no notable change in Einstein radius - there is a potential increase in EPL slope, decrease in shear magnitude and decrease in M4 strength, but all with errors making these changes consistent with zero.

	f444W	**f356W**	**f277W**
$\Delta\log(\mathcal{E})$ to Base	57.96	45.00	18.46
$\Delta\log(\mathcal{E})$ to M1+4 (no-sub)	10.97	9.96	2.07
Position y (arcsec)	$2.47^{+0.27}_{-0.33}$	$2.59^{+0.13}_{-0.25}$	$1.19^{+1.34}_{-1.55}$
Position x (arcsec)	$-0.07^{+0.29}_{-0.19}$	$-0.06^{+0.15}_{-0.13}$	$0.61^{+1.43}_{-1.48}$
$\log_{10}(M_{200}/M_\odot)$	$10.87^{+0.53}_{-0.71}$	$10.99^{+0.33}_{-0.37}$	$10.17^{+0.64}_{-2.12}$

Table 3.3: $\Delta\log(\mathcal{E})$ (log-evidence changes) and subhalo parameters for our prime model of EPLγ+M1+M4+subhalo. Errors quoted are 3σ. Evidences are quoted to 'Base' - the EPLγ model, and to 'M1+M4 (no-sub)' - the EPLγ+M1+M4 model before adding the subhalo. All values are consistent across three filters.

3.4.1.4 SPT2147 model residuals

The normalized residuals (i.e. the model residuals divided by the noise, from here forward just 'residuals') from the fits to SPT2147 of the Base, Base + Subhalo, Base + M1 + M4, and Base + M1 + M4 + subhalo models are shown in Figure 3.11. There are areas of the upper arc of the lensed source (marked with back boxes) which see noticeable changes in their residuals from the Base model to the model with multipoles and to the model with substructure, but the change is much less obvious going from these models to the model with multipoles *and* substructure, apart from in the f356W filter, which is a good indicator that the increase in bayesian evidences we see is due to improvements in the modelling of the lensed source and not the lens itself or the noise.

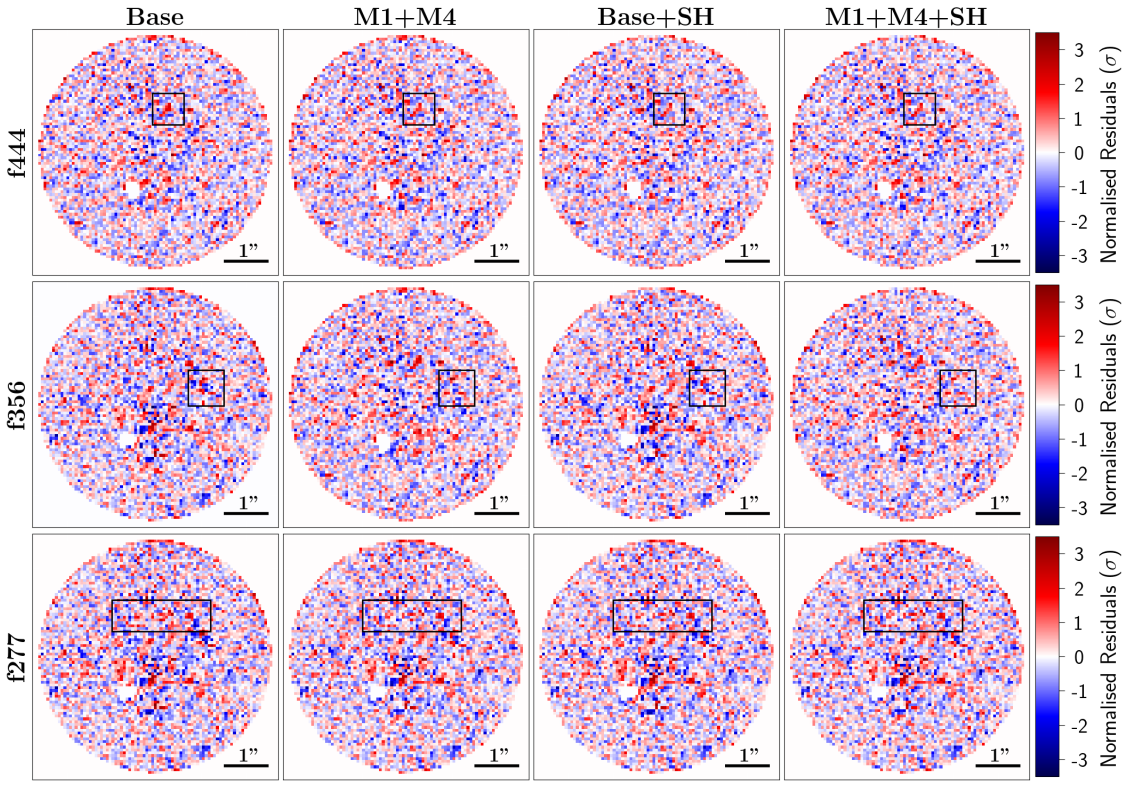

Figure 3.11: Normalized residuals (residuals divided by the noise in each pixel) from model fits to SPT2147-50 of the 'Base' EPLγ model and the model including $m = 1$ and $m = 4$ multipoles, and their corresponding fits with substructure additions ('SH'). The black boxes highlight areas where there are notable and correlated residual changes within a filter, all corresponding to the upper arc of the lensed source.

3.4.2 SPT0418-47 Results

3.4.2.1 Base model substructure results for SPT0418

Figure 3.12 shows the subhalo grid-search results for the f444W and f356W base models in SPT0418. The f277W filter had too low a source signal level to produce physically reasonable model results, so it is not shown. There is a potential indication of substructure signal towards the lower left of the image, but in only one grid cell in each filter, and moving closer to the Einstein ring in the lower-signal f356W filter. The grid-search evidences are $\Delta\log(\mathcal{E}) \sim 5$, and the finalised search evidences are $\Delta\log(\mathcal{E}) = 4.44, 4.31$ for f444W, f356W, meaning there is no appreciable evidence for substructure in this lens when using the base EPLγ model.

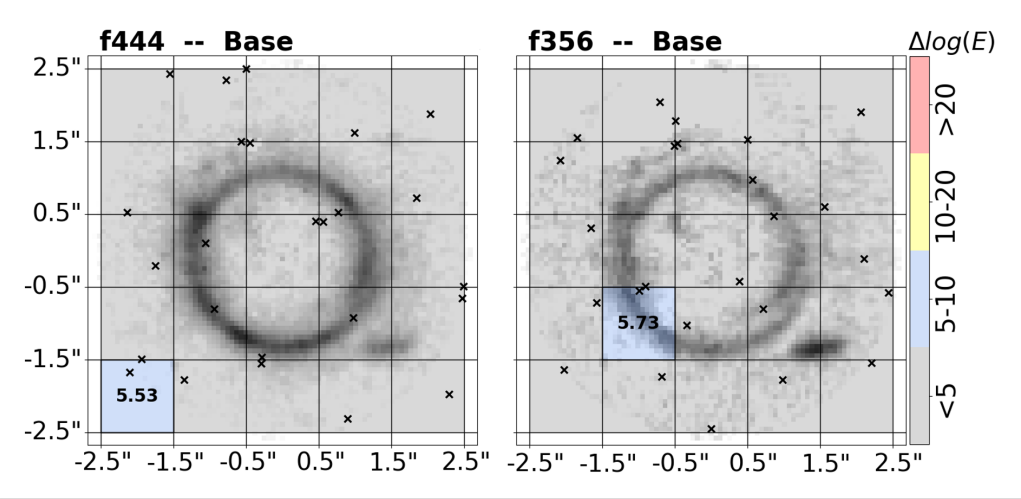

Figure 3.12: Results from the grid-based preliminary subhalo searches in SPT0418-47 for the base EPLγ model. The values and colours correspond to the Log-Evidence change ($\Delta\log(\mathcal{E})$) when a subhalo is modelled in a certain grid cell. Crosses mark the best fit position of the subhalo within each grid cell. The highest evidence grid-cells are marked in bold. $\Delta\log(\mathcal{E}) = 10$ is considered a roughly 5σ detection.

Obviously, the simple fact that we do not find any evidence for substructure does not mean that no substructure exists in this lens; rather it means that for the observation we have, we are unable to detect any substructures below a given mass as they do not provide strong enough perturbations to be detectable given the data. To fully understand the non-detections in this system, one would have to investigate the sensitivity function for this lens, which involves simulating many test masses to discover the lowest detectable mass in each position. One can make an estimate however of the lowest detectable mass (i.e. masses above this we rule out) in each grid cell position by using the 3-sigma upper limit of the mass posterior. Since the mass in that location gives no appreciable evidence increase, this should indicate that any larger mass structures in that location are not favoured in the data over this smaller mass structure as the larger mass would have a stronger perturbation on the system and the model is not requiring this. An example of this is shown in Figure 3.13, showing the $\log_{10}(M_{200}/M_\odot)$ for these minimum detectable masses, where these are in general higher for the f356W filter where we generally see very high mass exclusion thresholds (all $> 10^{10.3} M_\odot$), whereas for f444W we can generally go slightly lower - for the best grid cell we rule out masses only above $M_{200} = 10^{9.64} M_\odot$.

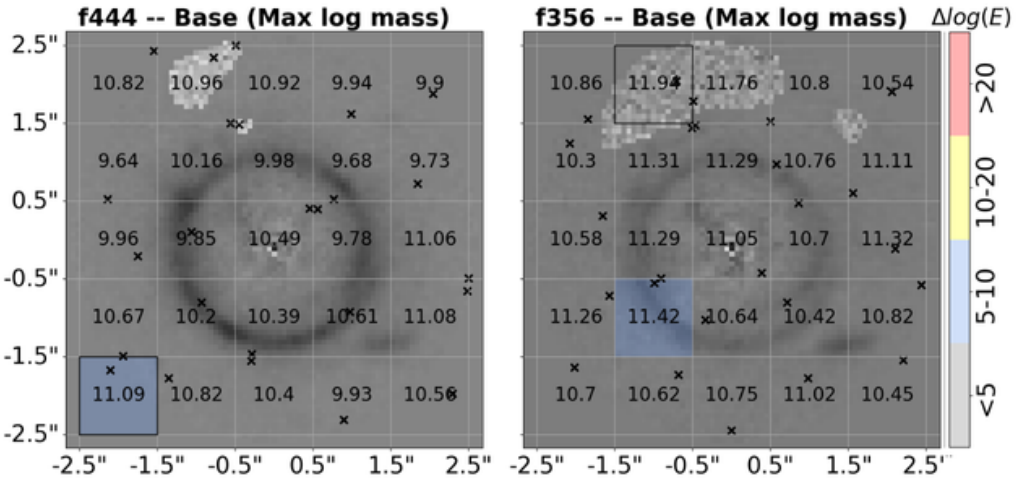

Figure 3.13: Results from the grid-based preliminary subhalo searches in SPT0418-47 for the base EPLγ model. The shading in the grid cells correspond to the Log-Evidence change ($\Delta\log(\mathcal{E})$) for the best fit subhalo in a certain grid cell, with the highest evidence grid cells outlined. The number values in each cell represent the 3-sigma upper limit on the M_{200} posterior, where masses above this value are ruled out within this location. Values are given as $\log_{10}(M_{200}/M_{\odot})$.

3.4.2.2 Results of multipole perturbations in SPT0418

Given that there is no evidence for substructure with the base EPLγ model, we already know that the model can fit the data reasonably well without any additional perturbations, and thus we do not expect strong evidences for multipole complexity in the mass model. Figure 3.14 shows $\Delta\log(\mathcal{E})$ (evidence - triangles) and $\Delta\log(\mathscr{L})$ (likelihood - crosses) when multipoles are added to the EPLγ model. The small positive log-likelihood increases indicate that multipole models produce a small improvement to the overall fit. However, the decrease in evidence implies that this does not outweigh the increase in model complexity and thus the multipole models are disfavoured overall.

The f444W filter has no increase in $\Delta\log(\mathcal{E})$ for any multipole addition, and in fact, as more multipoles are added, the magnitude of the evidence drop increases - as one would expect if adding further unnecessary complexity to the model. The f356W filter does show minor increases of $\Delta\log(\mathcal{E}) < 10$ in all additions except for M1-only and M3-only. Despite this, the fit to the f356W filter required the model to be initialised from the f444W model as the source signal was too low to provide a reasonable constraint on parameters

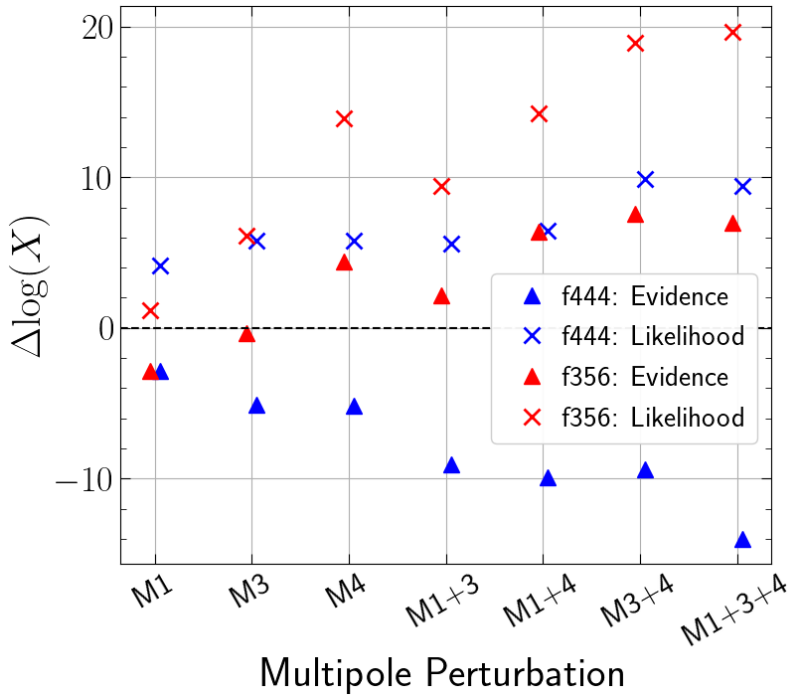

Figure 3.14: $\Delta\log(\mathcal{E})$ (Log-Evidence changes, triangles) and $\Delta\log(\mathscr{L})$ (Log-Likelihood changes, crosses) for the addition of multipole perturbations to the base model of SPT0418-47.

and as such we place much less value on the f356W results and show them primarily for completeness, using the f444W as the primary result set. Regardless, the low evidences for multipoles in f356W coupled with the negative evidences for multipoles in f444W lead to the conclusion that there is no basis to claim multipole angular complexity in the mass of lens - an important contrast to SPT2147. We show the parameters for the fits in Appendix A.3.1, Figure A.4 and show that they are all consistent across every model and filter, with the exception of f444W shear angles being generally higher than f356W. The consistency and the fact that all multipole strengths return close to zero strengthens the opinion of the Base model being most appropriate as the multipole models offer little to no difference.

3.4.2.3 Inclusion of both multipoles and substructure in SPT0418

As mentioned, the f356W model fit required initialising from the f444W model results, and therefore we primarily test the f444W model with substructure additions. The f444W model, however, had all negative log-evidence changes upon multipole addition, so we

therefore only test the addition of a substructure to the models with a single multipole perturbation. Figure 3.15 shows the finalised log-evidence changes from the smooth EPLγ model for the multipole additions (for reference) and the multipole+subhalo (or just subhalo for the Base model) additions for the f444W Base, M1, M3, M4 models and the f356 Base and M1 models.

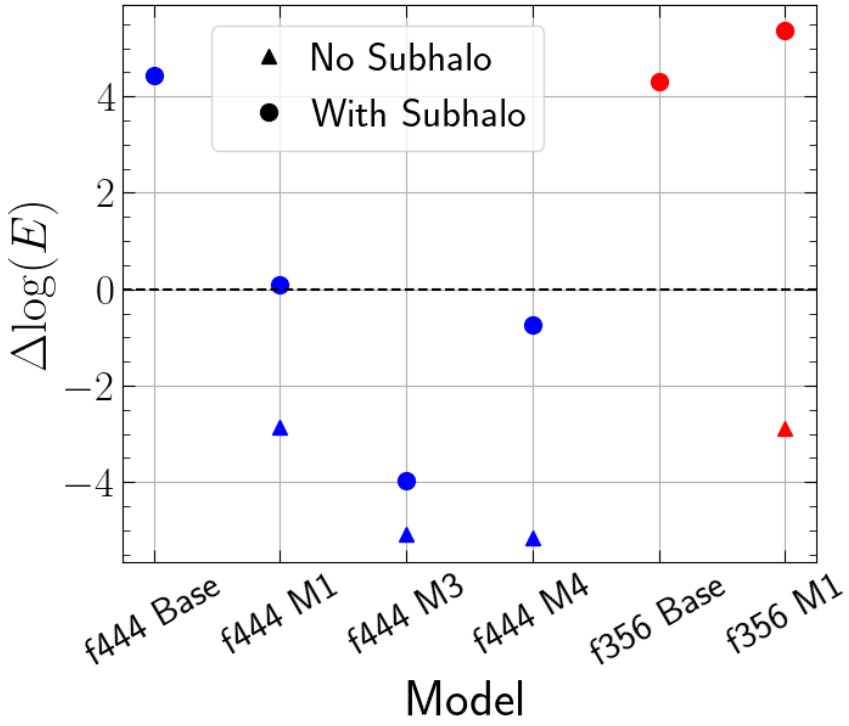

Figure 3.15: $\Delta\log(\mathcal{E})$ (Log-Evidence changes) for the addition of a multipole (triangles, for reference), and then subhalos (circles) to the best models for SPT0418-47. All evidences are compared to the Base EPLγ no-subhalo smooth model. The dashed line marks $\Delta\log(\mathcal{E}) = 0$.

The subhalo grid-searches for the multipole models are not shown as they contain no cells with $\Delta\log(\mathcal{E}) > 10$, and only one cell with $\Delta\log(\mathcal{E}) > 5$ in f444W, although interestingly this is now on the lower-right of the lens rather than the lower-left as seen in Figure 3.12, but is likely just fitting noise or compensating for the multipole addition. Figure 3.15 does show that the M1+subhalo fit in f356W has an evidence boost from the smooth M1 model of $\Delta\log(\mathcal{E}) = 8.25$, but considering that the addition of the M1 causes a drop in evidence of -2.88 from the base EPLγ model, we suspect the subhalo is primarily just compensating for this.

3.4.2.4 SPT0418 model residuals

We plot the normalized residuals for SPT0418 in Figure 3.16, showing the Base model, Base + subhalo model, and Base+M1+M3+M4 model. We see that, unlike in SPT2147 (section 3.4.1.4), there is no noticeable change in the residuals when adding either angular complexity or substructure to the Base model, which supports the narrative that this lens does not have detectable complexity.

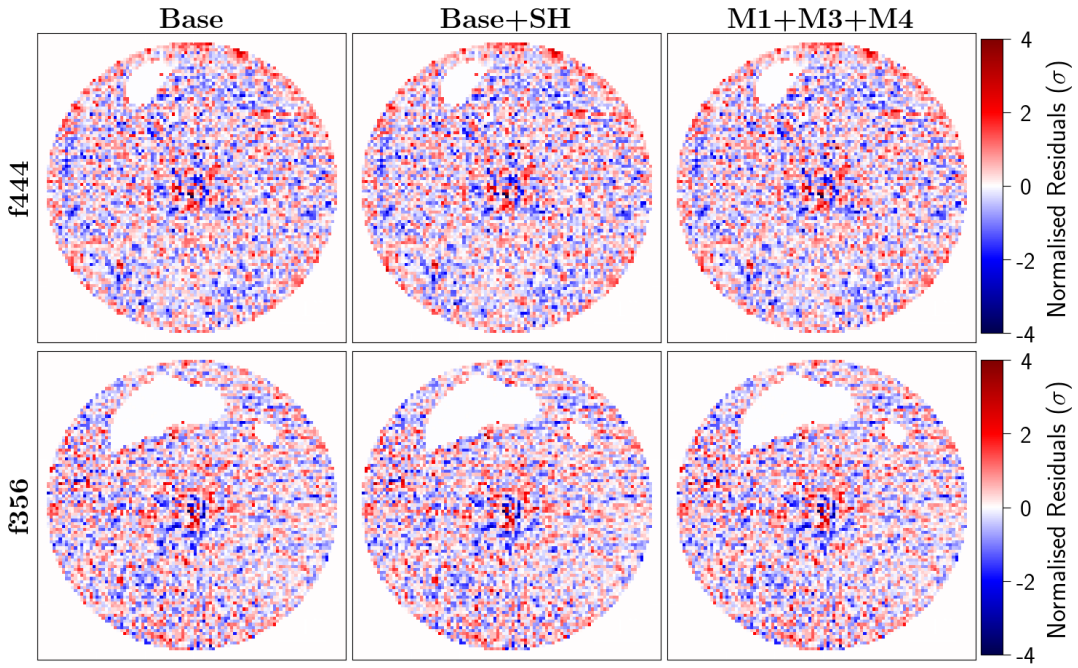

Figure 3.16: Normalized residuals (residuals divided by noise in each pixel) from the model fits to SPT0418-47 for the 'Base' EPLγ model, this model with subhalo ('SH'), and the model containing $m = 1$, $m = 3$ and $m = 4$ multipoles (but no substructure). We see no areas where there are major correlated residual changes when extra complexity (angular or substructure) is added to the model.

3.5 Discussion

3.5.1 Is there a dark subhalo in SPT2147?

The analysis of SPT2147 provides strong evidence (exceeding 10σ) for both: (i) models with angular complexity (multipoles) when a dark matter (DM) subhalo is omitted, and (ii) models including a DM subhalo when multipoles are omitted. The preferred model (criteria in section 3.3.2) includes both order 1 and order 4 multipoles and a DM subhalo, showing evidence increases of $\Delta\log(\mathcal{E}) = 10.97$, 9.96, and 4.3 compared to models without a DM subhalo, for the f444W, f356W and f277W filters respectively. This suggests that the mass structure of SPT2147 likely contains both angular complexity in the lens mass distribution and the presence of a further halo substructure. However, systematic uncertainties in strong lens modelling make it difficult to come to a definitive interpretation, leading us to consider three possibilities:

1. **Lens galaxy contains only angular complexity, without a DM subhalo:** In this scenario, the DM subhalo is producing a false positive detection with a large evidence increase ($\Delta\log(\mathcal{E}) > 50$) by compensating for missing complexity in the power-law lens mass model, an effect shown in e.g. He et al. (2023). However, the model including M1 and M4 multipoles still favours the DM subhalo with an evidence increase of 10.97, and even with all of M1+M3+M4, the evidence increase for substructure is 9.68, meaning that if a DM subhalo is truly not present the mass distribution must have complexity beyond what the combination of the order 1, 3 and 4 multipoles can capture.

2. **Lens galaxy contains a DM subhalo, without angular complexity:** Here, the multipole-only models are favoured because they are fitting themselves to the lensing signal of a genuine DM subhalo, a degeneracy outlined by O'Riordan et al. (2024). However, some models with the combination of multipoles and substructure are consistently a higher evidence than the models with substructure only, implying that there is excess lensing potential beyond what can be captured by a single subhalo.

3. **Lens galaxy contains both angular complexity and a DM subhalo:** A combination of the above cases. The models including a DM subhalo but lacking multipoles see evidence increases of $\Delta\log(\mathcal{E}) \sim 50$ because the subhalo primarily accounts for missing complexity in the power-law model of the central mass distribution (see He et al. 2023). However, even after the multipoles are added, accounting for this missing complexity, a DM subhalo remains necessary for an improved model fit as there is a true subhalo in the system.

Option **3** above, that this lens contains both substructure and multipoles, is the solution with the highest Bayesian evidence, and is a similar option to work by Enzi et al. (2024) on SDSSJ0946+1006, who find evidence for significant multipoles alongside the substructure in this lens, but note that the multiple source configuration of this lens (see Section 1.3.2) is essential to reducing the degeneracy between multipoles and other parameters - a luxury that we do not have with SPT2147-50.

Given the current evidence, we consider SPT2147 as a dark matter subhalo *candidate*. Future work will aim to refine this interpretation using more flexible lens mass models, such as potential corrections (Suyu et al., 2009; Vegetti et al., 2012). SPT2147 is an ideal target to investigate this approach, given the apparent need for both angular complexity and a DM subhalo in its modelling, along with the availability of multi-wavelength data for validation. Additionally, follow-up lensing analysis with ALMA data is planned, building on Amvrosiadis et al. (2025a). Whilst we are not there yet, SPT2147 suggests that separating a dark matter substructure from angular complexity in strongly lensed extended sources is a tractable task, ensuring that strong lensing can still provide a key test of the dark matter particle in the near future.

3.5.2 Candidate substructure position and mass

The best-fit position for the DM subhalo in SPT2147 lies approximately 1" north of the uppermost part of the lensed arc. In the f277W filter, the subhalo position shifts onto the lensed arc, however this is not in tension with the f444W and f356W results due to greatly

increased errors on the position. In the upper panels of Figure 3.10 we see that all subhalo x-positions agree to 3σ except in the M3+M4 f277W model, and subhalo y-positions agree except f277W-f444W results with the Base and M1+M3 models - the important point being that there is good agreement to 3σ in subhalo position (and masses) of our preferred model of M1+M4. The reason for the discrepancy in precision of the f277W results is likely due to the much lower signal-to-noise ratio of the lensed source in this filter (see Table 3.1) and the resultant need of the model to bring the subhalo closer to the arc to achieve a noticeable perturbation with this low signal. Due to this, we assume that the true subhalo position aligns with the fits from the f444W and f356W bands, at the centre-top of the image, and primarily look at these filters (and specifically f444W) from here forward.

It is known also that the inferred subhalo mass depends significantly on the choice of its density profile. Our analysis assumes an NFW profile, which has a shallower central density compared to the pseudo-Jaffe profile used in other works (e.g., Vegetti et al., 2010, 2012). This assumption leads to higher subhalo mass estimates, as seen in the analysis of SDSSJ0946+1006 by Nightingale et al. (2024), where the inferred mass was around $\sim 10^{10.5} M_{\odot}$, compared to masses in the region of $10^{9.5} M_{\odot}$ inferred from studies using more concentrated profiles (e.g. Minor et al., 2021). Additionally, Despali et al. (2018) demonstrated that masses derived using NFW profiles map to lower values when assuming pseudo-Jaffe profiles.

A recent study from Despali et al. (2024) found that for two detections of dark subhalos in the literature, these subhalos prefer a steeper density slope than the NFW profile, so it is likely that our quoted masses are an over-estimate due to a too-low concentration. Additionally, if the subhalo lies along the line-of-sight rather than within the lens plane, this could affect both its detectability and the inferred mass (e.g., He et al., 2022). The availability of multi-wavelength data for SPT2147 makes it an ideal candidate for future investigations into the subhalo density profile and its potential impact on mass estimates.

3.5.3 Candidate substructure visibility

Whilst the subhalo's relatively large inferred mass helps explain how it can still cause a lensing perturbation at a reasonable distance from the arc, a DM halo of $\sim 10^{11} M_{\odot}$ would typically be expected to host a visible dwarf galaxy; however, no such galaxy is observed. This lack of observation may be due to the non-existence of the object, an incorrect mass estimation, or the fact that its luminosity would be too low to be visible in the observation. We can check if we would actually be able to view the luminous component in by estimating the upper limit for the subhalo's observable SNR under the same conditions as experienced in the actual observing run.

Since the upper error on the (total) mass of the substructure is $M_{200} = 10^{11.4} M_{\odot}$ for f444W (Table 3.3), we approximate this as an analogue of the Large Magellanic Cloud, which has total mass $M_{\rm tot} \sim 10^{11.4} M_{\odot}$ (Peñarrubia et al., 2015; Shao et al., 2018), and absolute (Vega) v-band magnitude $M_V = -18.1$ (table 3 of McConnachie, 2012). Using the Ned Wright Cosmology Calculator* from the UCLA Cosmology Calculators†, with $H_0 = 67.8, \Omega_M = 0.31, \Omega_{\Lambda} = 0.69$ (Planck Collaboration et al., 2016), we estimate a luminosity distance at $z = 0.845$ for this object to be $d_L = 5512$Mpc, and thus calculate an expected apparent magnitude of $m_V = 25.6$.

We use the JWST Exposure Time Calculator (ETC)‡ (Pontoppidan et al., 2016) to then calculate the upper-limit signal-to-noise we would expect from an actual observation of this object with the stated apparent magnitude (we do not apply any extinction). We apply the same observing strategy from the *TEMPLATES* (Rigby et al., 2024) observing proposal§ and approximate the light as an extended source with a flat profile (simple uniform circle) with $r = 0.025$ arcseconds, based on the approximate size of the residuals in Figure 3.11. We choose a built-in SED of a 5-Gyr old elliptical galaxy to provide to the calculator to convert to the f444W filter flux. This SED comes from the SWIRE¶

*https://www.astro.ucla.edu/%7Ewright/CosmoCalc.html
†https://ned.ipac.caltech.edu/help/cosmology_calc.html
‡https://jwst.etc.stsci.edu/
§https://www.stsci.edu/jwst/phase2-public/1355.pdf
¶https://www.iasf-milano.inaf.it/~polletta/templates/swire_templates.html

template library (Polletta et al., 2007) and is obviously only an approximation of the true object SED but we consider the approximation to be reasonable, particularly regarding age given the lookback time of ~ 7 Gyr. We also use the ETC ability to extract and use a noise map generated from the day of the observation (09-Sep-2022) and apply this into the calculation.

The result is an expected SNR of approximately 0.26, indicating that the object would be indistinguishable from the background. A dwarf galaxy detection where the light is non-detectable is not unreasonable as an alternative to a dark subhalo; recent work from Ballard et al. (2024) showed that the substructure detection in SDSSJ0946+1006 is compatible with a dwarf galaxy which is too faint to be detected given the available data. If however this object is dark and has no luminous component, this leads to interesting questions regarding the nature of structure formation since we would expect there to be a galaxy formed within the subhalo if using classical models. One prime option if this were truly a dark subhalo is that the quoted mass value is incorrect as it assumes an incorrect mass-concentration value, i.e. the subhalo density profile could actually be much more centrally concentrated than is assumed in the model, which means that the mass required to reproduce the lensing effect would be lower. This would correlate with the theories surrounding the substructure in J0946 where, if the object is assumed to be fully dark, a very high concentration is required. The reason this is interesting is that, although these halo masses are not in the regime to contrast CDM and WDM, the high concentrations in the J0946 object are seen as being too high for a CDM subhalo, and thus an indicator of SIDM (e.g. Enzi et al., 2024; Li et al., 2025). Because of this, alternative models need to be applied in future work which include allowing the substructure to very its concentration, as well as models including a stellar component in the mass distribution of the substructure.

3.5.4 Redefining substructure detection criteria

Previous strong lens studies that assume a power-law plus shear mass model have adopted different Bayesian evidence criteria for identifying DM subhalo candidates. Detection thresholds vary: Vegetti et al. (2010, 2012) and Ritondale et al. (2019) use $\Delta\log(\mathcal{E})$ of 50,

corresponding to a roughly 10σ criterion, and Nightingale et al. (2024) use $\Delta\log(\mathcal{E}) = 10$, corresponding to a roughly 5σ criterion. Many sensitivity mapping studies (testing what simulated substructures are detectable in an image and by how much) set thresholds between 50 and 10 (Amorisco et al., 2021; Despali et al., 2022; O'Riordan et al., 2023, 2024). As mentioned throughout the previous sections, an increase of 10 corresponds to roughly a 5σ detection, making this an appropriate benchmark for considering a detection as significant.

This study shows that the significance of a DM subhalo detection is sensitive to the choice of mass model. For example, in SPT2147, the EPLγ model favoured a DM subhalo with evidence increases of $\Delta\log(\mathcal{E}) = 60.35, 42.13, 20.54$ in the f444W, f356W, and f277W bands, respectively. In contrast, when including a combination of order 1 and 4 multipoles, these values dropped to $\Delta\log(\mathcal{E}) = 10.97, 9.96, 4.3$. This pattern is also observed in other analyses. For example, Nightingale et al. (2024) found that the evidence for a DM subhalo in SDSSJ0946+1006, a lens with a confirmed/accepted substructure, varied from $\Delta\log(\mathcal{E})$ =72.36 for a power-law plus shear model to 22.52 for a decomposed stars-plus-dark matter model. These results suggest that more refined mass models can reduce the evidence threshold needed to detect subhalos, as they better capture the underlying complexity of the lens.

This has important implications for constraints on the mass of the dark matter particle. As mentioned, sensitivity mapping studies often assume a threshold for detection of up to 50, which may be conservative in their estimates of DM subhalo detectability. If improved mass models and cross-referencing across multiple filters allow for a lower detection threshold, these forecasts could be adjusted accordingly. This could lead to a scenario where fewer lenses are needed to achieve comparable constraints on the dark matter particle mass, even though more complex mass models are now assumed. A more thorough evaluation of how to establish robust detection criteria is therefore essential for future studies, and whether our implementation, as described in Section 3.3.2, remains appropriate.

3.5.5 Contrasting SPT2147 with SPT0418

The contrast in results between SPT2147 and SPT0418 shows that we do not just systematically 'detect' multipoles simply because they are included in the model. SPT0418 is a prime example that actually not all lens mass models require high levels of complexity, and it is important to note that this improves the confidence that the detections in SPT2147 are not systematics where complexity is added to artificially inflate the evidence (i.e the model doesn't just want all the parameters it can get), since that would then also be the case here. Further, as mentioned in sections 3.4.1.4 & 3.4.2.4, there is a difference in the effects of the complexity additions on the model residuals - where SPT2147 shows evidence of a correlated improvement to the residuals along the lensing arcs, whereas SPT0418 shows no such improvements. This shows the physical meaning behind the changes (or lack thereof) seen in the Bayesian evidences.

Given some of the recovered axis ratio parameters, the SPT0418 lens mass could likely be reasonably well described by a singular isothermal sphere mass model ('SIS': the simplest applicable model which is the EPL with $q = 1, \gamma = 2$, i.e. a spherical version of the SIE). This dramatic mass simplicity could have numerous explanations: the level of source signal observed may be too weak to constrain any complexity in the lens mass; the source itself, which is a merger of two elliptical galaxies (Cathey et al., 2024), may, despite its large span over the source plane, lack suitably placed features to enable detection of complexity (i.e. reconstruction of a spiral has fewer lensing solutions than reconstruction of a blob); or alternatively, this lensing galaxy may genuinely have little to no angular structure. Regardless, the lack of multipole evidence in SPT0418 makes the indications shown of angular complexity in SPT2147 that much more compelling, and enhances the argument for further study of this lens. What would additionally be interesting is deeper imaging of SPT0418, in order to provide higher levels of source signal in order to re-test the application of multipoles to see if the evidences change.

3.6 Conclusions for this work

This Chapter reported work where I investigated multi-wavelength images from JWST of two strongly lensed systems to test the effects of angular (multipole) perturbations to the standard elliptical power-law mass model, and the impact of these perturbations on substructure detection (Lange et al., 2025). We find that SPT2147-50 has evidence for angular complexity (of 1st and 4th order multipole combination), with Bayes Factor $\Delta\log(\mathcal{E}) \sim 47, 35, 16$ in f444W, f356W, f277W imaging respectively and that the inclusion of these multipoles reduces the Bayes Factor for substructure by $\sim 46, 16, 18$ for f444W, f356W, f277W.

Irrespective of complexity, our highest SNR filter (f444W) always gives a substructure detection in SPT2147 above 4σ. We will refer to this as a dark subhalo *candidate*, as we still require further modelling such as non-parametric potential corrections (Vegetti et al., 2009) since we currently do not have sufficient understanding of possible multipole-subhalo degeneracies. If testing using ALMA data (which probes a different source morphology from longer-wavelength emission), using further models including alternative profiles for the substructure (e.g. Pseudo-Jaffe) or freeing the concentration of the NFW also provide detections, this could provide further evidence that this is a real object and not a degeneracy specifically caused by the NFW and multipoles interacting within the model. Differently however we do not find any evidence for complexity in SPT0418 (angular or substructure) which indicates that the detections in SPT2147 are less likely to be systematics related to the general modelling process, although we require formal sensitivity mapping of the SPT0418 data to test whether any reasonable constraints could actually be placed on complex perturbations.

A quantitative summary for SPT2147 is:

- When assuming only a standard power law plus external shear model for the lens galaxy mass, we favour a dark matter subhalo inclusion with Bayes factor $\Delta\log(\mathcal{E}) = 56.90, 25.70, 19.84$ in filters f444W, f356W, f277W. These are all well above 5σ.

- We find similarly strong evidence for angular mass complexity in the lens galaxy mass distribution. Inclusion of a combination of first, third and fourth order multipoles is favoured by Bayes factors $\Delta\log(\mathcal{E}) = 45.19, 33.54, 12.05$ and inclusion of only first and fourth order multipoles is favoured by Bayes factors $\Delta\log(\mathcal{E}) = 46.99, 35.04, 16.39$ (in filters f444W, f356W, f277W respectively; again all well above 5σ).

- Based on the higher source-SNR filters f444W and f356W only, depending on the combinations of multipoles and substructure used, the first order multipole has best-fit magnitude in the range $2.43 - 9.52\%$; the third order multipole has best-fit magnitude $0.29 - 1.34\%$; and the fourth order multipole has best-fit magnitude $0.30 - 1.48\%$.

- A dark substructure is still favoured in models that include multipoles, but to a lesser extent. By implementing a 'confidence region' of $\Delta\log(\mathcal{E}) < 5$ from the highest evidence model in each filter, the best applicable model (within this region in all three filters) includes only first and fourth order multipoles (plus substructure), and the Bayes factors for substructure additions are $\Delta\log(\mathcal{E}) = 10.97, 9.96, 4.35$ in f444W, f356W, f277W ($\sim 5.05, 4.85, 3.4\sigma$).

- This best model substructure *candidate* has mass $\log_{10} M_{200} = 10.87^{+0.53}_{-0.71} M_\odot$ in f444W and $\log_{10} M_{200} = 10.99^{+0.33}_{-0.37} M_\odot$ in f356W.

Chapter 4

The elliptical structure of the light and mass of lens galaxies

4.1 Preamble

This chapter primarily discusses work that will be released in upcoming papers, and together with Chapter 5, follows on from some of the questions raised in Chapter 3, regarding our confidence in the modelling of angular complexity in lens galaxies. Specifically in this chapter, we want to test whether radially variable models would have any effect on the results of lens models. We will approach this by fitting both the lens mass (with a standard EPLγ), but also the lens light, using ellipses to fit the isophotes (e.g. Hao et al., 2006; Chaware et al., 2014). We do not yet apply multipoles, leaving this for Chapter 5, but instead we fit a pair of light models - one where the parameters of the ellipses that fit the isophotes is constant at all radii (like the parameters for the mass distribution would be, given it is only parametrised by one profile - the EPL), and another where the orientation and ellipticity of these ellipses can vary with radii. We can then launch a two pronged investigation: firstly by looking at agreement between the three models we can discern whether light is a good tracer of mass in these galaxies and whether the two light models yield similar results, allowing us to make inferences on the suitability of only using one mass profile (a single EPL) in lens modelling; secondly we can investigate the external

shear. Whilst the external shear was not discussed to great length in Chapter 3, when it was introduced in Section 2.4 it was noted that frequently in lens modelling shears have potentially inflated values with the literature concluding that the model solvers are likely using the shears to compensate for missing complexity in the provided models of the main deflector mass distribution (e.g. Keeton et al., 1997; Treu et al., 2008; Etherington et al., 2024). Now that we are fitting a flexible light model, we can compare directly any light variability against the shears that are returned from the mass modelling, and begin to make inferences on whether this type of variance may correlate with the external shear magnitudes.

Investigations of the light and mass agreement in lens galaxies is not a new concept. Keeton et al. (1998) was an early paper using a method similar to ours in fitting various light profiles to an image and finding that the projected light and mass distributions of 17 HST imaged lens galaxies were aligned to within 10°. Koopmans et al. (2006) perform an analysis on the same sample we use as part of its sample release paper series, with Ferreras et al. (2008) performing an independent analysis of a subset of the sample. They both use stellar dynamics and population synthesis methods to fit the stellar light distribution of galaxies as opposed to our method of ellipse fits to the image, but both find close alignment between the mass and light orientations, but disagree on whether ellipticities are correlated - with Koopmans et al. (2006) reporting strong correlation and Ferreras et al. (2008) reporting weak correlation. Gavazzi et al. (2012) study a different sample of HST imaged lenses and use parametric Sérsic light profiles (Sersic, 1968) to compare to the mass profiles, and Shajib et al. (2018) perform a similar analysis using a lens sample containing quadruply-imaged point sources instead of extended background sources, with both again finding general agreement in the alignment of mass and light distributions but disagreeing over whether ellipticity is strongly (Gavazzi et al., 2012) or weakly/not (Shajib et al., 2018) correlated.

This chapter is structured as follows. In Section 4.2, we discuss the data and the sample of lenses that we will study. In Section 4.3 we detail the specifics of the mass modelling and introduce the isophote ellipse fitting formalism. In Section 4.4 we will look in detail

at the results from 4 lenses in our sample, and the conclusions that can be drawn from them. In Section 4.5 we will investigate the sample-level results and inferences that we can make, including on the suitability of the EPL and the correlation of isophote variance to the external shear magnitude. Finally in Section 4.6 we summarise the main conclusions of this chapter.

4.2 The sample: *SLACS* and *BELLS-GALLERY*

Both this Chapter (4) and Chapter 5 use two lens samples, used in many strong lensing studies (e.g. Vegetti et al., 2014; Etherington et al., 2023; Nightingale et al., 2024). These samples are: the SLACS survey (Bolton et al., 2008a,b, and their related papers), and the BELLS-GALLERY survey (Shu et al., 2016a). The lenses in these samples were found originally in the Sloan Digital Sky Survey (SDSS), through use of spectroscopic analysis which identifies higher-redshift emission lines after subtraction of the lower-redshift central galaxy profile (see e.g. Bolton et al., 2006), with the BELLS-GALLERY lens sources being higher-redshift Lyman-α emitters (Shu et al., 2016a).

Both lens samples had follow-up imaging performed by HST, for SLACS the Advanced Camera for Surveys (ACS) band F814W was used (Bolton et al., 2006), and for the BELLS-GALLERY lenses, the Wide Field Camera 3 (WFC3) band F606W was used (Shu et al., 2016b). The data pipelines are described in the cited papers, and produce images with pixel scales 0.05” for SLACS and 0.04” for BELLS-GALLERY. The PSF was produced by the `TINY TIM` software (Krist, 1993).

4.2.1 Post-processing and sample selection

From the full SLACS and BELLS-GALLERY samples, we use only a specific fraction of these that provide reasonably straightforward modelling and plausible lens reconstructions. We begin with the ‘Gold’ sample of Etherington et al. (2022). The full selection criteria are detailed in the paper with the main steps as follows: initially take the 43 lenses from

Sample	System	Redshift		θ_E		Light extent	
		Lens	Source	(arcsec)	(kpc)	(arcsec)	(kpc)
Slacs	J0008-0004	0.4400	1.1924	1.16	6.79	2.50	14.65
Slacs	J0029-0055	0.2270	0.9313	0.99	3.73	4.75	17.83
Slacs	J0157-0056	0.5132	0.9243	0.98	6.25	2.75	17.53
Slacs	J0216-0813	0.3317	0.5235	1.21	5.95	4.75	23.37
Slacs	J0252+0039	0.2803	0.9818	1.02	4.45	2.75	12.04
Slacs	J0330-0020	0.3507	1.0709	1.12	5.71	3.00	15.31
Slacs	J0728+3855	0.2058	0.6877	1.30	4.52	4.75	16.55
Slacs	J0737+3216	0.3223	0.5812	0.97	4.67	4.75	22.90
Slacs	J0822+2652	0.2414	0.5941	1.17	4.60	4.75	18.65
Slacs	J0903+4116	0.4204	1.0645	1.29	7.47	3.00	17.34
Slacs	J0912+0029	0.1642	0.3239	1.62	4.71	4.75	13.80
Slacs	J0936+0913	0.1897	0.5880	1.12	3.66	4.75	15.53
Slacs	J1020+1122	0.2822	0.5530	1.20	5.28	4.75	20.90
Slacs	J1023+4230	0.1912	0.6960	1.45	4.77	4.75	15.60
Slacs	J1029+0420	0.1045	0.6154	1.08	2.12	4.75	9.37
Slacs	J1032+5322	0.1334	0.3290	1.10	2.69	4.75	11.58
Slacs	J1142+1001	0.2218	0.5039	0.93	3.42	4.75	17.53
Slacs	J1143-0144	0.1060	0.4019	1.68	3.36	4.75	9.52
Slacs	J1205+4910	0.2150	0.4808	1.25	4.50	4.75	17.11
Slacs	J1213+6708	0.1229	0.6402	1.55	3.53	4.75	10.84
Slacs	J1218+0830	0.1350	0.7172	1.43	3.53	4.75	11.73
Slacs	J1250+0523	0.2318	0.7953	1.13	4.30	4.75	18.12
Slacs	J1420+6019	0.0629	0.5351	1.17	1.47	4.75	5.95
Slacs	J1430+4105	0.2850	0.5753	1.46	6.49	4.75	21.05
Slacs	J1525+3327	0.3583	0.7173	1.36	7.01	4.75	24.55
Slacs	J1627-0053	0.2076	0.5241	1.24	4.34	4.75	16.68
Slacs	J1630+4520	0.2479	0.7933	1.80	7.23	4.75	19.05
Slacs	J2238-0754	0.1371	0.7126	1.27	3.18	4.75	11.88
Gallery	J0029+2544	0.5869	2.4504	1.40	9.51	1.00	6.81
Gallery	J0113+0250	0.6230	2.6088	1.35	9.48	1.00	7.00
Gallery	J0201+3228	0.3957	2.8209	1.73	9.51	2.00	11.00
Gallery	J0742+3341	0.4936	2.3633	1.60	9.98	1.25	7.81
Gallery	J0755+3445	0.7224	2.6347	1.93	14.39	1.00	7.44
Gallery	J0856+2010	0.5074	2.2335	0.92	5.85	1.00	6.33
Gallery	J0918+5104	0.5811	2.4030	1.60	10.88	1.00	6.78
Gallery	J1110+2808	0.6073	2.3999	0.92	6.92	1.00	7.49
Gallery	J1110+3649	0.7330	2.5024	1.19	8.08	1.00	6.81
Gallery	J1116+0915	0.5501	2.4536	1.01	6.70	1.00	6.60
Gallery	J1141+2216	0.5858	2.7624	1.25	8.53	1.00	6.81
Gallery	J1201+4743	0.5628	2.1258	1.26	7.88	1.00	6.27
Gallery	J1226+5457	0.4980	2.7322	1.37	9.34	1.50	10.22
Gallery	J2228+1205	0.5305	2.8324	1.34	8.67	1.00	6.48
Gallery	J2342-0120	0.5270	2.2649	1.45	9.40	1.00	6.46

Table 4.1: Details of the lens systems used in Chapters 3 and 4. Redshifts are taken from Bolton et al. (2008a), and Shu et al. (2016a). The Einstein radii are the best fit values from our EPLγ mass models. The 'light extent' is the major axis of the largest fit ellipse.

SLACS, and 17 from BELLS-GALLERY with minimum one-orbit HST depth, following this, one BELLS-GALLERY lens is dropped due to having two equal brightness lens galaxies (SDSSJ0918+4518), and then 5 SLACS lenses are dropped due to poor light subtractions causing degraded lens models. This leaves a sample of 54 lenses, with 38 from SLACS and 16 from BELLS-GALLERY.

Following this, we drop a further set of lenses due to difficulties in modelling using multipoles (so as to keep the same sample for Chapters 4 and 5), as well as one lens with a confirmed substructure detection (SDSSJ0946+1006: Vegetti et al., 2010), leaving a sample of 43 lenses: 28 SLACS and 15 BELLS-GALLERY lenses. These lenses are listed in Table 4.1, along with their redshifts, Einstein radii (θ_E, from our EPLγ mass modelling) and light extents (from ellipse fitting). Both the Einstein radii and the light extents are given in arcseconds (image plane units) but also converted to a physical side in the lens plane in kiloparsecs (kpc, conversion based on Planck Collaboration et al. (2016) cosmology). See Section 4.3.2 for an explanation of the 'light extent' column.

4.3 Methodology

4.3.1 Mass modelling

The mass modelling for this project was carried out by my collaborator Dr. James Nightingale, as a continuation of the work in Nightingale et al. (2024) and Etherington et al. (2022). It follows the same processes as Section 3.3 and Table 3.2, up until the multipole and subhalo applications. Substructure obviously is not modelled in this work, and multipoles are not investigated this chapter. Example images from the mass modelling are shown in Figure 4.1. We use the mass model to produce the data for the ellipse fitting by subtracting the model source image from the data to produce a source-subtracted image of only the lens galaxy light.

4.3.2 Light modelling: Ellipse fitting formalism

To investigate the structure of the light of lens galaxies, we use the method of isophote fitting, which has long been used to build piecewise models of galaxy light by fitting elliptical paths of constant intensity (e.g. Jedrzejewski, 1987; Hao et al., 2006; Goullaud et al., 2018). The code that we use is based on Amvrosiadis et al. (2025b), and is integrated into the `PyAutoGalaxy`* software. The general philosophy is that for a given major axis, the code will attempt to draw an ellipse with the minimum chi-squared difference between the intensity at set points on the ellipse, and the average intensity along the ellipse. An example of the ellipse fits is shown in Section 4.3.5.2 and Figure 4.2.

The polar equation of an ellipse centred on (x_0, y_0) can be written as

$$r_p(\phi) = \frac{ab}{\sqrt{a^2 \sin^2(\phi - \phi_e) + b^2 \cos^2(\phi - \phi_e)}}, \tag{4.1}$$

where r_p is the distance from the centre to any point p, a and b are the semi-major and semi-minor axes respectively, and ϕ is the angle to the point, defined counter-clockwise from the angle of the major axis of the ellipse, ϕ_e (ellipse position angle, defined counter-clockwise from the positive x-axis). The Cartesian coordinates (x_p, y_p) of any point $p(r, \phi)$ are therefore:

$$\begin{aligned} x_p &= x_0 + r_p(\phi)\cos(\phi) \\ y_p &= y_0 + r_p(\phi)\sin(\phi). \end{aligned} \tag{4.2}$$

We use the usual style of `PyAutoGalaxy` to fit for the elliptical components ϵ_y, ϵ_x in order to work with the axis ratio $q = b/a$ as well as the position angle ϕ_e (the formalism for the conversion being identical to the mass fitting, with $\epsilon_y = \epsilon_1$ and $\epsilon_x = \epsilon_2$ - see Equation 2.3).

To optimise the parameters of the ellipse, we use the non-linear nested sampling tool `dynesty`† (Speagle, 2020) and we maximise the (natural) logarithm of the Likelihood

$$\log \mathscr{L} = -\frac{1}{2} \sum_p \left(\frac{I(p|\boldsymbol{\theta}_e) - \langle I(p|\boldsymbol{\theta}_e) \rangle}{\sigma_p} \right)^2, \tag{4.3}$$

*`PyAutoGalaxy`: Nightingale et al. (2023) `https://github.com/Jammy2211/PyAutoGalaxy`
†`dynesty`: `https://doi.org/10.5281/zenodo.3348367`

where this is proportional to the sum of the chi-squared (χ^2) values at various points p along the ellipse. Equation 4.3 shows the full formalism of the chi-squared sum, where $I(p|\boldsymbol{\theta}_e)$ is the (interpolated) intensity of the data at point p, given ellipse parameters $\boldsymbol{\theta}_e$, $\langle I(p|\boldsymbol{\theta}_e)\rangle$ is the mean value of the intensity from all calculated points on the ellipse, and σ_p is the (interpolated) noise value at point p.

Note that for all χ^2, parameter estimations, likelihoods, etc., we will only use ellipses between $0.5-3.0$ arcseconds (inclusive) so as to not extend too far from the Einstein radii (although plots of the ellipse fits over the data may show ellipses with larger extents), and to reduce computing power required for the Gaussian process interpolations. Not all lenses however have light at a meaningful SNR out to 3.0 arcseconds - we judge the maximal number of ellipses to use through a pre-fitting stage where we fit 5 ellipses across the image extent, and using an interpolation over major axis of their average intensity and SNR, we estimate the highest major axis value an ellipse could have with average SNR>2. The upper limit of the ellipse major axis is then this value (given as the 'light extent' in Table 4.1). We will attempt to fit ellipses from 0.25 to 4.75 arcseconds (inclusive), or to this upper SNR value, evenly spaced at 0.25 arcsecond intervals. For models that use constant parameters for all ellipses, we use ellipses evenly spaced between 0.5 to 2.0 (or the upper SNR limit) arcseconds (inclusive) to fit for the parameters, and then apply these parameters across the full ellipse range (major axis 0.25 to 4.75 or upper SNR limit). We fit the model in this way to better match the mass fitting, since the mass similarly only fits one parameter value independent of radius/major axis and the constraining information primarily comes from the mass enclosed within the Einstein Radius, which for all lenses in our sample falls between 0.5 to 2.0 arcseconds (see Table 4.1).

In addition we do not include the PSF in our light profile modelling since the inner ellipse is made at 0.25 arcseconds, and the full-width at half-maximum (FWHM) of the pre-pixelized PSF is given* as 0.067 arcseconds at 600nm (centre of F606W filter). This means that even with pixelisation and the possibility of PSF modelling errors, the PSF

*FWHM from: `https://hst-docs.stsci.edu/wfc3ihb/chapter-6-uvis-imaging-with-wfc3/6-6-uvis-optical-performance`

should not affect the light distribution at the scales of even our smallest ellipse. This is another reason why we model ellipses with major axes at fixed intervals of arcseconds rather than physical units such as kiloparsecs as physical scales vary with redshift and may enter the regime where the PSF becomes important.

4.3.3 Dealing with light contamination

For the mass fitting, we process the lensing images, applying masks over any regions where there is light contamination, in line with Etherington et al. (2022) and Section 2.2. Once the mass fits are complete, we take the 'source subtracted image' (which is the data minus the intensity of the source in the image plane at each pixel) and perform our light analysis on this image. We cannot however continue to use the masks in their current form since despite the fact that these pixels will not contribute to the χ^2, the ellipses will still attempt (and fail) to fit the remaining pixel *signal* with isophotes in this region, impacting the accuracy and computation time (see Section 4.3.5.1 and the discussion of Figure 4.1). We therefore convert the 'noise-mask' of Section 2.2 to a pixel removal mask, where we fully remove pixels from the analysis based on whether they previously had a noise increase for the mass fitting stage. This can be seen more clearly in Figure 4.2 where the mask now has holes in it compared to the messy but still included regions in Figure 4.1.

When fitting to our data however, the code itself still does not recognise if an ellipse passes over a masked out region. We therefore adjust the fitting through an iterative process where the points on the ellipse are tested to see if any hit the mask. If any do, the points are relocated until the original number of required points hitting active pixels is achieved. For example: we have an ellipse that needs 50 points to be well sampled, however, say two of these points hit a masked region, we therefore try drawing 51 evenly spaced points from the ellipse, and then 52 and so on, until we have a set of 50 points (which are still evenly spaced) outside the mask. In this way, we continue to sample the rest of the ellipse smoothly with an appropriate number of points, rather than blindly relocating the masked points and thereby sampling some regions of the ellipse better than others.

Figure 4.2 will show an example where our pixel-removal mask has been applied, and the ellipses have been plot over the data. The drawing function of the plot draws a straight line across the mask, so that if two ellipses go through the same masked region, one can keep track of which one enters/exits where, but the fitting function has automatically removed and relocated any points falling within those masked regions during the modelling so that they do not contribute to the final result.

4.3.4 Model variants and comparison methods

We fit two types of model ellipses to our lens light: model $\mathcal{F}_1$ holds the ellipse axis ratio q_e and position angle ϕ_e constant across all ellipses, and model $\mathcal{F}_2$ allows for the ellipse axis ratio and position angle to be varied across ellipses. The first investigation possible from these models is agreement between light and mass - primarily through a direct comparison of the constant-ellipse model $\mathcal{F}_1$ to the mass model ($\mathcal{F}_{EPL}$), since both of these models fit one q and ϕ value for the entire distribution. The second investigation regards whether fitting one value for these parameters is sufficient, or if a better fit to the light can in be achieved through variance in the parameters at different radii, which would lend support for piecewise or non-parametric mass models. This will be investigated through analysis of the angular and elliptical variance within the variable-ellipse model $\mathcal{F}_2$, where we will note the maximal difference between the different size ellipses.

We use the reduced chi-squared, χ^2_ν as the figure of merit for the ellipse fits. The reduced chi-squared is the chi-squared χ^2, divided by the number of degrees of freedom, which is equivalent to the number of data points minus the number of model parameters $(n - m)$. The chi-squared is calculated using all ellipses that are available between 0.5" to 3.0" (inclusive) and is treated as:

$$\chi^2_{\nu,\text{var}} = \frac{\sum_e \chi^2_e}{\sum_e (n_e - m)} \tag{4.4}$$

for the variable model, where this is the sum of the chi-squared values from each ellipse divided by the sum of all the degrees of freedom from the ellipses; and given as:

$$\chi^2_{\nu,\text{const}} = \frac{\sum_e \chi^2_e}{(\sum_e n_e) - m} \tag{4.5}$$

where this is the sum of all the ellipse chi-squareds, divided by the total degrees of freedom, equal to the total number of data points across the ellipses, minus the total number of parameters, 2.

Importantly for our results, we will see that most of our ellipse models, both constant or variable, have $\chi^2_\nu < 1$, which would normally indicate over-fitting of the model. For ellipse fitting however, we reduce data from 2D-image scales to 1D-ellipse path scales, allowing the model to flexibly adjust the data points it compares against, introducing covariances in the data and noise that render the usual aim of $\chi^2_\nu = 1$ to be inaccurate for this type of modelling, and as such, we are only interested in a reduction of χ^2_ν, regardless of the starting value.

A key question is how to compare the actual model results when one model ($\mathcal{F}_1$) has a single resultant value for a parameter, and one model ($\mathcal{F}_2$) has a result value for that parameter which varies with major axis. We opt against choosing a fixed major axis value to take the model values for $\mathcal{F}_2$, in favour of taking the model values at the Einstein radius (θ_E) of the lens. Although using the Einstein radius requires an extra step, and requires consideration of both the $\mathcal{F}_2$ ellipse model errors *and* $\mathcal{F}_{EPL}$ mass model errors (see Section 4.3.4.1), we believe that this provides a better opportunity to compare all three models in context, operating under and testing the assumption that whilst lensing is sensitive to the total mass enclosed within the Einstein radius, the strongest constraints on the mass model come from the mass distribution *around* the Einstein radius.

4.3.4.1 Interpolation of the variable ellipse model

To interpolate a value of a parameter from model $\mathcal{F}_2$ at the Einstein radius, taking into account both the errors on the ellipse and mass models, we use a Monte Carlo sampled Gaussian process regression* algorithm from `scikit-learn`† to resample a set of parameter space covering the possible model values across the Einstein radius error range. The steps are as follows:

*Algorithm based on Rasmussen et al. (2006).

†`sklearn`: Pedregosa et al. (2011), `https://scikit-learn.org/stable/`

1. **Monte Carlo sample Einstein radius.** We draw 10000 points each from two truncated normal distributions to sample the lower and upper values for the Einstein radius (θ_E) - i.e 10000 points from a normal with $\mu = \theta_E$, $\sigma = \sigma_{\text{E, lower}}$, truncated between the minimum allowed major-axis value (0.5 arcsec) and θ_E, and then the same for the upper. This upper/lower draw is done due to the upper and lower sigma on the parameter not being equal.

2. **Interpolate using Gaussian process regression.** We setup Gaussian processors to interpolate the parameter values across the entire range of major axis values*. The interpolation is done separately for the best-fit parameter values and for the upper and lower 1-sigma bounds, to create effectively three fit curves, however the fit for the length scale of the error curves is initialised from the fit main curve length scale. An example of this stage is shown in Section 4.3.5.3 and Figure 4.3.

3. **Predict parameter** at each new major axis point (from the Einstein radius draw). This is done using the Gaussian processes we set up previously, and a value is drawn for the best-fit, upper bound and lower bound at point x.

4. **Build new sample.** At each major axis point x, we take the predicted best-fit parameter value, along with an equal plus/minus error, which is either the magnitude of the predicted upper or predicted lower error (based on a single random uniform $\mathcal{U}(0, 1)$ draw being greater or less than 0.5). We then draw a single value from a normal distribution with this mean and sigma.

5. **Extract new sample statistics.** Once each of the 10,000 points has been sampled as in the above point, we can take the median and the separate upper and lower sigma percentiles (68, 95 & 99.7 for 1, 2 & 3 σ respectively).

*Uses an optimised multiplication of a Constant Kernel (bounds 10^{-3} : 10^{3}) and a Matérn Kernel (length bounds 10^{-1} : 10^{2}). More information on Gaussian processes and kernels is at `https://scikit-learn.org/stable/modules/gaussian_process.html`

4.3.5 Modelling example: SLACS:J2238-0754

We now show some examples of the modelling process, so that the reader can better understand both the methodology and the results. We use the SLACS lens J2238-0754 and show the mass modelling, ellipse modelling, Gaussian process interpolation, and example parameter extraction.

4.3.5.1 Mass modelling

Figure 4.1 shows select images from the mass modelling for this lens, with all images (except for the residuals) on a $\log_{10}$ colour scale. The top left panel shows the data, with a 4 arcsecond radius circular mask applied and our noise-increase 'mask' technique applied to the top of the image. The top-centre panel then shows the image produced from our lens and source model, with the critical curve overlaid in black, and the top right panel shows the normalised residuals (residuals/noise) from this fit - again at the top of the image the effect of the 'noise-mask' can be seen reducing the normalised residuals to 0, meaning these pixels contribute nothing to the likelihood.

The lower panels of Figure 4.1 show the lens light subtracted image and the source light subtracted image (left and centre respectively) - which is just the data minus the model image of either the lens or the source. The lower right panel is the convergence map from the fit, with iso-κ contours.

The lower central panel (source subtracted image) is what we take as the data input to perform the ellipse fitting, and has isophote contours overlaid. The isophotes of the source subtracted image reveal why it is necessary to use a different masking technique for ellipse fitting: at the top of the image, where we have used a 'noise-mask', the image points appear black instead of white/green as in the lens subtracted image - this is because isophote contours have been applied to this region and are picking up the remaining light and noise here. Since ellipse fitting is isophote fitting, leaving this region in the data would provide a nuisance set of isophotes that the ellipses would try but fail to include in the model, hence we must apply the full pixel-removal mask from Section 4.3.3.

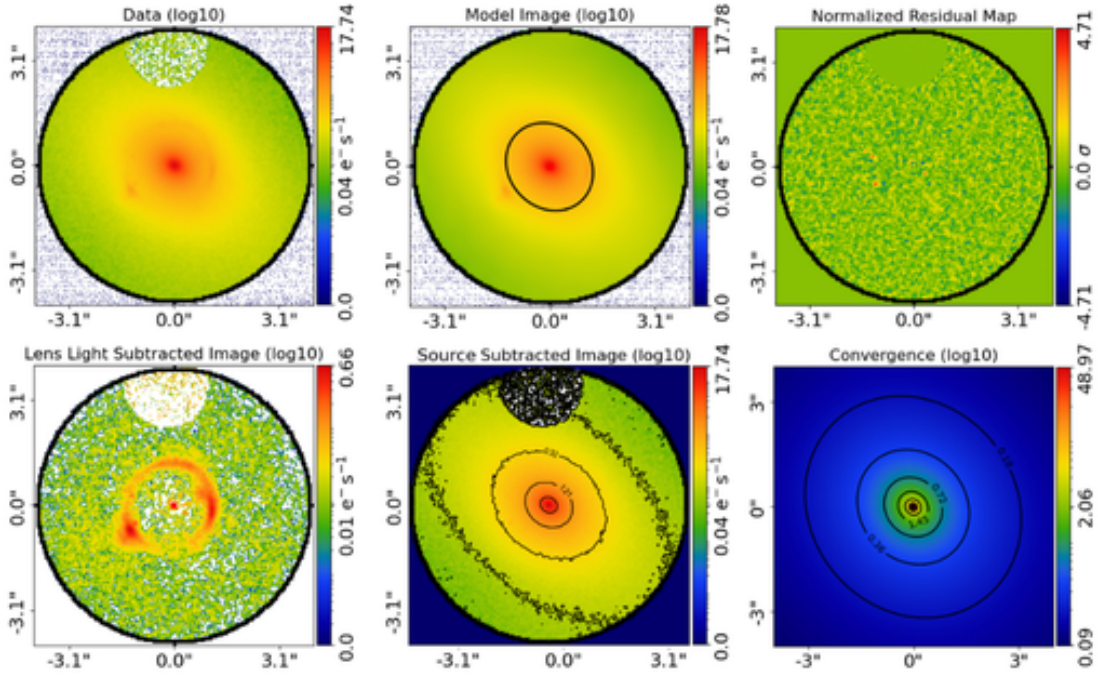

Figure 4.1: Model output images from the EPLγ model $\mathcal{F}_{EPL}$ of SLACS lens J2238-0754. Upper panels show the data (left), model image, with critical curve overlaid (centre) and normalised residuals (right). Lower panels show the lens-subtracted image (left), source-subtracted image with isophote contours overlaid (centre) and convergence map with iso-κ contours overlaid (right). All images except the normalised residuals are in $\log_{10}$ colour scale. The source-subtracted image is used as the input data for the ellipse fitting.

4.3.5.2 Ellipse fits

Figure 4.2 shows images of the ellipse fits from both models $\mathcal{F}_1$ and $\mathcal{F}_2$. The upper panels show only the ellipses, whilst the lower panels show the ellipses, as well as the isophote contours of the data that matches the fit intensity of the ellipses. We can see that for both models the central ellipses fit the data reasonably well but as the major axis of the ellipse increases and the SNR of the data drops, the real isophote contours get much more noisy (as expected) until the ellipses and the data contours cannot even be distinguished from one another when all ellipses are plotted together. For this reason, we will generally only show figures containing only the fit ellipse contours and not the corresponding noisy data isophote contours.

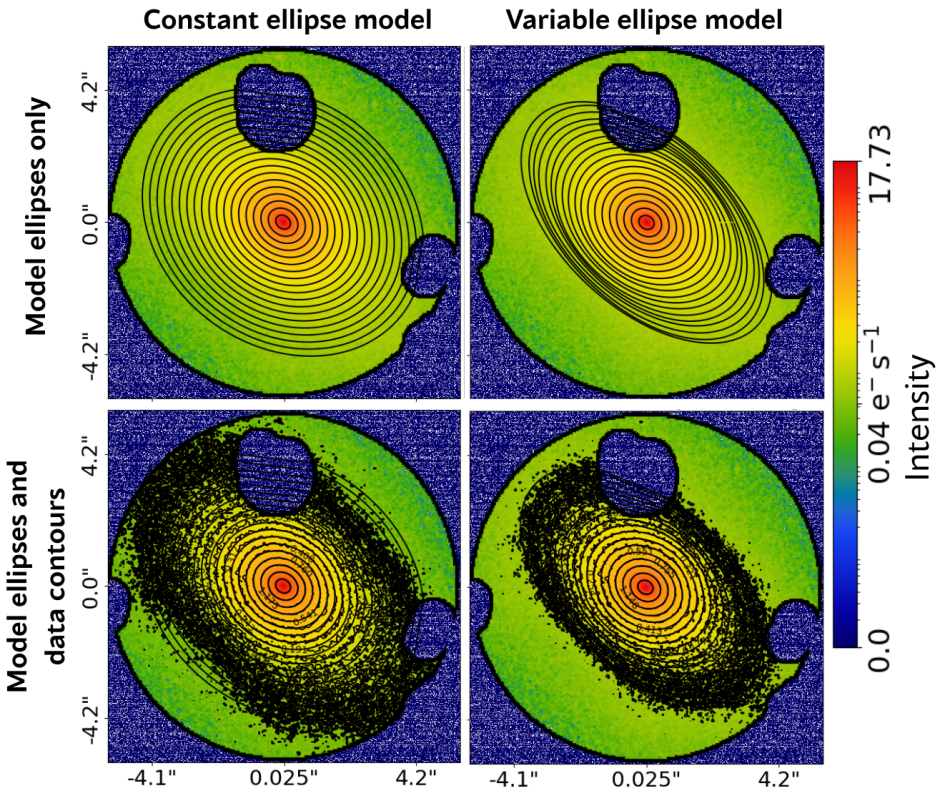

Figure 4.2: Ellipse fits to SLACS lens J2238-0754 from our two smooth-ellipse models. The left column shows the $\mathcal{F}_1$ model with all ellipses having the same constant axis ratio (q) and position angle (ϕ_e), the right hand column shows model $\mathcal{F}_2$ where the ellipses can vary with their own independent q and ϕ_e. The upper panels show the fit ellipses, with the lower panels showing these ellipses and also the contours of the data that has the corresponding fit intensity. The data intensity has a $\log_{10}$ colour scale.

4.3.5.3 Gaussian processing

Figure 4.3 shows an application of the Gaussian process regression from Section 4.3.4.1. For the investigations of the variable ellipses of model $\mathcal{F}_2$, we use this Gaussian process and then Monte Carlo estimate the value at the Einstein radius. For this figure, we only use the first part, interpolating the values and errors of the axis ratio and position angle from each ellipse (orange points) to make a smooth distribution that we could sample from at any point (black lines). The figure shows that the process is highly accurate in predicting the correct values at the known data points, and allows for reasonably good error interpolation when the errors are similar in size between data points. There are two

main problems with this approach (with further plots shown in Appendix A.4.1): firstly if errorbars are uneven the process struggles to smoothly and physically interpolate the errors; secondly the extrapolation is not necessarily reliable beyond one or two further points due to the nature of the interpolation used. We therefore do not use any values that are *extrapolated* using this method, only those that are interpolated, and we take special care when drawing conclusions based on errors generated from this process.

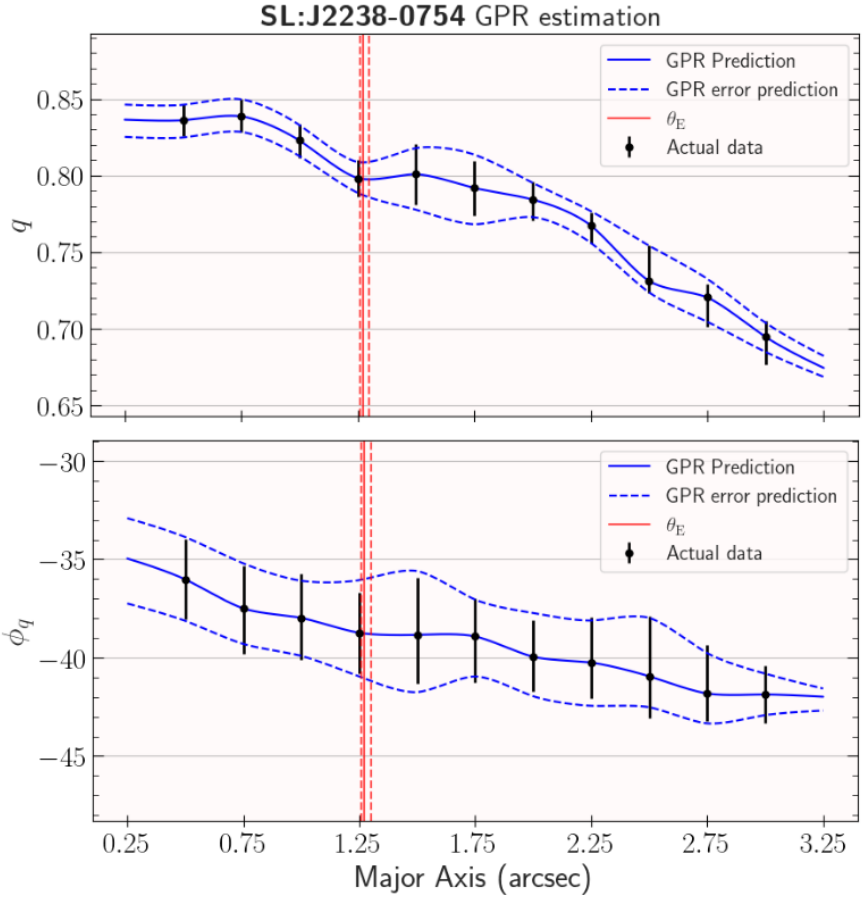

Figure 4.3: An example of the Gaussian process interpolation (Section 4.3.4.1) on the variable ellipse model $\mathcal{F}_2$ fit to SLACS lens J2238-0754. The best fit data points and 3-sigma errors are plotted in cyan for each ellipse of the fit, and then the best fit interpolation line with the 3-sigma interpolation dashed lines are plotted in black.

4.3.5.4 Parameter extraction

Finally, Figure 4.4 shows the 'lens summary' plot for J2238-0754. These lens summaries are available for all lenses on github* and contain the fit q and ϕ values with 3-sigma errors from all three models ($\mathcal{F}_{EPL}, \mathcal{F}_1, \mathcal{F}_2$), plus the reduced chi-squared values per ellipse for the light models, and the Einstein radius (with 3-sigma errors - vertical solid and dashed lines). Whilst we may fit ellipses at 0.25" and out to 4.75", we show only the ellipses 0.5-3.0" as these are the ellipses used in all analysis.

The upper panel shows the reduced chi-squared value, χ^2_ν, per ellipse. For the variable ellipse model $\mathcal{F}_2$, χ^2_ν is plotted as normal. For the constant ellipse model $\mathcal{F}_1$, the χ^2_ν per ellipse is not available since all ellipses are fit simultaneously with shared parameters. We therefore use an effective reduced chi-squared, which calculates the degrees of freedom ($n_{\text{data points}} - n_{\text{parameters}}$) as if each ellipse had been fit independently. On these plots therefore, the per-ellipse χ^2_ν for $\mathcal{F}_1$ is technically over-estimated, however since generally $n_{\text{data points}} >> n_{\text{parameters}}$, this skew is negligible. We note that the total $\chi_n u^2$, which is used for model discrimination is calculated accurately as per Section 4.3.4.

The lower panels of Figure 4.4 show the extracted parameter values for the axis ratio (q, centre) and position angle (ϕ, lower). For models $\mathcal{F}_{EPL}, \mathcal{F}_1$, one value is fit for the whole image, so these are plotted as horizontal lines at the best-fit value, and shaded regions for the 3-sigma errors. For model $\mathcal{F}_2$, each ellipse has a value for each parameter, so these are plotted as points with error-bars.

*`https://github.com/samlange04/slacs_bells_structure`

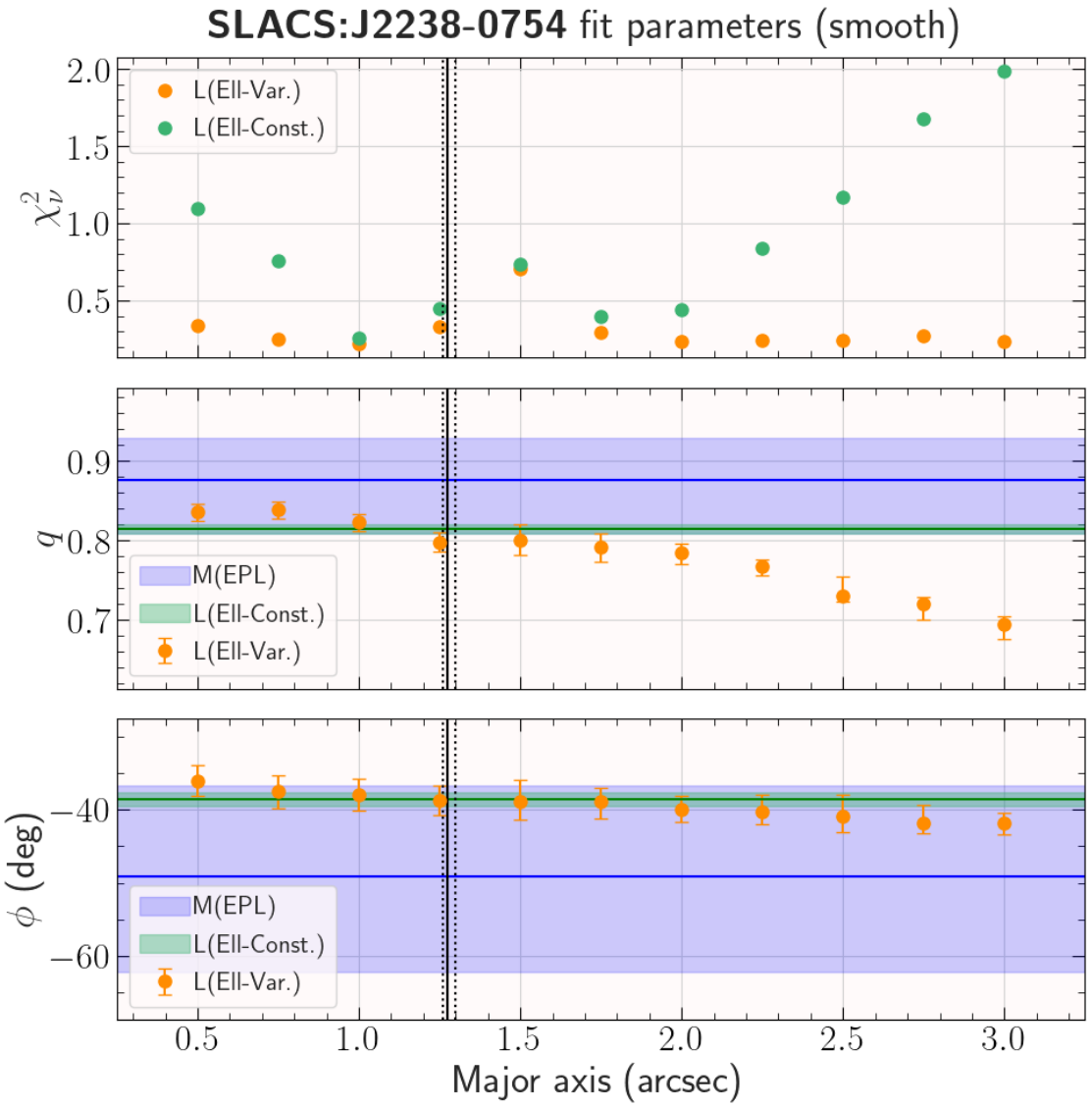

Figure 4.4: 'Paramaters' plot for the 'smooth' models ($\mathcal{F}_1, \mathcal{F}_2, \mathcal{F}_{EPL}$) of SLACS lens J2238-0754. Upper panel shows the reduced chi-squared value for each individual ellipse of the light models. The middle panel shows the fit axis ratios q, and the lower panel the fit position angles ϕ along with their 3-sigma errors. For the mass and constant ellipse models, the best fit value is the solid line, and the shaded region contains the error bounds. For the variable ellipse model $\mathcal{F}_2$, the best fit value and errors is plotted as individual points for each ellipse. The vertical line is the Einstein radius θ_E from the mass fit, with the 3-sigma errors as dotted vertical lines.

4.4 Results and Discussion: Lens case studies

We run through three examples showing the extremes of results, before moving on to sample-level inference in Section 4.5. For each example, we will present the parameters recovered from the fits, and show the ellipse fits for those lenses. There is a wide range of information to be gleaned from this study, and full results for all lenses can be found on github*.

4.4.1 J1630+4520: No radial light variance, light and mass align

SLACS lens J1630+4520 is a prime example in favour of both the assumptions that light traces mass, and that the mass/light profiles can be described by non-radially varying models. From the parameter plots of Figure 4.5, we see firstly that the models are very tightly constrained, with small 3-sigma error bounds on the fit parameters. In addition, in comparing the constant ellipse model to the EPLγ mass model, which is the most like-for-like comparison that can be made, the axis ratio agrees well within 3-sigma, and the position angle agrees perfectly, indicating that the light distribution in this lens very closely traces the mass distribution.

For this lens, if we move from the constant ellipse model to the variable ellipse model, we also see that whilst there is some minor variation in axis ratio across the lens, the variable ellipse model remains consistent at 3-sigma to both the constant ellipse model and the EPLγ mass model, meaning that ellipse variability is not required in this lens. This is confirmed by $\Delta\chi^2_\nu = -0.028$ going from the constant ellipse to the variable ellipse model, which is not significant (note that all lenses have $\Delta\chi^2_\nu < 0$) and is in fact the smallest chi-squared reduction of all the SLACS lenses.

*`https://github.com/samlange04/slacs_bells_structure`

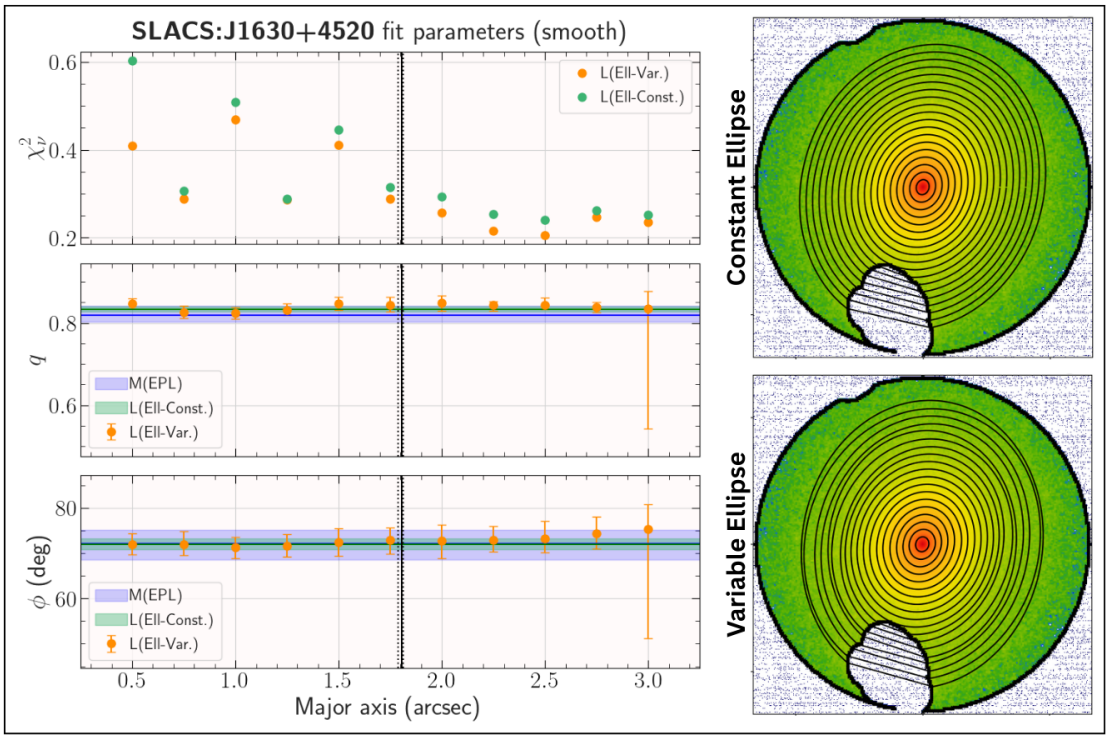

Figure 4.5: Parameters and ellipse fits for the smooth models $\mathcal{F}_{EPL}, \mathcal{F}_1, \mathcal{F}_2$ of SLACS lens J1630+4520. For parameter plot explanation, see Section 4.3.5.4. This lens shows no radial light variation and almost perfect agreement of light and mass.

4.4.2 J1143-0144 and J2238-0754: Radial light variance, but still mass agreement

SLACS lens J1143-0144 is a perfect 'middle-ground' example of these investigations. There is a very clear variation in the light of the galaxy at different major axes, however the light distribution still generally agrees with the mass distribution. From Figure 4.6 we see firstly in the parameter plots that whilst the light models are still well constrained, the errors on the mass model are larger than for J1630+4520, especially for the axis ratio, meaning that for both light models the axis ratios are consistent at 3-sigma and the position angles are similarly consistent for both the constant ellipse model and the variable ellipse out to 2.5 arcseconds. Specifically making the most like-for-like mass to light comparison (EPLγ to constant ellipses - see Section 4.3.4), the light parameters are well contained within the errorbars of the mass, however we note that the best-fit mass parameters fall outside the 3-sigma range of the much more tightly constrained light parameters.

Comparing the two light models directly, there is again a very clear variation in axis ratio across major axis with this becoming slightly more circular past the Einstein radius. Primarily however, there is a sharp change in position angle past the Einstein radius - a clear isophote twist that is required for a good fit, causing the χ^2_ν values for the variable ellipse model to be much smaller than the constant ellipse model past the Einstein radius. The cause of the isophote twist is however up for debate - there could be a genuine galaxy structure that causes this, such as a bulge/disk structure, a double-disk or a spiral structure, but we must also be aware of the possibility that there is a slight systematic arising from the mask. A mask systematic could arise from the increase in masked regions at higher major axis values, meaning that the ellipses are less constrained. For this lens however the first ellipse crosses a mask at 2.5" and the isophote twist begins before this, so this makes a systematic cause of the twist less likely.

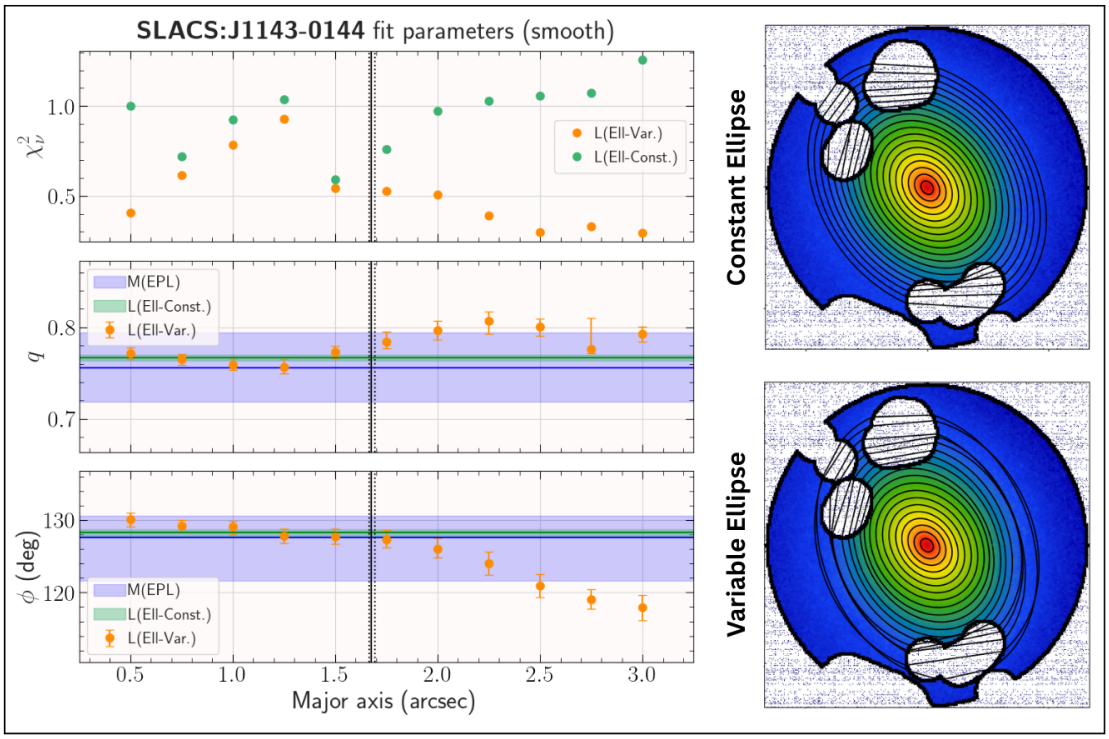

Figure 4.6: Parameters and ellipse fits for the smooth models $\mathcal{F}_{EPL}, \mathcal{F}_1, \mathcal{F}_2$ of SLACS lens J1143-0144. For parameter plot explanation, see Section 4.3.5.4. This lens shows radial light variation in position angle and axis ratio, but still good agreement between light and mass.

Aside from isophote twists, there is another way for the variable ellipse model to differ from the constant ellipse model - that is bulge-disk ellipticity variance. This is seen quite clearly in SLACS lens J2238-0754, which we used for our modelling examples in Section 4.3.5. Looking at Figure 4.2, we see again that the EPLγ mass model is consistent at 3-sigma with the constant ellipse model, in a similar manner to J1143-0744, where the large errors on the mass completely encompass the light results. For this lens however, when comparing the light models, the position angle is generally consistent with some slight radial variation, but there is a clear sharp decrease in axis ratio with major axis, where the model requires the light distribution to become more elliptical, again causing a large decrease in χ^2_ν for these ellipses. This circular centre-elliptical outskirts model would be expected for a galaxy with a visible bulge and disk for example.

Both of these galaxies serve as a warning that, despite the fact that the constant ellipse light model is suitable out to the Einstein radius, a more radially flexible model would be a better fit to the data, and since the constant ellipse model appears to trace the mass well, the assumption would be that a radially-variable mass model would also therefore produce a more accurate lensing model.

4.4.3 J1032+5322: Light variance, and mass-light disagreement

Our final case-study is SLACS lens J1032+5322, one of the most highly elliptical lenses in the sample, and a clear violator of both assumptions that light should trace mass and that a constant-ellipse model is suitable. We see in Figure 4.7 that again, the light models are very tightly constrained - likely almost too tightly with possible underestimated errors. Comparing the constant ellipse model to the EPLγ mass model, the light is fit to be more elliptical than the mass, and at a different position angle - with no agreement even at 3-sigma.

Exploring the difference in light models for this lens becomes even more interesting. The first result of note is that the constant ellipse model completely fails to fit the central region of the light, with effective-χ^2_ν over 300 at 0.5" and over 60 at 0.75". The total

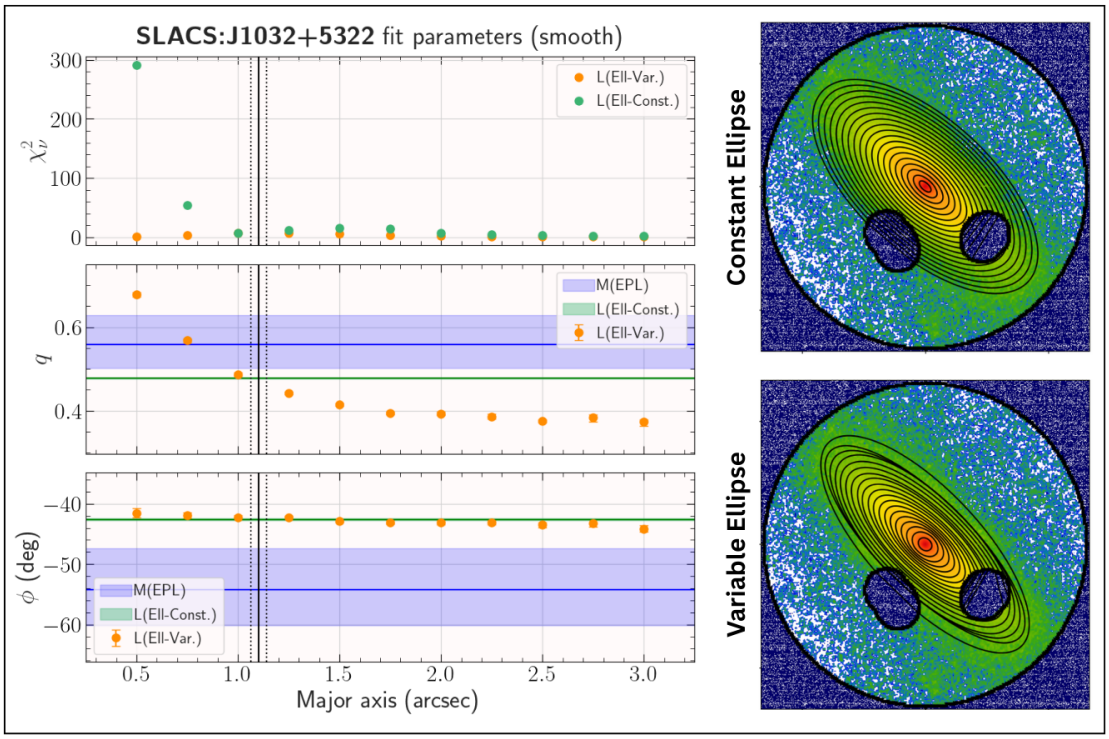

Figure 4.7: Parameters and ellipse fits for the smooth models $\mathcal{F}_{EPL}, \mathcal{F}_1, \mathcal{F}_2$ of SLACS lens J1032+5322. For parameter plot explanation, see Section 4.3.5.4. This is a highly elliptical lens and shows a strong radial variation of axis ratio, and disagreement between light and mass models.

χ^2_ν change when going from the constant ellipse model to the variable ellipse model is -13.36, the highest of any lens by some considerable margin (see appendix Figure A.9). The reason for this is clear when looking at the axis ratio results: similarly to J2238-0754, this lens requires a more circular centre and more elliptical outskirts, however the change is much more marked than J2238, with this lens exhibiting a clear bulge-disk structure. Disky lenses have caused problems for mass-light investigations previously, with one of the three outliers to the general mass-light agreement in lens galaxies in Gavazzi et al. (2012) being attributed to a disk-like structure in the stellar distribution. Interestingly, the light models roughly agree around the Einstein radius, similarly to J2238, which shows that our technique of using only the ellipses from 0.75" to 2.0" may be effective at estimating the light in this region using a constant parameter set.

4.5 Results and Discussion: Sample-level inference

Having looked at the case-study lenses to describe the range of our results, we now turn to sample-level views in order to address the questions of whether light traces mass and whether light varies radially. Due to the limit that we place on an ellipse SNR (which is in fact generously low), we do not manage to fit ellipses to all lenses past the Einstein radii. As discussed in Sections 4.3.5.3 & A.4.1, the Gaussian process interpolation methods cannot reliably extrapolate the light to the Einstein radius, as such, we cannot discuss the variable ellipse models in the context of the Einstein radius. In comparing the 'light extent' to the Einstein radii in Table 4.1, we see that for most BELLS-GALLERY lenses, due to the high lens redshift, we have this problem, we therefore take special note of these lenses and remove them from discussions regarding the variable ellipse model $\mathcal{F}_2$. No SLACS lenses are affected by this, but we discount all BELLS-GALLERY lenses except: J0201+3228, J0856+2010, J1110+2808 and J1226+5457. The discounted lenses are still shown on χ^2_ν plots, but either grayed-out or completely removed from any other plots that include the $\mathcal{F}_2$ model results.

4.5.1 Comparisons of constant to variable ellipse fits

4.5.1.1 Chi-Squared differences between light models

When investigating the radial dependence of light, we compare the constant ellipse models to the variable ellipse models, comparing the χ^2_ν difference between these models. Three lenses are outliers and have extreme $\Delta\chi^2_\nu$ values compared to the other lenses, and therefore are not shown on the plots in the main body of the text, but are shown in copies of the plots in Appendix A.4 which have the full χ^2_ν range included. These lenses are: J1032+5322 ($\Delta\chi^2_\nu = -13.36$), J1420+6019 ($\Delta\chi^2_\nu = -6.25$) and J1029+0420 ($\Delta\chi^2_\nu = -3.69$). A summary parameter plot for J1032 has already been shown as a case-study in Figure 4.7, the summaries of the other two lenses can be found in Appendix A.4.2.

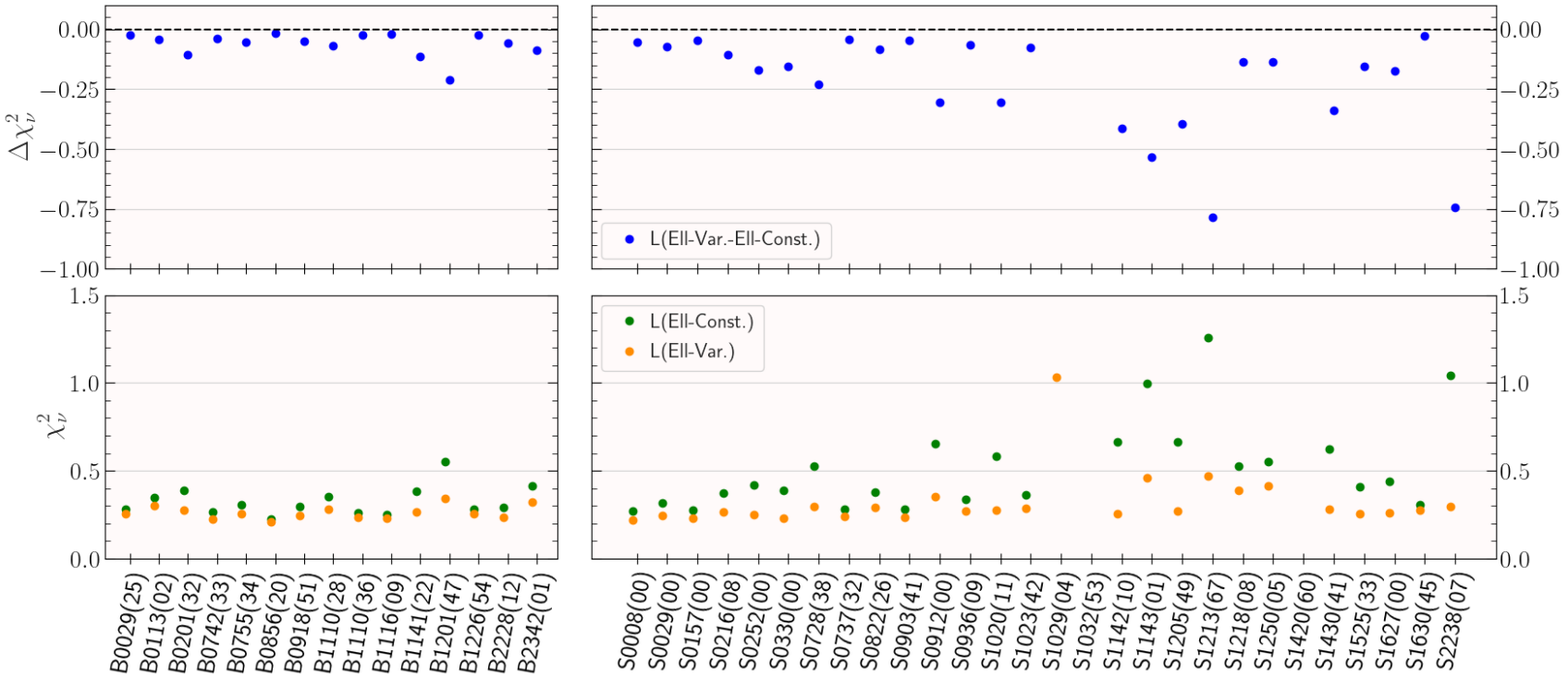

Figure 4.8: Reduced chi-squared (χ^2_ν) values for the elliptical light models. Upper panels (blue) show the difference ($\Delta\chi^2_\nu$) between the Variable model and the Constant model. Lower panels show the actual χ^2_ν for the Variable (orange) and Constant (green) models. Negative $\Delta\chi^2_\nu$ means that the variable model has a smaller chi-squared and therefore is a better fit. Points for J1029+0420, J1032+5322 and J1420+6019 are cut off from this figure for ease of viewing as their values are an order of magnitude different to all other lenses, they can be seen in the full-range figure: Appendix Figure A.9.

Figure 4.8 shows the $\Delta\chi^2_\nu$ values (upper panels) and actual χ^2_ν per model (lower panels) for all lenses except our three outliers*, with the full-range plot in Appendix Figure A.9. We see that for all lenses, applying the variable ellipse model causes a decrease in χ^2_ν. This result may appear alarming at first, however, most of the changes are small and so are likely due to small parameter variations within the errors, the stochastic nature of the modelling, or low-levels of noise fitting.

4.5.1.2 Radial variations in ellipticity and angle

Figure 4.9 shows a three-panel plot investigating the angular and elliptical variance of light in the variable ellipse $\mathcal{F}_2$ models, excepting the BELLS-GALLERY lenses removed due to low-SNR. Here, we consider 'elliptical variance' to be the largest difference in axis ratio between any two ellipses between 0.5" to 3.0" (inclusive). Similarly 'angular variance' is the largest difference in position angle between any two of the aforementioned ellipses, provided the ellipses are non-circular ($q < 0.85$). We make comparisons between the angular and elliptical variances, and between each variance and the χ^2_ν change from the constant ellipse model to the variable ellipse model. The chi-squared plots remove the three outlier lenses, which have the following variances: J1032 - $\Delta q = 0.42, \Delta\phi = 2.6°$; J1420 - $\Delta q = 0.18, \Delta\phi = 1.7°$; J1029 - $\Delta q = 0.26, \Delta\phi = 1.8°$. Appendix A.4.2 contains a plot with the full chi-squared range (Figure A.6), as well as a plot with a breakdown of the elliptical and angular variances for each lens (Figure A.10).

This Figure (4.9), along with the results from the three lenses with largest $\Delta\chi^2_\nu$, shows that the key improvement to be made when going from a constant ellipse model to a variable ellipse model is in the ellipticity of the light distribution, not necessarily in the angle of the ellipse (isophote twisting). To test this, we apply a Pearson-r correlation test† on this data (between each variance and the $\Delta\chi^2_\nu$) to test for linear correlation against the null hypothesis of uncorrelated, normally-distributed datasets, where a 'p-value' below 0.05 indicates an acceptance of the correlation hypothesis. Including the whole sample,

*The $\Delta\chi^2_\nu$ for the variable ellipse model of J1029 is low enough to still be included on the lower panel.

†See `https://docs.scipy.org/doc/scipy/reference/generated/scipy.stats.pearsonr.html` and links therein.

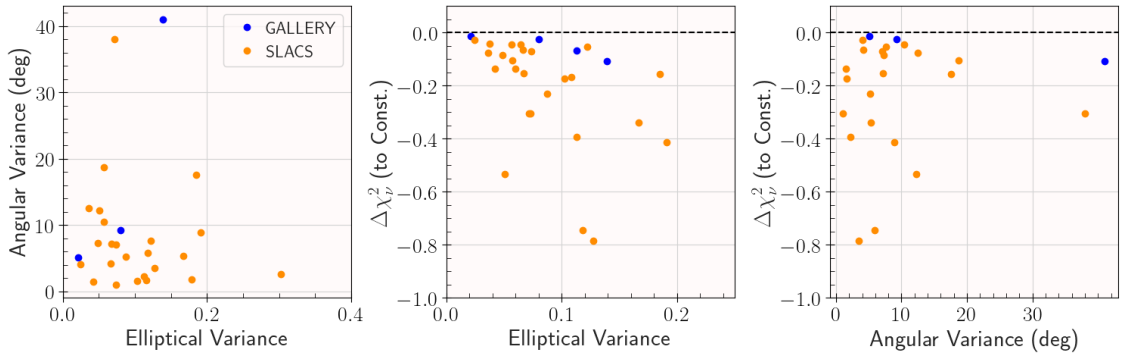

Figure 4.9: Comparison of elliptical to angular variance in the variable ellipse model, and of both quantities to the difference in reduced chi-squared χ^2_ν between this model and the constant ellipse model. Negative $\Delta\chi^2_\nu$ means that the variable model has a smaller chi-squared and therefore is a better fit. Elliptical variance is the maximal axis ratio difference between ellipses $0.5 - 3.0$ arcseconds, and angular variance is the maximal position angle difference between any of these ellipses with $q < 0.85$. Points for J1029+0420, J1032+5322 and J1420+6019 are cut off from the chi-squared plots for ease of viewing as their $\Delta\chi^2_\nu$ values are an order of magnitude different to all other lenses, they can be seen in the full-range plot: Appendix Figure A.6.

we get p-values of $p = 0.25$ for $\Delta\chi^2_\nu$ to angular variance, and $p = 2.6 * 10^{-5}$ for $\Delta\chi^2_\nu$ to elliptical variance, meaning there is very strong evidence that $\Delta\chi^2_\nu$ and elliptical variance are (negatively, $c = -0.67$) correlated. There are outliers in the data however that could skew the results - J1032 has both an outlying angular and elliptical variance, and given the results seen previously, removal of this lens is straightforward. The other outlying angular variance is from BELLS-GALLERY lens J0201, by visual inspection of the results, we conclude that there was a possible modelling error in this lens, since seven ellipses have reasonably consistent position angles and one is then offset for no discernable reason, leading us to remove this data point. The conclusion of no correlation to angular variance does not change upon removal of outliers, but the conclusion that $\Delta\chi^2_\nu$ is correlated with elliptical variance does change - removing only J1032 causes the p-value to increase to $p = 0.076$, meaning that this lens was driving that correlation, and a result should not be driven only by one target from a whole sample.

4.5.1.3 Fit parameter differences between light models

Operating under the assumption that the strongest constraints on the mass model from strong lensing comes from the galaxy mass around the Einstein radius, we can test whether a simple parametric mass model is appropriate, or if a radially-variable mass model would be a better choice. We do this by comparing the parameters of the simple constant ellipse model $\mathcal{F}_1$ (the light model which most accurately reflects the way we model mass) to parameters recovered from the variable ellipse model at the Einstein radius. If the light models generally agree, then this is evidence in support of the fact that single power-law mass models are appropriate in most lensing cases (on HST-style datasets like SLACS), although of course this conclusion also rests upon the assumption that light is a good tracer of mass (see Section 4.5.2).

Figure 4.10 shows the axis ratio and position angle differences between the light models, with values given as constant ellipse parameter minus variable ellipse parameter, meaning that a negative value of Δq for example indicates that the constant-ellipse model is more elliptical than the variable-ellipse model (at the Einstein radius). As mentioned at the start of this section, the greyed-out BELLS-GALLERY points are the lenses we ignore due to their light at the Einstein radius being extrapolated rather than interpolated. We find that most lenses have a consistent axis ratio within 3-sigma ($\Delta q = 0$ is contained within the errorbars), with none of the 4 BELLS-GALLERY lenses and only 8 out of the 28 SLACS lenses - J0330, J0912, J1032, J1143, J1213, J1420, J1430, J2238 being inconsistent at 3-sigma. The vast majority of lenses also have position angles consistent at 3-sigma, with only J0201 and J1525 inconsistent, and of these, J0201 has Gaussian processing problems with the error interpolation, and thus should be discounted. If we wish to place a tighter 1-sigma constraint, we find that all 4 BELLS-GALLERY lenses are inconsistent in axis ratio, and 2 in position angle, with 17 SLACS lenses inconsistent in axis ratio and 19 in position angle. We consider a 1-sigma constraint as overly restrictive however, given the overly-flexible nature of the Gaussian interpolation and that the fit errors themselves are often incredibly small (Figure 4.10 and Appendix Figure A.11).

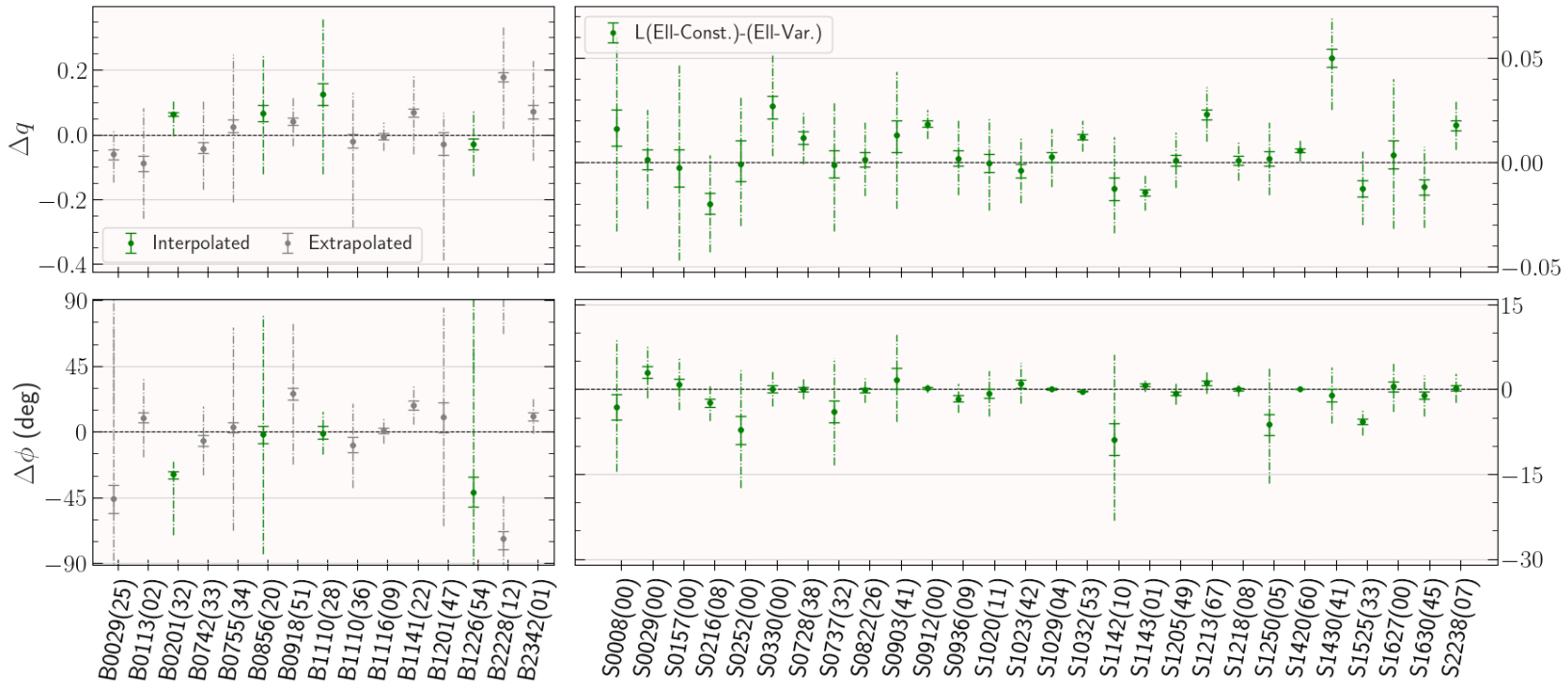

Figure 4.10: Difference in the recovered axis ratio (Δq) and position angle ($\Delta\phi$) between the constant and variable ellipse models. Negative Δq means that the variable model has a larger axis ratio (more circular). Solid-capped errorbars are the 1-sigma errors, dot-dashed errorbar continuation denotes the 3-sigma errors. BELLS-GALLERY position angles are 'wrapped' around the angular symmetry values of an ellipse since -90 and +90 correspond to the same physical difference in orientation. Values from the variable ellipse model are estimated at the Einstein radius. Greyed-out BELLS-GALLERY lenses are those that do not have light to the Einstein radius and parameters have been (unreliably) extrapolated and should be discounted.

If we take the 3-sigma results, this therefore shows moderate but compelling evidence for the hypothesis that the radially-constant models are appropriate to describe the light distribution of strong lensing galaxies (around the Einstein radius). If we look at some lenses inconsistent at 3-sigma; J2238 has already been discussed in Section 4.4 regarding a notable ellipticity increase from centre to outskirts, and J1430 matches this case with a similar elliptical variance. If we discount J0201 due to the error interpolation problems, J1032 is the only lens where the light models are fully inconsistent (both parameters at 3-sigma), and this lens was shown earlier to be one of the most highly elliptical lenses, and a fairly clear example of a bulge-disk light distribution, which a radially-constant model would not be able to sufficiently constrain.

4.5.2 Comparison of mass to light

As discussed from Figure 4.10, we have evidence that radially-constant light models are, in general, appropriate to place constraints around the Einstein radius, as long as the light is only fit around that region. The remaining question is whether the light is an appropriate tracer of the mass, which would indicate that radially-constant lens mass models are also appropriate, since their primary constraints come from the mass distribution around the Einstein radius. As mentioned at the start of this Chapter, based on previous works (e.g. Koopmans et al., 2006; Ferreras et al., 2008; Gavazzi et al., 2012; Shajib et al., 2018) we expect that mass and light results should have consistent alignments (position angles), but have no expectation on whether axis ratios will agree due to conflicting previous evidence.

4.5.2.1 Differences in model parameters between mass and light

Figure 4.11 shows the difference in axis ratio (Δq) and position angle ($\Delta \phi$) between the mass model and the two light models (i.e.$X_{\rm mass} - X_{\rm light}$), where again we estimate the variable model at the Einstein radius and ignore the majority of the BELLS-GALLERY lenses due to lack of light (greyed-out points).

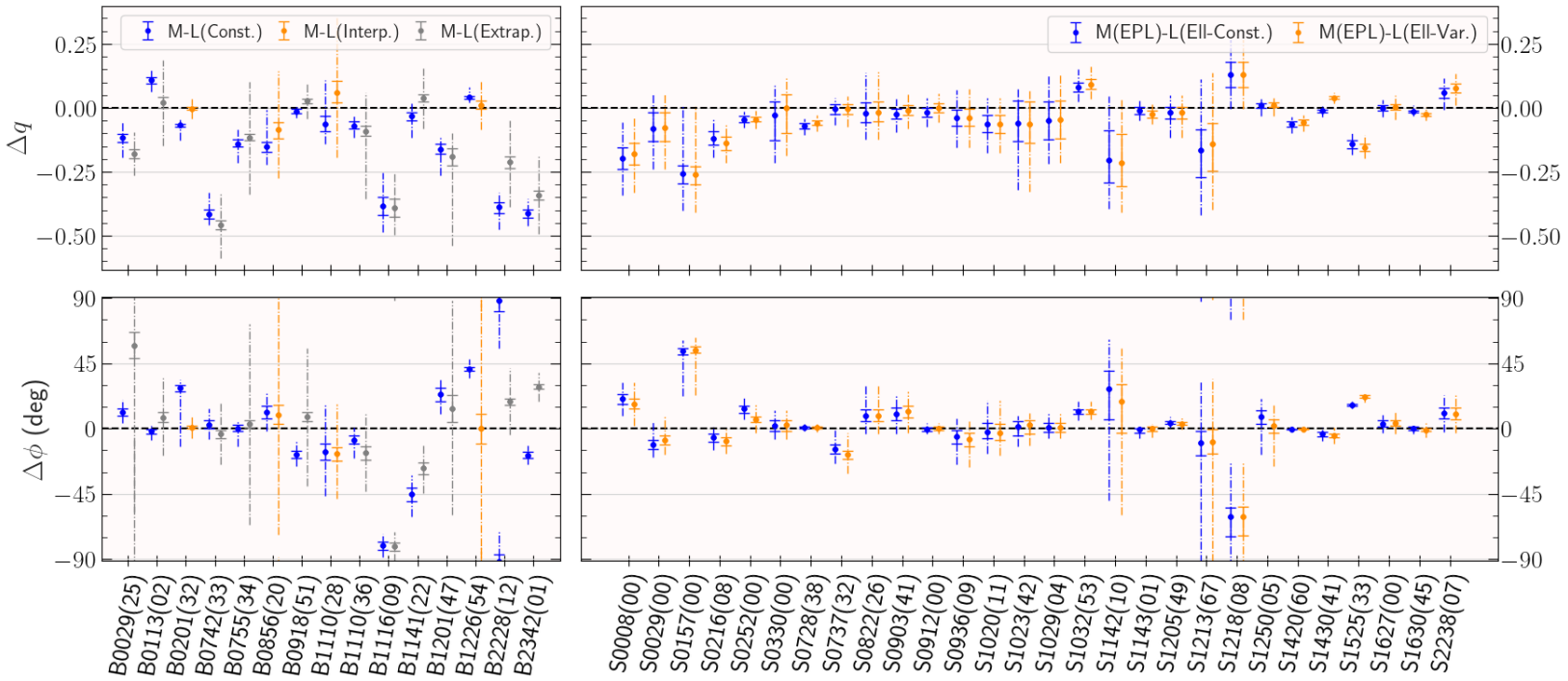

Figure 4.11: Difference in the recovered axis ratio (Δq) and position angle ($\Delta\phi$) between the EPLγ mass model and the constant (blue) and variable (orange) ellipse models. $\Delta\phi$ is 'wrapped' around the angular symmetry values of an ellipse since -90 and +90 correspond to the same physical difference in orientation. Negative Δq means that the light model has a larger axis ratio (more circular). Solid-capped errorbars are the 1-sigma errors, dot-dashed error-bar continuation denotes the 3-sigma errors. Values from the variable ellipse model are estimated at the Einstein radius. Greyed-out BELLS-GALLERY lenses are those that do not have light to the Einstein radius and parameters have been (unreliably) extrapolated and should be discounted.

Comparing first the mass model to the constant ellipse model, where we theoretically can include all BELLS-GALLERY lenses in our comparisons, we find that 12 of the 15 BELLS-GALLERY lenses are inconsistent at 3-sigma in axis ratio (including 3 of the 4 'reliable' lenses), and 8 are inconsistent in position angle (including only 1 of the 'reliable' lenses). The poor consistency of the BELLS-GALLERY lenses indicates problem that arises from low SNR: that we do not probe a large range of ellipse major axes. This means firstly that we do not have a lot of constraints to put on the recovered parameters, and secondly that since we cannot use the light from around the Einstein radius to constrain the parameters, we are not probing the same region of the galaxy that the mass model is.

Turning to SLACS, we find 7 out of 28 lenses are inconsistent at 3-sigma in axis ratio, and 8 are inconsistent in position angle, with J0008, J0252, J1032 and J1525 being the lenses that are fully inconsistent for both parameters. Again, similarly to the light-light comparison, the tightly constrained error-bars mean that 19 lenses are inconsistent in axis ratio at 1-sigma, with 21 inconsistent in position angle. The reasonable consistency (75%) of the 3-sigma results however indicates that the light distribution of the SLACS lenses is a reasonable approximation of their mass distribution, with the main differences to the BELLS-GALLERY sample being the SNR and thereby the probed region of light. This result seems to imply that the radially constant mass profile is an appropriate strong lensing model, given firstly that the primary lensing constraints come from the Einstein radius, secondly that the mass model is generally consistent with the radially constant light model within 3-sigma, and thirdly that the radially constant light model and radially variable light model generally agree at the Einstein radius (Section 4.5.1.3). This agrees with the findings in Koopmans et al. (2006), Ferreras et al. (2008), Gavazzi et al. (2012), Shajib et al. (2018) that the mass and light are generally well aligned to 3-sigma, and sides with Koopmans et al. (2006) and Gavazzi et al. (2012) inferring that generally the ellipticities of the mass and light are in agreement/aligned/correlated, in opposition to Ferreras et al. (2008) and Shajib et al. (2018).

We can test this idea by also comparing the variable ellipse light results to the EPLγ mass model results. For the axis ratio, 9 out of the 28 SLACS (with none of the 4

BELLS-GALLERY lenses) are inconsistent at 3-sigma, and for position angle 7 SLACS (again, no BELLS-GALLERY) are inconsistent at 3-sigma. This radially-variable model seems to be more accurate for the BELLS-GALLERY lenses than the radially constant model, and could possibly mean that this type of model is in fact more appropriate for high-redshift lens galaxies, however it could also be due to SNR effects and we would need a larger sample of adequate-SNR lenses to confirm this. For SLACS, where we can draw the main conclusions, this result does confirm that the radially variable and radially constant light models do in fact both draw similar conclusions to the mass model regarding the distributions around the Einstein radius, and with all the same lenses (plus or minus a couple) being inconsistent for both models, it seems that these lenses may be true mass-light mismatches where the stellar and dark/gas components of the galaxy are slightly misaligned due to e.g. interactions, tidal forces, mergers (aside from J0252 which is only inconsistent in the constant model for ϕ, and J0216 which is only inconsistent in the variable model for ϕ).

4.5.2.2 Comments on the external shear

One key ongoing debate in the modelling of galaxy-scale strong lenses is anomalously high values for the 'external shear' (Section 2.4), which has been investigated for not actually being true shear due to nearby and line-of-sight masses, but rather excess complexity in the mass distribution of the lensing galaxy that cannot be captured by the EPLγ (e.g. Etherington et al., 2024). We approach this question by looking at the angular and elliptical variances (see Section 4.5.1.2) from the radially variable ellipse model, and testing their correlation with the external shear from the mass model, as shown in Figure 4.12, removing the outlier angular variances from J0201 and J1032, and the outlying elliptical variance from J1032 (as detailed in Section 4.5.1.2). We find that whilst there may be some indication by eye of correlations, a Pearson-r correlation coefficient test returns p-values $p > 0.4$ for both angular and elliptical variance, meaning there is no statistical evidence for correlation in these quantities across the whole sample. The Pearson-r has some caveats however, the largest being that it does not take the errors into account

and the second being that it tests against a null hypothesis of independent, normally distributed parameters, which is assumed but unverified.

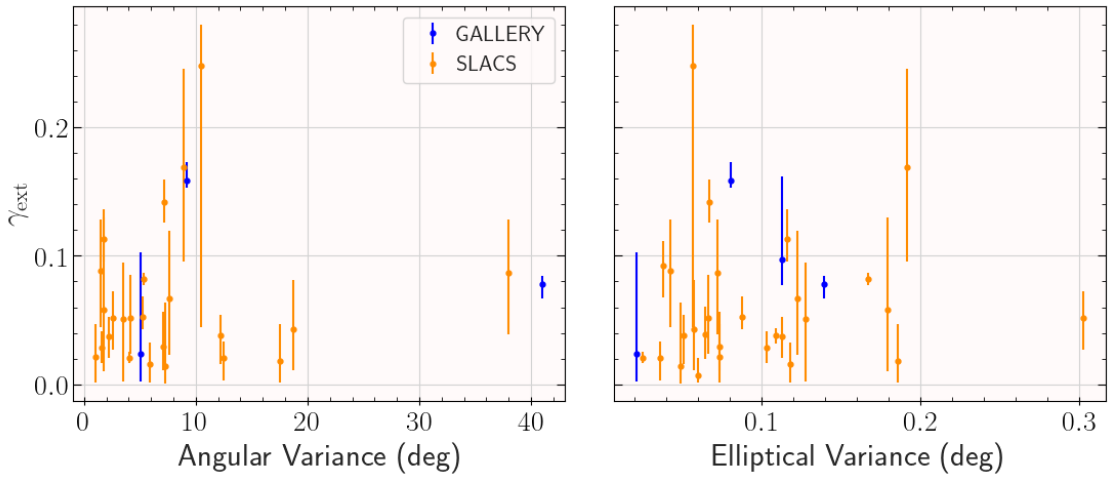

Figure 4.12: Comparisons of the elliptical and angular variance of the variable ellipse model, to the external shear of the EPLγ mass model. Errors shown are 3-sigma.

Of course, effects which cause anomalously high shears should only be correlated to those shears, therefore, if we assume that the distribution we are looking at is actually a superposition of two populations (those with 'true' shears and those with artificially inflated shears), we can repeat the correlation test on only the high-shear population. Treu et al. (2008) studied the environment of SLACS lenses and concluded that in the most overdense regions, a shear of only around 0.05 was required, therefore, we set our upper expected limit of shear to this value, and designate any shears with $\gamma_{\rm ext} > 0.05$ to be anomalously high shears. Using this test, we return a p-value of $p = 0.004$ for the correlation between angular variance and anomalously high shear ($\gamma_{\rm ext} > 0.05$), with a coefficient (linear relationship slope) of $c = 0.73$. This therefore indicates that, whilst the radially constant ellipse model and radially constant mass model may be sufficient in the majority of cases, angular variance required in the mass model may cause anomalously high shear magnitudes to be fit, since the radially-constant EPL model cannot account for this complexity. Interestingly, most (but not all) of the lenses where the light and mass model parameters disagree also return high shear magnitudes ($\gamma_{\rm ext} > 0.05$), lending more support to the possibility that the shear in the EPLγ models can be attempting to absorb missing complexity in the lens galaxy mass distribution that is not captured by the EPL.

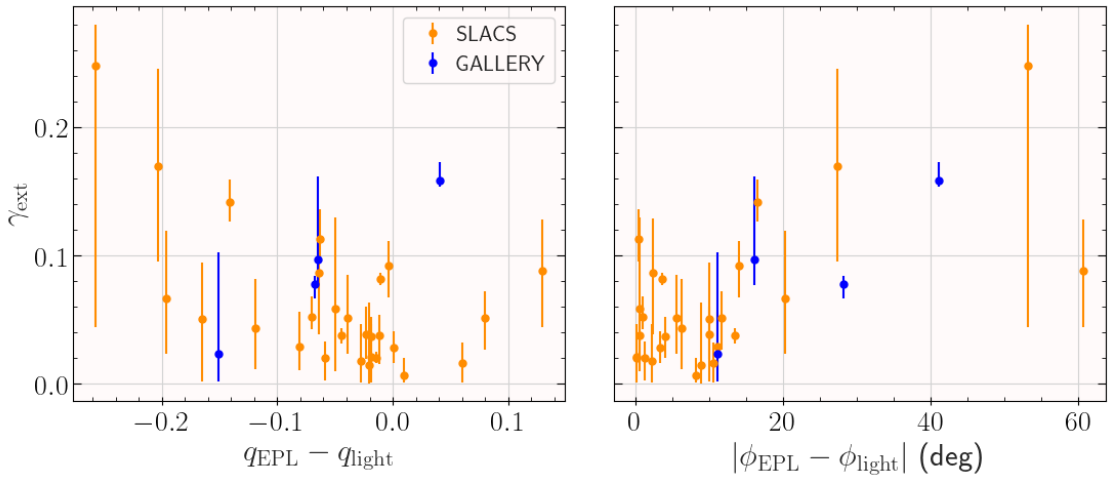

Figure 4.13: Comparisons of the misalignment between mass and light in angle and axis ratio, to the magnitude of the external shear of the EPLγ mass model. Errors shown on the shear magnitude are 3-sigma. Misalignment values are absolute differences for angle, and mass-light for axis ratio. Negative Δq means that mass is more elliptical than light.

On a similar note, Shajib et al. (2018) find a strong correlation between the misalignment angle between mass and light and the external shear magnitude when fitting to lens galaxies of quadruply-imaged point source systems. Gavazzi et al. (2012) find that in their sample of 16 extended-source lens systems, two out of the three systems that have disagreement between light and mass distributions also have nearby galaxies that cause high-magnitude external shears. In order to compare to these and similar studies, we have repeated our correlation tests of the shear magnitude against the misalignment of axis ratio and position angle between the mass model and radially constant light model from above (Section 4.5.2.1) with the comparison plot in Figure 4.13. We compare the external shear magnitude with the *absolute* difference in position angle due to the continuous/repetitive nature of the position angle. We do however split the positive and negative Δq sections into separate correlation tests as they have different physical meanings (negative means a more spherical light than mass, and vice versa).

We find strong evidence for a moderate positive correlation between the shear magnitude and the (absolute) angle difference between mass and light ($p = 2.8 \times 10^{-5}$, $c = 0.70$). The positive Δq section only has 6 data points (only 6 lenses have the mass more spherical than the light) so no significant correlations can be drawn from this section. We do however

find evidence for moderate negative correlation between shear magnitude and the negative Δq values ($p = 5.0 \times 10^{-4}$, $c = -0.63$) implying that the shear magnitude increases as the light becomes more spherical compared to the mass (or as the mass becomes more elliptical compared to the light). Correlations with similar coefficients ($\pm 10\%$) are seen with weaker (but still significant) p-values $\sim 0.01 - 0.02$ for the same comparisons with the high-shear lenses only, however the fact that these trends are seen over the whole shear distribution shows that this is a whole-population phenomena and not specific to the high shears. In fact this agrees with the findings of Gavazzi et al. (2012) and Shajib et al. (2018) that mass-light misalignments and increased (total) mass ellipticity compared to stellar distributions is correlated to stronger external shears, implying that the interactions of the lens galaxy with nearby galaxies *does* cause an offset between the total mass and the stellar mass.

4.6 Conclusions

We summarise the main conclusions of this chapter below:

- Lens galaxies come in many forms, and expecting one modelling approach to be able to fully account for all mass/light distributions is unlikely to achieve success.
- The low-SNR at and past the Einstein radii of the BELLS-GALLERY lenses makes confident determination of light distribution parameters near-impossible.
- 8 out of 28 SLACS lenses are inconsistent at 3-sigma for the axis ratio, q, of the constant ellipse model vs the variable ellipse model at the Einstein radius (J0330, J0912, J1032, J1143, J1213, J1420, J1430, J2238), where many of these lenses have high elliptical variance (bulge-disk indications). Only J1525 is inconsistent in position angle.
- 7 of 28 SLACS lenses are inconsistent at 3-sigma for the axis ratio, q, of the constant ellipse model and the EPLγ mass model (J0008, J0216, J0252, J0728, J1032, J1420,

J1525), with the same 7 plus J1430 and J2238 inconsistent between the variable ellipse model and the EPLγ mass model.

- 8 of 28 SLACS lenses are inconsistent at 3-sigma for the position angle, ϕ, of the constant ellipse model and the EPLγ mass model (J0008, J0157, J0252, J0737, J1032, J1205, J1218, J1525), with the same 8 minus J0252 & J1205 and plus J0216, inconsistent between the variable ellipse model and the EPLγ mass model.

- The radially-constant ellipse model is therefore a generally suitable model for the light distribution of a SLACS-like galaxy around the Einstein radius. The EPLγ mass model is also generally a good match to both the constant and variable light models, around the Einstein radius. **Therefore the EPLγ mass model is a generally suitable model for the mass of a SLACS-style lensing galaxy**, provided the galaxy does not have a strong bulge-disk structure.

- The external shear from the EPLγ mass distribution does not have any significant sample-wide correlation with either angular or elliptical variance in the light distributions. However, **there is evidence (Pearson-r $p = 0.004$) for correlation ($c = 0.73$) between anomalously high shears ($\gamma_{\rm ext} > 0.05$) and angular variance in the light distribution**.

- There is also evidence for correlation between the external shear magnitude and differences in angle and ellipticity between the mass and light distributions. Pearson-r results are: $\gamma_{\rm ext} : |\Delta\phi|$ has $p = 2.8 \times 10^{-5}$, $c = 0.67$; $\gamma_{\rm ext} : (q_{\rm EPL} - q_{\rm light}) < 0$ has $p = 5.0 \times 10^{-4}$, $c = -0.63$. In physical terms, larger angle misalignments and mass becoming more elliptical than light are linked to higher shear magnitudes. The correlation is over the whole sample not just the lenses with anomalously high shears, implying that nearby galaxies may cause offsets between the stellar and total mass components of lens galaxies.

Chapter 5

Angular 'multipole' complexity in the light and mass of lens galaxies

5.1 Preamble in the context of Chapter 4

Having looked at the relationships between light and mass in Chapter 4, and the effect of allowing a more complex model with ellipse variability, we now turn to a different form of model complexity known as 'multipoles', as introduced in Section 2.5. In the mass modelling of strong lenses, there is not currently the capability to confidently apply a variable-ellipse style model, therefore, a commonly used technique (e.g. O'Riordan et al., 2024) to increase the angular complexity of the mass models is to apply a 'multipole' sine & cosine-based expansion, as seen in Chapter 3. As more and more new high-resolution strong lensing data becomes available, the need for an increase to the complexity of our models is becoming more urgent and apparent (e.g. Cao et al., 2021; Powell et al., 2022; Barone et al., 2024; O'Riordan et al., 2024; Stacey et al., 2024). Whilst the conclusion from Chapter 4 was that the EPLγ model is seemingly generally appropriate for SLACS-like datasets and does not require a piecewise radial variance, these newer datasets from e.g. JWST and ALMA are not SLACS-like.

Multipoles in the light distributions of galaxies have been studied for decades, primarily in the form of 'boxiness' and 'diskiness' (e.g. Nieto et al., 1989; Hao et al., 2006). He et al. (2024) indicated that a multiple-Gaussian breakdown of the light of SLACS lenses

showed evidence for multipole-like structure, and we have already seen in Chapter 4 that our mass-light and constant model-variable model agreements tend to break down when galaxies become disc-like, therefore an investigation of the multipoles in these lenses is still warranted. Mass modelling including multipoles is also not a new idea (e.g. Congdon et al., 2005; Claeskens et al., 2006; Hezaveh et al., 2016; Cohen et al., 2024) but linking mass multipoles to light shapes is less common despite the concept being around for over two decades. Trotter et al. (2000) compared mass multipoles in the quadruple-image lens MG J0414+0534 to elliptical isophotes of the same lens galaxy from Falco et al. (1997), finding that the quadrupole was aligned with the isophotes. The Trotter study however only compared mass multipoles to light *ellipses*. In fact, the first detailed comparison of multipole perturbations in the mass to multipole perturbations in the light (on a galaxy scale) was performed in Stacey et al. (2024) who looked at three lenses, inferring the mass including order $m = 3, 4$ multipoles from ALMA interferometry data at 30 mas resolution and fitting the light from HST infrared observations in two bands using multipole-perturbed ellipses in the same way that will be presented in this Chapter. The Stacey study finds strong evidence in the mass models for multipoles, but that the ellipticity angles are misaligned for two out of the three lenses, and that there are some potential disagreements in the multipoles for the same two lenses with one having a lower k_3 strength and the other having misaligned ϕ_4 angles (at the einstein radius). The fact that there is such little previous work on this topic in the literature is a contrast to Chapter 4 where we had plenty of background to compare our results to, and means that this Chapter could generate new insights into this field.

This chapter is structured as follows. In Section 5.2 we detail the extensions to the methods presented previously that allow for the inclusion of multipoles into both the mass and light models. In Section 5.3 we present detailed results of four lenses from the sample, and discuss the possible inferences that we will be able to make using these results. In Section 5.4, we present the sample-level results, with particular focus on the multipole strengths. In Section 5.5 we summarise the main conclusions of this work and the requirements for future studies.

5.2 Methodology

We use the exact same dataset as Chapter 4, and we refer the reader back to Section 4.2 and Table 4.1 for details.

5.2.1 Mass modelling

As mentioned, we follow on from Chapter 4, extending the results from the EPLγ pipeline to include order 3 and 4 multipoles. The formalism behind multipole additions to the EPLγ is in Section 2.5, and we have already seen them applied in Chapter 3. We do not include the $m = 1$ order multipole in order to closely examine the more commonly used $m = 3, 4$ multipoles. We reiterate an important note that was made in Section 2.5, that the current implementations of mass model multipoles (including in this work) are 'circular' multipoles - i.e. expansions based on an underlying circular distribution and thus are only approximations when the underlying model (the EPL) is non-circular, with the approximation becoming less accurate as the axis ratio decreases (Paugnat et al., 2025). This is important to bear in mind when forming hard conclusions from this work, however this work with the application of circular multipoles can still provide good indicators of the full results one could get from 'elliptical' multipoles, and provides a good base to begin sample-level studies of multipoles in strong lenses.

To determine any improvement in model fitting from the EPLγ to EPLγ+Multipole, we use the change in log likelihood ($\Delta \log \mathscr{L}$) between these models, where a positive change means a better model. We use Likelihood instead of Bayesian Evidence here (as opposed to the method in Chapter 3) since the work presented so far has shown us that we do not have clear information about how to define the priors on multipoles, and therefore the Bayesian Evidence (which is prior-dependant) is skewed and would not be a useful model discriminator when we are actively trying to constrain the priors.

5.2.2 Ellipse fitting with multipoles

The extension of the ellipse fitting formalism is well documented (e.g. Hao et al., 2006; Amvrosiadis et al., 2025b), and continues from the basic formalism in 4.3.2. We use the same datasets and light masking techniques as Chapter 4 and optimise the same likelihood function (4.3). The multipoles are applied in a method which adds a perturbation to the equation of a point on the ellipse (4.1), with the addition of the form:

$$r_m(\phi) = a_m \cos\left[m(\phi - \phi_e)\right] + b_m \sin\left[m(\phi - \phi_e)\right], \tag{5.1}$$

where $r_m(\phi)$ is the distance from the ellipse centre to the point at angle ϕ, ϕ_e is the position angle of the *ellipse* (not the multipole), and a_m & b_m are the 'multipole components' that are fit for in the non-linear search (as analogue to the $\epsilon_1^{\rm mp}, \epsilon_2^{\rm mp}$ components for the mass multiples), and can be transformed into a multipole strength, multipole angle and shape angle in the same method as for the mass (Equations 2.11, 2.12):

$$\begin{aligned} \phi_m &= \frac{1}{m} \arctan \frac{a_m}{b_m}, \\ k_m &= \sqrt{a_m^2 + b_m^2}. \end{aligned} \tag{5.2}$$

The total equation for a point on a perturbed ellipse with centre (x_0, y_0) is therefore

$$r_p(\phi) = r_{p,0}(\phi) + \sum_m r_m(\phi), \tag{5.3}$$

where $r_{p,0}(\phi)$ is the equation for a point on the unperturbed ellipse (Equation 4.1). This application method means that the multipole parameters for light and mass are identical (i.e. if a light multipole and mass multipole have the same strength k_m and shape s_m values, then the resulting perturbation is identical), this is despite the fact that the multipoles in ellipse fitting are applied as a *perturbation* (Equation 5.1) whereas the multipoles in mass fitting are applied directly to the convergence by using a new equation unrelated to the underlying EPL (Equation 2.9).

5.2.3 Light model variants

Similarly to Chapter 4, we fit two models to the lens light: model $\mathcal{F}_3$ holds the multipole parameters constant across all ellipses, and model $\mathcal{F}_4$ allows for the multipoles to vary

across the ellipses. For both models the elliptical parameters (q, ϕ_e) are held constant across all ellipses (as in model $\mathcal{F}_1$ from Chapter 4). For the 'constant' multipole model $\mathcal{F}_3$, the multipoles are fit such that they optimise the same 'scaled' multipole strength across all ellipses, $k_{\rm scale} = k_{\rm n}/a_{\rm n}$, where the subscript n denotes the multipole parameter value at any specific perturbed ellipse. The radially-variable multipole model will again be interpolated through our Gaussian process (Section 4.3.4.1) and the value and errors estimated at the Einstein radius. The strength of the variable model will be quoted as k_n/a also, but where a is now the best-fit Einstein radius.

Similarly to the comparisons made in Chapter 4, the EPLγ+Multipole mass model ($\mathcal{F}_{\rm MPL}$) will be *primarily* compared to the radially constant multipole model since this is the most like-for-like comparison of mass and light (although the $\mathcal{F}_{\rm MPL}$ and $\mathcal{F}_4$ models will still be compared), and then the light models will also be compared against each other. We have seen in Chapter 4 that the use of the reduced chi-squared (χ^2_ν) as a model discriminator could be slightly misleading due to additional considerations such as data covariance and noise. We therefore use a slightly different criterion to decide whether a light model requires multipoles which we refer to as the minimum error value (MEV) (although we still show the $\Delta\chi^2_\nu$ values in Appendix A.5.1 for completeness). The MEV requires an understanding of the lowest value a parameter can have before it begins to have an impact on the model - i.e at what point does the parameter become non-negligible. If the 3-sigma error bound on this parameter is past this MEV point, then the parameter is necessary for the model, having a non-negligible impact. We apply this through requiring that for a model to require multipoles, the lower bound of the 3-sigma error must be above $k_m/a = 0.005$. This threshold is somewhat arbitrary due to the lack of literature knowledge regarding multipoles in the mass of lens galaxies, however it is based on Stacey et al. (2024) stating $k_m > 0.01$ as non-negligible and O'Riordan et al. (2024) showing that $k_m = 0.01$ multipoles can cause significant lens modelling discrepancies (no smaller value was tested). We use 0.005 instead of 0.01 for two reasons: firstly in order to attempt to probe any small multipole effects, and secondly since we use the 3-sigma error bound which is a stringent constraint. There are two notes on the application of this method:

firstly if *either* the $m = 3$ or $m = 4$ multipole is above the threshold then this is counted as a detection (we do not require a lens to have both types of multipole); secondly, for the radially-variable multipole model we mean of the lower 3-sigma errors of the closest two data points to the best-fit Einstein radius (one either side) to calculate the MEV, in order to avoid any uncertainties arising from the interpolations. We do not therefore return any MEVs for those BELLS-GALLERY lenses that do not have ellipses fit past the Einstein radius.

The primary model discriminator for mass models will continue to be the log-likelihood, as mentioned in Section 5.2.1, and we will take an a-priori threshold of $\Delta \log \mathscr{L} = 10$ for significance. The somewhat arbitrary MEV threshold of $k_m/a = 0.005$ can allow for some ambiguity in light model results as we use the fairly rigid terminology of 'detections' and 'non-detections'. This terminology does not reflect the lack of information available in deciding the MEV threshold and so the MEV method with the same threshold will be applied to the mass results and the resulting 'detections' will be compared to the detections from the log-likelihood method as a test of the robustness of the MEV discriminator (see Section 5.4.1.1).

5.2.4 Multipole modelling example: J0008-0004

We show brief light model examples of the ellipse fits and the recovered parameter plots* from the multipole-perturbed ellipses for SLACS lens J0008-0004, similar to Section 4.3.5.

Figure 5.1 shows the ellipse fits for the two multipole-perturbed light models, with the upper panels showing only the fit ellipses, and the lower panels showing also the contours of the data corresponding to the same fit intensity as the ellipses. We can immediately see the differences caused by the multipoles, first in the constant model, where the general shape of the ellipses has taken on a parallelogram-style boxiness, and differently in the variable model where the shapes of all ellipses are fairly different to each other. We also notice that the inner ellipses of the variable model are not strongly perturbed by the multipoles,

*All plots are again available at `https://github.com/samlange04/slacs_bells_structure`.

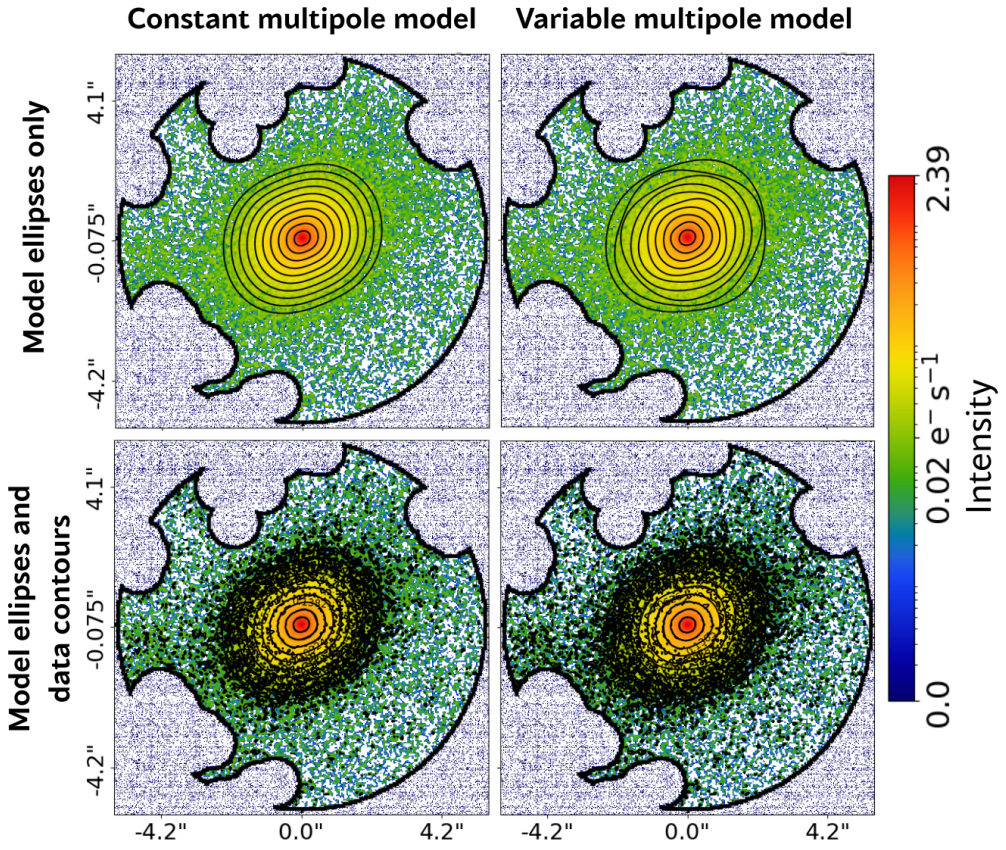

Figure 5.1: Ellipse fits to SLACS lens J0008-0004 from the two multipole-perturbed models. The left column shows the $\mathcal{F}_3$ model with the multipoles having the same multipole angle ϕ_m, and the same scaled multipole strength $k_{\mathrm{m,scale}}$ across all ellipses. The right hand column shows model $\mathcal{F}_4$ where the multipoles can vary with their own independent k_m and ϕ_m for the different ellipses. The upper panels show the fit perturbed ellipses, with the lower panels showing these ellipses and also the contours of the data that has the corresponding fit intensity. The data intensity has a $\log_{10}$ colour scale.

which fits with the assumption that the inner light distributions of galaxies are much more smoothly distributed than the outskirts. The upper left hand panel also demonstrates the nature of the scaled multipole strength $k_{\mathrm{m,scale}}$ that is applied in the constant multipole model $\mathcal{F}_3$: since the scaled multipole strength is multiplied by the major axis to get the specific strength k_m for each ellipse, the inner ellipses are less perturbed than the outer ellipses, allowing for a coherent shape to be formed across the whole galaxy.

Figure 5.2 shows the recovered parameters from the multipole models $\mathcal{F}_3, \mathcal{F}_4, \mathcal{F}_{MPL}$ and their figures of merit. The figures of merit are as stated in Section 5.2.3 and show that

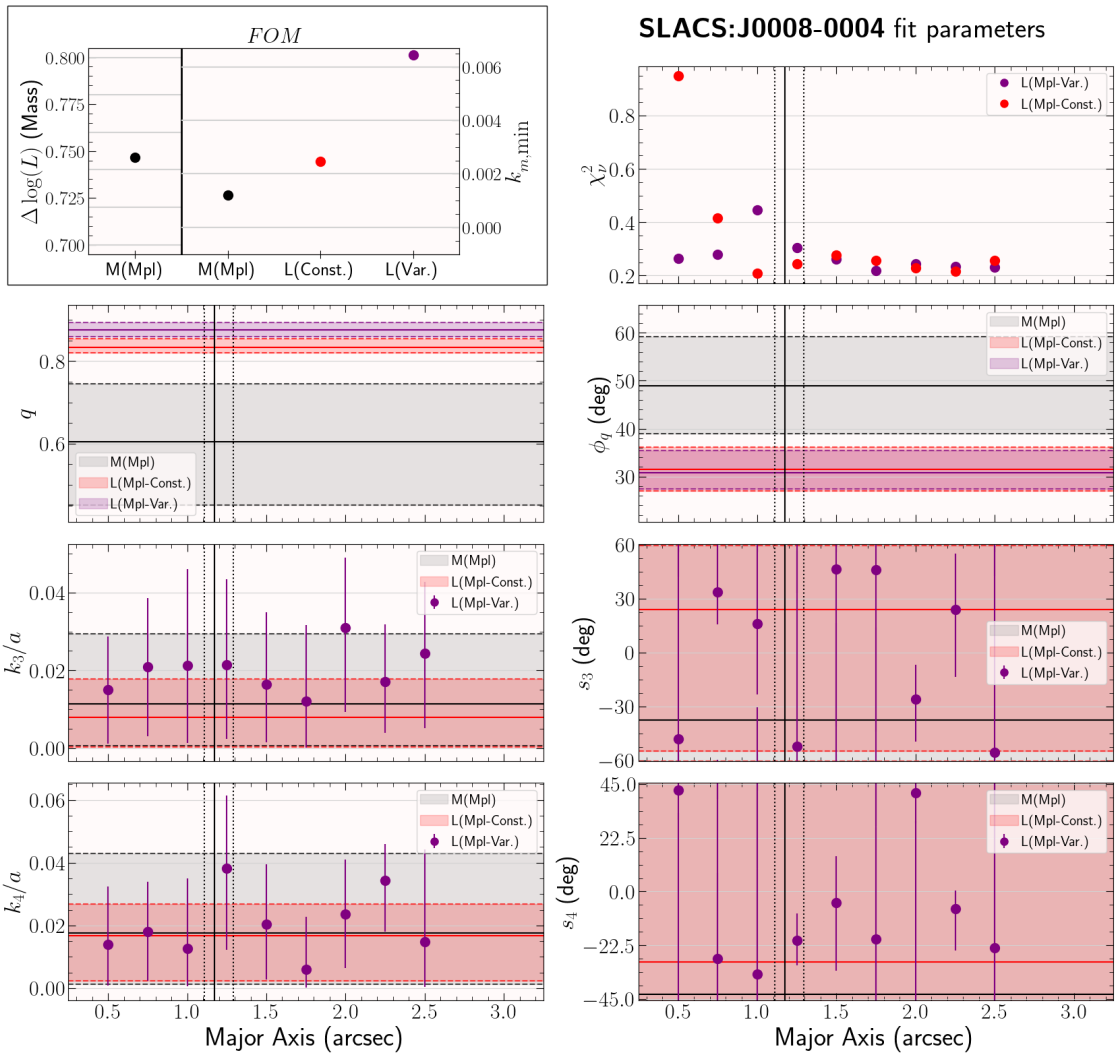

Figure 5.2: Parameters and isophote fits for the multipole-perturbed models $\mathcal{F}_{\rm MPL}, \mathcal{F}_3, \mathcal{F}_4$ of SLACS lens J0008-0004. Upper left panel shows the figures of merit (FOM) for these models - the FOM for mass is the change in log-likelihood $\Delta \log \mathscr{L}$ (positive means EPLγ+Multipole is a better model), and for light is the higher of the two 3-sigma lower error bounds from the k_3/a and k_4/a multipole strengths (see Section 5.2.3), where the threshold for significant multipole strength is $k_m/a = 0.005$. The other panels show the fit χ^2_ν per ellipse for the light models (top right), axis ratio q and position angle ϕ_q (row 2), and multipole strengths k_m/a and shape angles s_m for the order 3 and 4 multipoles (bottom rows). Solid lines and shaded regions mark the best-fit value and 3-sigma ranges for values which are constant over all radii/major axis values, purple points with errorbars are the values for each ellipse in the radially-variable multipole model. Vertical lines mark the best-fit value of the Einstein radius θ_E (solid) and its 3-sigma errors (dashed).

the EPLγ+Multipole mass model is not preferred over the EPLγ model from its near-zero change in log likelihood, and its near-zero minimal error bound on the multipole strengths. For the light models, the constant light model multipoles are below the MEV threshold of 0.005, however the radially-variable multipole bound is above this threshold, meaning that the addition of radially-variable multipoles could have some significant impact on the resulting light distribution. Looking at individual ellipse reduced chi-squared values in the top right panel, we see that the constant multipole model does worse at fitting the model in the inner ellipses, better than the radially-variable multipole model around the Einstein radius (vertical lines), and then about the same further out. In terms of parameters, there is a range of agreements and disagreements - none of the three models agree at 3-sigma in axis ratio, and only the light models agree in position angle (neither agree with the mass model). There is however good agreement in the multipole strengths between all three models. As expected with a non-detection of multipoles in the mass and the constant light model, the shape angles are completely unconstrained to 3-sigma, with errors spanning the whole available angle range (hence no dashed lines in the lower right panels of Figure 5.2 marking the 3-sigma edges). We also see that really only the two ellipses just past the Einstein radius have a well constrained s_4 angle for the radially-variable model, which fits with the lower left panel of the figure where we see that the ellipse immediately after the Einstein radius is the only one with a non-negligible k_4 strength - meaning that this mismatch in multipole detection in the two light models could be driven by a single stochastic modelling offset on this one ellipse.

5.3 Results and Discussion: Lens case-studies

5.3.1 J0755+3445: Problems with low-signal lens light

Our first case study in this chapter is the BELLS-GALLERY lens J0755+3445. This lens is a prime example of a problem affecting the whole BELLS-GALLERY sample (and potentially even some of the SLACS lenses) - that is the problem of low lens galaxy SNR. As seen in Chapter 4, the majority of the BELLS-GALLERY lenses do not have signal

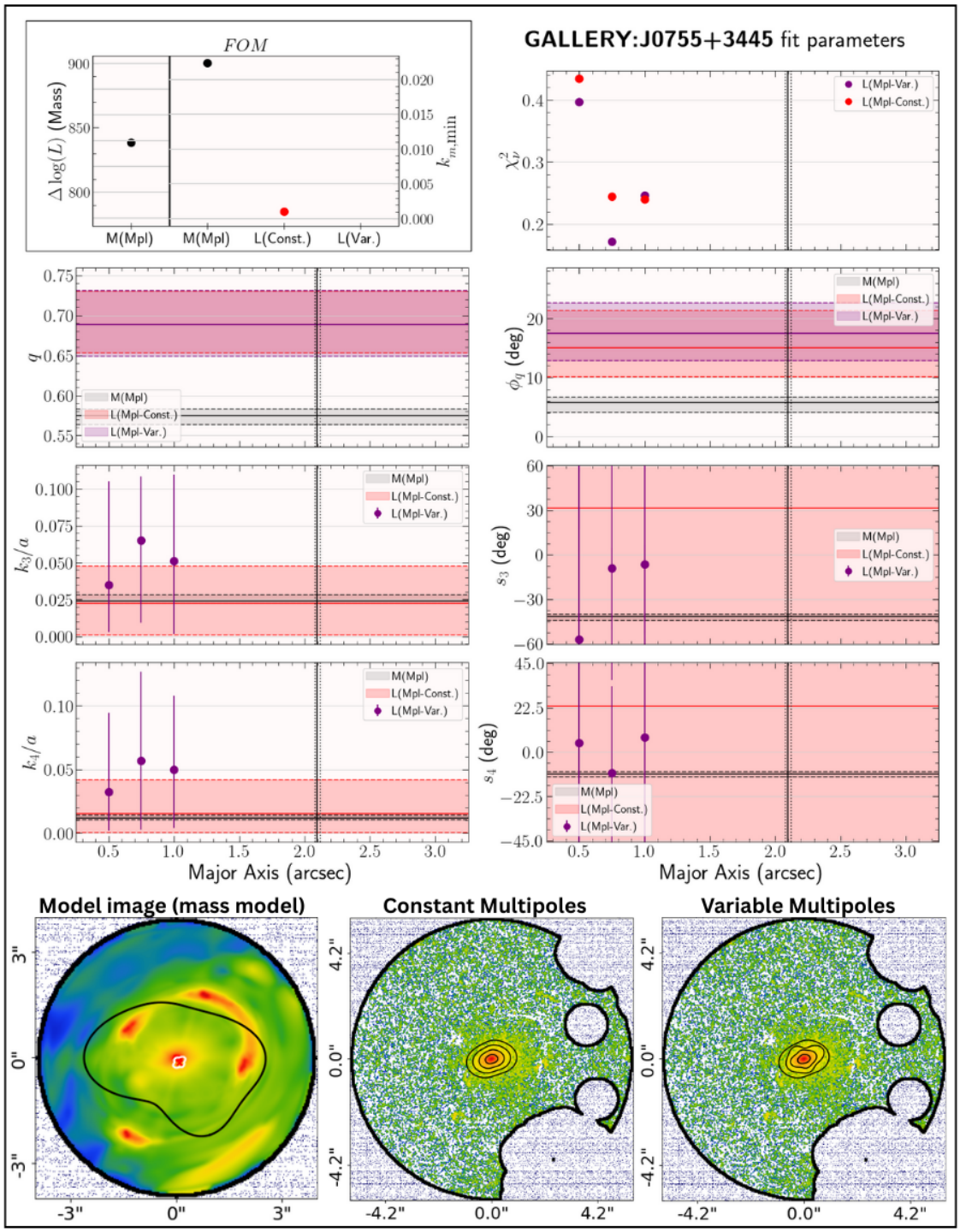

Figure 5.3: Parameters and ellipse fits for the multipole-perturbed models $\mathcal{F}_{\mathrm{MPL}}, \mathcal{F}_3, \mathcal{F}_4$ of BELLS-GALLERY lens J0755+3445. For parameter plot explanation, see Section 5.2.4. There is low SNR from the lens in this case and we see the discrepancy where the mass model strongly detects multipoles but there is insufficient information to constrain these in the light.

that extends out past the Einstein radius, due to their high redshift, and as such, we can only constrain the inner regions of the light distribution (usually up to 1 arcsecond - see Table 4.1). For Chapter 4, we deemed any amount of light sufficient to attempt to constrain the simple constant ellipse model $\mathcal{F}_1$, however, we can see that this is not the case for the more complex model $\mathcal{F}_3$, where in the lower right panels of Figure 5.3, we see that the constant (and variable model) multipole shapes are fully unconstrained at 3-sigma with the errors spanning the entire range of available values (-60 to +60 for s_3 and -45 to +45 for s_4). The strengths of the multipoles in both light models are also very low and weakly constrained, with this reflected by the radially constant light model giving no multipole detection (from the MEV in the top left panel - the radially variable model does not have ellipses fit past the Einstain radius and so does not have an MEV). On the other hand, the strengths and shapes of the multipoles in the mass model are very well constrained, with multipoles clearly detected in this model at a likelihood increase of $\Delta \log \mathscr{L} > 800$ (and lower bounds on the strength errors at $k_{3,\min} \sim 0.02, k_{4,\min} \sim 0.01$).

The significant mass multipole detection in this lens is also seen in the literature, with Barone et al. (2024) also finding strong evidence for the requirement of multipoles in the mass model of this lens and Ritondale et al. (2019) finding that this lens has a complex mass distribution beyond a simple EPL but not well explained by substructures, meaning that the strong multipole detection we see in the mass model is likely genuine. This is indicative of results to come (Section 5.4), with the main conclusion being that without sufficient SNR from the light of the lens galaxy, we cannot hope to detect multipoles in the light, even if the mass distribution of the galaxy has clear and strong multipoles associated with it.

5.3.2 J1420+6019: Light multipole in the absence of mass multipole

The next case study for this Chapter is effectively the opposite to what was seen previously for J0755. In that lens, there is strong evidence for multipoles in the mass distribution, but not in the light distribution (due to insufficient SNR of the lensing galaxy). For J1420+6019 however, we see a case where there is a detection of multipoles in the light of

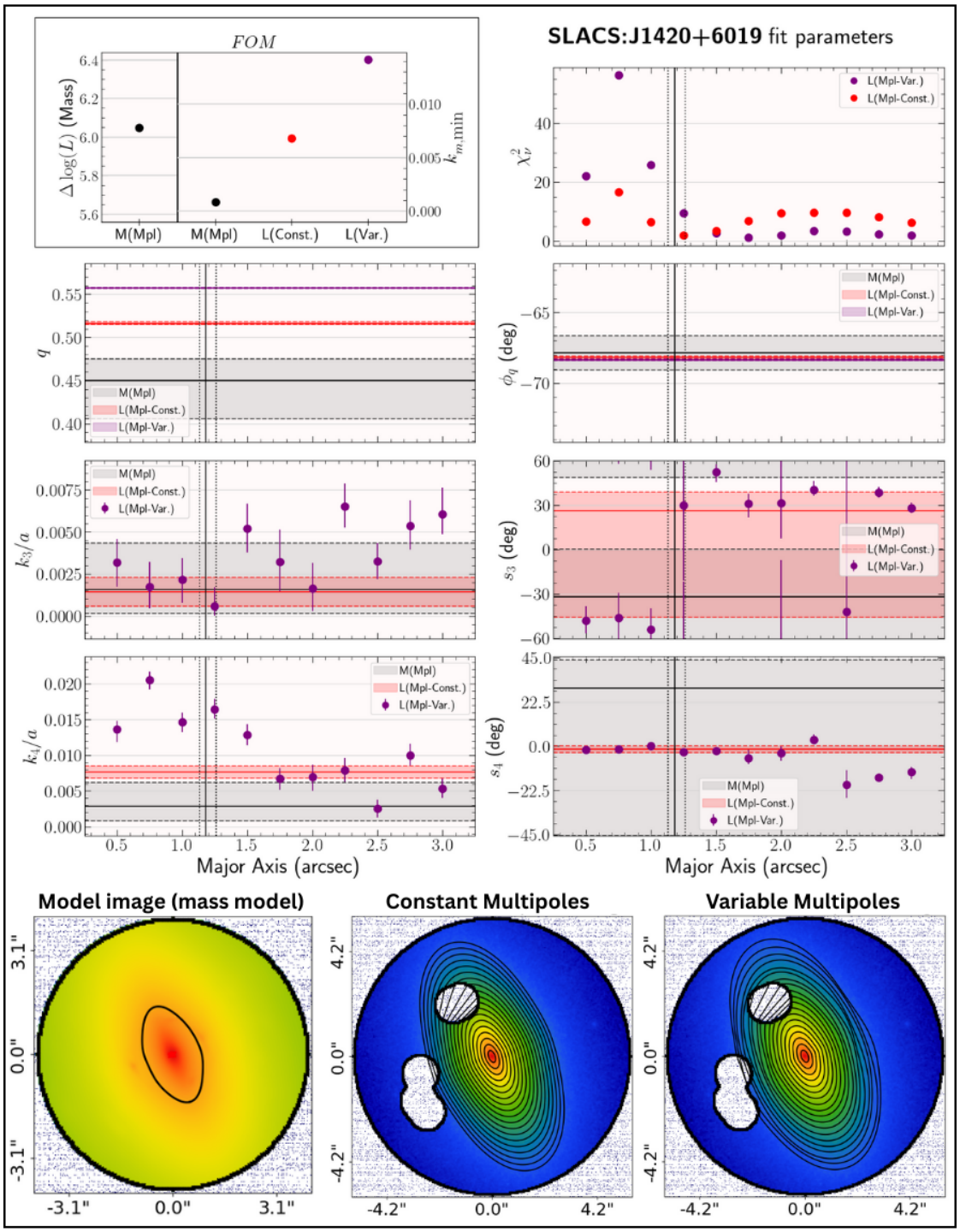

Figure 5.4: Parameters and ellipse fits for the multipole-perturbed models $\mathcal{F}_{\mathrm{MPL}}, \mathcal{F}_3, \mathcal{F}_4$ of SLACS lens J1420+6019. For parameter plot explanation, see Section 5.2.4. This lens is highly elliptical and we detect an $m = 4$ multipole in both light models with $s_4 \sim 0$ indicating diskiness, but no multipoles are detected in the mass model.

the lensing galaxy, but not in its mass. Figure 5.4 shows the fit overview of this lens, and we can see firstly in the top left panel, that the multipoles in the mass have an insignificant likelihood increase over the EPLγ model ($\Delta \log \mathscr{L} \sim 6 < 10$), and both the $m = 3$ and $m = 4$ mass multipoles have strengths nearly consistent with 0, as well as reasonably large errors on their angles covering around half the available angle ranges. Differently however, whilst neither light model seems to need an $m = 3$ multipole to fit the data, they both fit an $m = 4$ multipole with strengths inconsistent at 3-sigma (at the Einstein radius) with the mass model (note that the s_4 shape is fully unconstrained for the mass model).

The radially-variable multipole model makes full use of its variance, with $k_{4,\mathrm{var}} > k_{4,\mathrm{const}}$ for the inner 5 ellipses (inconsistent to 3-sigma) and s_4 being inconsistent to 3-sigma for the outer 3 ellipses shown. The consistency of the shape between the light models (with small errors) for the majority of the ellipses implies that a disk structure is strongly preferred for the stellar distribution in this lens and that the extra freedom in the radially-variable model allows it to better fit the strength of this structure towards the lens centre. Looking at the ellipse fit plots at the bottom of Figure 5.4, we see that this is a very elliptical lens (although all models disagree to 3-sigma on the axis ratio value), which may be why the inner ellipses want a relatively stronger disk structure than the mid and outer ellipses. The fact that this disk structure is detected in the light but not in the mass has three possible explanations - firstly that the *total* mass distribution that strong lensing is sensitive to is smoother than its stellar-only component; secondly that there are lenses where the mass model does not have the information (e.g. too low *source* SNR) to constrain multipoles properly, given the model complexity that this entails; or thirdly, that the mass model is able to achieve a reasonable fit by only increasing the ellipticity of the lens compared to the light models.

5.3.3 J0029-0055: All models agree that multipoles are not required

We now move on to case studies of lenses where the models *do* agree to some extent between mass and light. J0029-0055 is a case where all models agree that there is no need for multipoles in the mass or the light. Figure 5.5 shows the fit summary for this lens, and

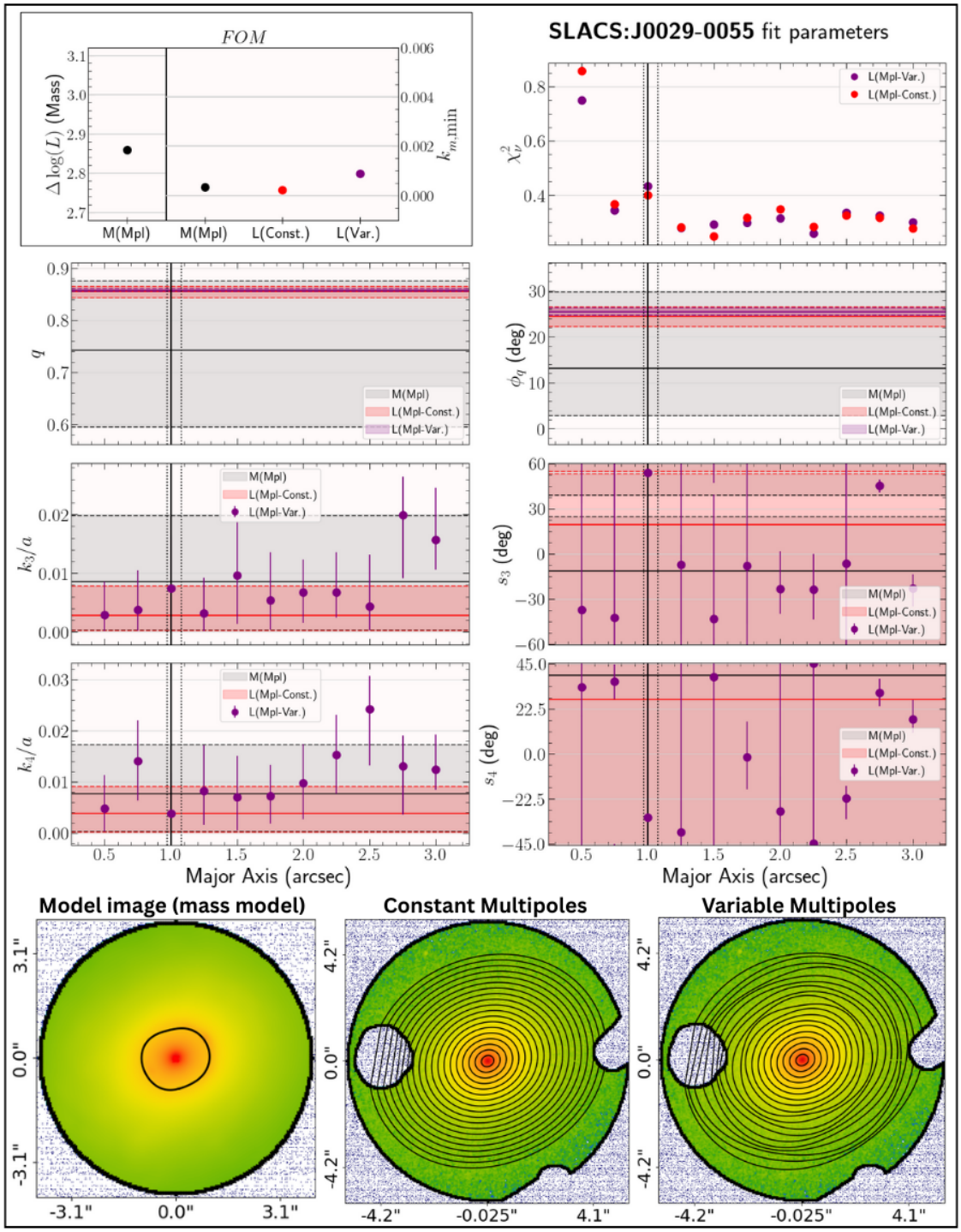

Figure 5.5: Parameters and ellipse fits for the multipole-perturbed models $\mathcal{F}_{\rm MPL}, \mathcal{F}_3, \mathcal{F}_4$ of SLACS lens J0029-0055. For parameter plot explanation, see Section 5.2.4. This lens has no detection of multipoles in either mass or light.

we see in the top left panel that the log-likelihood difference is well below the detection threshold for multipoles in the mass, and that both the mass and constant multipole light models have multipole strengths approximately consistent with 0 (the radially-variable multipole strength is a little higher, but still well below the significance threshold for a detection). We also see that the multipole shapes are nearly all unconstrained at 3-sigma for both multipoles across all three models. The mass model does have large errors on the multipole strengths (and the axis ratio/position angle), which contribute to the agreement of no multipoles, despite its best-fit value of k_3 & $k_4 \sim 0.01$. We see an interesting indication however of what could be happening in this case by looking at the k_4 multipole strength: the purple points indicating the radially-variable multipole light model indicate that the inner regions of the galaxy have slightly lower-strength k_4/a values whereas the ellipses at the outer regions have higher-strength multipoles. There is a possibility that this is an effect arising from the decrease in SNR at the outer regions that leads to weaker constraints on the model however the inner regions appear to agree more closely to the best fit strengths from the constant multipole model and the outer region radially-variable multipole strengths appear to drift closer to the best-fit mass model strengths. Regardless, this case study shows that we can get consistent non-detections of multipoles across all models.

5.3.4 J1143-0144: Models generally agree, with some caveats

The final lens that we will look at in this section is J1143-0144. In this lens, all three models require multipoles, and there is general 3-sigma agreement on the parameters produced by the model, with a few exceptions. Looking at the fit summary in Figure 5.6, we see that the mass model prefers to use a stronger $m = 3$ and weaker $m = 4$ as opposed to the radially constant light model preferring a stronger $m = 4$ and weaker $m = 3$ (k_4 agrees to 3-sigma, k_3 does not). The radially variable multipole model gives a large variation in the k_4 strength across ellipses, which could potentially be the cause of the large errors on the k_4 from the mass model if there is this level of variation going out from the galaxy centre. The k_3 values for the radially variable model also change across ellipses, with

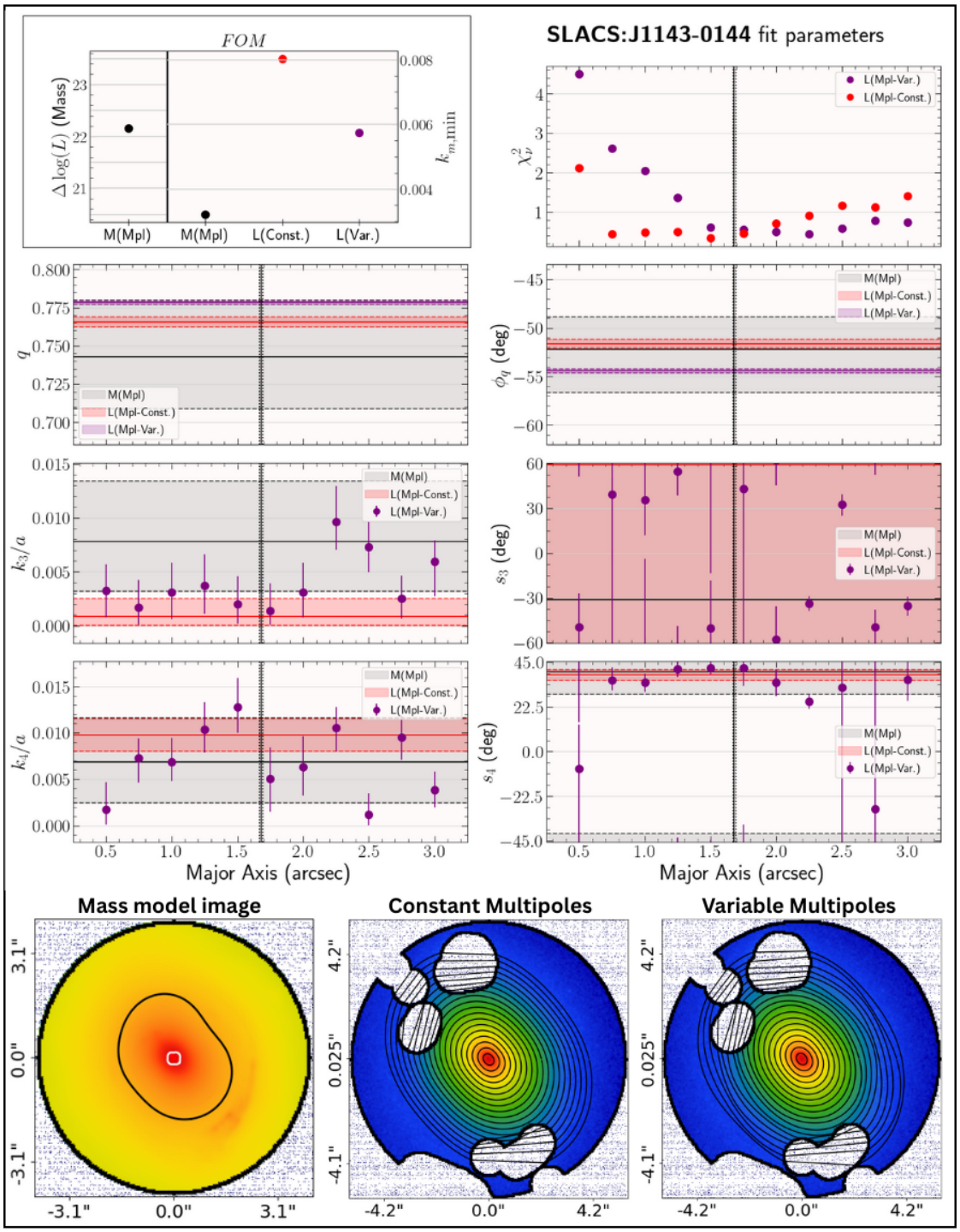

Figure 5.6: Parameters and ellipse fits for the multipole-perturbed models $\mathcal{F}_{\rm MPL}, \mathcal{F}_3, \mathcal{F}_4$ of SLACS lens J1143-0144. For parameter plot explanation, see Section 5.2.4. This lens detects multipoles using all three models, but disagrees strongly on which multipole is stronger ($m = 3$ for mass, $m = 4$ for light), and on the orientation of the $m = 4$ angle.

values for ellipses up to 2 arcseconds being in closer agreement with the radially constant light model, whereas after this point the values are generally in better agreement with the mass model. This could be a reason for mass-light mismatches if there is true variation across a galaxy which cannot be fully captured by radially constant mass or light models.

The s_3 values are generally unconstrained for the radially variable light model and fully unconstrained for the mass and radially constant light models at 3-sigma, however the s_4 values are generally constrained since this is the primary multipole used by the models. There is agreement to 3-sigma between the three models that this lens exhibits a mainly boxy structure, which is reflected in the general agreement between the boxy ellipses shown in the bottom panels and the mass model critical curve. The mass model however shows a bump at the top where the high best-fit k_3 strength is affecting the curve. This could possibly be due to the fact that this galaxy is in the most overdense region of all SLACS galaxies as it is at the centre of a cluster (Treu et al., 2008), which could cause large external shears that are being absorbed by the multipoles, or extra dark matter overdensities that are not reflected in the stellar distribution.

5.4 Results and Discussion: Sample-level inference

5.4.1 Multipole detections in mass versus light

Figure 5.7 shows the MEV (light and mass - see Section 5.2.3) and $\Delta \log \mathscr{L}$ (mass) for our models, indicating where we see detections and non-detections of multipoles in the sample. Looking firstly at the mass model, we immediately notice that the BELLS-GALLERY lenses have a higher rate of multipole detections ($\Delta \log \mathscr{L} > 10$), and at higher $\Delta \log \mathscr{L}$ values, than the SLACS lenses. Two BELLS-GALLERY lenses even had extremely high outlier values of $\Delta \log \mathscr{L}$ and had to be removed from the plot for scaling purposes (J0755: $\Delta \log \mathscr{L} = 838$ and J0918: $\Delta \log \mathscr{L} = 392$). This indicates that lenses at higher redshift are less likely to have smooth mass distributions since they are more likely to require angular complexity to be added to improve the mass model, which makes physical sense in the fact that galaxies at higher redshifts are likely to be less relaxed and undergoing more mergers than their low-redshift counterparts. This does highlight the problem addressed in the BELLS-GALLERY lens case study of J0755 (Section 5.3.1) that these lenses - which generally have stronger and more detectable mass multipoles - do not generally have enough SNR from the light of the lens galaxy to constrain multipoles in the light, making a thorough comparison of mass and light multipoles very difficult. Looking at the minimal light multipole strengths for BELLS-GALLERY, we see that we only detect multipoles in the light for two (J0201 and J0918) of the ten lenses where we detect multipoles in the mass, with J0755 (by far the strongest mass detection) not being one of these cases. Interestingly, there are two lenses (J1110+2808 & J1201) where multipoles are detected in the radially constant light model but not the mass model. This is likely due to poor constraints on the light models allowing for incorrect inference, however for J1110(28) we see that the MEV for the mass is above the detection threshold for the $m = 3$ multipole (matching the detection in the light generated by the $m = 3$ multipole), despite the likelihood not showing an increase.

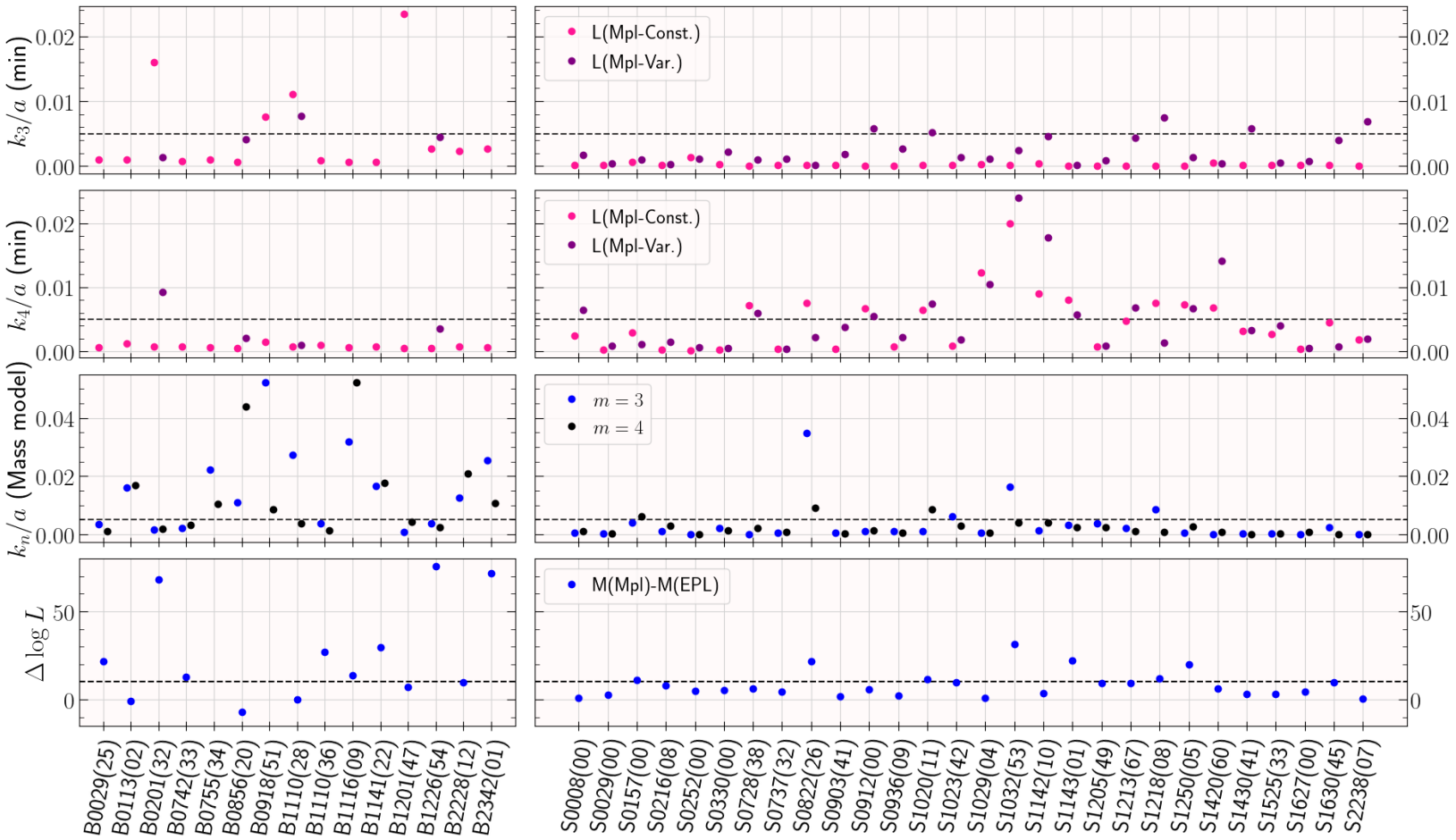

Figure 5.7: Minimal Error Values (MEV, i.e. the lower 3-sigma bound) for both k_3 and k_4 multipole strengths in the three multipole-perturbed models $\mathcal{F}_3, \mathcal{F}_4, \mathcal{F}_{\rm MPL}$ (upper panels), and log-likelihood change ($\Delta \log \mathscr{L}$) for the EPLγ+Multipole mass model over the EPLγ model (bottom panels). Dashed lines mark the significance for detection ($k_{m,\rm min}/a > 0.005$ for light, and $\Delta \log \mathscr{L} > 10$ for mass). The mass $k_{m,\rm min}$ values are not used as model discriminator, but are shown for comparison to the light models. Note that the outlier log-likelihoods of J0755 ($\Delta \log \mathscr{L} = 838$) and J0918 ($\Delta \log \mathscr{L} = 392$) are cut off for clarity of the remaining points.

For SLACS lenses, we detect multipoles in the mass for 7 of the 28 lenses (25% compared to 66% of BELLS-GALLERY), but with 6 of those 7 lenses also having detections in the light (primarily due to the $m = 4$ multipole), with the mismatch lens being J0157, which also has an offset in axis ratio where the mass model is more elliptical and in 3-sigma disagreement with the light models, which could be the driver of this disagreement with the light model finding it can fit the data with a more circular solution as opposed to the mass model fitting a more elliptical solution then adding the multipoles. Differently to the BELLS-GALLERY lenses, the SLACS lenses have more lenses that detect multipoles in the light only than lenses that detect multipoles in both the light and the mass. There are 9 lenses which have a light multipole detection without corresponding mass detection - 4 of those only from the radially variable model, and 5 detecting multipoles in both the radially variable and radially constant light models. This flips the previous problem around, as we saw in the case study of J1420 (Section 5.3.2), that we can potentially achieve better constraints on the complexity of galaxy light than on its lensing mass, if we have good SNR of the lens galaxy (and for instance poor SNR of the source galaxy, which would lead to weak constraining power on the mass distribution).

5.4.1.1 Detections in the mass models: MEV versus Likelihood

As stated in Section 5.2.3, the use of the MEV threshold of $k_m > 0.005$ is a slightly arbitrary choice due to lack of prior work on the expected multipole priors of lens galaxies, despite some motivation coming from O'Riordan et al. (2024) and Stacey et al. (2024). Using Figure 5.7 we can compare the mass model detections we would have returned using the MEV method compared to those we do return using the $\Delta \log \mathscr{L} > 10$ criterion. If we assume that a 'true-positive' MEV detection is one with a corresponding likelihood detection, 'true-negative' is both having non-detections, 'false-positive' is an MEV detection *without* likelihood detection, and 'false-negative' is a likelihood detection without an MEV detection, we can produce the confusion matrix shown in Figure 5.8

We see that the metrics agree for 6 out of the 15 BELLS-GALLERY lenses, and for 25 out of 28 SLACS lenses (importantly though, the BELLS-GALLERY agreement includes

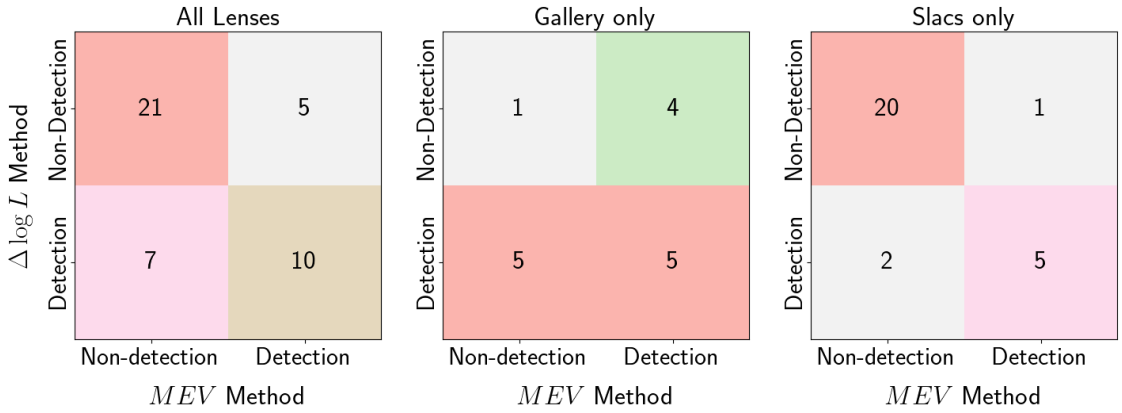

Figure 5.8: Confusion matrix showing the comparison of multipole detections from the mass model returned by the MEV and the $\Delta \log \mathscr{L} > 10$ methods. The leftmost panel includes all lenses in the sample, the centre panel is only BELLS-GALLERY lenses, and the rightmost panel is only SLACS lenses.

both high-likelihood mass detections in J0755 and J0918). This therefore indicates that although any of our light multipole detections must be treated with caution, the metric is generally sound, with accuracy 72%, precision 67% (percentage of MEV detections that are also likelihood detections), specificity 75% (percentage of MEV non-detections that are also likelihood non-detections), and recall 59% (percentage of likelihood detections that are also MEV detections).

5.4.2 Parameter agreement within and between models

Figure 5.9 shows the differences between the parameters of the $m = 3$ and $m = 4$ multipoles recovered from the EPLγ+Multipole mass model and those from the light models (actual fit parameter values shown in Appendix Figures A.13 & A.14 and a comparison of the axis ratio and position angles in Appendix Figure A.15). What is immediately apparent from the Appendix figures is that the multipole shapes are often poorly or fully unconstrained at 3-sigma, spanning the whole range of available values (the figures have their angles 'wrapped' such that they continue through the angular symmetry of the multipole), and therefore the difference in shape between mass and light from Figure 5.9 is also unconstrained to 3-sigma. This unconstrained nature is also seen in the multipole

strengths and is particularly strong for the BELLS-GALLERY lenses in the light, as expected due to their low SNR, and for the SLACS lenses in the mass. This overall shows that whilst this study is a useful starting point for investigations into multipoles in strong lens galaxies, we require deeply imaged high-redshift lenses in order to make real progress. Shape agreements and disagreements will not be discussed in detail due to these large uninformative errorbars, however there are some lenses with small errors that disagree between mass and one or both light models at 3-sigma: BG-J0918, BG-J1201, SL-J0912 for s_3 and SL-J0912, SL-J1020, SL-J1032, SL-J1250 for s_4.

Regardless, if we do attempt to make parameter comparisons, we can see that the majority of lenses are consistent at 3-sigma between mass and light on their multipole strengths. In BELLS-GALLERY, taking only the 4 lenses with ellipses past the Einstein radius, the mass and radially constant light models agree in k_3 for all except for J1226, and in k_4 for all except J0856; the variable-multipole model agrees both in k_3 and k_4 for J0856 and J1110(28) but disagrees for both in J0201 or J1226. Obviously, it is difficult to draw conclusions from the BELLS-GALLERY lenses, however J0201 and J1226 have mass multipole detections, whilst J0856 and J1110(28) do not, with J0201 having light multipole detections in both models (from $m = 3$ in radially constant, $m = 4$ in radially variable model), J1110(28) in $m = 3$ from both models and J0856 and J1226 in neither. We outline this purely for informative purposes as there is no pattern to discern from only 4 lenses.

For a parameter comparison in the SLACS sample, there are 11 lenses that disagree at 3-sigma between the mass and radially constant light model in either k_3 or k_4, and 9 between the mass and radially the variable light model, however the magnitudes of this disagreement is generally of the order of $10^{-3}-10^{-4}$ past the edge of the 3-sigma boundary, compared to the order of the best-fit parameters of k_m being $\sim 10^{-2}-10^{-3}$, meaning non-negligible, but not worrying. The largest 3-sigma tensions are in the k_3 values for J0822, which has a 3-sigma tension of +0.032 for the constant model and +0.025 for the variable model - i.e. the mass model wants an $m = 3$ multipole much stronger than the light models. This is reflected in the fact that the lens has a mass multipole detection with

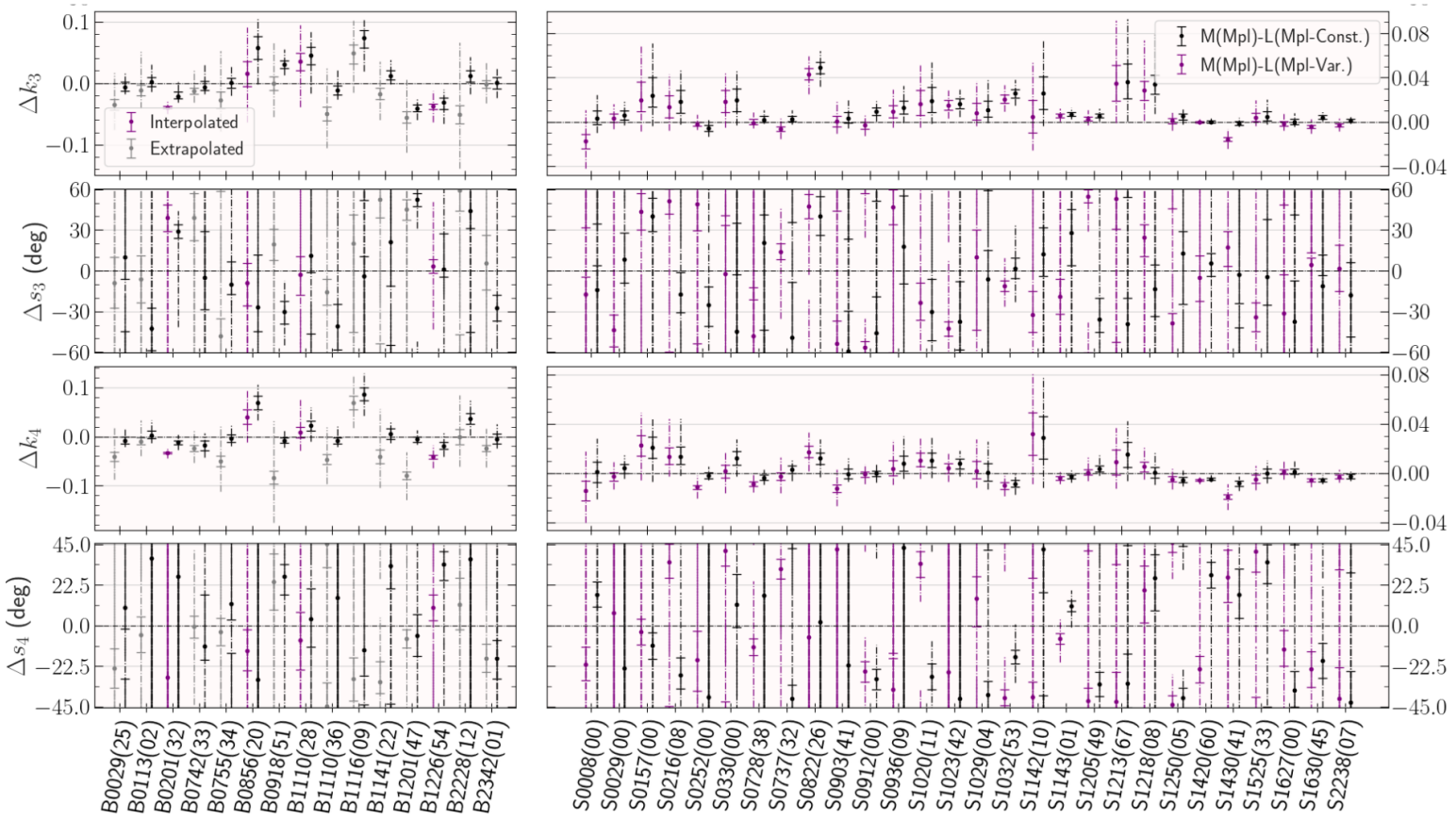

Figure 5.9: Differences in the fit $m = 3$ and $m = 4$ model parameters between the multipole-perturbed mass model $\mathcal{F}_{\rm MPL}$ (EPLγ+Multipole) and both multipole-perturbed light models (constant-multipole model $\mathcal{F}_3$ - black points, and variable-multipole model $\mathcal{F}_4$ - purple points). Positive values means that the mass model has a higher value for that parameter. Greyed-out BELLS-GALLERY lenses are those with no ellipses fit past the Einstein radius due to low SNR. Values for the radially-variable multipole model are interpolated at the Einstein radius. Angles are 'wrapped' to maintain continuity around angular symmetry points of ± 60 degrees for $m = 3$ and ± 45 degrees for $m = 4$. Solid errorbars with caps are 1-sigma, dot-dash errorbars are 3-sigma, solid errorbars with no caps spanning the whole y-axis for shape angles means that the 1-sigma error spans the whole available parameter space.

a very strong $m = 3$ multipole ($k_3 \sim 0.05$), $k_{3,\,\mathrm{min}} \sim 0.034$) as well as its strong $m = 4$ ($k_4 \sim 0.02$, $k_{4,\,\mathrm{min}} \sim 0.009$) but it has a radially-constant light model detection by virtue of *only* the $m = 4$ multipole ($k_4 \sim 0.01$, $k_{4,\,\mathrm{min}} \sim 0.008$). The majority of lenses shown here do not produce a multipole detection in both light and mass, but it remains true that discrepancies between mass and light in k_3 generally have the mass at a higher k_3 strength, whilst in k_4 the mass is generally at a lower strength, with this not being an offset caused by each other, since the lenses that disagree in one multipole generally still agree in the other. Only J0822, J1430 and J1630 have disagreements for both k_3 and k_4 between the mass and one of the light models, and only J1032 - our highly elliptical bulge-disk lens - has these 3-sigma tensions for *both* light models when compared to the mass model. This is a case where the mass model is less elliptical and has weaker $m = 4$ multipoles than the light (although it has stronger $m = 3$) which could indicate that mass to light mismatches could be generated when a strong stellar disk is formed whilst the dark matter halo remains more spherical (as is expected for a collisionless dark matter).

We can compare our results to the literature for other possible explanations for the mass-light mismatches. J0822 (the lens with the strongest 3-sigma tension) was discussed in Tessore et al. (2016) who struggled to fit the system using a smooth lens model, with this leaving a circular residual. The primary solution proposed for this system was the inclusion of a second source galaxy at a different redshift to the original, however the authors also suggested that the residual could be due to the galaxy having a mismatch between the mass and light profile centres (these were fixed to the same position). For our fit the mass model has much stronger multipoles than the light models and these cause the critical curve to take on a reasonably unphysical shape, which could possibly be explained by a secondary source - in fact our pixelized source reconstruction does produce two distinct sources but these are confined to the same redshift, whereas if the sources are actually at different redshifts this would cause a systematic error that could result in inflated multipole strengths as the mass model struggles to produce a reasonable fit. Regarding J1430, Eichner et al. (2012) specifically investigate this lens, decomposing the mass model into a stellar and dark component and finding that these components are likely aligned

with the same axis ratio. This agrees with our findings (Figure A.12) that the mass and light agree to 3-sigma except for the axis ratio in the radially variable light model, which is likely affected by the mass-light multipole disagreements. The cause of the multipole disagreement may be based in another finding of Eichner et al. (2012), which is that the lens model could not be fit with a mass model solely based on a stellar component, but rather it required a stellar+dark matter model, which gave a dark matter fraction within the Einstein radius of 20-40%. If a lens has a reasonably high dark matter fraction in its central regions, then mismatches between the stellar and total mass distributions may be expected. We can compare this to other lenses by using the best fit dark matter fractions within half of the effective radius from Auger et al. (2010) - regardless of the initial mass function, there are 5 other also from within our sample that have a dark matter fraction equal or higher than the J1430 fraction at half the effective radius of 0.63 (Chabrier IMF)/0.35 (Salpeter IMF). These lenses are J0216, J0912, J1143, J1205, J1525 and of these five lenses, three also have some form of disagreement between light and mass multipoles (specifically the k_3 strength) at 3-sigma, suggesting that a high dark matter fraction may make what could be natural/minor stellar-dark distribution mismatches more detectable. Obviously since the dark matter fraction is taken at the point of half the effective radius rather than at the Einstein radius, it is not an exact analogue, but the matching is expected to be close enough for an approximation.

5.4.3 Correlations in multipole strength

Please note that for all correlation discussions, only the 4 BELLS-GALLERY lenses with ellipses fit past the Einstein radius are included in any tests involving a light model or its variances. Tests that include only mass model parameters use all lenses (unless otherwise specified here or in Chapter 4).

Figure 5.10 shows comparisons within models of the k_3 and k_4 multipole strengths. The lower right panel also shows the variances of the multipole strength across the ellipses of

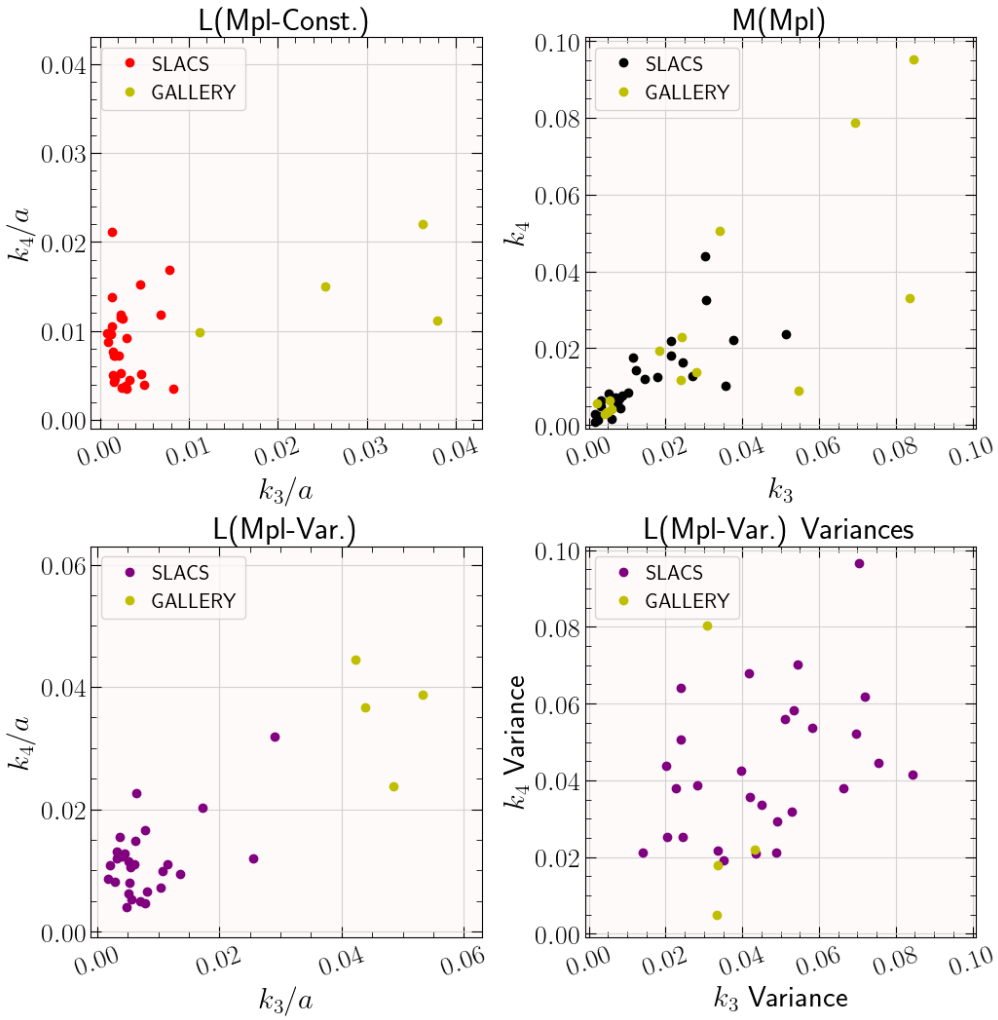

Figure 5.10: Comparison of k_3 and k_4 multipole strengths within each multipole perturbed model, as well as comparison of strength variance in the variable-multipole light model $\mathcal{F}_4$. The 'variance' is the maximum difference in best-fit k_m/a strength for all ellipses with major axes a from $0.5 - 3.0$ arcseconds. Each axis has an equal aspect ratio to aid comparison. The mass model comparison uses all BELLS-GALLERY lenses, but the light models take only the 4 lenses with light that extends past the Einstein radius. Correlations are quantified in Table 5.1.

the variable-multipole model $\mathcal{F}_4$, which are calculated in a similar manner to the ellipse angle and axis ratio variation seen in Chapter 4, Section 4.5.1.2 - the maximal difference in the best fit value of the k_m strength for all ellipses with semi-major axes $0.5 - 3.0$ arcseconds. These relationships are tested using the Pearson-r test to a significance level of $p = 0.05$, with the results shown in Table 5.1. We find highly significant evidence for strong correlations between k_3 and k_4 (if one multipole is strong, the other is likely to be

Sample	L(Mpl-Const.)	L(Mpl-Var.)	M(Mpl)	Variances
Full	$p = 0.012$ $c = 0.44$	$p = 6 \cdot 10^{-9}$ $c = 0.83$	$p = 1 \cdot 10^{-10}$ $c = 0.80$	$p = 0.053$ $c = N/A$
SLACS-only	$p = 0.91$ $c = N/A$	$p = 0.005$ $c = 0.51$	$p = 5 \cdot 10^{-6}$ $c = 0.75$	$p = 0.035$ $c = 0.40$
Mass-detected only	$p = 0.075$ $c = N/A$	$p = 8 \cdot 10^{-4}$ $c = 0.90$	$p = 1 \cdot 10^{-4}$ $c = 0.80$	$p = 0.039$ $c = 0.50$

Table 5.1: Results (p-values, p and linear correlation coefficients, c) from Pearson-r correlation tests comparing the strengths of the $m = 3$ and $m = 4$ multipoles within each of our three models. The fourth column adds a comparison of the variance in those multipole strengths within the variable-multipole light model. $p < 0.05$ means there is evidence for non-random correlation. Rows describe the test applied to the full sample (top), SLACS lenses only (middle) and lenses where multipoles are detected in the mass only (lower). The mass model comparison includes all BELLS-GALLERY lenses, but the light models take only the 4 lenses with light that extends past the Einstein radius. This table corresponds to Figure 5.10.

also) in both the mass model and the radially-variable multipole model, as well as evidence for a weak correlation between the variances of the multipole strengths across the ellipses of the radially-variable multipole model. Differently in the constant multipole light model, despite the p-value for the entire sample ($p = 0.012 < 0.05$) being significant, if we remove the BELLS-GALLERY lenses from the test and only test on the SLACS lenses, there is no longer any significant correlation found ($p > 0.9$), since most lenses fit a k_3/a strength in the radially constant light model of close to zero. This is another sign that we need a deeply imaged sample of high-redshift lens galaxies in order to apply this method properly and with confidence - although there is no reason why the multipole strengths *have* to be correlated for these lenses, and this could be a correct distribution, albeit the strong mass correlation indicates that this may not be the case.

Looking between models rather than within models however, we turn to Figure 5.11, which shows the comparison of (best-fit) multipole strength for each multipole order between each of the three models, and Table 5.2 which shows the results of the Pearson-r correlation tests. We see clearly that there is a strong correlation for each multipole between the light models, with $p \ll 0.05$, which lends support to the idea that the radially constant multipole model may be appropriate to fit the light around the Einstein radius, despite the instances

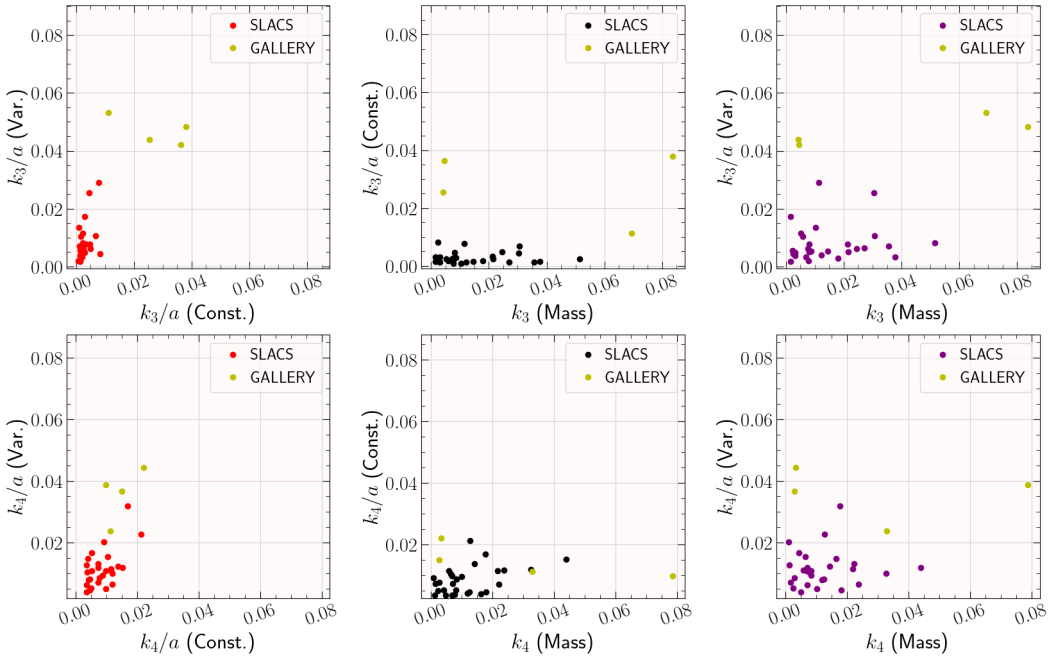

Figure 5.11: Comparisons of multipole strength between all three multipole-perturbed models $\mathcal{F}_3, \mathcal{F}_4, \mathcal{F}_{\text{MPL}}$. Top row is comparisons of k_3 and bottom row is k_4. Columns (left to right) are: constant-multipole to variable-multipole, constant-multipole to mass model, variable-multipole to mass model. All axes have the same, equal aspect ratio to aid comparison. Correlations are quantified in Table 5.2.

	L(Const.):L(Var.)		M(Mpl):L(Const.)		M(Mpl):L(Var.)	
Sample	k_3	k_4	k_3	k_4	k_3	k_4
Full	$p = 1 \cdot 10^{-8}$ $c = 0.82$	$p = 8 \cdot 10^{-5}$ $c = 0.65$	$p = 0.054$ $c = N/A$	$p = 0.29$ $c = N/A$	$p = 0.006$ $c = 0.47$	$p = 0.11$ $c = N/A$
SLACS-only	$p = 0.009$ $c = 0.48$	$p = 0.002$ $c = 0.56$	$p = 0.94$ $c = N/A$	$p = 0.017$ $c = 0.45$	$p = 0.61$ $c = N/A$	$p = 0.73$ $c = N/A$
Mass-detected only	$p = 2 \cdot 10^{-5}$ $c = 0.97$	$p = 0.008$ $c = 0.80$	$p = 0.14$ $c = N/A$	$p = 0.43$ $c = N/A$	$p = 0.18$ $c = N/A$	$p = 0.12$ $c = N/A$

Table 5.2: Results (p-values, p and linear correlation coefficients, c) from Pearson-r correlation tests comparing the strengths of the $m = 3$ and $m = 4$ multipoles *between* each of our three models. $p < 0.05$ means there is evidence for correlation. Rows describe the test applied to the full sample (top), SLACS lenses only (middle) and lenses where multipoles are detected in the mass only (lower). This table corresponds to Figure 5.11.

seen above where this model cannot match the k_3-k_4 correlations of the EPLγ+Multipole mass model or the radially variable light model. Regarding the correlations between the mass and light, we have already seen above in Section 5.4.2 that the mass and light do have some slight general disagreements. Despite this, for the k_3 strength, when using the entire

SLACS plus BELLS-GALLERY sample, we get p-values for moderate-weak correlation between the mass and the radially-variable light model, and for the k_4 strength, there is possible correlation between the mass and radially-constant multipole light model when looking at only the SLACS lenses. This means that there is hope for the matching of mass to light multipoles, depending on the sample.

5.4.4 Relationships between shear, multipoles and ellipse variance

Figure 5.12 shows the relationships between the magnitudes of the shears from the EPLγ+Multipole model and the multipole amplitudes. As a reminder, we have included all of the BELLS-GALLERY lenses in the mass model comparison, since this compares mass model to mass model parameters, and therefore needs no exclusion (however we only include the 4 BELLS-GALLERY lenses with light past the Einstein radius for the light models). If we apply Pearson-r correlation tests to these relationships, we find that all six relationships have evidence for moderate positive correlation, as seen in Table 5.3, meaning that the shear fit by the EPLγ+Multipole mass model for that lens is generally larger for those lenses that *also* fit large multipole amplitudes. The BELLS-GALLERY lenses are driving the majority of these correlations as for the SLACS-only sample only the k_4 mass strength is correlated to the magnitude of the shear, however it is still positively correlated, meaning that the mass models that fit higher shears also fit higher strength $m = 4$ multipoles. There may be some model systematic here with the model spuriously including either a higher shear or higher k_4 and then using the other to offset it, and more work is required on better quality and larger size datasets in order to understand if this is a genuine issue. We note that there are no correlations however between multipoles and shear if we take only the lenses which have multipoles detected in the mass, making it more plausible that the relationship between shear and k_4 in the mass of the SLACS lenses is a systematic modelling issue similar to that given by e.g. Etherington et al. (2024) for the external shear itself in not fitting what it is physically meant to - here the $m = 4$ multipole could be coupling with the shear to model some other physical attribute.

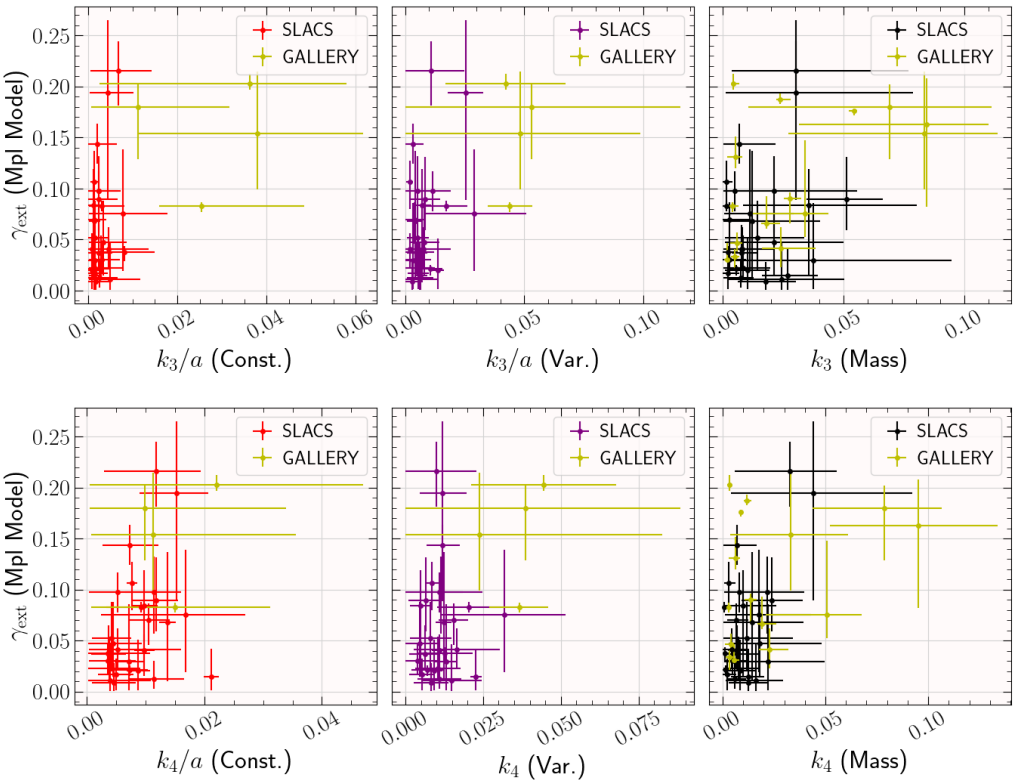

Figure 5.12: Magnitudes of the external shear from the EPLγ+Multipole model, compared to the multipole strengths from the EPLγ+Multipole mass model and the two multipole-perturbed light models. Errors shown are 3-sigma. Values for the variable-multipole light model are interpolated at the Einstein radius. Only the 4 BELLS-GALLERY lenses with light past the Einstein radius are included on the light plots, but all lenses are included on the right-hand column mass model plots.

	L(Mpl-Const.)		L(Mpl-Var.)		M(Mpl)	
Sample	k_3/a	k_4/a	k_3/a	k_4/a	k_3	k_4
Full	$p = 0.003$ $c = 0.51$	$p = 0.007$ $c = 0.47$	$p = 3 \cdot 10^{-4}$ $c = 0.59$	$p = 0.011$ $c = 0.45$	$p = 0.001$ $c = 0.47$	$p = 0.002$ $c = 0.46$
SLACS-only	$p = 0.13$ $c = N/A$	$p = 0.075$ $c = N/A$	$p = 0.050$ $c = N/A$	$p = 0.84$ $c = N/A$	$p = 0.17$ $c = N/A$	$p = 7 \cdot 10^{-4}$ $c = 0.60$

Table 5.3: Results (p-values, p and linear correlation coefficients, c) from Pearson-r correlation tests for the magnitude of the external shear from the EPLγ+Multipole model, to the multipole strengths of the multipole-perturbed mass and light models. $p < 0.05$ means there is evidence for non-random correlation. No positive results were found for the mass-detected-only sample, so this row is not shown.

A similar test of the external shear can be performed using Figure 5.13 and Table 5.4. Since multipoles are one possible answer to the questions posed from e.g. Etherington et al. (2024) where the lensing community asks whether internal complexity in the galaxy can artificially inflate the magnitudes of the inferred external shears, we would expect to see that the magnitude of shear generally goes down when stronger multipoles are applied. If we look at the correlation between the mass multipoles and the shear change however we see no discernable correlation. Despite this, there is a correlation between the shear change and the multipoles in the light models: for the radially constant light model there is a weak positive correlation with k_3, and for the radially variable light model there is a positive correlation with k_3 and a moderate positive correlation with k_4. This matches the previous conclusion that lenses with stronger multipoles may exhibit stronger shears, however the correlation is driven by the BELLS-GALLERY lenses, with no significant results found if they are removed from the sample. This also matches recent work by Hogg et al. (2025) who found that additions of $m = 4$ multipoles in models of SLACS lenses do not generally result in reductions to the external shear magnitude.

Another question is whether the multipoles will tend to compensate for features such as angular or elliptical variance. If they do we would expect those lenses with a high variance to have a larger multipole strength. As a reminder, angular variance is the maximal difference between the position angles of any two ellipses that have $q < 0.85$, and elliptical variance is the maximal difference in the axis ratio of any two ellipses, with the ellipses in the semi-major axis range $0.5 - 3.0$ arcseconds. These variances are taken from the variable ellipse model of Chapter 4, as described in Section 4.5.1.2, with outliers of angular variance$>$ 30 and elliptical variance > 0.3 removed also as per this Section. Looking at the light models (first two columns) of the lower two rows of Figure 5.13, and at Table 5.4, we see firstly that the k_3 of the constant-multipole model is moderately correlated ($p = 0.041, c = 0.43$) to the angular variance and secondly that the k_4 of the variable-multipole model is weakly correlated ($p = 0.049, c = 0.38$) to the elliptical variance. We also see strong correlations between the elliptical variance and both multipoles in the variable light model for those lenses with mass model multipole detections, although this

is driven apparently solely by the 4 BELLS-GALLERY lenses (when they are removed, neither multipole has a significant correlation). Overall this shows that variable angular or elliptical structures in a galaxy could possibly be modelled with a static non-varying multipole, however we require a larger, more deeply imaged sample to be confident in any conclusions drawn.

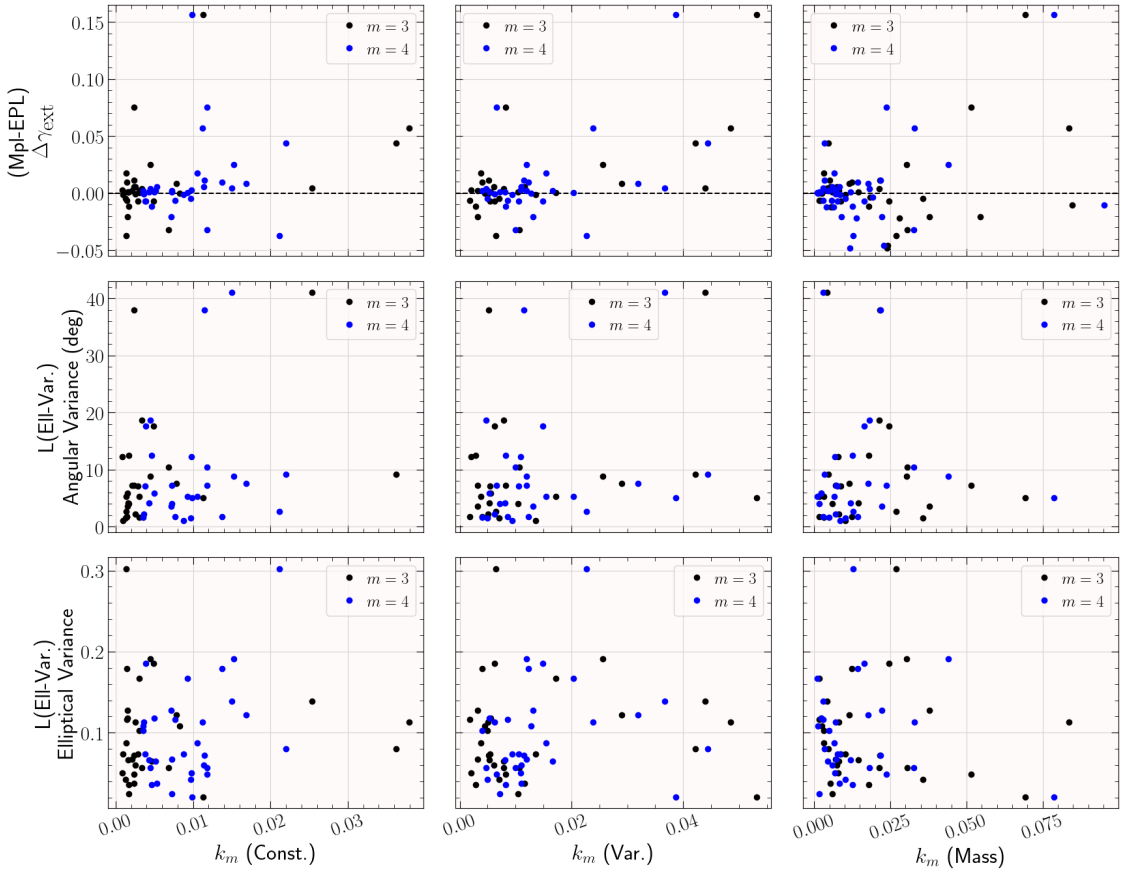

Figure 5.13: Comparisons between the multipole strengths of the three multipole-perturbed models and: 1. The change in external shear when going from the EPLγ to the EPLγ+Multipole mass model models (top panels). 2. The angular variance of the variable-ellipse model $\mathcal{F}_2$ from Chapter 4 (middle panels). 3. The elliptical variance of the variable-ellipse model $\mathcal{F}_2$ (lower panels). Dashed line in the upper panels marks $\Delta\gamma_{ext} = 0$ - positive (negative) values mean that the EPLγ+Multipole model has a larger (smaller) shear magnitude than the EPLγ model. Only best-fit values are shown and used without errors. Correlations are quantified in Table 5.4.

	Sample	L(Mpl-Const.) k_3/a	L(Mpl-Const.) k_4/a	L(Mpl-Var.) k_3/a	L(Mpl-Var.) k_4/a	M(Mpl) k_3	M(Mpl) k_4
$\Delta\gamma_{\rm ext}$	Full	$p = 0.028$ $c = 0.39$	$p = 0.36$ $c = N/A$	$p = 4 \cdot 10^{-5}$ $c = 0.66$	$p = 0.007$ $c = 0.46$	$p = 0.071$ $c = N/A$	$p = 0.10$ $c = N/A$
	SLACS-only	$p = 0.88$ $c = N/A$	$p = 0.80$ $c = N/A$	$p = 0.31$ $c = N/A$	$p = 0.44$ $c = N/A$	$p = 0.34$ $c = N/A$	$p = 0.43$ $c = N/A$
	Mass-detected only	$p = 0.45$ $c = N/A$	$p = 0.96$ $c = N/A$	$p = 0.51$ $c = N/A$	$p = 0.78$ $c = N/A$	$p = 0.86$ $c = N/A$	$p = 0.73$ $c = N/A$
Angular Variance	Full	$p = 0.34$ $c = N/A$	$p = 0.62$ $c = N/A$	$p = 0.81$ $c = N/A$	$p = 0.80$ $c = N/A$	$p = 0.63$ $c = N/A$	$p = 0.64$ $c = N/A$
	SLACS-only	$p = 0.042$ $c = 0.43$	$p = 0.40$ $c = N/A$	$p = 0.77$ $c = N/A$	$p = 0.91$ $c = N/A$	$p = 0.35$ $c = N/A$	$p = 0.10$ $c = N/A$
	Mass-detected only	$p = 0.59$ $c = N/A$	$p = 0.75$ $c = N/A$	$p = 0.72$ $c = N/A$	$p = 0.80$ $c = N/A$	$p = 0.35$ $c = N/A$	$p = 0.81$ $c = N/A$
Elliptical Variance	Full	$p = 0.53$ $c = N/A$	$p = 0.35$ $c = N/A$	$p = 0.68$ $c = N/A$	$p = 0.47$ $c = N/A$	$p = 0.54$ $c = N/A$	$p = 0.70$ $c = N/A$
	SLACS-only	$p = 0.21$ $c = N/A$	$p = 0.30$ $c = N/A$	$p = 0.13$ $c = N/A$	$p = 0.049$ $c = 0.38$	$p = 0.85$ $c = N/A$	$p = 0.25$ $c = N/A$
	Mass-detected only	$p = 0.059$ $c = N/A$	$p = 0.21$ $c = N/A$	$p = 0.014$ $c = 0.82$	$p = 0.028$ $c = 0.76$	$p = 0.15$ $c = N/A$	$p = 0.31$ $c = N/A$

Table 5.4: Results (p-values, p and linear correlation coefficients, c) from Pearson-r correlation tests comparing the strengths of the $m = 3$ and $m = 4$ multipoles in each of our three models to: 1. The change in external shear going from the EPLγ to EPLγ+Multipole mass models (top 3 rows); 2. The angular variance from the variable-ellipse fits of Chapter 4 (middle 3 rows); 3. The elliptical variance from the variable-ellipse fits of Chapter 4 (bottom 3 rows). $p < 0.05$ means there is evidence for non-random correlation. Rows within each set of 3 describe the test applied to the full sample (top), SLACS lenses only (middle) and lenses where multipoles are detected in the mass only (lower). This table corresponds to Figure 5.13.

5.5 Conclusions

We have demonstrated a key issue in this work regarding the study of multipoles in lens galaxies, which is that multipoles are more often detected in the mass if the lens redshift is higher, and since these galaxies often have lower lens light SNR due to their distance, we will likely require a new sample of intermediate or high-redshift lens galaxies ($z_{\rm lens} \gtrsim 0.5$) with deep imaging, in order to draw significant and confident conclusions on the relationship between multipoles in lens galaxy mass and light. The Euclid space telescope is on track to deliver over 100,000 strong lenses over 6 years (Lines et al., 2025), and whilst many lenses will likely have low lens light SNR due to the wide nature of the survey, the sheer volume of lenses will mean that many usable lenses with SLACS-like lens light strength should still be found. One caveat of Euclid is that its PSF FWHM of is over twice as wide as HST, and over 5 times as wide as JWST NIRCam (Walmsley et al., 2025) at $\sim 0.16^{"}$ (VIS 700nm), meaning that the innermost ellipses fit in this work at $0.25^{"}$ would not be applicable, nor would small structure perturbations on that scale. JWST lenses (which will be fewer in number but more deeply imaged) such as those from `COWLS` (Mahler et al., 2025) may be a better source of lenses to extend the current sample, along with other existing HST samples such as `SL2S` (Gavazzi et al., 2012).

We have discussed some possible reasons for mismatches in the mass and light multipoles of lens galaxies:

- The dark matter halos of galaxies may not form as strong a disk structure as the most elliptical and disky stellar distributions as in J1032+5322. Simulations (e.g. Emami et al., 2021) have shown that the dark halo can be influenced to align with the baryonic disk, so an investigation would be needed to test at what point this breaks down or how quickly the halo responds.
- A high dark matter fraction in the central (lensing-sensitive) region of the galaxy will make natural dark-stellar mismatches more detectable. Mukherjee et al. (2021) showed that SLACS dark matter fractions matched those of simulations, so with the

release of new suites of hydrodynamical simulations (e.g. COLIBRE: Schaye et al., 2025) probing to smaller and smaller mass scales, we should be able to investigate in simulated galaxies with high central dark matter fractions whether these also have complex angular structures and mass-light mismatches.

- There is a correlation ($p = 1 \cdot 10^{-4}$, $c = 0.60$) between the $m = 4$ multipole strength and the magnitude of the external shear in the mass models of the SLACS galaxies. It is unknown if this is a systematic error where the two components simply offset each other, however there is no significant correlation found using only those lenses with actual multipole detections (i.e. where the likelihood favours a multipole) which supports this theory. A wider sample is required here to achieve many more mass model multipole detections to ensure there is no effect from low number statistics.

A summary of the other primary conclusions for this Chapter is below:

- There are cases where multipoles are detected in the light of SLACS lenses but not their mass, however it is unclear whether this is a failure of the light modelling or of the mass modelling (or indeed a true mismatch).
- Multipoles are not frequently detected in the mass of SLACS or the light of BELLS-GALLERY lenses, and as such, their shapes are frequently unconstrained, spanning the entire error range at 3-sigma.
- When light and mass multipole strengths are in 3-sigma tension, it is generally the k_3 of the mass being greater than the light, or the k_4 of the *light* being greater than the mass.
- Only J1032+5322, one of the most highly elliptical bulge-disk-like systems, is in full 3-sigma tension for multipole strengths between the mass model and both a radially constant and radially-variable multipole light model.
- We detect multipoles in the light of 2 out of 10 BELLS-GALLERY lenses that have mass detections, and 6 out of 7 SLACS lenses that have mass detections (J0157 being the only SLACS lens where we detect in mass but not light).

- There is evidence for strong correlation (in all subsamples) between the k_3 and k_4 multipole strengths within the EPLγ+Multipole mass model ($p = 1 \cdot 10^{-10}, c = 0.80$), and within the radially variable light model ($p = 6 \cdot 10^{-9}, c = 0.83$). There is moderate correlation ($p = 0.012, c = 0.44$) between these parameters in the radially constant light model using the full sample but there is no evidence for correlation in this model if only the SLACS lenses are sampled or if only the lenses which have mass multipole detections are sampled.

- There is evidence for strong correlation for both the k_3 and the k_4 multipole strengths when compared between the light models ($p = 1 \cdot 10^{-8}, c = 0.82$ for k_3 and $p = 8 \cdot 10^{-5}, c = 0.65$ for k_4). This implies that a model that does not vary multipoles with distance from the centre is a reasonable approximant (at the Einstein radius) to a model that does allow for radial variations in the multipoles. There is also evidence for correlation in the k_4 multipole strength when only looking at the SLACS lenses, between the radially constant light model and the EPLγ+Multipole mass model ($p = 0.017, c = 0.45$), meaning that there is the potential for light multipoles to successfully inform about mass multipoles.

- There is no evidence for correlation between the mass model multipole strengths and the change in external shear when going from the EPLγ to the EPLγ+Multipole mass model, in agreement with Hogg et al. (2025).

- There is some evidence for correlation when only looking at SLACS lenses, between the k_3/a strength in the constant-multipole light model, and the angular variance in the variable smooth-ellipse model from Chapter 4 ($p = 0.042, c = 0.43$), as well as between the k_4/a strength from the variable-multipole model and the elliptical variance ($p = 0.049, c = 0.38$).

Chapter 6

Summary and Conclusions

Returning to the beginning of this Thesis, the overarching aim of the studies brought together here is to refine our understanding of galaxy-scale strong lensing, specifically the modelling techniques we can use and the true underlying mass distributions of the main lens deflectors, in order to detect (with confidence) dark matter substructures and thus constrain the nature of dark matter through the subhalo mass function. New strong lens surveys such as `COWLS` (Mahler et al., 2025) from JWST, and the expected influx of lenses from Euclid (e.g. Collett, 2015; Lines et al., 2025) and other sources will provide the sample size required to start drawing statistical conclusions on the distribution of subhalo mass function, based on the number of detections of dark substructures or the non-detection of substructures we would expect to be sensitive to if they were there (e.g. Vegetti et al., 2014; Gilman et al., 2020; O'Riordan et al., 2023).

This thesis developed through the various stages that we as lens modellers will have to undertake before being able to draw dark matter inferences. In Chapter 3, we attempted to use data from JWST, a (relatively) new telescope that will provide higher-SNR and higher-redshift lenses than in the samples of the previous decades (e.g. Bolton et al., 2006; Brownstein et al., 2011; Shu et al., 2016a). The modelling and investigation of two new lenses was intended to be a reasonably quick project, given that the lenses were released as part of the Early Release Science program of JWST (Rigby et al., 2024), however, as modelling techniques developed, the problem that this entire thesis now addresses became

apparent - that of angular complexity in the main deflector, and the question of how we should be modelling it alongside dark substructures (Lange et al., 2025). We saw in Chapter 3, that we draw different conclusions about the existence and nature of a dark substructure in SPT2147-50 based upon whether or not we include angular complexity in the form of multipoles in the main deflector mass model, with the conclusions even varying based on which combinations of multipole order were applied. With very little information in the literature that we can use to constrain our expectations (priors) on the types and strengths of multipoles in the mass of lens galaxies (which have a specific selection function (e.g. Sonnenfeld et al., 2023) meaning we cannot just take information from the wider study of galaxy multipoles), we had to devise a bayesian trade-off for Chapter 3 where we did not search for specifically substructure, but rather, the combination of multipoles with or without substructure that would give the most consistent increase in Bayesian Evidence across multiple filter images of the same system, since we were not able to define the extent to which a substructure and multipole could be degenerate, other than to say that the degeneracy exists (O'Riordan et al., 2024). Despite the setbacks, we concluded in Chapter 3 that the best mass model for SPT2147-50 (in a bayesian sense) was an elliptical power-law perturbed by order 1 and 4 multipoles, in addition to external shear and a dark substructure (EPLγ+M1+M4+Subhalo), which was a major find, given that until recently only two dark substructures had been confidently detected and reproduced using strong lensing (Vegetti et al., 2010, 2012). We held short however in the work presented in Chapter 3 in announcing a new subhalo detection, due to the uncertainty provided by the unknown degeneracy between multipoles and substructure. Use of data from other sources such as ALMA, which probes a different aspect of the source and does not have the complication of observing lens light (as it is a much lower wavelength observation) will help to check if the result is reproducible. Re-modelling using alternative dark matter profiles and freeing the concentration of the subhalo is also required, along with the calculation of a sensitivity function and the application of non-parametric potential correction.

The requirements generated by Chapter 3 to better understand the angular complexity of lens galaxies in context, lead directly to the work presented in Chapters 4 & 5. Instead

of solely focusing on multipoles, the decision was taken to investigate angular complexity in the broader sense, as well as the general suitability of the EPLγ model in relation to matching the lens mass and light distributions. In Chapter 4, we start by investigating simpler models, not touching the idea of multipoles at all, by fitting the EPLγ mass model to galaxies from the SLACS (Bolton et al., 2008a) and BELLS-GALLERY (Shu et al., 2016b) samples, and fitting the isophotes of the lens galaxy light through ellipse fitting. We enabled the two-pronged investigation into light-mass agreement and angular complexity by fitting two light models using these ellipses, one where the ellipses had consistant parameters at various major-axes (a direct comparison to the EPL which fits a single set of mass model parameters to the entire mass distribution), and one where the ellipse parameters could vary at different major axis values, which could capture variations of angle and ellipticity in the light distribution. There was generally good agreement found between the parameters of the constant-parameter light model and mass model, leading to the conclusion that the light and mass traced each other in a reasonably consistent manner. Furthermore, operating under the assumption that strong lensing is only sensitive to mass within the Einstein radius, and that the primary constraints on the mass model parameters come from the mass distribution at or near the Einstein radius, we tested whether the two light models agree by comparing the constant-parameter model to the parameters of the variable model at the Einstein radius of each lens. From this we found that there is generally good agreement between the models, implying that actually, the EPLγ model may be reasonably appropriate to apply as a mass model for the types of lenses found in these (primarily the SLACS) samples, at least with regards to multiple-power law models or piecewise Gaussian expansion models of the mass distribution. An additional investigation was to test for any relationships between the external shear from the mass model, and either radial variance in the lens light (Chapter 4) or multipole strength in the lens mass (Chapter 5). The external shear has been investigated (e.g. Etherington et al., 2024) under the suspicion that strong lens models are actually using the shear (increasing its magnitude or changing its orientation) to account for missing complexity in the main deflector mass distribution, rather than (or as well as) modelling the actual

shearing effects of line-of-sight mass overdensities. Based on Treu et al. (2008) setting an expected maximal shear requirement for the SLACS lenses around 0.05, we discovered in Chapter 4 that there is a strong correlation between shears with magnitudes above this limit, and the angular variance of the ellipses fit in the radially-variable ellipse light model.

Having discovered that we can efficiently investigate the EPL and make comparisons of the mass to light of strong lenses in Chapter 4, we moved on to the work of Chapter 5, where we hoped to answer directly some of the questions posed from Chapter 3 regarding multipoles, testing again a mass model (this time EPLγ+Multipole) against radially-constant and radially-variable multipole-perturbed light models. What we found however was primarily that the lenses that we have were not suitable to test multipoles on a wide-scale, with the SLACS lens galaxies generally not detecting multipoles in the mass, and the BELLS-GALLERY lens galaxies being too low SNR to apply any meaningful sample-wide constraints on the multipoles in light, despite there being many strong detections of multipoles in the lens mass models. We do however find that models with stronger $m = 3$ multipoles usually also fit stronger $m = 4$ multipoles. We also saw that there is possible evidence that the mass and light agree on which lenses require stronger $m = 4$ multipoles (i.e. k_4 is correlated between the mass model and constant-parameter light model), but that there are still many tensions between the recovered parameters from the mass and light models, and having so few detections of multipoles it is too difficult to tell what is genuine and what may be modelling uncertainty. We also discussed the origins of offsets in the complexity of the mass and light models (with regards to multipoles), showing that these could be linked to extreme stellar disks where the dark halo may not follow the baryonic distribution as strongly, or increased central dark matter fractions making natural mismatches more detectable, and that this should be testable in new simulations such as `COLIBRE` (Schaye et al., 2025). We also showed however that there was a link between the strength of the external shear and the strength of the $m = 4$ multipole, which could indicate a systematic modelling error. We also found no correlations in Chapter 5 between multipole strength and a decrease in shear between the EPLγ and EPLγ+Multipole models which is in agreement with the literature, although we leave this open to be re-tested with

future samples.

Overall therefore, the work in this Thesis beings together the aims and setbacks that are applicable to most astronomers that use strong lensing with the goal of constraining dark matter - specifically that if we wish to confidently model dark substructures in the lensing mass, we must first understand the expected mass distributions of the main deflectors. Future studies are required, both using simulations to understand the link between dark and stellar components in the centres of galaxies, and using new lens samples to repeat and extend the investigations performed in Chapter 4 and especially Chapter 5. The hundreds of thousands of new strong lenses expected from Euclid (Collett, 2015) may not be quite as useful to this work due to the wide Euclid PSF compared to HST and especially JWST (0.16", 0.07" and 0.03" respectively Walmsley et al., 2025) and shallower imaging required of a wide-field survey, however this sample size will provide an excellent statistical overview of the mass model parameters of strong lenses even if it cannot provide on their light models. A sample of lenses this size will help to answer some of the questions posed regarding correlations of parameters within the mass model in Chapters 4 & 5, as well as provide an empirical prior to be placed on multipole amplitudes, as was shown to be needed in Chapter 3. For a continuation of the work directly comparing mass to light however, smaller samples that are able to achieve the specific conditions we require (intermediate redshift lenses with deep imaging) will be the best option. These samples are likely to come from JWST (e.g. `COWLS`: Mahler et al., 2025) and will allow us to (hopefully) directly compare multipoles (or other complexity) detected in the mass and the light so that we at least double our sample in the near future.

Whilst this Thesis provides good results and shows both the power of strong lensing (Chapter 3) and the success of techniques used to compare lens galaxy mass and light (Chapter 4), it can hopefully be used to motivate many further studies based on these successes and utilising the information on the current limitations in this field, in order to assuredly refine our understanding of lens galaxy structure, thereby allowing us to more confidently model dark substructures and constrain the subhalo mass function such that we may constrain also the nature of the dark matter particle.

Appendix A

A.1 Chapter 1 Appendix

There is no content appended for Chapter 1.

A.2 Chapter 2 Appendix

A.2.1 Examples of circular critical curves perturbed by multipoles and shear

Figure A.1 shows a simple example of the effects on the lensing of a simple Sersic-light source of the first 4 multipole orders when added to a circular Power-Law mass distribution with slope $\gamma_{\rm lens} = 2.1$. Note that we demonstrate a multipole strength of 0.1 for $m = 1$ and 0.05 for $m = 3, m = 4$ as the $m = 1$ multipole requires a greater strength to produce its effects (Amvrosiadis et al., 2025b). Also note that in these perfect systems the multipole perturbation creates $2m$ multiple images, however, if we added noise, lens light and source complexity, some of these multiple images will blur back into the Einstein ring based on the system configuration.

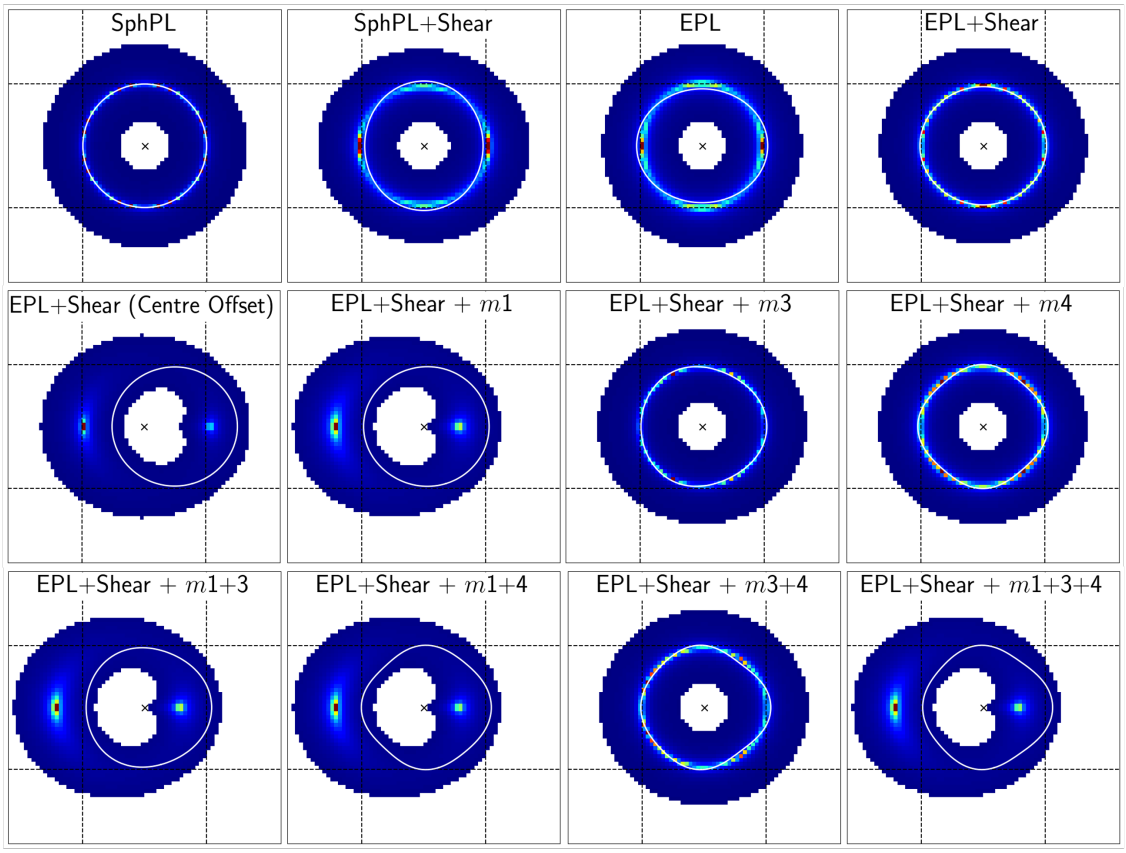

Figure A.1: A simple system (circular sersic source at $z = 4$ perfectly aligned with circular Power-Law mass, slope=2.1, $z = 0.5$), showing the effects of changes to centre ($\Delta x = +0.5$arcsec), mass ellipticity ($q = 0.85$), addition of external shear ($\gamma_{\rm ext} = 0.05$), and addition of multipole perturbations of order $m = 1, 3, 4$ with strengths $k_m = 0.05, 0.01, 0.01$. The image is a noiseless image, the white lines represent the lensing critical curves, and the dashed lines are drawn for reference at ± 1 arcsec, with the origin marked with the black cross. Shear angle, position angle and multipole angles in the mocks are all set to zero (aligned with positive x-axis).

A.3 Chapter 3 Appendix

A.3.1 Additional fit parameter plots

We show here first the parameters from the finalised fits in each filter for the subhalo models of SPT2147 in Figure A.2, with the prime M1+M4 model highlighted. Most parameters are consistent between filters within a model, but there are some 3σ tensions, including importantly f277W-f356W position angle tension in the primary M1+M4 model. Additional tensions beyond 3σ are: f356W-f444W tension in the Einstein radius for the Base model; f277W-f444W tension in the position angle for the Base model, and f277W-f356W position angle tension in M4, (M1+M4), M3+M4 and M1+M3+M4 models; f277W-f356W tension in the shear angle for the M1+M3+M4 model.

Next, in figure A.3 we show the change in the parameters of the fits from before adding a subhalo to after this addition, with the prime M1+M4 model highlighted. We draw solid lines at zero to show the lines of no change - errors are the quadrature sum of the parameter 3σ errors from the fits before and after and if errorbars cross the zero-line, the parameter change is consistent with zero. There are some non-zero-consistent parameters, but all M1+M4 prime model parameters are consistent before and after the subhalo addition, excepting a small negative change in the f356W model for the M4 angle. Parameters with changes outside of zero are: f444W Base and f356W M3+M4 positive change of centre x position; f277W, f356W, f444W Base, f356W M4, f356W M3+M4, f444W M1+M3+M4 decrease in Einstein radius; f277W Base increase and f356W M3+M4 decrease in position angle; f444W Base and f444W M1+M3+M4 decrease in power-law slope; f444W Base decrease in shear magnitude; f356W M3+M4 increase in shear angle; f444W M1+M3 decrease in M1 strength, f356W M3+M4 increase in M3 strength; f356W M4 and f356W M1+M4 decrease in M4 angle.

We also show in Table A.1 specific values for the $\Delta\log(\mathcal{E})$ evidence changes, maximal normalised residuals from the fits, and multipole strengths, for all the models fit both with and without the subhalo.

We finally show in figure A.4 the parameters for the fits to SPT0418. We recall that no multipole models provide a high enough evidence increase to be worth using, so the prime model here is the Base model. The position angles for the f356W fits are unconstrained (errors span the whole range), since to the high axis ratio ($q = 1$) implies a circular system therefore the position angle has no physical meaning at this point. Shear angles are generally inconsistent between the f356W and f444W filters within a model, with f444W being higher. All other parameters are fully consistent between all models and filters, which is expected when all models have a similar bayesian evidence. All multipole strengths reach down very close to zero with their errorbars, again showing that the multipole models are not required for this lens.

Filter	Model	PRE-sub $\Delta\log(\mathcal{E})$ (to Base)	PRE-sub Max Norm. Residual (σ)	PRE-sub Multipole Strengths ($k_m * 10^{-2}$)			WITH-sub $\Delta\log(\mathcal{E})$ (to Previous)	WITH-sub Max Norm. Residual (σ)	WITH-sub Multipole Strengths ($k_m * 10^{-2}$)		
				m1	**m3**	**m4**			**m1**	**m3**	**m4**
f444W	Base	-	3.58	-	-	-	56.90	3.59	-	-	-
f444W	M1	2.36	3.67	4.98	-	-	55.83	3.71	3.94	-	-
f444W	M3	21.81	3.63	-	0.94	-	28.98	3.60	-	0.29	-
f444W	M4	43.13	3.66	-	-	1.48	12.15	3.59	-	-	1.11
f444W	M1+3	48.16	3.73	9.52	0.94	-	13.36	3.74	6.79	0.54	-
f444W	M1+4	46.99	3.59	2.81	-	1.41	10.97	3.50	2.96	-	0.80
f444W	M3+4	38.01	3.58	-	0.57	0.98	13.03	3.54	-	0.29	0.90
f444W	M1+3+4	45.19	3.59	2.43	0.49	1.10	9.68	3.75	5.23	0.36	0.46
f356W	Base	-	3.83	-	-	-	25.70	3.77	-	-	-
f356W	M1	10.66	3.94	5.99	-	-	28.77	4.05	4.87	-	-
f356W	M3	4.79	3.80	-	0.67	-	40.99	3.87	-	1.34	-
f356W	M4	24.31	3.88	-	-	0.92	15.57	3.76	-	-	0.62
f356W	M1+3	38.69	4.04	8.11	0.84	-	2.04	3.99	7.30	1.04	-
f356W	M1+4	35.04	4.08	5.97	-	0.76	9.96	4.06	3.97	-	0.43
f356W	M3+4	18.61	3.85	-	0.31	0.96	22.40	3.87	-	1.05	0.61
f356W	M1+3+4	33.54	4.08	7.62	0.62	0.30	7.31	4.03	6.78	1.21	0.44
f277W	Base	-	3.47	-	-	-	19.84	3.49	-	-	-
f277W	M1	4.10	3.48	5.30	-	-	13.82	3.49	3.51	-	-
f277W	M3	5.68	3.44	-	1.72	-	10.58	3.47	-	1.37	-
f277W	M4	16.29	3.72	-	-	1.18	4.25	3.46	-	-	0.87
f277W	M1+3	12.99	3.45	9.00	1.33	-	6.78	3.48	5.67	1.63	-
f277W	M1+4	16.39	3.56	3.58	-	1.20	2.07	3.47	2.31	-	0.88
f277W	M3+4	11.23	3.51	-	0.46	1.10	4.35	3.72	-	0.57	1.00
f277W	M1+3+4	12.05	3.55	4.12	0.54	1.00	-0.99	3.49	3.99	0.57	0.99

Table A.1: Evidence boosts, maximum normalised residuals, and multipole strengths for SPT2147 over all models both with and without the addition of a Subhalo. All multipole 'pre-sub' evidences are compared to the Base 'pre-sub' evidence. All 'post-sub' evidences are compared to the corresponding model without a subhalo.

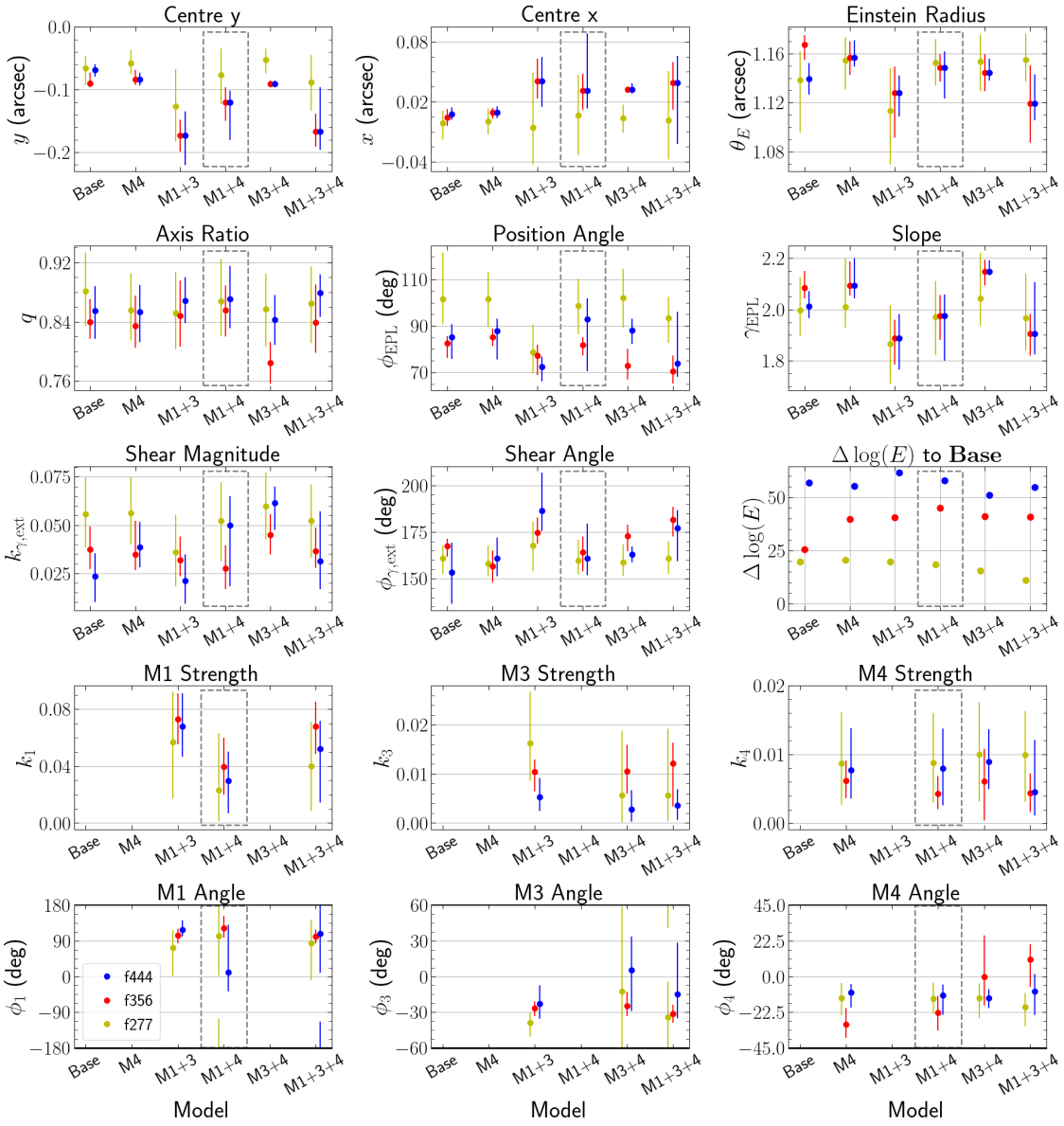

Figure A.2: Reported parameters and associated errors for the fits after adding a subhalo to the highest evidence macro-models in SPT2147-50, as well as the Base model. $\Delta\log(\mathcal{E})$ shown here is the total difference to the Base no-subhalo model. Multipole angles have a symmetry through $360/n$ - i.e. a 90 degree error on the M4 multipole means it is unconstrained as this multipole has rotational symmetry through 90 degrees, and so the errors are wrapped around $\pm(360/n)/2$. Evidence changes shown are in comparison to the Base EPLγ model. We highlight with the gray box our preferred final model of EPLγ+M1+M4.

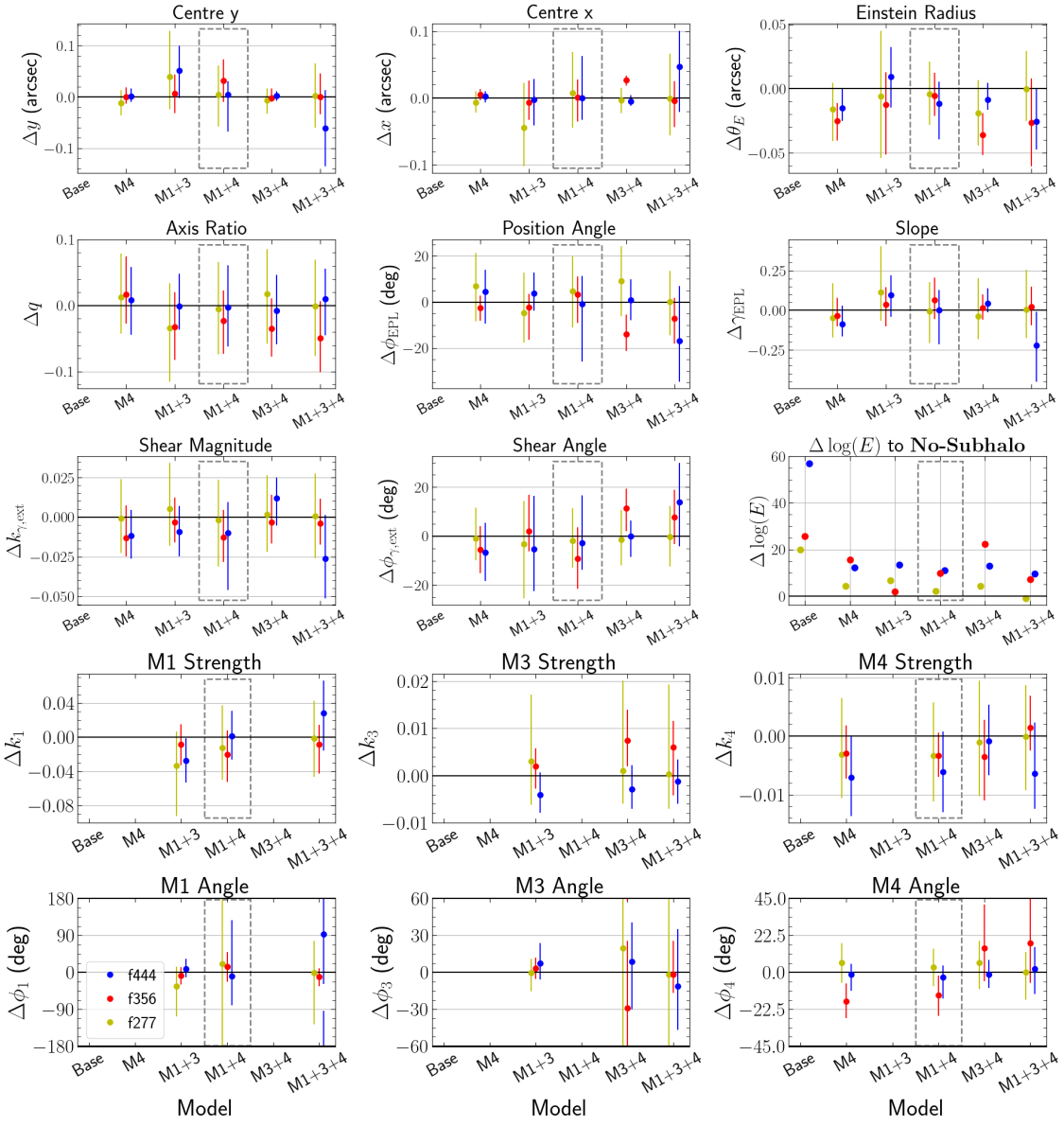

Figure A.3: Changes in the mass macro-model parameters for SPT2147-50 once we add a substructure, as well as the associated error on the change. Solid lines are drawn at a change of 0. Multipole angles have a symmetry through $360/n$ - i.e. a 90 degree error on the M4 multipole means it is unconstrained as this multipole has rotational symmetry through 90 degrees, and so the errors are wrapped around $\pm(360/n)/2$. Evidence changes shown are the total difference to the Base no-subhalo model. We highlight with the gray box our preferred final model of EPLγ+M1+M4.

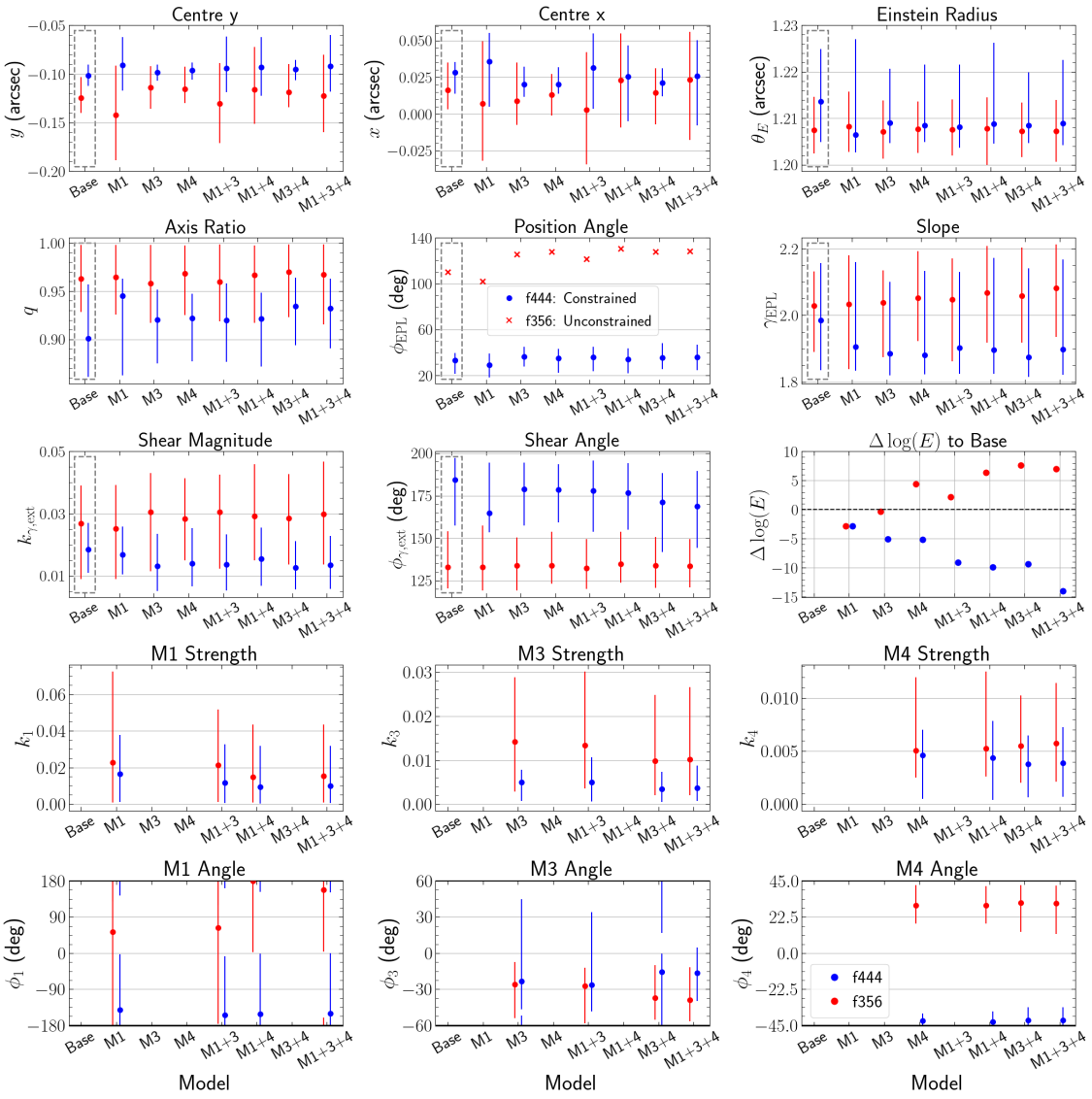

Figure A.4: Reported parameters and associated errors for all fits (without a subhalo) to SPT0418-47. Multipole angles have a symmetry through $360/n$ - i.e. a 90 degree error on the M4 multipole means it is unconstrained as this multipole has rotational symmetry through 90 degrees, and so the errors are wrapped around $\pm(360/n)/2$. Evidence changes shown are in comparison to the Base EPLγ model. We highlight with the gray box our preferred final model (Base). The position angles in f356W show only the median value as the errors span the full parameter space leaving this angle unconstrained - this is due to the highly circular axis ratio.

A.4 Chapter 4 Appendix

A.4.1 Dangers of using the Gaussian process to extrapolate data

Figure A.5 shows two panels of Gaussian processing that is performed on the variable-ellipse model $\mathcal{F}_2$ (see Sections 4.3.4.1 & 4.3.5.3). These interpolations are performed on two of the BELLS-GALLERY lenses and show the weaknesses of this method when applied in this manner. Firstly, the upper panel shows the interpolation of the axis ratio, q, of J0201+3228. This panel shows that, whilst the interpolation method works fine on actual data points, it fails to interpolate variable errors properly - we see that where the errors start to vary around $a = 1.5$, the process cannot cope and makes the variability in the interpolation too extreme. There are two concerning items to note here - first is that this extreme disagreement in interpolation to actual errors occurs at the Einstein radius, meaning that all our results for this lens will be skewed by underestimated errors; secondly, the upper error actually falls below the data line just past $a = 1.75$, which is clear sign that the process is not behaving as intended. Whilst there are checks in place to ensure that errors are reset to zero and the actual interpolated values never get used, only fed into a Monte Carlo draw around the Einstein radius, this is still a sign that the method (possibly the Gaussian kernel) needs to be adjusted to better cope with high variability.

The lower panel of Figure A.5 shows the interpolation and attempted extrapolation of the position angle of another BELLS-GALLERY lens, J0918+5104. In this case, the interpolation of errors is better (although far from perfect) compared to J0201, however we can see that the model defaults all values to zero past the final data point at $a = 1$, rather than interpolating them. This is why we ignore the results for the variable-ellipse model from the BELLS-GALLERY lenses that do not have data points beyond the Einstein radius.

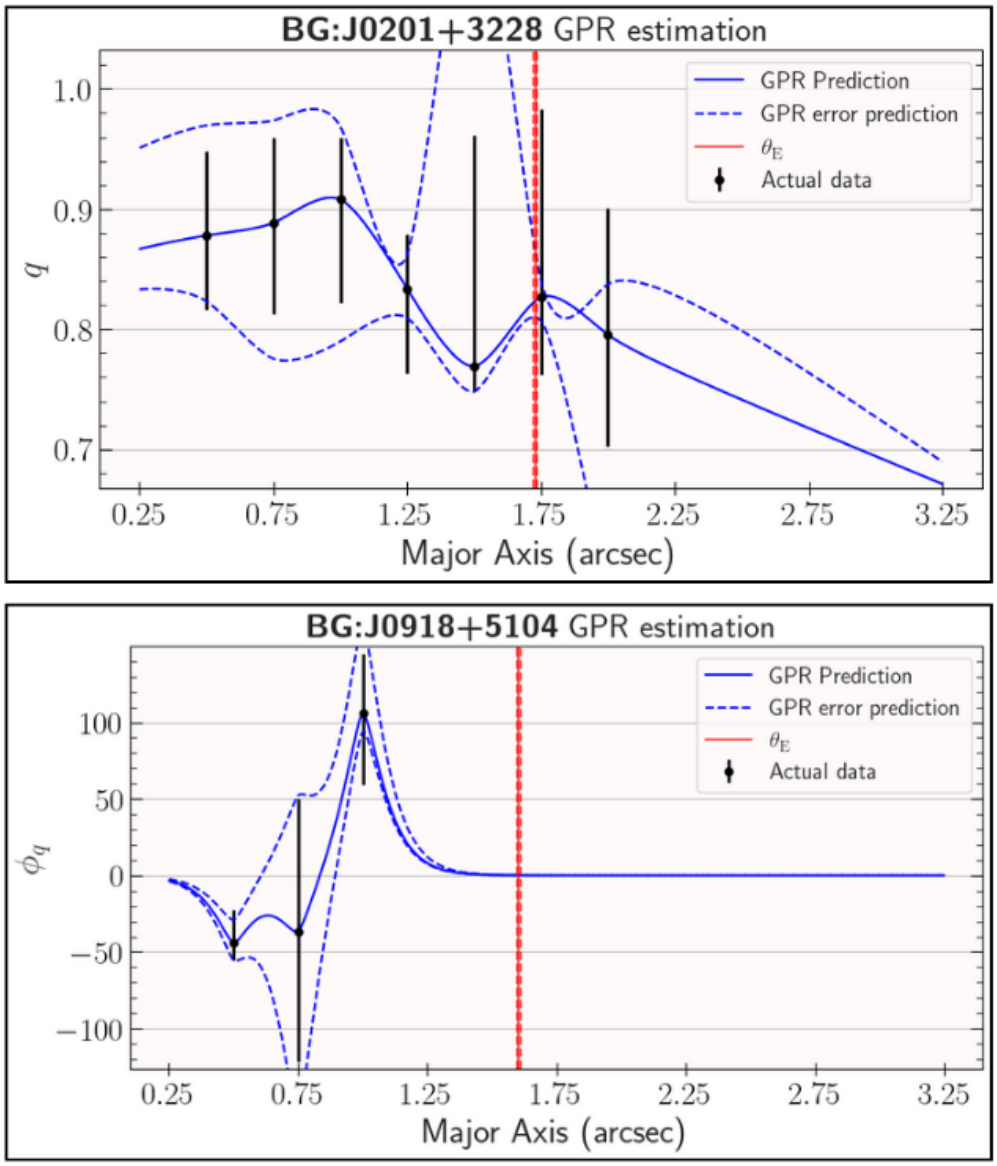

Figure A.5: An example of the Gaussian process interpolation and extrapolation (Section 4.3.4.1) on the variable ellipse model $\mathcal{F}_2$ fit to BELLS-GALLERY lenses J0201+3228 (axis ratio - upper panel), and J0918+5104 (position angle - lower panel). Both are examples are drawbacks in the Gaussian processing - J0201 due to the inconsistent errors and J0918 due to the failure to extrapolate.

A.4.2 Additional plots for Chapter 4

In this section we present a range of plots that may be informative to the reader, but would cause too much clutter to be included in the main body of the text. These plots generally require no further explanation than their captions, providing the relevant main body section has been read. We present the following:

- Parameter summaries of two extra lenses (J1029+0420 - Figure A.7 and J1420+6019 - Figure A.8) for the fitting of the EPLγ and smooth ellipse models. For an explanation of the parameter plots, see Section 4.3.5.4.
- Plots showing the $\Delta\chi^2_\nu$ between the light models (Figure A.9) and comparing these to the angular and elliptical variances in the variable-ellipse model (Figure A.6). These plots have not been scaled to remove those points with outlying $\Delta\chi^2_\nu$, unlike the ones in the main body which cut these outlying points off.
- Plots showing the recovered angular and elliptical variances (Figure A.10) and the recovered axis ratio and position angle (Figure A.11) for each lens in the sample.

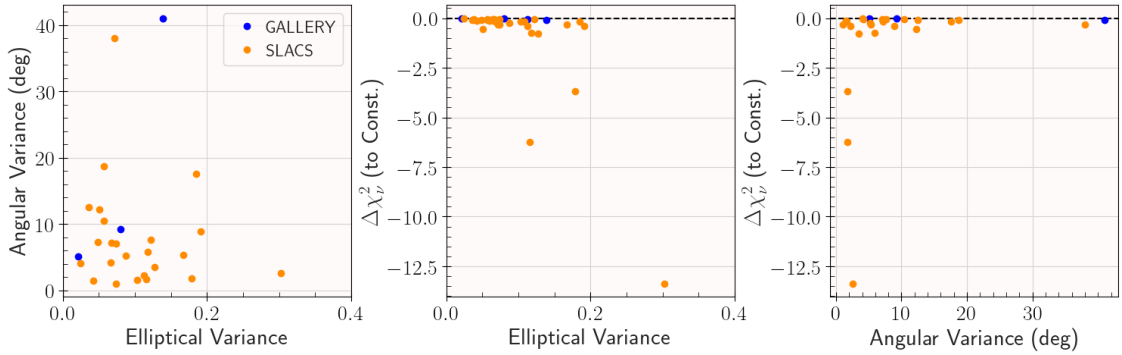

Figure A.6: Comparison of elliptical to angular variance in the variable ellipse model, and of both quantities to the difference in reduced chi-squared χ^2_ν between this model and the constant ellipse model. This figure includes the full $\Delta\chi^2_\nu$ range. Negative $\Delta\chi^2_\nu$ means that the variable model has a smaller chi-squared and therefore is a better fit. Elliptical variance is the maximal axis ratio difference between ellipses 0.5"-3.0", and angular variance is the maximal position angle difference between any of these ellipses with $q < 0.85$.

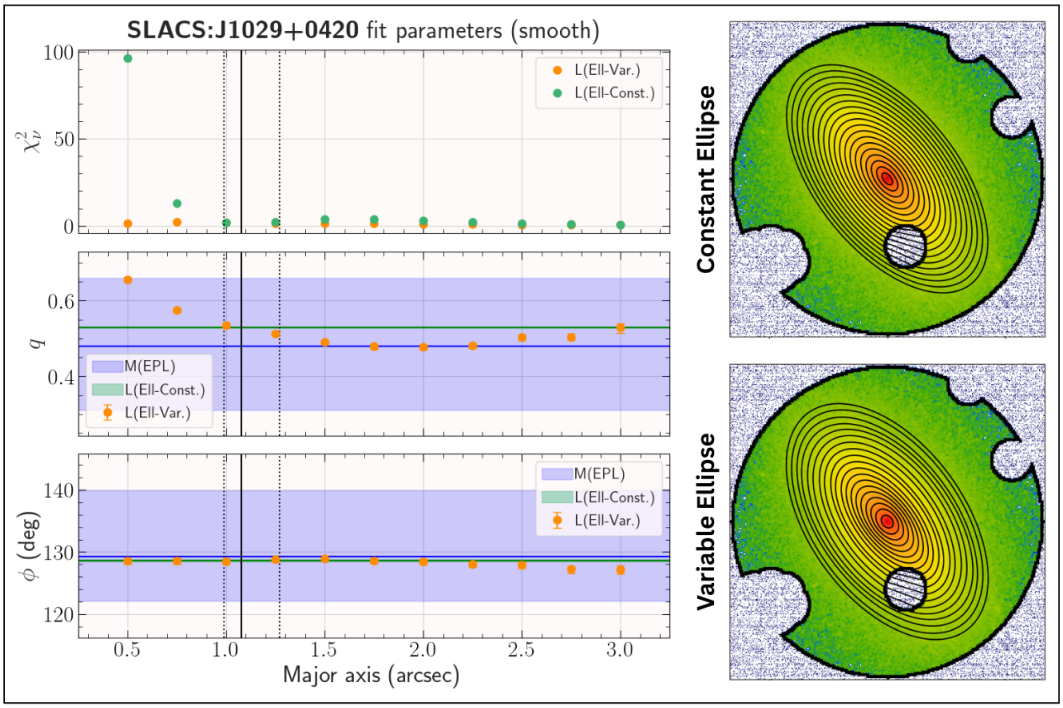

Figure A.7: Parameters and ellipse fits for the smooth models $\mathcal{F}_{EPL}, \mathcal{F}_1, \mathcal{F}_2$ of SLACS lens J1029+0420. For parameter plot explanation, see Section 4.3.5.4. This lens is an outlier where the variable ellipse model is highly preferred to the constant ellipse model, with $\Delta\chi^2_\nu = -3.69$.

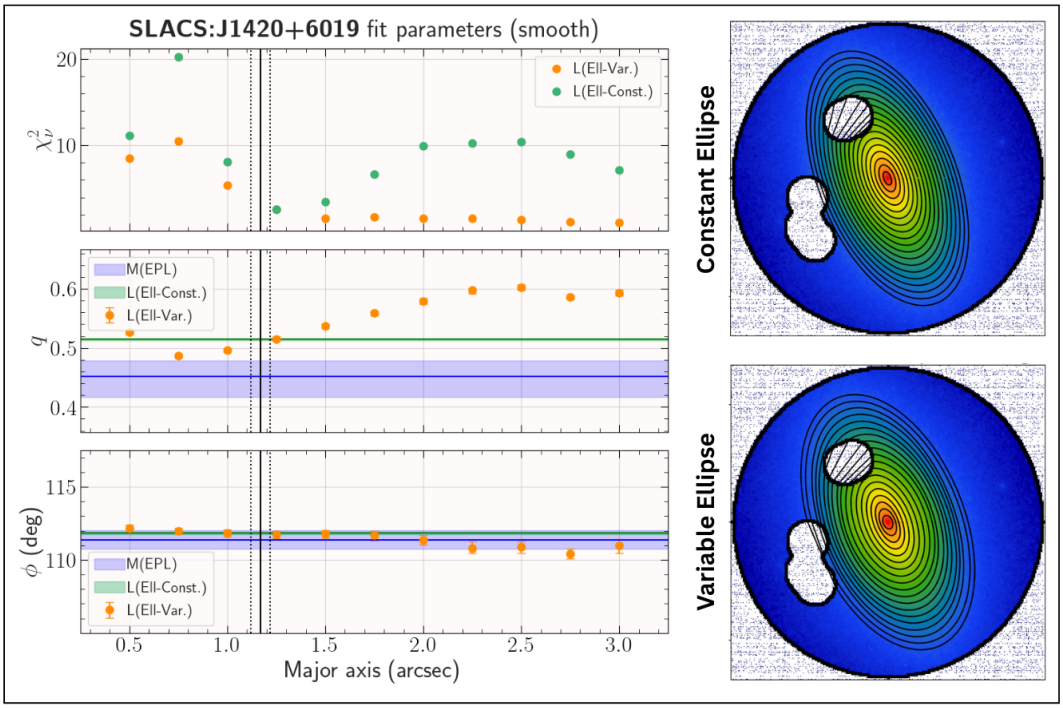

Figure A.8: Parameters and ellipse fits for the smooth models $\mathcal{F}_{EPL}, \mathcal{F}_1, \mathcal{F}_2$ of SLACS lens J1420+6019. For parameter plot explanation, see Section 4.3.5.4. This lens is an outlier where the variable ellipse model is highly preferred to the constant ellipse model, with $\Delta\chi^2_\nu = -6.25$.

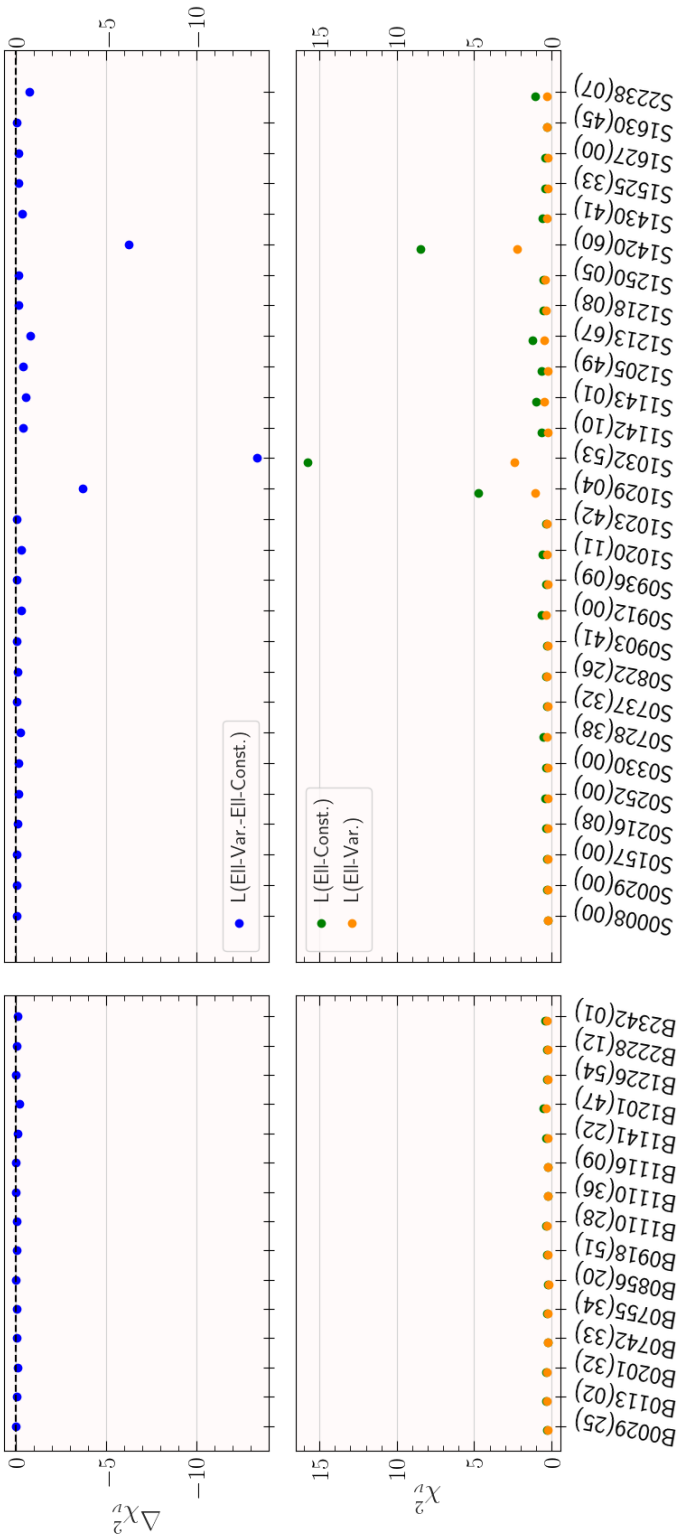

Figure A.9: Full range of reduced chi-squared (χ^2_ν) values for the elliptical light models. Upper panels (blue) show the difference ($\Delta\chi^2_\nu$) between the Variable model and the Constant model. Lower panels show the actual χ^2_ν for the Variable (orange) and Constant (green) models. Negative $\Delta\chi^2_\nu$ means that the variable model has a smaller chi-squared and therefore is a better fit.

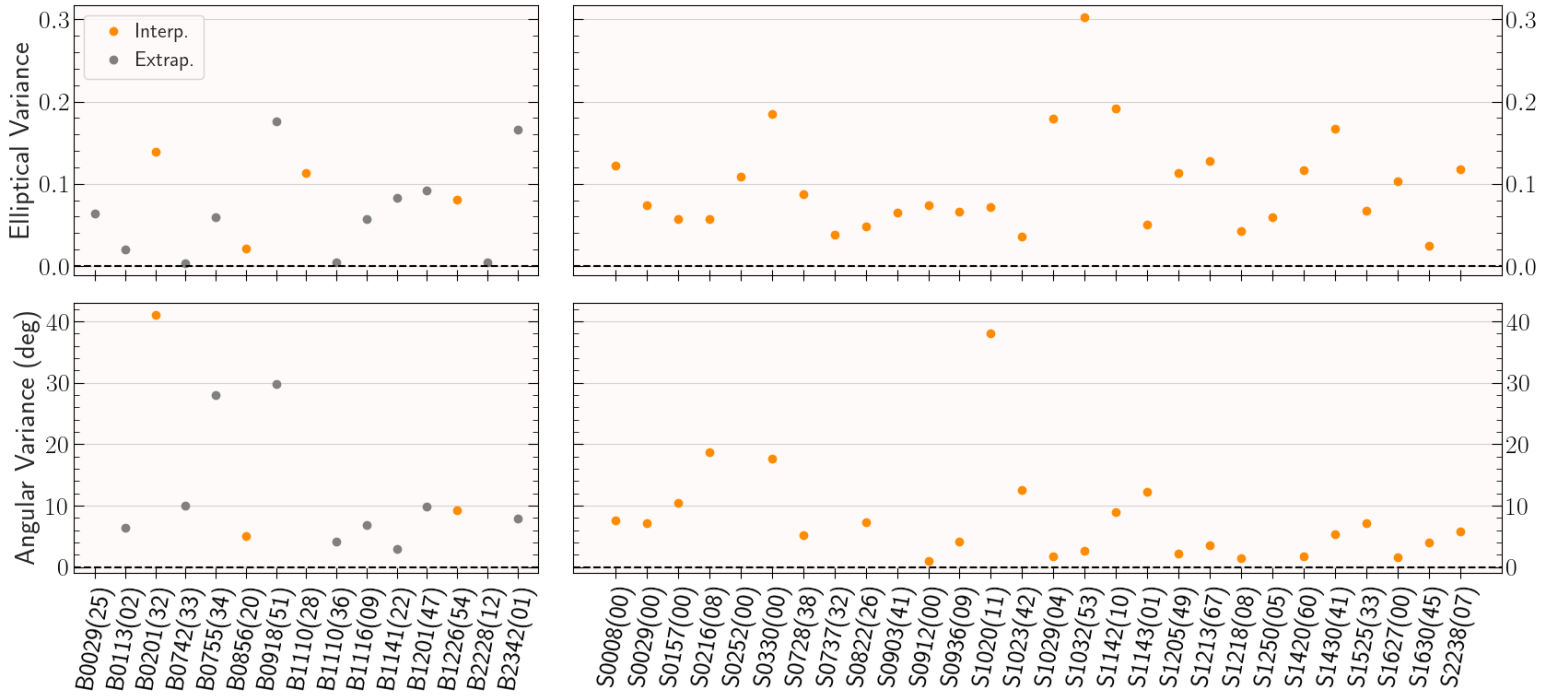

Figure A.10: Elliptical and angular variances for the variable ellipse model for each lens. Elliptical variance is the maximal axis ratio difference between ellipses 0.5"-3.0", and angular variance is the maximal position angle difference between any of these ellipses with $q < 0.85$.

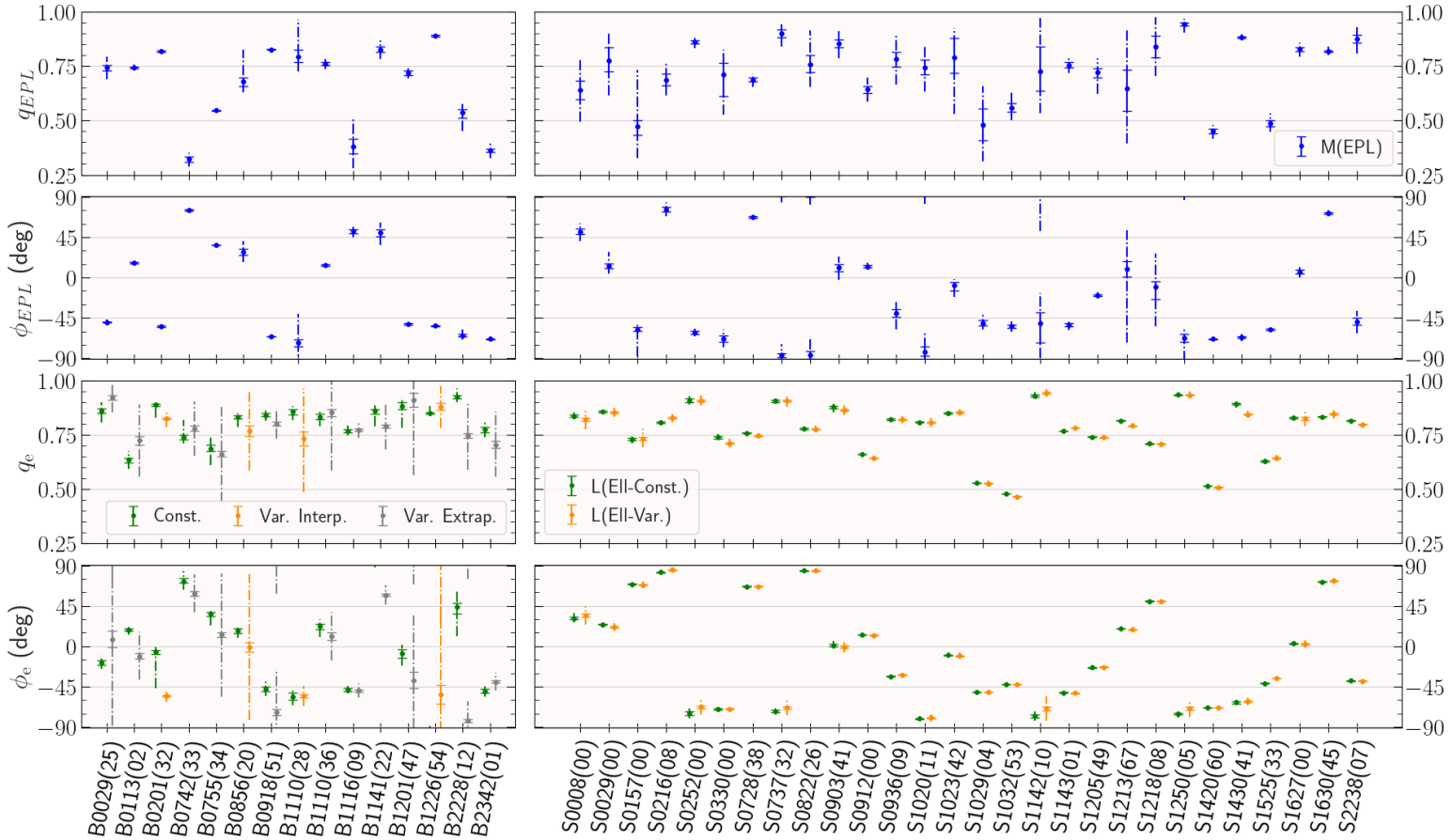

Figure A.11: Recovered axis ratio (q) and position angle (ϕ) for the EPLγ mass model (blue, upper two panels) and the constant (green) and variable (orange) ellipse models (lower two panels). Solid-capped errorbars are the 1-sigma errors, dot-dashed errorbar continuation denotes the 3-sigma errors. Values from the variable ellipse model are estimated at the Einstein radius. Greyed-out BELLS-GALLERY lenses are those that do not have light to the Einstein radius and parameters have been (unreliably) extrapolated and should be discounted. Angles are 'wrapped' to maintain continuity around ±90 degrees, accounting for the angular symmetry of the position angle.

A.5 Chapter 5 Appendix

A.5.1 Values of fit parameters and differences between models

We include below a number of plots which the reader may find informative, but would clutter the main body of text and are not directly relevant to the conclusions of the work. These plots require no further explanation that that which is provided in the figure captions and the main body of text in which they are referenced. They are:

- Plots of the recovered parameters from each of the multipole-perturbed models. Figure A.12 shows the axis ratios and position angles for all models. Figures A.13 and A.14 show the multipole strengths and angles for first the light models, then the EPLγ+Multipole mass model.
- Figure A.15 shows differences in the recovered axis ratios and position angles between the mass model and the two light models, as well as between the light models themselves. Figure A.16 makes a comparison between Chapters 4 and 5, showing the differences in axis ratio and position angle between the EPLγ+Multipole and EPLγ mass models and between the constant-multipole and constant-ellipse light model.

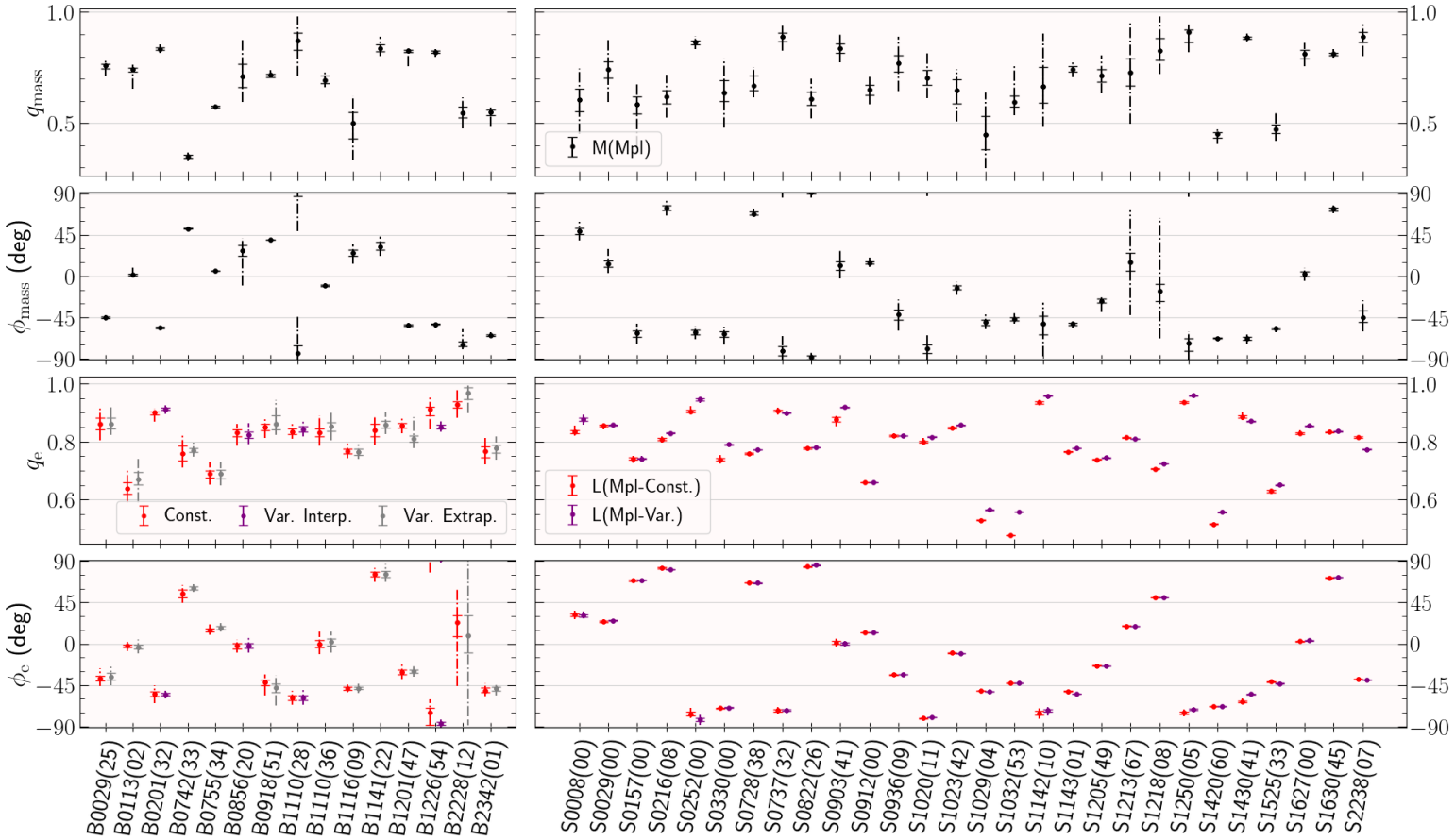

Figure A.12: Recovered axis ratio (q) and position angle (ϕ) for the EPLγ+Multipole mass model (black points, upper two panels) and the constant (red points) and variable (purple points) multipole light models (lower two panels). Solid-capped errorbars are the 1-sigma errors, dot-dashed errorbar continuation denotes the 3-sigma errors. Values from the variable light model are estimated at the Einstein radius. Greyed-out BELLS-GALLERY lenses for the variable light model are those that do not have light to the Einstein radius and parameters have been (unreliably) extrapolated and should be discounted. Angles are 'wrapped' to maintain continuity around ±90 degrees, accounting for the angular symmetry of the position angle.

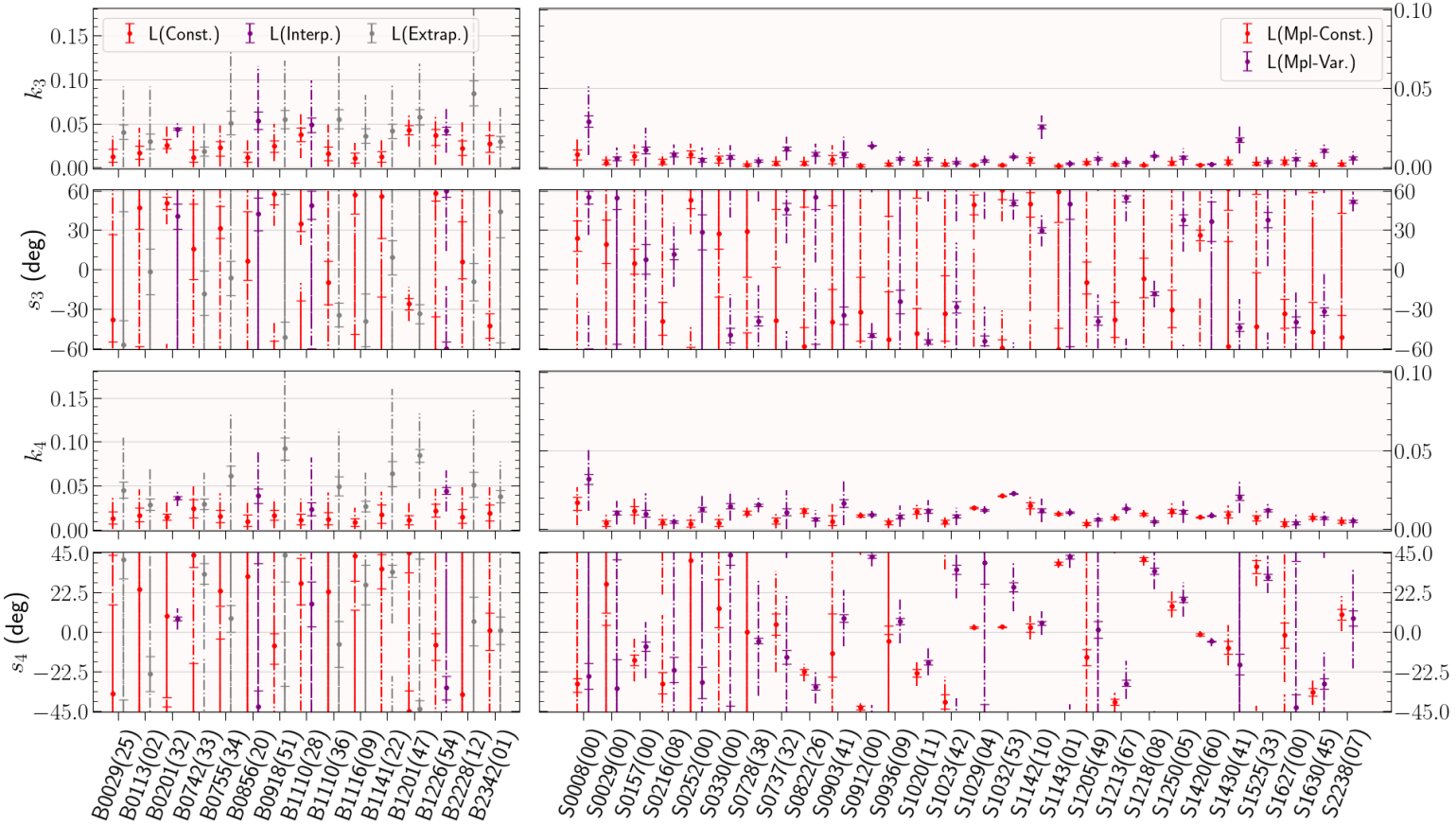

Figure A.13: Recovered multipole strengths (k_3 - top row, k_4 - third row) and multipole angles (ϕ_3 - second row, ϕ_4, bottom row) for the constant (red points) and variable (purple points) multipole light models (lower two panels). Solid-capped errorbars are the 1-sigma errors, dot-dashed errorbar continuation denotes the 3-sigma errors. Values from the variable light model are estimated at the Einstein radius. Greyed-out BELLS-GALLERY lenses for the variable light model are those that do not have light to the Einstein radius and parameters have been (unreliably) extrapolated and should be discounted. Angles are 'wrapped' to maintain continuity around angular symmetry points of ± 60 degrees for $m = 3$ and ± 45 degrees for $m = 4$.

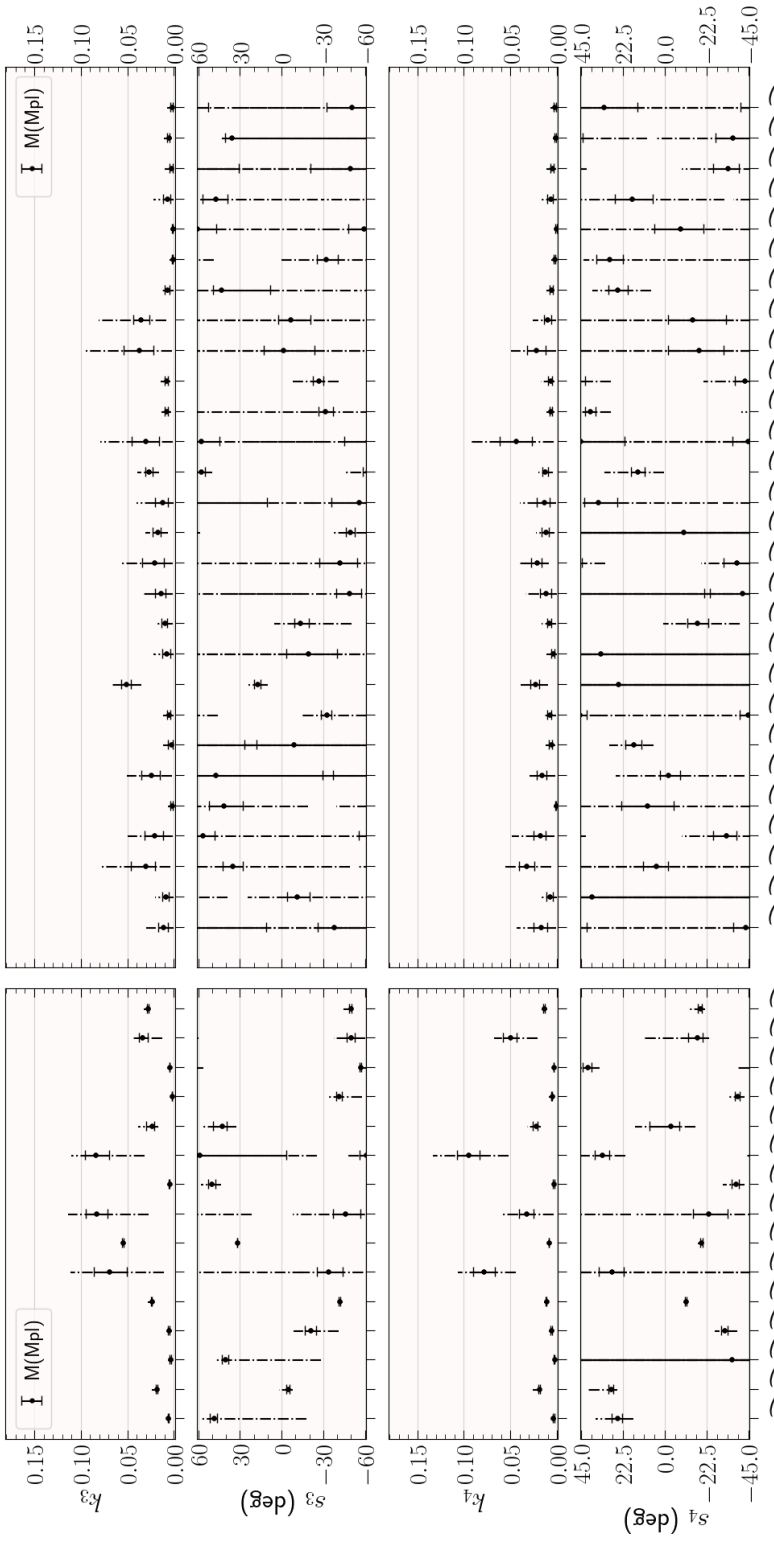

Figure A.14: Recovered multipole strengths (k_3 - top row, k_4 - third row) and multipole angles (ϕ_3 - second row, ϕ_4, bottom row) for the EPLγ+Multipole mass model (black points). Solid-capped errorbars are the 1-sigma errors, dot-dashed errorbar continuation denotes the 3-sigma errors. Angles are 'wrapped' to maintain continuity around angular symmetry points of ± 60 degrees for $m = 3$ and ± 45 degrees for $m = 4$.

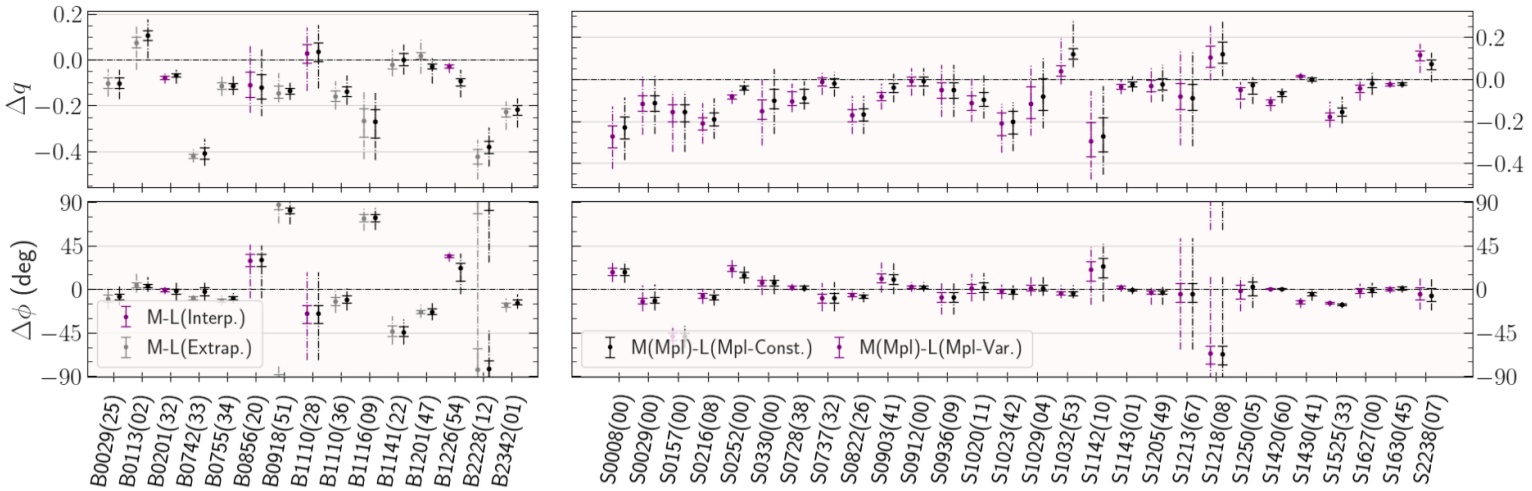

Figure A.15: Differences in the fit axis ratios and position angles (q - top row and ϕ - bottom row) between the multipole-perturbed mass model $\mathcal{F}_{\rm MPL}$ (EPLγ+Multipole) and the two multipole-perturbed light models (constant-multipole model $\mathcal{F}_3$ - black points, and variable-multipole model $\mathcal{F}_4$ - purple points). Positive values means that the mass model has a higher value for that parameter. Greyed-out BELLS-GALLERY lenses for the variable light model are those that do not have light to the Einstein radius and parameters have been (unreliably) extrapolated and should be discounted. Corresponding differences in the multipole parameters are in Section 5.4. Values for the variable multipole model are interpolated at the Einstein radius. Angles are 'wrapped' to maintain continuity around ±90 degrees, accounting for the angular symmetry of the position angle.

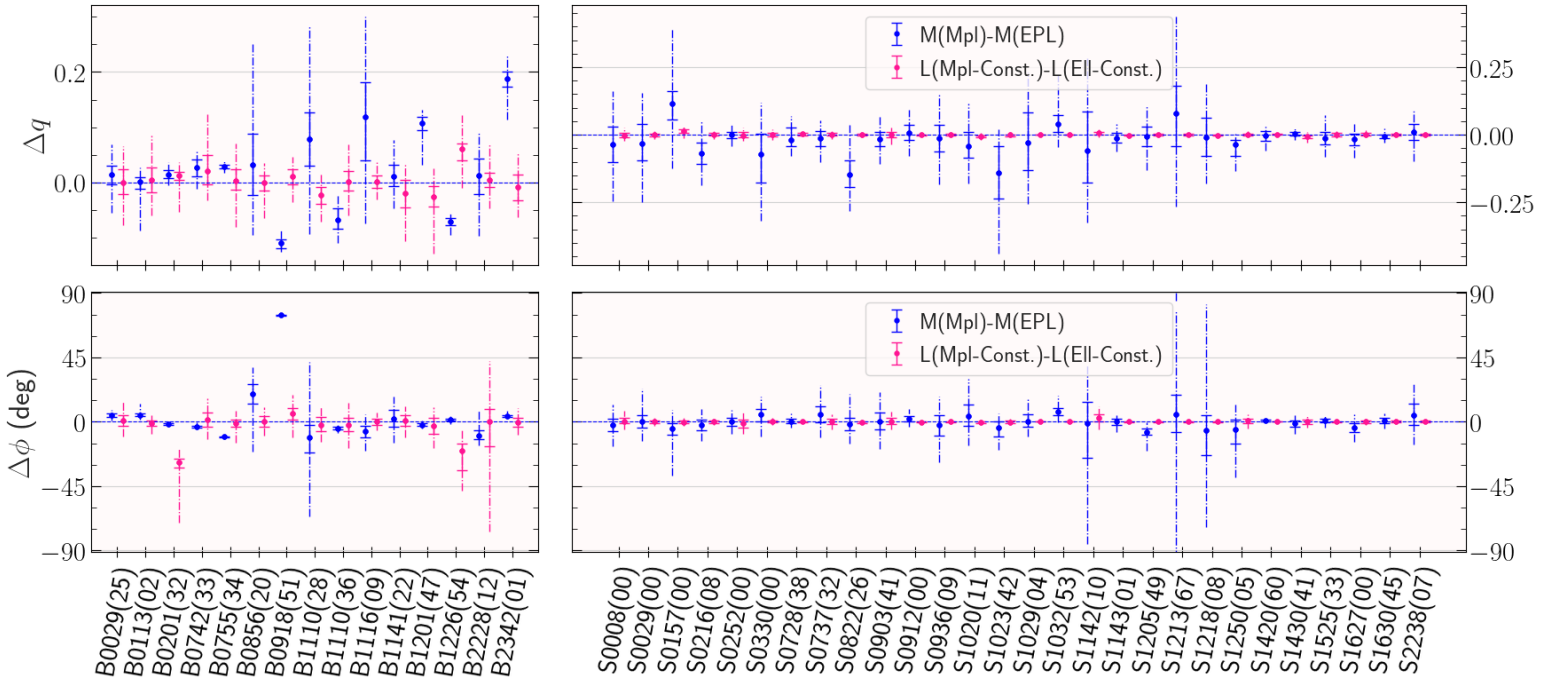

Figure A.16: Differences in the fit axis ratios and position angles (q - top row and ϕ - bottom row) between the EPLγ+Multipole and EPLγ mass models (blue points) and between the constant-multipole and constant-ellipse light models (pink points). This uses the results from both Chapters 4 and 5. Angles are 'wrapped' to maintain continuity around ±90 degrees, accounting for the angular symmetry of the position angle.

Bibliography

Amorisco, N. C., Nightingale, J., He, Q. et al. (2021). 'Halo concentration strengthens dark matter constraints in galaxy–galaxy strong lensing analyses'. In: *Monthly Notices of the Royal Astronomy Society* 510 (2), pp. 2464–2479.

Amvrosiadis, A., Lange, S., Nightingale, J. W. et al. (2025a). 'The onset of bar formation in a massive galaxy at z $\sim$ 3.8'. In: *Monthly Notices of the Royal Astronomy Society* 537 (2), pp. 1163–1181.

Amvrosiadis, A., Nightingale, J. W., He, Q. et al. (2025b). 'Lopsidedness in early-type galaxies: the role of the m= 1 multipole in isophote fitting and strong lens modelling'. In: *Monthly Notices of the Royal Astronomy Society* 540 (4), pp. 3281–3288.

Aravena, M., Spilker, J. S., Bethermin, M. et al. (2016). 'A survey of the cold molecular gas in gravitationally lensed star-forming galaxies at z> 2'. In: *Monthly Notices of the Royal Astronomy Society* 457 (4), pp. 4406–4420.

Auger, M., Treu, T., Bolton, A. et al. (2010). 'The Sloan Lens ACS Survey. X. Stellar, dynamical, and total mass correlations of massive early-type galaxies'. In: *The Astrophysical Journal* 724 (1), p. 511.

Babcock, H. W. (1939). 'The rotation of the Andromeda Nebula'. In: *Lick Observatory Bulletin* 498, pp. 41–51.

Ballard, D. J., Enzi, W. J. R., Collett, T. E., Turner, H. C. and Smith, R. J. (2024). 'Gravitational imaging through a triple source plane lens: revisiting the ΛCDM-defying dark subhalo in SDSSJ0946+1006'. In: *Monthly Notices of the Royal Astronomy Society* 528 (4), pp. 7564–7586.

Barone, T. M., Kacprzak, G. G., Nightingale, J. W. et al. (2024). 'Gravitational lensing reveals cool gas within 10-20 kpc around a quiescent galaxy'. In: *Communications Physics* 7 (1), p. 286.

Benacchio, L. and Galletta, G. (1980). 'Triaxiality in elliptical galaxies'. In: *Monthly Notices of the Royal Astronomy Society* 193 (4), pp. 885–894.

Bender, R., Surma, P., Doebereiner, S., Moellenhoff, C. and Madejsky, R. (1989). 'Isophote shapes of elliptical galaxies. II-Correlations with global optical, radio and X-ray properties'. In: *Astronomy & Astrophysics* 217, pp. 35–43.

Benson, A. J., Farahi, A., Cole, S. et al. (2012). 'Dark matter halo merger histories beyond cold dark matter – I. Methods and application to warm dark matter'. In: *Monthly Notices of the Royal Astronomical Society* 428 (2), pp. 1774–1789.

Bergamini, P., Acebron, A., Grillo, C. et al. (2023). 'The GLASS-JWST Early Release Science Program. III. Strong-lensing model of Abell 2744 and its infalling regions'. In: *The Astrophysical Journal* 952 (1), p. 84.

Bertone, G. and Hooper, D. (2018). 'History of dark matter'. In: *Rev. Mod. Phys.* 90 (4), p. 045002.

Birkin, J. E., Hutchison, T. A., Welch, B. et al. (2023). 'JWST's TEMPLATES for Star Formation: The First Resolved Gas-phase Metallicity Maps of Dust-obscured Star-forming Galaxies at z 4'. In: *The Astrophysical Journal* 958 (1), p. 64.

Birrer, S., Millon, M., Sluse, D. et al. (2024). 'Time-delay cosmography: measuring the Hubble constant and other cosmological parameters with strong gravitational lensing'. In: *Space science reviews* 220 (5), p. 48.

Bolton, A. S., Burles, S., Koopmans, L. V. et al. (2008a). 'The sloan lens ACS survey. V. The full ACS strong-lens sample'. In: *The Astrophysical Journal* 682 (2), p. 964.

Bolton, A. S., Treu, T., Koopmans, L. V. et al. (2008b). 'The Sloan Lens ACS Survey. VII. Elliptical galaxy scaling laws from direct observational mass measurements'. In: *The Astrophysical Journal* 684 (1), p. 248.

Bolton, A. S., Burles, S., Koopmans, L. V. E., Treu, T. and Moustakas, L. A. (2006). 'The Sloan Lens ACS Survey. I. A Large Spectroscopically Selected Sample of Massive Early-Type Lens Galaxies'. In: *The Astrophysical Journal* 638 (2), p. 703.

Bond, J. R., Efstathiou, G. and Silk, J. (1980). 'Massive Neutrinos and the Large-Scale Structure of the Universe'. In: *Phys. Rev. Lett.* 45 (24), pp. 1980–1984.

Bothwell, M., Aguirre, J., Aravena, M. et al. (2017). 'ALMA observations of atomic carbon in z 4 dusty star-forming galaxies'. In: *Monthly Notices of the Royal Astronomy Society* 466 (3), pp. 2825–2841.

Boylan-Kolchin, M., Bullock, J. S. and Kaplinghat, M. (2012). 'The Milky Way's bright satellites as an apparent failure of ΛCDM'. In: *Monthly Notices of the Royal Astronomical Society* 422 (2), pp. 1203–1218.

Bro, R. and De Jong, S. (1997). 'A fast non-negativity-constrained least squares algorithm'. In: *Journal of Chemometrics* 11 (5), pp. 393–401.

Brownstein, J. R., Bolton, A. S., Schlegel, D. J. et al. (2011). 'The BOSS emission-line lens survey (BELLS). I. A large spectroscopically selected sample of lens galaxies at redshift 0.5'. In: *The Astrophysical Journal* 744 (1), p. 41.

Bull, P., Akrami, Y., Adamek, J. et al. (2016). 'Beyond ΛCDM: Problems, solutions, and the road ahead'. In: *Physics of the Dark Universe* 12, pp. 56–99.

Bullock, J. S. and Boylan-Kolchin, M. (2017). 'Small-Scale Challenges to the ΛCDM Paradigm'. In: *Annual Review of Astronomy and Astrophysics* 55 (1), pp. 343–387.

Cao, X., Li, R., Nightingale, J. et al. (2021). 'Systematic errors induced by the elliptical power-law model in galaxy-galaxy strong lens modeling'. In: *Research in Astronomy and Astrophysics*.

Cao, X., Li, R., Nightingale, J. W. et al. (2025). 'Probing Dark Matter Substructures with Free-Form Modelling: A Case Study of the 'Jackpot' Strong Lens'. In: *arxiv preprint (arxiv:2504.19177)*.

Cappellari, M. (2002). 'Efficient multi-Gaussian expansion of galaxies'. In: *Monthly Notices of the Royal Astronomy Society* 333 (2), pp. 400–410.

— (2016). 'Structure and Kinematics of Early-Type Galaxies from Integral Field Spectroscopy'. In: *Annual Review of Astronomy and Astrophysics* 54 (Volume 54, 2016), pp. 597–665.

Carlson, E. D., Machacek, M. E. and Hall, L. J. (1992). 'Self-interacting Dark Matter'. In: *The Astrophysical Journal* 398, p. 43.

Carnall, A. C., McLure, R. J., Dunlop, J. S. and Davé, R. (2018). 'Inferring the star formation histories of massive quiescent galaxies with bagpipes: evidence for multiple quenching mechanisms'. In: *Monthly Notices of the Royal Astronomy Society* 480 (4), pp. 4379–4401.

Cathey, J., Gonzalez, A. H., Lower, S. et al. (2024). 'TEMPLATES: Characterization of a Merger in the Dusty Lensing SPT0418–47 System'. In: *The Astrophysical Journal* 967 (1), p. 11.

Chaware, L., Cannon, R., Kembhavi, A. K., Mahabal, A. and Pandey, S. K. (2014). 'Isophotal shapes of early-type ellioptical galaxies to very faint levels'. In: *The Astrophysical Journal* 787 (2), p. 102.

Chu, Z., Lin, W., Li, G. and Kang, X. (2013). 'Multipole Gravitational Lensing and High-order Perturbations on the Quadrupole Lens'. In: *The Astrophysical Journal* 765 (2), p. 134.

Claeskens, J.-F., Sluse, D., Riaud, P. and Surdej, J. (2006). 'Multi wavelength study of the gravitational lens system RXS J1131-1231 - II. Lens model and source reconstruction'. In: *Astronomy & Astrophysics* 451 (3), pp. 865–879.

Cohen, J. S., Fassnacht, C. D., O'Riordan, C. M. and Vegetti, S. (2024). 'General multipoles and their implications for dark matter inference'. In: *Monthly Notices of the Royal Astronomy Society* 531 (3), pp. 3431–3443.

Collett, T. E. and Smith, R. J. (2020). 'A triple rollover: a third multiply imaged source at z6 behind the Jackpot gravitational lens'. In: *Monthly Notices of the Royal Astronomical Society* 497 (2), pp. 1654–1660.

Collett, T. E. (2015). 'The Population of Galaxy-Galaxy Strong Lenses in Forthcoming Optical Imaging Surveys'. In: *The Astrophysical Journal* 811 (1), 20, p. 20.

Congdon, A. B. and Keeton, C. R. (2005). 'Multipole models of four-image gravitational lenses with anomalous flux ratios'. In: *Monthly Notices of the Royal Astronomical Society* 364 (4), pp. 1459–1466.

Cowsik, R. and McClelland, J. (1973). 'Gravity of neutrinos of nonzero mass in astrophysics'. In: *The Astrophysical Journal* 180, pp. 7–10.

Creasey, P., Sameie, O., Sales, L. V. et al. (2017). 'Spreading out and staying sharp – creating diverse rotation curves via baryonic and self-interaction effects'. In: *Monthly Notices of the Royal Astronomy Society* 468 (2), pp. 2283–2295.

De Breuck, C., Weiß, A., Béthermin, M. et al. (2019). 'A dense, solar metallicity ISM in the z= 4.2 dusty star-forming galaxy SPT 0418- 47'. In: *Astronomy & Astrophysics* 631, A167.

Despali, G., Heinze, F. M., Fassnacht, C. D. et al. (2024). 'Detecting low-mass haloes with strong gravitational lensing II: constraints on the density profiles of two detected subhaloes'. In: *arXiv preprint (arXiv:2407.12910)*.

Despali, G., Vegetti, S., White, S. D., Giocoli, C. and Bosch, F. C. van den (2018). 'Modelling the line-of-sight contribution in substructure lensing'. In: *Monthly Notices of the Royal Astronomy Society* 475 (4), pp. 5424–5442.

Despali, G., Vegetti, S., White, S. D. et al. (2022). 'Detecting low-mass haloes with strong gravitational lensing I: the effect of data quality and lensing configuration'. In: *Monthly Notices of the Royal Astronomy Society* 510 (2), pp. 2480–2494.

Dodelson, S. and Widrow, L. M. (1994). 'Sterile neutrinos as dark matter'. In: *Phys. Rev. Lett.* 72 (1), pp. 17–20.

Dong, C., Spilker, J. S., Gonzalez, A. H. et al. (2019). 'Source structure and molecular gas properties from high-resolution CO imaging of SPT-selected dusty star-forming galaxies'. In: *The Astrophysical Journal* 873 (1), p. 50.

Eichner, T., Seitz, S. and Bauer, A. (2012). 'Golden gravitational lensing systems from the Sloan Lens ACS Survey – II. SDSS J1430+4105: a precise inner total mass profile from lensing alone'. In: *Monthly Notices of the Royal Astronomical Society* 427 (3), pp. 1918–1939.

Ellis, J., Hagelin, J. S., Nanopoulos, D. V., Olive, K. and Srednicki, M. (1984). 'Supersymmetric relics from the big bang'. In: *Nuclear Physics B* 238 (2), pp. 453–476.

Emami, R., Hernquist, L., Alcock, C. et al. (2021). 'Inferring the Morphology of Stellar Distribution in TNG50: Twisted and Twisted-stretched Shapes'. In: *The Astrophysical Journal* 918 (1), p. 7.

Enzi, W., Murgia, R., Newton, O. et al. (2021). 'Joint constraints on thermal relic dark matter from strong gravitational lensing, the Ly α forest, and Milky Way satellites'. In: *Monthly Notices of the Royal Astronomical Society* 506 (4), pp. 5848–5862.

Enzi, W. J. R., Krawczyk, C. M., Ballard, D. J. and Collett, T. E. (2024). 'The overconcentrated dark halo in the strong lens SDSS J0946+1006 is a subhalo: evidence for self interacting dark matter?' In: *arXiv preprint (arXiv:2411.08565)*.

Etherington, A., Nightingale, J. W., Massey, R. et al. (2022). 'Automated galaxy–galaxy strong lens modelling: No lens left behind'. In: *Monthly Notices of the Royal Astronomy Society* 517 (3), pp. 3275–3302.

Etherington, A., Nightingale, J. W., Massey, R. et al. (2023). 'Beyond the bulge–halo conspiracy? Density profiles of early-type galaxies from extended-source strong lensing'. In: *Monthly Notices of the Royal Astronomy Society* 521 (4), pp. 6005–6018.

Etherington, A., Nightingale, J. W., Massey, R. et al. (2024). 'Strong gravitational lensing's 'external shear' is not shear'. In: *Monthly Notices of the Royal Astronomy Society* 531 (3), pp. 3684–3697.

Falco, E. E., Lehar, J. and Shapiro, I. I. (1997). 'HST Observations and Models of the Gravitational Lens System MG 0414+0534'. In: *The Astronomical Journal* 113, p. 540.

Ferreras, I., Saha, P. and Burles, S. (2008). 'Unveiling dark haloes in lensing galaxies'. In: *Monthly Notices of the Royal Astronomical Society* 383 (3), pp. 857–863.

Frenk, C. and White, S. (2012). 'Dark matter and cosmic structure'. In: *Annalen der Physik* 524 (9-10), pp. 507–534.

Frenk, C. S., White, S. D., Efstathiou, G. and Davis, M. (1985). 'Cold dark matter, the structure of galactic haloes and the origin of the Hubble sequence'. In: *Nature* 317 (6038), pp. 595–597.

Gao, L., White, S. D., Jenkins, A., Stoehr, F. and Springel, V. (2004). 'The subhalo populations of ΛCDM dark haloes'. In: *Monthly Notices of the Royal Astronomy Society* 355 (3), pp. 819–834.

Gavazzi, R., Treu, T., Marshall, P. J., Brault, F. and Ruff, A. (2012). 'The SL2S galaxuy-scale gravitational lens sample. I. The alignment of mass and light in massive early-type galaxies at z = 0.2–0.9'. In: *The Astrophysical Journal* 761 (2), p. 170.

Gilman, D., Birrer, S., Nierenberg, A. et al. (2020). 'Warm dark matter chills out: constraints on the halo mass function and the free-streaming length of dark matter with eight quadruple-image strong gravitational lenses'. In: *Monthly Notices of the Royal Astronomical Society* 491 (4), pp. 6077–6101.

Goldberg, H. (1983). 'Constraint on the Photino Mass from Cosmology'. In: *Phys. Rev. Lett.* 50 (19), pp. 1419–1422.

Goullaud, C. F., Jensen, J. B., Blakeslee, J. P. et al. (2018). 'The MASSIVE survey. IX. Photometric analysis of 35 high-mass early-type galaxies with HST WFC3/IR'. In: *The Astrophysical Journal* 856 (1), p. 11.

Hao, C. N., Mao, S., Deng, Z. G., Xia, X. Y. and Wu, H. (2006). 'Isophotal shapes of elliptical/lenticular galaxies from the Sloan Digital Sky Survey'. In: *Monthly Notices of the Royal Astronomy Society* 370 (3), pp. 1339–1350.

He, Q., Li, R., Frenk, C. S. et al. (2022). 'Galaxy–galaxy strong lens perturbations: line-of-sight haloes versus lens subhaloes'. In: *Monthly Notices of the Royal Astronomy Society* 512 (4), pp. 5862–5873.

He, Q., Nightingale, J., Robertson, A. et al. (2023). 'Testing strong lensing subhalo detection with a cosmological simulation'. In: *Monthly Notices of the Royal Astronomy Society* 518 (1), pp. 220–239.

He, Q., Nightingale, J. W., Amvrosiadis, A. et al. (2024). 'Unveiling lens light complexity with a novel multi-Gaussian expansion approach for strong gravitational lensing'. In: *Monthly Notices of the Royal Astronomy Society* 532 (2), pp. 2441–2462.

He, Q., Robertson, A., Nightingale, J. W. et al. (2025). 'Not so dark, not so dense: an alternative explanation for the lensing subhalo in SDSSJ0946+ 1006'. In: *arXiv preprint arXiv:2506.07978*.

Hezaveh, Y. D., Dalal, N., Marrone, D. P. et al. (2016). 'Detection of lensing substructure using ALMA observations of the dusty galaxy SDP. 81'. In: *The Astrophysical Journal* 823 (1), p. 37.

Hogg, N. B., Fleury, P., Larena, J. and Martinelli, M. (2023). 'Measuring line-of-sight shear with Einstein rings: a proof of concept'. In: *Monthly Notices of the Royal Astronomical Society* 520 (4), pp. 5982–6000.

Hogg, N. B., Shajib, A. J., Johnson, D. and Larena, J. (2025). 'Line-of-sight shear in SLACS strong lenses I: shear and mass model parametrisations'. In: *arXiv preprint arXiv:2501.16292*.

Hu, W., Barkana, R. and Gruzinov, A. (2000). 'Fuzzy Cold Dark Matter: The Wave Properties of Ultralight Particles'. In: *Phys. Rev. Lett.* 85 (6), pp. 1158–1161.

Iršič, V., Viel, M., Haehnelt, M. G. et al. (2017). 'New constraints on the free-streaming of warm dark matter from intermediate and small scale Lyman-α forest data'. In: *Phys. Rev. D* 96 (2), p. 023522.

Jedrzejewski, R. I. (1987). 'CCD surface photometry of elliptical galaxies–I. Observations, reduction and results'. In: *Monthly Notices of the Royal Astronomy Society* 226 (4), pp. 747–768.

Johnson, D., Collett, T., Li, T. and Fleury, P. (2025). 'Line-of-sight effects on double source plane lenses'. In: *Journal of Cosmology and Astroparticle Physics* 2025 (08), p. 067.

Keeton, C. R., Kochanek, C. S. and Falco, E. E. (1998). 'The Optical Properties of Gravitational Lens Galaxies as a Probe of Galaxy Structure and Evolution*'. In: *The Astrophysical Journal* 509 (2), p. 561.

Keeton, C., Kochanek, C. and Seljak, U. (1997). 'Shear and ellipticity in gravitational lenses'. In: *The Astrophysical Journal* 482 (2), p. 604.

Klypin, A., Kravtsov, A. V., Valenzuela, O. and Prada, F. (1999). 'Where Are the Missing Galactic Satellites?' In: *The Astrophysical Journal* 522 (1), pp. 82–92.

Koopmans, L. V. E., Treu, T., Bolton, A. S., Burles, S. and Moustakas, L. A. (2006). 'The Sloan Lens ACS Survey. III. The Structure and Formation of Early-Type Galaxies and Their Evolution since z 1'. In: *The Astrophysical Journal* 649 (2), p. 599.

Kormann, R., Schneider, P. and Bartelmann, M. (1994). 'Isothermal elliptical gravitational lens models'. In: *Astronomy & Astrophysics (ISSN 0004-6361), vol. 284, no. 1, p. 285-299* 284, pp. 285–299.

Krist, J. (1993). 'Astronomical Data Analysis Software and Systems II'. In: *ASP Conference Series*. Ed. by R. J. Hanisch, R. J. V. Brissenden and B. J. Vol. 52. Astron. Soc. Pac. San Francisco, p. 536.

Kroupa, P., Theis, C. and Boily, C. M. (2005). 'The great disk of Milky-Way satellites and cosmological sub-structures'. In: *Astronomy & Astrophysics* 431, pp. 517–521.

Lange, J. U. (2023). 'nautilus: boosting Bayesian importance nested sampling with deep learning'. In: *Monthly Notices of the Royal Astronomy Society* 525 (2), pp. 3181–3194.

Lange, S. C., Amvrosiadis, A., Nightingale, J. W. et al. (2025). 'Galaxy mass modelling from multiwavelength JWST strong lens analysis: dark matter substructure, angular mass complexity, or both?' In: *Monthly Notices of the Royal Astronomical Society* 539 (2), pp. 704–726.

Li, R., Frenk, C. S., Cole, S. et al. (2016). 'Constraints on the identity of the dark matter from strong gravitational lenses'. In: *Monthly Notices of the Royal Astronomy Society* 460 (1), pp. 363–372.

Li, S., Li, R., Wang, K. et al. (2025). 'The" Little Dark Dot": Evidence for Self-Interacting Dark Matter in the Strong Lens SDSSJ0946+ 1006?' In: *arXiv preprint arXiv:2504.11800*.

Lines, N. E. P., Li, T., Collett, T. E. et al. (2025). 'The revolution in strong lensing discoveries from Euclid'. In: *Nature Astronomy* 9 (8), pp. 1116–1122.

Lovell, M. and Zavala, J. (2023). 'Matching the mass function of Milky Way satellites in competing dark matter models'. In: *Monthly Notices of the Royal Astronomical Society* 520 (1), pp. 1567–1589.

Lovell, M. R., Cautun, M., Frenk, C. S., Hellwing, W. A. and Newton, O. (2021). 'The spatial distribution of Milky Way satellites, gaps in streams, and the nature of dark matter'. In: *Monthly Notices of the Royal Astronomical Society* 507 (4), pp. 4826–4839.

Lovell, M. R., Frenk, C. S., Eke, V. R. et al. (2014). 'The properties of warm dark matter haloes'. In: *Monthly Notices of the Royal Astronomy Society* 439 (1), pp. 300–317.

Ludlow, A. D., Bose, S., Angulo, R. E. et al. (2016). 'The mass–concentration–redshift relation of cold and warm dark matter haloes'. In: *Monthly Notices of the Royal Astronomy Society* 460 (2), pp. 1214–1232.

Ma, J., Gonzalez, A. H., Spilker, J. et al. (2015). 'Stellar masses and star formation rates of lensed, dusty, star-forming galaxies from the SPT survey'. In: *The Astrophysical Journal* 812 (1), p. 88.

Mahler, G., Nightingale, J. W., Hogg, N. B. et al. (2025). 'The COSMOS-Web Lens Survey (COWLS) II: depth, resolution, and NIR coverage from JWST reveal 17 spectacular lenses'. In: *arXiv preprint (arXiv:2503.08782)*.

McConnachie, A. W. (2012). 'The observed properties of Dwarf Galaxies in and around the Local Group'. In: *The Astronomical Journal* 144 (1), p. 4.

Meneghetti, M. (2021). *Introduction to gravitational lensing: with Python examples*. Vol. 956. Springer Nature.

Mercier, W., Shuntov, M., Gavazzi, R. et al. (2024). 'The COSMOS-Web ring: In-depth characterization of an Einstein ring lensing system at z $\sim$ 2'. In: *Astronomy & Astrophysics* 687, A61, A61.

Minor, Q., Gad-Nasr, S., Kaplinghat, M. and Vegetti, S. (2021). 'An unexpected high concentration for the dark substructure in the gravitational lens SDSSJ0946+1006'. In: *Monthly Notices of the Royal Astronomy Society* 507 (2), pp. 1662–1683.

Moore, B., Ghigna, S., Governato, F. et al. (1999). 'Dark Matter Substructure within Galactic Halos'. In: *The Astrophysical Journal* 524 (1), pp. L19–L22.

Mukherjee, S., Koopmans, L. V. E., Tortora, C. et al. (2021). 'SEAGLE – III: Towards resolving the mismatch in the dark-matter fraction in early-type galaxies between simulations and observations'. In: *Monthly Notices of the Royal Astronomical Society* 509 (1), pp. 1245–1251.

Narayanan, V. K., Spergel, D. N., Davé, R. and Ma, C.-P. (2000). 'Constraints on the Mass of Warm Dark Matter Particles and the Shape of the Linear Power Spectrum from the Lyα Forest'. In: *The Astrophysical Journal* 543 (2), p. L103.

Navarro, J. F., Frenk, C. S. and White, S. D. (1997). 'A universal density profile from hierarchical clustering'. In: *The Astrophysical Journal* 490 (2), p. 493.

Newton, O., Leo, M., Cautun, M. et al. (2021). 'Constraints on the properties of warm dark matter using the satellite galaxies of the Milky Way'. In: 2021 (8), 062, p. 062.

Nierenberg, A. M., Treu, T., Wright, S. A., Fassnacht, C. D. and Auger, M. W. (2014). 'Detection of substructure with adaptive optics integral field spectroscopy of the gravitational lens B1422+231'. In: *Monthly Notices of the Royal Astronomical Society* 442 (3), pp. 2434–2445.

Nieto, J. .-. and Bender, R. (1989). 'Boxiness in elliptical galaxies.' In: *Astronomy & Astrophysics* 215, pp. 266–271.

Nightingale, J. W. and Dye, S. (2015a). 'Adaptive semi-linear inversion of strong gravitational lens imaging'. In: *Monthly Notices of the Royal Astronomy Society* 452 (3), pp. 2940–2959.

Nightingale, J. W., Dye, S. and Massey, R. J. (2018). 'AutoLens: Automated modeling of a strong lens's light, mass, and source'. In: *Monthly Notices of the Royal Astronomy Society* 478 (4), pp. 4738–4784.

Nightingale, J. W., Hayes, R. G. and Griffiths, M. (2021a). ‘‘PyAutoFit‘: A Classy Probabilistic Programming Language for Model Composition and Fitting’. In: *J. Open Source Softw.* 6 (58), p. 2550.

Nightingale, J. W., Hayes, R. G., Kelly, A. et al. (2021b). ‘‘PyAutoLens‘: Open-Source Strong Gravitational Lensing’. In: *J. Open Source Softw.* 6 (58), p. 2825.

Nightingale, J. W., He, Q., Cao, X. et al. (2024). ‘Scanning for dark matter subhaloes in Hubble Space Telescope imaging of 54 strong lenses’. In: *Monthly Notices of the Royal Astronomy Society* 527 (4), pp. 10480–10506.

Nightingale, J. W., Amvrosiadis, A., Hayes, R. G. et al. (2023). ‘PyAutoGalaxy: Open-Source Multiwavelength Galaxy Structure & Morphology’. In: *J. Open Source Softw.* 8 (81), p. 4475.

Nightingale, J. and Dye, S. (2015b). ‘Adaptive semi-linear inversion of strong gravitational lens imaging’. In: *Monthly Notices of the Royal Astronomy Society* 452 (3), pp. 2940–2959.

O’Riordan, C. M., Despali, G., Vegetti, S., Lovell, M. R. and Moliné, A. (2023). ‘Sensitivity of strong lensing observations to dark matter substructure: a case study with Euclid’. In: *Monthly Notices of the Royal Astronomy Society* 521 (2), pp. 2342–2356.

O’Riordan, C. M. and Vegetti, S. (2024). ‘Angular complexity in strong lens substructure detection’. In: *Monthly Notices of the Royal Astronomy Society* 528 (2), pp. 1757–1768.

Ostriker, J. P. and Peebles, P. J. (1973). ‘A numerical study of the stability of flattened galaxies: or, can cold galaxies survive?’ In: *The Astrophysical Journal* 186, pp. 467–480.

Padilla, N. D. and Strauss, M. A. (2008). ‘The shapes of galaxies in the Sloan Digital Sky Survey’. In: *Monthly Notices of the Royal Astronomy Society* 388 (3), pp. 1321–1334.

Paugnat, H. and Gilman, D. (2025). ‘Elliptical multipoles for gravitational lenses’. In: *Phys. Rev. D* 111 (12), p. 123014.

Pedregosa, F., Varoquaux, G., Gramfort, A. et al. (2011). ‘Scikit-learn: Machine Learning in Python’. In: *Journal of Machine Learning Research* 12, pp. 2825–2830.

Peñarrubia, J., Gómez, F. A., Besla, G., Erkal, D. and Ma, Y.-Z. (2015). ‘A timing constraint on the (total) mass of the Large Magellanic Cloud’. In: *Monthly Notices of the Royal Astronomical Society: Letters* 456 (1), pp. L54–L58.

Peng, B., Vishwas, A., Stacey, G. et al. (2023). ‘Discovery of a Dusty, Chemically Mature Companion to az 4 Starburst Galaxy in JWST ERS Data’. In: *The Astrophysical Journal Letters* 944 (2), p. L36.

Perrin, M. D., Soummer, R., Elliott, E. M., Lallo, M. D. and Sivaramakrishnan, A. (2012). ‘Simulating point spread functions for the James Webb Space Telescope with WebbPSF’. In: *Space Telescopes and Instrumentation 2012: Optical, Infrared, and Millimeter Wave*. Ed. by M. C. Clampin, G. G. Fazio, H. A. MacEwen and J. M. Oschmann Jr. Vol. 8442. Society of Photo-Optical Instrumentation Engineers (SPIE) Conference Series, 84423D, p. 84423D.

Planck Collaboration, Ade, P. A. R., Aghanim, N. et al. (2016). 'Planck 2015 results. XIII. Cosmological parameters'. In: *Astronomy & Astrophysics* 594, A13, A13.

Polletta, M., Tajer, M., Maraschi, L. et al. (2007). 'Spectral energy distributions of hard X-ray selected active galactic nuclei in the XMM-Newton medium deep survey'. In: *The Astrophysical Journal* 663 (1), p. 81.

Pontoppidan, K. M., Pickering, T. E., Laidler, V. G. et al. (2016). 'Pandeia: a multi-mission exposure time calculator for JWST and WFIRST'. In: *Observatory Operations: Strategies, Processes, and Systems VI*. Ed. by A. B. Peck, R. L. Seaman and C. R. Benn. Vol. 9910. International Society for Optics and Photonics. SPIE, p. 991016.

Powell, D. M., McKean, J. P., Vegetti, S. et al. (2025). 'A million-solar-mass object detected at a cosmological distance using gravitational imaging'. In: *Nature Astronomy*.

Powell, D. M., Vegetti, S., McKean, J. P. et al. (2022). 'A lensed radio jet at milliarcsecond resolution I: Bayesian comparison of parametric lens models'. In: *Monthly Notices of the Royal Astronomical Society* 516 (2), pp. 1808–1828.

Preskill, J., Wise, M. B. and Wilczek, F. (1983). 'Cosmology of the invisible axion'. In: *Physics Letters B* 120 (1-3), pp. 127–132.

Rasmussen, C. and Williams, C. (2006). 'Gaussian Processes for Machine Learning'. In: *Adaptive Computation and Machine Learning*. Ed. by T. Dietterich. The MIT Press.

Reuter, C., Vieira, J., Spilker, J. et al. (2020). 'The complete redshift distribution of dusty star-forming galaxies from the SPT-SZ survey'. In: *The Astrophysical Journal* 902 (1), p. 78.

Rigby, J. R., Vieira, J. D., Phadke, K. A. et al. (2024). 'JWST Early Release Science Program TEMPLATES: Targeting Extremely Magnified Panchromatic Lensed Arcs and their Extended Star formation'. In: *The Astrophysical Journal* 978 (1), p. 108.

Ritondale, E., Vegetti, S., Despali, G. et al. (2019). 'Low-mass halo perturbations in strong gravitational lenses at redshift z 0.5 are consistent with CDM'. In: *Monthly Notices of the Royal Astronomy Society* 485 (2), pp. 2179–2193.

Rizzo, F., Vegetti, S., Powell, D. et al. (2020). 'A dynamically cold disk galaxy in the early Universe'. In: *Nature* 584 (7820), pp. 201–204.

Roberts, M. and Rots, A. (1973). 'Comparison of rotation curves of different galaxy types'. In: *Astronomy and Astrophysics* 26, pp. 483–485.

Robertson, A., Massey, R., Eke, V. et al. (2018). 'The diverse density profiles of galaxy clusters with self-interacting dark matter plus baryons'. In: *Monthly Notices of the Royal Astronomy Society: Letters* 476 (1), pp. L20–L24.

Rocha, M., Peter, A. H. G., Bullock, J. S. et al. (2013). 'Cosmological simulations with self-interacting dark matter – I. Constant-density cores and substructure'. In: *Monthly Notices of the Royal Astronomy Society* 430 (1), pp. 81–104.

Rubin, V. C. and Ford W. Kent, J. (1970). 'Rotation of the Andromeda Nebula from a Spectroscopic Survey of Emission Regions'. In: *The Astrophysical Journal* 159, p. 379.

Saha, P., Sluse, D., Wagner, J. and Williams, L. L. R. (2024). 'Essentials of Strong Gravitational Lensing'. In: *Space Science Reviews* 220 (1), p. 12.

Schaye, J., Chaikin, E., Schaller, M. et al. (2025). 'The COLIBRE project: cosmological hydrodynamical simulations of galaxy formation and evolution'. In: *arXiv preprint arXiv:2508.21126*.

Schneider, P., Kochanek, C. and Wambsganss, J. (2006). *Gravitational lensing: strong, weak and micro: Saas-Fee advanced course 33*. Vol. 33. Springer Science & Business Media.

Sersic, J. L. (1968). 'Atlas de galaxias australes'. In: *Cordoba*.

Shajib, A. J., Birrer, S., Treu, T. et al. (2018). 'Is every strong lens model unhappy in its own way? Uniform modelling of a sample of 13 quadruply+ imaged quasars'. In: *Monthly Notices of the Royal Astronomical Society* 483 (4), pp. 5649–5671.

Shajib, A. J., Vernardos, G., Collett, T. E. et al. (2024). 'Strong Lensing by Galaxies'. In: *Space Science Reviews* 220 (8), p. 87.

Shan, X., Jin, Y. and Mao, S. (2025). 'Gravitational lensing by a spiral galaxy I: the influence from bar's structure to the flux ratio anomaly'. In: *arXiv preprint (arXiv:2510.02805)*.

Shao, S., Cautun, M., Deason, A. J., Frenk, C. S. and Theuns, T. (2018). 'Evolution of LMC/M33-mass dwarf galaxies in the eagle simulation'. In: *Monthly Notices of the Royal Astronomical Society* 479 (1), pp. 284–296.

Shu, Y., Bolton, A. S., Kochanek, C. S. et al. (2016a). 'The BOSS emission-line lens survey. III. Strong lensing of Lyα emitters by individual galaxies'. In: *The Astrophysical Journal* 824 (2), p. 86.

Shu, Y., Bolton, A. S., Mao, S. et al. (2016b). 'The BOSS emission-line lens survey. IV. Smooth lens models for the BELLS GALLERY sample'. In: *The Astrophysical Journal* 833 (2), p. 264.

Sibson, R. (1981). 'Interpreting Multivariate Data'. In: ed. by V. Barnett. New York: John Wiley and Sons. Chap. A Brief Description of Natural Neighbor Interpolation.

Sonnenfeld, A., Li, S.-S., Despali, G. et al. (2023). 'Strong lensing selection effects'. In: *Astronomy & Astrophysics* 678, A4.

Speagle, J. S. (2020). 'DYNESTY: a dynamic nested sampling package for estimating Bayesian posteriors and evidences'. In: *Monthly Notices of the Royal Astronomical Society* 493 (3), pp. 3132–3158.

Spergel, D. N. and Steinhardt, P. J. (2000). 'Observational Evidence for Self-Interacting Cold Dark Matter'. In: *Phys. Rev. Lett.* 84 (17), pp. 3760–3763.

Spilker, J. S., Phadke, K. A., Aravena, M. et al. (2023). 'Spatial variations in aromatic hydrocarbon emission in a dust-rich galaxy'. In: *Nature* 618 (7966), pp. 708–711.

Stacey, H. R., Powell, D. M., Vegetti, S. et al. (2024). 'Complex angular structure of three elliptical galaxies from high-resolution ALMA observations of strong gravitational lenses'. In: *Astronomy & Astrophysics* 688, A110, A110.

Stacey, H., Powell, D., Vegetti, S., McKean, J. and Wen, D. (2025). 'Investigation of mass substructure in gravitational lens system SDP. 81 with ALMA long-baseline observations'. In: *arXiv preprint arXiv:2508.02776*.

Suyu, S., Marshall, P., Blandford, R. et al. (2009). 'Dissecting the gravitational lens B1608+ 656. I. Lens potential reconstruction'. In: *The Astrophysical Journal* 691 (1), p. 277.

Tessore, N., Bellagamba, F. and Metcalf, R. B. (2016). 'lensed: a code for the forward reconstruction of lenses and sources from strong lensing observations'. In: *Monthly Notices of the Royal Astronomical Society* 463 (3), pp. 3115–3128.

Tessore, N. and Metcalf, R. B. (2015). 'The elliptical power law profile lens'. In: *Astronomy & Astrophysics* 580, A79.

Tremblay, B. and Merritt, D. (1995). 'The Frequency Function of Elliptical Galaxy Intrinsic Shapes'. In: *The Astronomical Journal* 110, p. 1039.

Treu, T. (2010). 'Strong Lensing by Galaxies'. In: *Annual Review of Astronomy and Astrophysics* 48 (Volume 48, 2010), pp. 87–125.

Treu, T., Gavazzi, R., Gorecki, A. et al. (2008). 'The SLACS Survey. VIII. The relation between environment and internal structure of early-type galaxies.' In: *The Astrophysical Journal* 690 (1), p. 670.

Trotter, C. S., Winn, J. N. and Hewitt, J. N. (2000). 'A Multipole-Taylor Expansion for the Potential of the Gravitational Lens MG J0414+0534'. In: *The Astrophysical Journal* 535 (2), p. 671.

van Dokkum, P., Brammer, G., Wang, B., Leja, J. and Conroy, C. (2024). 'A massive compact quiescent galaxy at z = 2 with a complete Einstein ring in JWST imaging'. In: *Nature Astronomy* 8 (1), pp. 119–125.

Vegetti, S., Despali, G., Lovell, M. R. and Enzi, W. (2018). 'Constraining sterile neutrino cosmologies with strong gravitational lensing observations at redshift z 0.2'. In: *Monthly Notices of the Royal Astronomy Society* 481 (3), pp. 3661–3669.

Vegetti, S., Koopmans, L., Auger, M., Treu, T. and Bolton, A. (2014). 'Inference of the cold dark matter substructure mass function at z= 0.2 using strong gravitational lenses'. In: *Monthly Notices of the Royal Astronomy Society* 442 (3), pp. 2017–2035.

Vegetti, S., Koopmans, L., Bolton, A., Treu, T. and Gavazzi, R. (2010). 'Detection of a dark substructure through gravitational imaging'. In: *Monthly Notices of the Royal Astronomy Society* 408 (4), pp. 1969–1981.

Vegetti, S., Lagattuta, D., McKean, J. et al. (2012). 'Gravitational detection of a low-mass dark satellite galaxy at cosmological distance'. In: *nature* 481 (7381), pp. 341–343.

Vegetti, S., Birrer, S., Despali, G. et al. (2024). 'Strong Gravitational Lensing as a Probe of Dark Matter'. In: *Space Science Reviews* 220 (5), p. 58.

Vegetti, S. and Koopmans, L. V. E. (2009). 'Bayesian strong gravitational-lens modelling on adaptive grids: objective detection of mass substructure in Galaxies'. In: *Monthly Notices of the Royal Astronomy Society* 392 (3), pp. 945–963.

Walker, M. G. and Peñarrubia, J. (2011). 'A method for measuring slopes of the mass profiles of dwarf spheroidal galaxies'. In: *The Astrophysical Journal* 742 (1), p. 20.

Walmsley, M., Holloway, P., Lines, N. et al. (2025). 'Euclid Quick Data Release (Q1): The Strong Lensing Discovery Engine A–System overview and lens catalogue'. In: *arXiv preprint arXiv:2503.15324*.

Walsh, D., Carswell, R. F. and Weymann, R. J. (1979). '0957 + 561 A, B: twin quasistellar objects or gravitational lens?' In: *Nature* 279 (5712), pp. 381–384.

Weinberg, D. H., Bullock, J. S., Governato, F. and Naray Rachel Kuzio and. Peter, A. H. G. de (2015). 'Cold dark matter: Controversies on small scales'. In: *Proceedings of the National Academy of Sciences* 112 (40), pp. 12249–12255.

Weinberg, S. (1978). 'A new light boson?' In: *Physical Review Letters* 40 (4), p. 223.

Weiß, A., De Breuck, C., Marrone, D. et al. (2013). 'ALMA redshifts of millimeter-selected galaxies from the SPT survey: the redshift distribution of dusty star-forming galaxies'. In: *The Astrophysical Journal* 767 (1), p. 88.

White, Frenk and Davis (1983). 'Clustering in a neutrino-dominated universe'. In: *The Astrophysical Journal* 274, pp. L1–L5.

White, S. D. and Rees, M. J. (1978). 'Core condensation in heavy halos: a two-stage theory for galaxy formation and clustering'. In: *Monthly Notices of the Royal Astronomical Society* 183 (3), pp. 341–358.

Whitehurst, R. N. and Roberts, M. S. (1972). 'High-Velocity Neutral Hydrogen in the Central Region of the Andromeda Galaxy'. In: *The Astrophysical Journal* 175, p. 347.

Wilczek, F. (1978). 'Problem of Strong P and T Invariance in the Presence of Instantons'. In: *Physical Review Letters* 40 (5), p. 279.

Witt, H. J. and Mao, S. (1997). 'Probing the structure of lensing galaxies with quadruple lenses: the effect of 'external' shear'. In: *Monthly Notices of the Royal Astronomy Society* 291 (1), pp. 211–218.

Wong, K. C., Keeton, C. R., Williams, K. A., Momcheva, I. G. and Zabludoff, A. I. (2010). 'The effect of environment on shear in strong gravitational lenses'. In: *The Astrophysical Journal* 726 (2), p. 84.

Zwicky, F. (1937). 'On the Masses of Nebulae and of Clusters of Nebulae'. In: *The Astrophysical Journal* 86, p. 217.

Zwicky, F. (1933). 'The Redshift of Extragalactic Nebulae'. In: *Helvetica Physica Acta* 6, pp. 110–127.

Colophon

This Thesis is based on a template developed by Matthew Townson and Andrew Reeves. It was typeset with LaTeX 2_ε. It was created using the *memoir* package, maintained by Lars Madsen, with the *madsen* chapter style. The font used is Latin Modern, derived from fonts designed by Donald E. Kunith.